DISSERTATION / DOCTORAL THESIS

Titel der Dissertation / Title of the Doctoral Thesis

"Observational tests of an inhomogeneous cosmology"

verfasst von / submitted by

Mag. Christoph Saulder, Bakk. BSc

angestrebter akademischer Grad / in partial fulfilment of the requirements of the degree of

Doktor der Naturwissenschaften (Dr.rer.nat)

Wien, 2015 / Vienna 2015

Abstract

An observational test, which distinguishes between Λ-CDM cosmology and an alternative theory called timescape cosmology, is presented in this thesis. The latter theory may be able to explain the observed accelerated expansion of the universe only in terms of General Relativity without the need for a cosmological constant. That theory considers the observed inhomogeneities and predicts different expansion rates for voids and walls (filaments/clusters). To test this, an analysis of systematic variations in the local Hubble flow is required. The fundamental plane of elliptical galaxies is calibrated and used as a distance indicator for this investigation. Furthermore, a solid model of the matter distribution in the local universe is derived using SDSS and 2MRS data. Mock catalogues based on the Millennium simulation are created to compare the predictions of Λ-CDM cosmology and timescape cosmology with the observations. The collected data and mock catalogues undergo a detailed analysis to unravel if dark energy is indeed necessary to explain the accelerated expansion of the universe or if it is just a back-reaction effect from General Relativity. Strong indications were found that timescape cosmology cannot explain the accelerated expansion and that Λ-CDM cosmology is the, according to the observations, preferred model instead.

Contents

Chapter 1

Introduction

The main aim of this thesis is to provide an observational test of a cosmological theory called "timescape cosmology" (Wiltshire, 2007). This test is performed by comparing observational data to predictions from the standard model (Λ-CDM cosmology) and this alternative theory. Both theories explain the observed accelerated expansion (Riess et al., 1998; Perlmutter et al., 1999; Schmidt et al., 1998) of the universe, a phenomenon whose discovery was awarded with the Nobel prize in 2011[1], however in two radically different ways. The Λ-CDM cosmology introduces a new parameter/concept called dark energy to account for that effect, while timescape cosmology attributes it to backreactions from General relativity due to the inhomogeneous structure of the universe. Both theories are explained in greater detail later in the thesis. The idea of the test is to discriminate between the two theories by looking for a specific signal in the observational data, which is predicted in one theory, but not present in the other. Specifically, as outlined by Schwarz (2010), timescape cosmology predicts that the expansion of the universe occurs at a different speed in cosmological voids than in cosmological walls (clusters, filaments, etc.). The initial concept of the test is outlined in my proceedings paper (Saulder et al., 2012) (Paper I, hereafter), which is discussed in detail in Chapter 3. To provide a solid test, one has to consider and measure all possible biases and calibrate the tools required for the test very carefully to minimize systematic effects. Most of my thesis is about this last point.

The suggested test requires a dataset containing redshift measurements of as many galaxies as possible combined with a redshift-independent distance indicator. I chose the fundamental plane of elliptical galaxies to serve this purpose. The fundamental plane of elliptical galaxies (Dressler et al., 1987; Djorgovski & Davis, 1987) is a well-known empirical relation between three global parameters of early-type galaxies. It can be used as a reliable distance indicator after some careful calibrations, which are discussed and performed in my corresponding paper (Saulder et al., 2013) (Paper II, hereafter). This paper largely forms Chapter 4 of my thesis. Further improvement of the fundamental plane calibration can be found in Appendix A of Saulder et al. (2015) (Paper III hereafter, also see Chapter 5). Aside from the redshift-independent distance indicator, my test also requires a complete and reliable model of the matter distribution in the local universe. To this end, I use spectroscopic data from the SDSS (Ahn et al., 2014) and the 2MRS (Huchra et al., 2012b) and search for galaxy groups in it using a Friend-of-Friend algorithm inspired by Robotham et al. (2011). The results are presented in my submitted paper on this subject (Saulder et. al 2015b, Paper IV hereafter), which is discussed in Chapter 6.

---

[1] http://www.nobelprize.org/nobel_prizes/physics/laureates/2011/

With all tools and data at hand, I present the results of this test in the final chapters of my thesis.

Over the course of a large scale project like this, lots of data are acquired and processed, yielding additional results on the way and creating secondary research objectives alongside. The refereed papers that I published over the course of my thesis, except for the proceedings paper (Paper I), which only outlines the basic idea of the test, can stand on their own. Paper II contains the fundamental plane calibrations in all details. Paper III drifts a little bit aside from the main topic of this thesis. It considers a sample of the most extreme (the most compact high central velocity dispersion) early-type galaxies and helped to understand them better. In the process, it lead to a further improvement of the fundamental plane calibrations. In Paper IV, galaxy group catalogues based on SDSS (Sloan Digital Sky Survey, Stoughton et al. (2002); Ahn et al. (2014)) and 2MRS (2MASS Redshift Survey, Huchra et al. (2012b,a)) are provided alongside the model of matter distribution in the local universe ($z <\sim 0.1$), which is based on the before mentioned catalogues. In the following chapter, I present a summary of the current status of research of the most relevant topics for my thesis.

Chapter 2

Status of research

2.1 Dark energy and cosmology
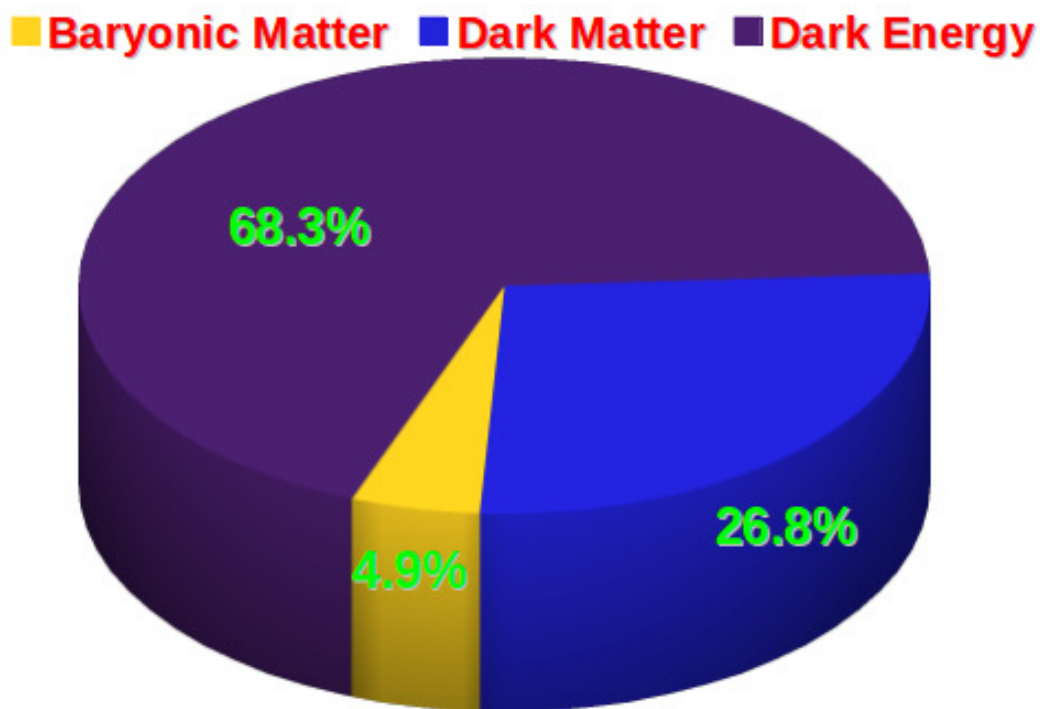
Figure 2.1: The energy content of the universe based on data from the Planck Collaboration et al. (2013).

According to the cosmological standard model (Λ-CDM model), the universe consists of about 68% dark energy, 27% dark matter and 5% baryonic matter (see Figure 2.1) and it is about 13.8 Gyr old (Planck Collaboration et al., 2013). This model provides a widely accepted and successful description of the general behaviour and appearance of our universe. But there is a big problem: more than 95% of the total energy content of the universe is hidden from direct observations. The nature of dark matter is still an enigma, while there are some observations that provide direct evidence for its existence (Clowe et al., 2006). Dark energy, which makes up more than 2/3rd of the universe's total energy content, is the greatest mystery in cosmology today. For more than one decade its true

nature puzzles physicists and astronomers alike. There have been numerous attempts (e.g. Zlatev et al. (1999); Steinhardt et al. (1999); Armendariz-Picon et al. (2000); Kai et al. (2007); Mavromatos (2007); Alexander et al. (2009)) to explain this phenomenon. The current model, a cosmological constant, is actually a very old idea, which got revived after the discovery of the accelerated expansion of the universe, because it provides a relatively simple way to fit the observed data. The cosmological constant Λ is added to the Einstein equations.

$$R_{\mu\nu} - \frac{1}{2}g_{\mu\nu}R + \Lambda g_{\mu\nu} = \frac{8\pi G}{c^4}T_{\mu\nu} \tag{2.1}$$

$R_{\mu\nu}$ is the Ricci-Tensor and R is the Ricci-Scalar, both depend on the metric $g_{\mu\nu}$ and its first and second derivative. G denotes the gravitational constant and c the speed of light. $T_{\mu\nu}$ is called the energy-momentum tensor and it describes the energy (and matter) content of the space-time (Peacock, 1999). The cosmological constant is only an effective model and a deeper physical motivation has not yet been clearly identified. E.g.: The value of the cosmological constant derived from quantum fields and standard model particle physics (Higgs condensate) is about 10^{56} times larger than the value actually measured (Bass, 2011). Basically all attempts to explain the accelerated expansion of the universe require either new physics (Λ as an extension of "classic" general relativity) or some special matter distribution (Zibin et al., 2008).

In contrast to this, it is also possible to take one step back to the very basics of modern cosmology, which will be done in the next subsection. The cosmological principle states that the universe is homogeneous and isotropic. However, this is not true on all scales: the universe is made of galaxies, clusters and voids and not a homogeneous distribution of stars, gas and dark matter. Only when one reaches scales of several 100 Mpc, one can average all smaller structures and the cosmological principle is fulfilled. The cosmological principle itself is very useful, because in the case of homogeneity and isotropy, one is able to find a simple solution of the Einstein field equations of general relativity. It is called the Friedmann-Lemaître-Robertson-Walker metric:

$$ds^2 = c^2 dt^2 - a(t)^2 \left[dr^2 + f(r) \left[d\theta^2 + \sin(\theta)d\phi^2 \right] \right] \tag{2.2}$$

The line element ds is given using spherical coordinates for the space components dr, $d\theta$ and $d\phi$ and the time coordinate dt. The function $f(r)$ depends on the global curvature of the universe and a is the dimensionless cosmological radius. The Friedman equations, which describe the general properties of the universe, can be derived using that metric.

$$H^2 = \left(\frac{\dot{a}}{a}\right)^2 = \frac{8\pi G}{3c^2}\rho - \frac{Kc^2}{a^2}$$
$$\dot{H} + H^2 = \frac{\ddot{a}}{a} = -\frac{4\pi G}{3c^2}\left(\rho + 3p\right) \tag{2.3}$$

Here H is the Hubble parameter and the dot denotes the time derivative. The total energy density is given by ρ and p denotes the pressure. K is the curvature parameter, which can be either negative if the universe is open (hyperbolic geometry) or exactly 0 if the universe is flat (Euclidean geometry) or positive if the universe is closed (spherical geometry). The average energy density yields the global curvature of the universe and therefore the overall expansion behaviour. A relative energy density Ω of 1 corresponds to a flat universe. If the relative energy density is greater than 1, it will describe a closed universe and if it is less than 1, it corresponds to an open universe. The currently available data is consistent with a flat universe.
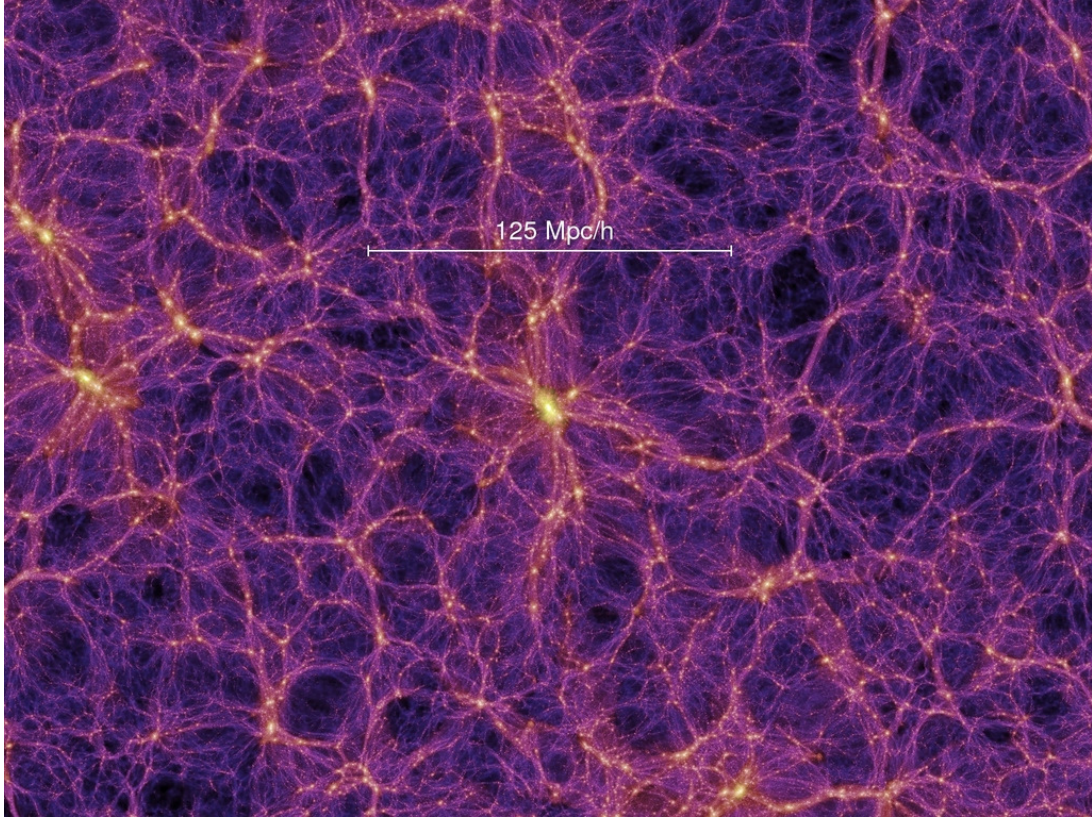
2.2 Timescape cosmology

Figure 2.2: A visualisation of cosmic web based on a numerical simulation (by MPA Garching, Millennium Simulation (Springel et al., 2005)).

Most research, which has been carried out on timescape cosmology so far, has been of theoretical nature. The general idea, that inhomogeneities have to be taken into account in cosmology, is already quite old (Tolman, 1934). The first notable consideration on this subject were done by Szekeres (1975), Ellis & Stoeger (1987), Ellis & Jaklitsch (1989) Zalaletdinov (1992) and Harwit (1995). Substantial progress has been made in the description of the effects of inhomogeneities in the context of general relativity during the past 15 years. The inhomogeneities' influence on the average properties of cosmological parameters was considered in several works (Buchert et al., 2000; Buchert, 2000a,b, 2001) using perturbation theory and general relativity. Since Einstein's field equations are a set of 10 non-linear partial differential equations, one can not average as usual (in the case of linear equation), if there are significant inhomogeneities (such as entirely empty voids and clusters with densities far higher than the critical density of the universe). A backreaction (feedback) caused by these inhomogeneities, is expected due to the non-linear nature of general relativity. This backreaction and a volume effect cause the observed (or "dressed") values of cosmological parameters to be different from the "real"(or bare) values (Buchert & Carfora, 2003). Therefore, one has to recalibrate cosmological measurements, which were made under the assumption of a homogeneous universe (Friedmann equations), in the framework of inhomogeneous cosmology. In the simple case of general relativistic dust, the equations, which describe the cosmic expansion, have to be modified to the Buchert's

scheme (Buchert, 2000b).

$$3\left(\frac{\dot{\bar{a}}}{\bar{a}}\right)^2 = 8\pi G \left\langle \rho \right\rangle - \frac{1}{2} \left\langle R \right\rangle - \frac{1}{2} Q$$

$$3\frac{\ddot{\bar{a}}}{\bar{a}} = -4\pi G \left\langle \rho \right\rangle + Q$$

$$\partial_t \left\langle \rho \right\rangle + \frac{\ddot{\bar{a}}}{\bar{a}} \left\langle \rho \right\rangle = 0$$

$$Q = \frac{2}{3} \left\langle (\theta - \left\langle \theta \right\rangle)^2 \right\rangle - 2 \left\langle \sigma \right\rangle^2 \tag{2.4}$$

The backreaction Q is defined by the expansion θ and the shear σ on a compact domain
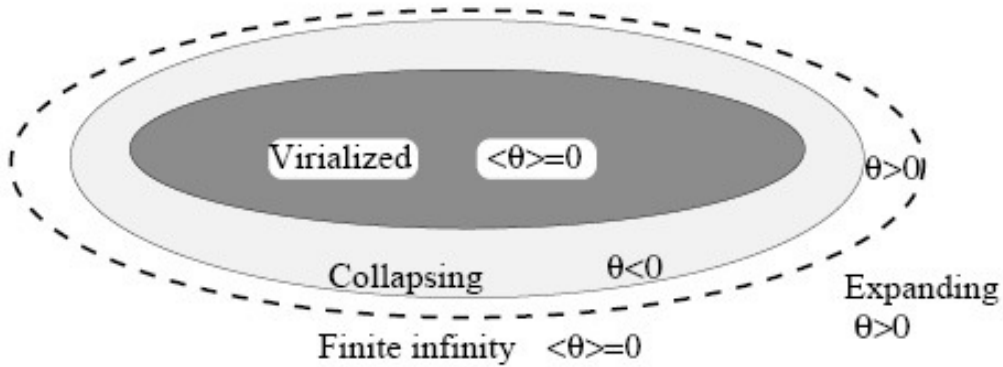

Figure 2.3: A schematic illustration of the concept of finite infinity. A more detail description of this new concept can be found in Wiltshire (2007).

$D.$ The variable $\bar{a}$ is a redefined (bare) cosmological radius based only on the spatial part of the local metric and R an analogously redefined curvature parameter.

A few years later we learned that the acceleration expansion of the universe cannot be fully understood in a simple pertubative approach alone (Räsänen, 2006; Kolb et al., 2006; Ishibashi & Wald, 2006).

The most advanced model of an inhomogeneous cosmology, which can mimic dark energy, was created by David Wiltshire and it is called "timescape cosmology" (Wiltshire, 2007). It uses a simple two-phase model (with a fractal bubble or Swiss cheese like distribution of matter) consisting of empty voids and dense walls (clusters and filaments). Hence, the matter distribution in this model is a simplified cosmic web (see Figure 2.2). The concept of finite infinity (Ellis (1984); Wiltshire (2007), also see Figure 2.3) is introduced, which marks the boundary between regions that may become gravitationally bound and regions that are expanding freely due to the Hubble flow. In the timescape model, one has to treat both areas independently. Inside a finite infinity boundary, the average geometry can be approximated to be flat, while voids are defined by an open geometry. In this model, the backreactions cause significant differences in the time flow, due to effects of quasilocal gravitational energy, so that the universe in the middle of a void is older than in the centre of a cluster by several Gigayears (due to this effect, this specific theory of inhomogeneous cosmology is also called "timescape cosmology"). The empty voids, which locally have an open geometry, expand faster than the dense walls

with their locally flat geometry. In a simplified pictures this means that at large scales these different expansion rates are manifested in an apparent accelerated expansion of the universe for an observer located in wall-environment, because the fraction of the total volume in the universe occupied by voids constantly increases due to their higher expansion rate and structure formation. Consequently, the average expansion rate approaches the void expansion rate in later times. The dynamics of this fractal bubble model can be described by following equations.

$$\left(\frac{\dot{\bar{a}}}{\bar{a}}\right)^2 + \frac{\dot{f}_v^2}{9 f_v \left(1 - f_v\right)} - \frac{\alpha^2 f_v^{\frac{1}{3}}}{\bar{a}^2} = \frac{8\pi G}{3} \bar{\rho}_0 \frac{\bar{a}_0^3}{\bar{a}^3}$$

$$\ddot{f}_v + \frac{\dot{f}_v^2 \left(2 f_v - 1\right)}{2 f_v \left(1 - f_v\right)} + 3 \frac{\dot{\bar{a}}}{\bar{a}} \dot{f}_v - \frac{3 \alpha^2 f_v^{\frac{1}{3}} \left(1 - f_v\right)}{2 \bar{a}^2} = 0 \tag{2.5}$$

The variable f_v denotes the volume fraction of voids in the universe, which is of course time dependent. The parameter α^2 depends on the curvature and ρ_0 is the critical density.

Timescape cosmology and similar inhomogeneous cosmologies might be possible solutions for the dark energy problem, but estimates of the magnitude of the backreactions from inhomogeneities and their influence on the expansion of the universe are difficult and range from negligible to extremely important (Marra & Pääkkönen, 2010; Mattsson & Mattsson, 2010; Kwan et al., 2009; Clarkson et al., 2009; Paranjape, 2009; van den Hoogen, 2010). Lately, also new arguments appeared that if backreactions are not be a sufficiently strong effect to get rid of dark energy completely, they will have an impact on the cosmological parameters and distance measurements on a few percent level (Clarkson et al., 2012; Umeh et al., 2014a,b; Clarkson et al., 2014). In contrast to these claims, the calculations of Kaiser & Peacock (2015) suggest that such an effect would be insignificantly tiny, which is supported by other recent work (Lavinto & Rasanen, 2015). This shows that observational tests for timescape cosmology are essential for the ongoing debate and may also help to better understand similar models. Wiltshire proposes several tests for timescape cosmology (Wiltshire, 2010, 2011), most of which are rather complex. So far, they have not been able to produce striking evidence neither for nor against timescape cosmology. But there is a rather simple, yet labour-intensive, experiment, which will be able to decide if timescape cosmology provides an accurate description of the universe or not.

As already mentioned before, voids expand faster than walls in the framework of timescape cosmology. The difference in the expansion rate should be measurable at cosmologically small scales (a few hundred Mpc) (Schwarz, 2010). If one observes a galaxy by looking through a void, its redshift is expected to be greater than that of another galaxy at the same distance observed along a wall. Assuming that timescape cosmology is a valid description of the universe, the Hubble parameter for dense environment is expected to be $\sim$50 km s^{-1} Mpc^{-1} and the empty voids to be $\sim$65 km s^{-1} Mpc^{-1} (Wiltshire, 2007; Leith et al., 2008) according to the best fit on supernovae Typ Ia (Riess et al., 2007), CMB (Bennett et al., 2003; Spergel et al., 2007) and Baryonic acoustic oscillations (Cole et al., 2005; Eisenstein et al., 2005) data within the framework of the simple two phase model presented in Wiltshire (2007). Adopting those values, timescape cosmology can reproduce the observed accelerated expansion without having to introduce dark energy. The measured Hubble parameter depends on the density profile of the line of sight to a galaxy. Since voids make up the largest volume fraction of the universe now, the value of the average observed Hubble parameter should be close to the one of the void environment. For the same reason, it will be relatively easy to find galaxies with many voids in

the line of sight. Finding and observing galaxies with mainly a high density environment in line of sight, which means the bigger part of the line of sight is located within finite infinity regions, will be more difficult. To test the validity of timescape cosmology using this feature, one has to compare the redshift of a galaxy to another independent distance indicator or standard candle to calculate its "individual Hubble parameter" (the Hubble parameter measured for one singular galaxy or cluster). Since the area of interest for this investigation ranges up to a few 100 Mpc, it cannot be covered by Cepheid variable stars with present observing tools and supernovae type Ia are too rare. Consequently, one has to use techniques like the surface brightness fluctuation method, the fundamental plane of elliptical galaxies, the Tully-Fischer relation or similar methods. Since any variances of the Hubble flow (except due to coherent infall of galaxies into clusters) should not depend on the line of sight density in the Λ-CDM model, discovering these would provide strong support for timescape cosmology (Wiltshire, 2011).

Additional motivation is found in observational claims that galaxies at the other side of voids indeed have larger than expected redshifts (Tomita, 2001; Tikhonov & Karachentsev, 2006). Nevertheless, this has to be investigated systematically on a large area of the sky and compared to mock catalogues to find conclusive and statistically relevant evidence.

2.3   Early-type galaxies

Early-type galaxies are the main tool in my thesis, but also objects of investigation. Early-type galaxies, generally speaking, have a relatively simple morphology, very little cold gas and consequently an extremely low star formation rate, and they are dominated by the light of old red stellar populations. Their smooth profiles make them well suited to be studied in large-scale survey by automated pipelines, which is one of the main arguments for choosing them as tools for this thesis.

When looking into more detail on early-type galaxies, they turn out to be complex objects. Especially their kinematics are highly complex. The vast majority of early-type galaxies are fast rotators (Emsellem et al., 2011), which exhibit a regular rotation throughout the galaxy. About 15% (Emsellem et al., 2011) are slow rotators, which are generally more massive than fast rotators and often posses kinematically distinct cores and complex stellar velocity fields (Krajnović et al., 2011; Emsellem et al., 2011). The fast rotators on the other hand are very similar to spiral galaxies, but with most of the gas and dust removed and star-formation ceased (Cappellari et al., 2011). By their morphological appearance, they are typically classified as lenticular galaxies or elliptical galaxies with disky isophotes (Cappellari et al., 2011).

Due to the, with very few exceptions (Crocker et al., 2009), very low to zero star formation rate, the light of the early-type galaxies is dominated by old red populations. Hence they form the red sequence (Gladders et al., 1998; Bell et al., 2004; Harker et al., 2006; Graves et al., 2009a,b; Graves & Faber, 2010; Graves et al., 2010; Bundy et al., 2010; Chilingarian & Zolotukhin, 2012) in a colour magnitude diagram of galaxies (Wyder et al., 2007; Martin et al., 2007) opposed to the blue cloud (Nandra et al., 2007; Coil et al., 2008; Simon et al., 2009; Schawinski, 2009; Zehavi et al., 2011; Basu et al., 2015), where most late-type galaxies can be found. The photometric profiles of early-type galaxies are in general relative simple and smooth. They can be well-fitted by de Vaucoleurs profiles and even better by Sersic profiles and only a small fraction of early-type galaxies show significant peculiar features (Krajnović et al., 2011). Most slow-rotating early-type galaxies have boxy isophotes and show signs of an underlying triaxial structure and anisotropic velocity fields (Cappellari et al., 2007).

The properties of early type galaxies follow several scaling relation such as the CO Tully-Fisher relation (Davis et al., 2011), the M-σ relation (Ferrarese & Merritt, 2000; Gebhardt et al., 2000) and the fundamental plane (Dressler et al., 1987; Djorgovski & Davis, 1987) and its projections like the Faber-Jackson relation. The fundamental plane will be discussed in great detail in Chapter 4.

Among the broad category of early-type galaxies, several groups of exotic objects can be found. One example are extremely compact massive galaxies, which will be discussed in detail in Chapter 5. Recently an isolated giant elliptical galaxy (NGC 7507) was found to be (almost) dark matter free (Lane et al., 2014) and Nigoche-Netro et al. (2014) showed that there might be some early-type galaxies with much lower dark matter ratios in the inner areas than expected. Early-type galaxies cover a wide range in mass and size, but are connected by strong morphological similarities. Despite complex inner kinematics, they follow several tight scaling relations such as the later used fundamental plane.

Chapter 3

Observational Aspects of an Inhomogeneous Cosmology

The conference proceedings paper presented in this chapter describes the initial concept of the test of timescape cosmology. Over the further course of the research project several effects and biases, which were not yet considered at that stage of the research, were included in the test design. Furthermore, newer and better calibrations were used in the final results than for the preliminary data presented here. However, the main idea behind the test remained unchanged: I compare expansion rates of voids and wall, which should be notably different according to timescape cosmology. If different expansion rates are detected, it will provide support for this alternative theory, if they are not detected, it will strongly disqualify that theory. This proceedings paper provides a good introduction into my work.

The conference proceedings paper "Observational Aspects of an Inhomogeneous Cosmology" was published in Proceedings of VIII International Workshop on the Dark Side of the Universe (DSU 2012). June 10-15, 2012. Buzios, Rio de Janeiro, Brasil [1]. As the first author of this paper, I have written the entire text. Steffen Mieske and Werner Zeilinger helped me in proof-reading the text and straightening out the discussion. Furthermore, I mention their assistance in designing the test presented in the proceedings paper.

---

[1]More information is available on ADS: `http://adsabs.harvard.edu/abs/2012dsu..workE..18S`

Observational Aspects of an Inhomogeneous Cosmology

Christoph Saulder[*]

European Southern Observatory, Chile & Department of Astrophysics, University of Vienna
E-mail: `csaulder@eso.org`

Steffen Mieske

European Southern Observatory, Chile
E-mail: `smieske@eso.org`

Werner W. Zeilinger

Department of Astrophysics, University of Vienna
E-mail: `werner.zeilinger@univie.ac.at`

One of the biggest mysteries in cosmology is Dark Energy, which is required to explain the accelerated expansion of the universe within the standard model. But maybe one can explain the observations without introducing new physics, by simply taking one step back and re-examining one of the basic concepts of cosmology, homogeneity. In standard cosmology, it is assumed that the universe is homogeneous, but this is not true at small scales (<200 Mpc). Since general relativity, which is the basis of modern cosmology, is a non-linear theory, one can expect some backreactions in the case of an inhomogeneous matter distribution. Estimates of the magnitude of these backreactions (feedback) range from insignificant to being perfectly able to explain the accelerated expansion of the universe. In the end, the only way to be sure is to test predictions of inhomogeneous cosmological theories, such as timescape cosmology, against observational data. If these theories provide a valid description of the universe, one expects aside other effects, that there is a dependence of the Hubble parameter on the line of sight matter distribution. The redshift of a galaxy, which is located at a certain distance, is expected to be smaller if the environment in the line of sight is mainly high density (clusters), rather than mainly low density environment (voids). Here we present a test for this prediction using redshifts and fundamental plane distances of elliptical galaxies obtained from SDSS DR8 data. In order to get solid statistics, which can handle the uncertainties in the distance estimate and the natural scatter due to peculiar motions, one has to systematically study a very large number of galaxies. Therefore, the SDSS forms a perfect basis for testing timescape cosmology and similar theories. The preliminary results of this cosmological test are shown in this contribution.

---

[*]Speaker.

1. Timescape cosmology

Inhomogeneous cosmology has been around since the days of Tolman [1] and Bondi [2], but for a very long time it was a rather quiet and exotic topic. During the last 15 years significant advances were made on this field, mainly due to the work of groups around Buchert [3, 4, 5, 6, 7, 8, 9, 10] , Räsänen [11, 12, 10, 13], Wiltshire [14, 15, 16, 17, 18] and others. The basic assumption is that since general relativity is a non-linear theory, inhomogeneities like voids and cluster can cause some backreactions (feedback) on cosmological parameters, which may explain the observed accelerated expansion of the universe. Buchert constructed a scheme [4], which is based on perturbation theory and general relativity, and it considers the inhomogeneities' influence on the average properties of cosmological parameters. In the simple case of a general relativistic dust, the equations, which describe the cosmic expansion, have to be modified to the Buchert's scheme:

$$3\left(\frac{\dot{\bar{a}}}{\bar{a}}\right)^2 = 8\pi G\langle\rho\rangle - \frac{1}{2}\langle R\rangle - \frac{1}{2}Q \qquad\qquad 3\frac{\ddot{\bar{a}}}{\bar{a}} = -4\pi G\langle\rho\rangle + Q$$
$$\partial_t\langle\rho\rangle + \frac{\dot{\bar{a}}}{\bar{a}}\langle\rho\rangle = 0 \qquad\qquad Q = \frac{2}{3}\left\langle(\theta-\langle\theta\rangle)^2\right\rangle - 2\langle\sigma\rangle^2 \tag{1.1}$$

The backreaction Q is defined by the expansion θ and the shear σ. $\bar{a}$ is the scaling parameter of the universe, $\langle R\rangle$ the average spatial curvature, $\langle\rho\rangle$ the average energy density and G the gravitational constant. But the acceleration of the universe's expansion cannot be fully understood in a simple pertubative approach alone [12, 19, 20]. One of the most advanced conceptions of an inhomogeneous cosmology, which can mimic dark energy, was created by Wiltshire [14] and it is called "timescape cosmology". He uses a simple two-phase model consisting of a fractal bubble of empty voids and dense walls (clusters and filaments). Both regions are separated by the finite infinity boundary (see Fig 1), which encloses gravitationally bound regions and disconnects them from the freely expanding voids. In this model, a backreaction also causes significant differences in the time
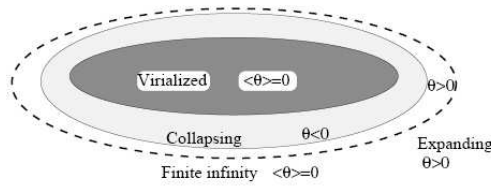
Figure 1: A schematic illustration of the concept of finite infinity (by David Wiltshire [14]).

flow, due to effects of quasilocal gravitational energy: the universe in the middle of a void is older than in the centre of a cluster. Due to this effect, this specific model of inhomogeneous cosmology is also called timescape cosmology. As a consequence of the importance of the local geometry in this model, the Hubble flow is not uniform any more and the empty voids expand faster than the dense walls. At large scales, these different expansion rates will lead to the signature of an overall accelerated expansion of the universe, because in timescape cosmology the fraction of the volume occupied by voids constantly increases with time. According to Wiltshire [14], the dynamics of

2

this fractal bubble model can be described by following equations:

$$\left(\frac{\dot{\bar{a}}}{\bar{a}}\right)^2 + \frac{\dot{f_v}^2}{9f_v(1-f_v)} - \frac{\alpha^2 f_v^{\frac{1}{3}}}{\bar{a}^2} = \frac{8\pi G}{3}\bar{\rho}_0\frac{\bar{a}_0^3}{\bar{a}^3}$$

$$\ddot{f_v} + \frac{\dot{f_v}^2(2f_v-1)}{2f_v(1-f_v)} + 3\frac{\dot{\bar{a}}}{\bar{a}}\dot{f_v} - \frac{3\alpha^2 f_v^{\frac{1}{3}}(1-f_v)}{2\bar{a}^2} = 0$$

(1.2)

The variable f_v denotes the volume fraction of voids in the universe, which is of course time dependent and $\bar{\rho}_0$ is the true critical density [14, 6, 8]. Recently there have been several papers [21, 22, 23, 24, 25, 26, 27, 18, 10] , which show that the magnitude and importance of these backreactions is still a topic of hot discussion. Timescape cosmology and similar inhomogeneous cosmologies may provide possible solutions for the dark energy problem, but the estimates of the magnitude of backreaction from voids and their influence on the expansion of the universe range from negligible to extremely important [28, 29, 26, 14]. Therefore, observational tests are essential for the ongoing debate.

2. Predictions of the theory

There are several predictions of timescape cosmology, which can be used as potential tests. Most of them are extremely difficult and not possible with today's technology or leave quite some space for interpretation and therefore, they cannot produce striking evidence neither for nor against the theory. Here we focus on a very direct test which was proposed [30, 17], namely measuring the different expansion rates of voids and walls directly. Those should differ by about 17 to 22% [18], in order to fully explain the observed accelerated expansion with timescape cosmology: The Hubble parameter is larger, if the foreground is void dominated, rather than wall dominated (for a better illustration of this feature see Fig. 2). This test requires: 1. redshift data, 2. a redshift independent
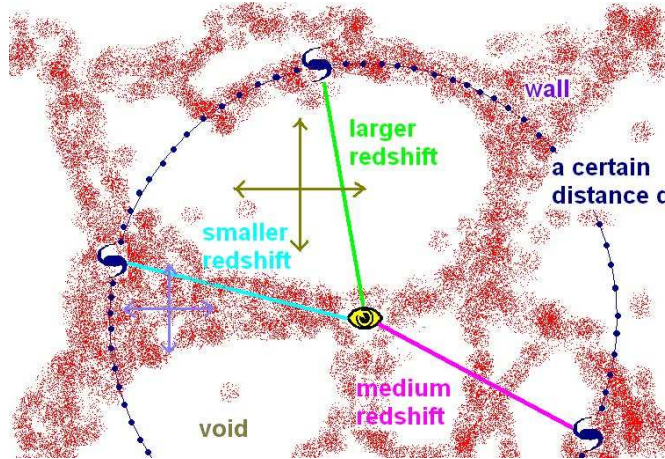

Figure 2: The measured redshift at a fixed distance depends on matter distribution in the line of sight.

distance indicator and 3. a model of the matter distribution in the line of sight. While performing

3

this test one might encounter potential problems like uncertainties in the distance measurement, peculiar motions of the galaxies and difficulties in mass estimates for matter distribution. Due to the statistical nature of these problems, one can handle them quite well using a large homogeneous sample.

3. Testing the predictions

We use data from the Sloan Digital Sky Survey (SDSS) DR8 [31] in order to perform our test. We take redshifts, central velocity dispersions, the different apparent model magnitudes in the 5 SDSS filters and the corresponding effective radii of these models from the SDSS DR8 database. Furthermore, we make use of third party information, which is also implemented in the SDSS database such as the extinction map of Schlegel [32] and Galaxy classification from the citizen-science project GalaxyZoo [33, 34], which is based on SDSS. In addition to that, we also use masses from the SDSS-based catalogue of groups and clusters by Yang et al. [35] and the new high-quality K-correction by Chilingarian et al. [36].

3.1 Calibrate the fundamental plane

The fundamental plane of elliptical galaxies is an empirical relation between the effective radius R_0, the mean surface brightness $-2.5 \cdot \log(I_0)$ and the central velocity dispersion σ_0 of these galaxies, which can be used as redshift independent distance indicator.

$$R_0 = a \cdot \log(I_0) + b \cdot \log(\sigma_0) + c \tag{3.1}$$

We calibrate this relation, in a similiar manner as Bernardi et al. [37] did, but using more than 90 000 elliptical galaxies from SDSS, which were classified by GalaxyZoo [33, 34] and by applying some additional constraints to avoid misclassifications. One can derive all three parameters of the fundamental plane directly from observables which are already in SDSS data only using the Schlegel extinction maps [32] and the Chiligarian K-corrections [36] for corrections. The resulting fit for r-band data can be seen in Fig. 3 for which we obtain a root mean square of about 10%. The results will be published in an upcoming paper (Saulder et al. 2012, in preparation). We will use the fundamental plane to calculate distances to a quality selected subsample of about 10 000 elliptical galaxies.

3.2 The foreground model

We use data of more than 350 000 galaxies to model the foreground. The masses of galaxy groups and clusters are taken from the Yang catalogue [35] and since it is only based on DR4, which has a smaller sky coverage than DR8, we extended it using mass-light ratios for all missing objects. We plan to do this more sophisticated in the future and create a similar (using the same methods) but larger catalogue as Yang et al. We calculate the radii of homogeneous spheres with renormalized critical density (finite infinity regions) around the clusters and galaxies in our foreground model. The distances for the objects in the foreground model are simply estimated using a redshift-distance relation. A part of our foreground model can be see in Fig. 4.

4
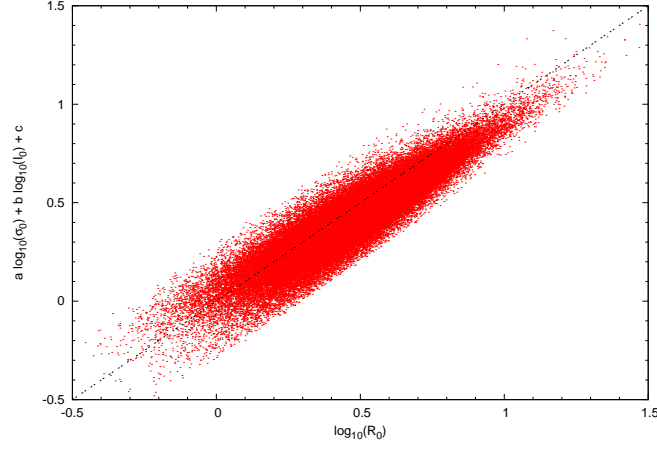
Figure 3: The fundamental plane of elliptical galaxies fitted for the SDSS r-band using 90 000 galaxies.
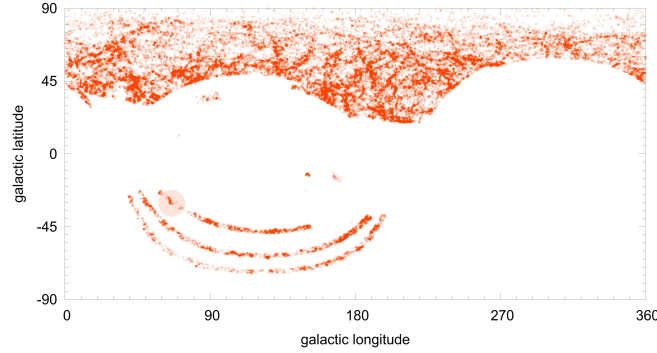
Figure 4: A part of the foreground model between 100 and 150 h^{-1} Mpc. One can also see the sky coverage of SDSS here.

3.3 Testing timescape cosmology

For the final analysis, we use redshifts and fundamental plane distances to calculate "individual Hubble parameters" for every galaxy in the sample. Furthermore, the fraction of the line of sight which is in wall environment (inside a finite infinity boundary) is calculated using the foreground model. This can be done using simple geometry (intersecting straight lines with spheres) and interval nesting, but it has to be done more than 10 000 × 350 000 times. Consequently, this requires a lot of computational power for which we use the ViennaAstroCluster. In a final step, one has to put the fraction of the line of sight inside wall environment in relation to the "individual Hubble parameters".

5

4. Preliminary results

Our preliminary analysis yields systematically larger Hubble parameters for low density environment (voids) in the line of sight (see Fig. 5). The distribution is not as smooth as may be expected, given the dearth of galaxies for void foreground and below average Hubble parameter. This is still a matter of concern for us in this analysis. It might be due to yet unknown biases or unknown systematic effects or maybe further improvements in the foreground model are necessary (Saulder et al. 2013b, in preparation). Concerning Fig. 5: The Λ-CDM estimate of no dependence on the line of sight environment at all is too naïve since it does not take into account coherent infall into clusters, which creates a similar effect of yet unknown magnitude (a comparison with large cosmological N-body simulations will be included in an upcoming paper (Saulder et al. 2013b, in preparation)). Furthermore, it should be noted that any fit to a distribution with such a scatter strongly depends on the fitting method (for example using a binned fit instead of the least square method for which the result is shown in Figure 5, one can get a very different dependence) and therefore, we cannot yet conclude any clear evidence although the preliminary data looks promising. We also want to point out that this project creates quite some additional science output on its
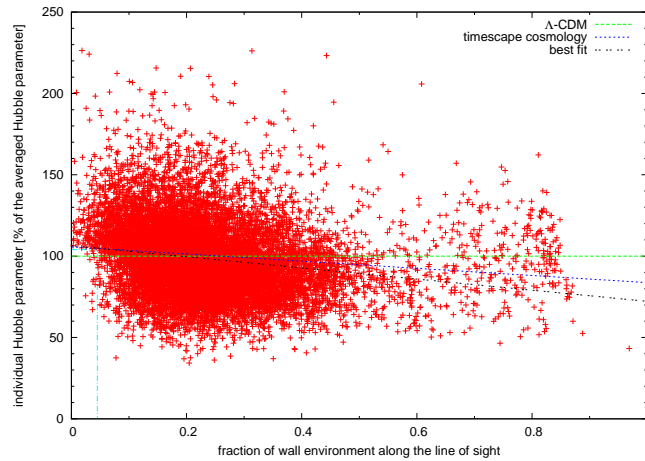

Figure 5: This plot shows the dependence of the Hubble parameter on the foreground matter distribution.

way, because we obtain new fits for the fundamental plane (Saulder et. al, 2013a in preparation) and it yields lots of data on peculiar velocities of galaxies and on the large scale structure of the local universe aside from testing timescape cosmology.

Acknowledgements

6

References

[1] R.C. Tolman, *Effect of Inhomogeneity on Cosmological Models*, *Proceedings of the National Academy of Science* **20** (1934) 169.

[2] H. Bondi, *Spherically symmetrical models in general relativity*, *MNRAS* **107** (1947) 410.

[3] T. Buchert, *Averaging inhomogenous cosmologies - a dialogue*, in proceedings of *Research in Particle-Astrophysics* (1997) 71 [arXiv:astro-ph/9706214].

[4] T. Buchert, *On Average Properties of Inhomogeneous Fluids in General Relativity: Dust Cosmologies*, *General Relativity and Gravitation* **32** (2000) 105 [arXiv:gr-qc/9906015].

[5] T. Buchert and M. Kerscher and C. Sicka, *Back reaction of inhomogeneities on the expansion: The evolution of cosmological parameters*, *PRD* **62** (2000) 4 [arXiv:astro-ph/9912347].

[6] T. Buchert and M. Carfora, *Regional averaging and scaling in relativistic cosmology*, *Classical and Quantum Gravity* **19** (2002) 6109 [arXiv:gr-qc/0210037].

[7] T. Buchert and M. Carfora, *The cosmic quartet: cosmological parameters of a smoothed inhomogeneous spacetime*, *Journal of Geophysical Research (Biogeosciences)* (2003) 157 [arXiv:astro-ph/0312621].

[8] T. Buchert and M. Carfora, *Cosmological Parameters Are Dressed*, *Physical Review Letters* **90** (2003) 3 [arXiv:gr-qc/0210045].

[9] J. Larena and J.-M. Alimi and T. Buchert and M. Kunz, *Testing backreaction effects with observations*, *PRD* **79** (2009) 8 [arXiv:0808.1161].

[10] T. Buchert and S. Räsänen, *Backreaction in late-time cosmology*, *ArXiv e-print* (2011) [arXiv:1112.5335].

[11] S. Räsänen, *Dark energy from back-reaction*, *JCAP* **2** (2004) 3 [arXiv:astro-ph/0311257].

[12] S. Räsänen, *Accelerated expansion from structure formation*, *JCAP* **15** (2006) 2141 [arXiv:astro-ph/0607626].

[13] S. Räsänen, *Backreaction: directions of progress*, *Classical and Quantum Gravity* **28** (2011) 16 [arXiv:1102.0408].

[14] D.L. Wiltshire, *Cosmic clocks, cosmic variance and cosmic averages*, *New Journal of Physics* **9** (2007) 377 [gr-qc/0702082].

[15] D.L. Wiltshire, *Exact Solution to the Averaging Problem in Cosmology*, *Physical Review Letters* **99** (2007) 25 [arXiv:0709.0732].

[16] B.M. Leith and S.C.C. Ng and D.L. Wiltshire, *Gravitational Energy as Dark Energy: Concordance of Cosmological Tests*, *APJL* **672** (2008) L91 [arXiv:0709.2535].

[17] D.L. Wiltshire, *Average observational quantities in the timescape cosmology*, *PRD* **80** (2009) 12 [arXiv:0909.0749].

[18] D.L. Wiltshire, *Gravitational energy as dark energy: Cosmic structure and apparent acceleration*, *ArXiv e-prints* (2011) [arXiv:1102.2045].

[19] E.W. Kolb and S. Matarrese and A. Riotto, *On cosmic acceleration without dark energy*, *New Journal of Physics* **8** (2006) 322 [arXiv:astro-ph/0506534].

[20] A. Ishibashi and R.M. Wald, *Can the acceleration of our universe be explained by the effects of inhomogeneities?*, *Classical and Quantum Gravity* **23** (2006) 235 [arXiv:gr-qc/0509108].

7

[21] N. Bose and A.S. Majumdar, *Future deceleration due to cosmic backreaction in presence of the event horizon*, *MNRAS* **418** (2011) L45 [arXiv:1010.5071].

[22] C. Clarkson and O. Umeh, *Is backreaction really small within concordance cosmology?*, *Classical and Quantum Gravity* **28** (2011) 16 [arXiv:1105.1886].

[23] O. Umeh and J. Larena and C. Clarkson, *The Hubble rate in averaged cosmology*, *JCAP* **3** (2011) 29 [arXiv:1011.3959].

[24] P. Bull and T. Clifton, *Local and nonlocal measures of acceleration in cosmology*, *PRD* **85** (2012) 10 [arXiv:1203.4479].

[25] T. Clifton and K. Rosquist and R. Tavakol, *An exact quantification of backreaction in relativistic cosmology*, *PRD* **86** (2012) 4 [arXiv:1203.6478].

[26] A. Paranjape and R.P. Singh, *Cosmic Inhomogeneities and Averaged Cosmological Dynamics*, *Physical Review Letters* **101** (2008) 18 [arXiv:0806.3497].

[27] B. Bochner, *Apparent Acceleration and an Alternative Concordance from Causal Backreaction*, *ArXiv e-prints* (2012) [arXiv:1207.6119].

[28] M. Mattsson and T. Mattsson, *On the role of shear in cosmological averaging II: large voids, non-empty voids and a network of different voids*, *JCAP* **5** (2011) 3 [arXiv:1012.4008].

[29] J. Kwan and M.J. Francis and G.F. Lewis, *Fractal Bubble cosmology: a concordant cosmological model?*, *MNRAS* **399** (2009) L6 [arXiv:0902.4249].

[30] D.J. Schwarz, *Cosmological backreaction*, *ArXiv e-prints* (2010) [arXiv:1003.3026].

[31] SDSS-III collaboration, *The Eighth Data Release of the Sloan Digital Sky Survey: First Data from SDSS-III*, *APJS* **193** (2011) 29 [arXiv:1101.1559].

[32] D.J. Schlegel and D.P. Finkbeiner and M. Davis, *Maps of Dust Infrared Emission for Use in Estimation of Reddening and Cosmic Microwave Background Radiation Foregrounds*, *APJ* **500** (1998) 525 [arXiv:astro-ph/9710327].

[33] C.J. Lintott and K. Schawinski and A. Slosar and K. Land and S. Bamford and D. Thomas and M.J. Raddick and R.C. Nichol and A. Szalaz and D. Andreescu and P. Murray and J. Vandenberg, *Galaxy Zoo: morphologies derived from visual inspection of galaxies from the Sloan Digital Sky Survey*, *MNRAS* **389** (2008) 1179 [arXiv:0804.4483].

[34] C.J. Lintott and K. Schawinski and S. Bamford and A. Slosar and K. Land and D. Thomas and E. Edmondson and K. Masters and R.C. Nichol and M.J. Raddick and A. Szalaz and D. Andreescu and P. Murray and J. Vandenberg, *Galaxy Zoo 1: data release of morphological classifications for nearly 900 000 galaxies*, *MNRAS* **389** (2011) 166 [arXiv:1007.3265].

[35] X. Yang and H.J. Mo and F.C. van den Bosch and A. Pasquali and C. Li and M. Barden, *Galaxy Groups in the SDSS DR4. I. The Catalog and Basic Properties*, *APJ* **671** (2007) 153 [arXiv:0707.4640].

[36] I.V. Chilingarian and A.L. Melchior and I.Y. Zolotukhin, *Analytical approximations of K-corrections in optical and near-infrared bands*, *MNRAS* **405** (2010) 1409 [arXiv:1002.2360].

[37] M. Bernardi and R.K. Sheth et al., *Early-Type Galaxies in the Sloan Digital Sky Survey. III. The Fundamental Plane*, *AJ* **125** (2003) 1866 [arXiv:astro-ph/0301626].

8

Chapter 4

Calibrating the fundamental plane with SDSS DR8 data

The test presented in my thesis requires a redshift-independent distance indicator. To this end, the fundamental plane of elliptical galaxies was chosen and calibrated in the paper presented in this chapter. I used the largest available sample at that time to calibrate the fundamental plane, which has so far only been surpassed by Joachimi et al. (2015) and in Paper III, which is presented in the next chapter. Our calibrations help us to understand the biases introduced by using early-type galaxies to our test, but also to minimize and better quantify the scatter of the fundamental plane and the uncertainties in our distance measurements. Therefore, this paper is a fundamental pillar of my cosmological test.

The paper "Calibrating the fundamental plane with SDSS DR8 data" was published in Astronomy & Astrophysics, Volume 557, id.A21, 36 pp [1]. As the first author of this paper, I wrote the majority of the text. Igor Chilingarian provided the coefficients of the K-corrections listed in Appendix C and he was also the driving force behind the Section 5.3 Correlations of the residuals. Werner Zeilinger and Steffen Mieske provided continuous assistance and help over the entire work leading to this paper. Furthermore, all collaborators were proof-readers of this paper and made several suggestions, which improved its quality.

---

[1]More information is available on ADS: `http://adsabs.harvard.edu/abs/2013A%26A...557A..21S`

Calibrating the fundamental plane with SDSS DR8 data

Christoph Saulder[1,2], Steffen Mieske[1], Werner W. Zeilinger[2], and Igor Chilingarian[3,4]

[1] European Southern Observatory, Alonso de Córdova 3107, Vitacura, Casilla 19001, Santiago, Chile
   e-mail: csaulder@eso.org,smieske@eso.org
[2] Department of Astrophysics, University of Vienna, Türkenschanzstraße 17, 1180 Vienna, Austria
   e-mail: werner.zeilinger@univie.ac.at
[3] Smithsonian Astrophysical Observatory, Harvard-Smithsonian Center for Astrophysics, 60 Garden St. MS09 Cambridge, MA
   02138, USA
   e-mail: igor.chilingarian@cfa.harvard.edu
[4] Sternberg Astronomical Institute, Moscow State University, 13 Universitetski prospect, 119992 Moscow, Russia

Abstract

We present a calibration of the fundamental plane using SDSS Data Release 8. We analysed about 93000 elliptical galaxies up to $z < 0.2$, the largest sample used for the calibration of the fundamental plane so far. We incorporated up-to-date K-corrections and used GalaxyZoo data to classify the galaxies in our sample. We derived independent fundamental plane fits in all five Sloan filters u, g, r, i and z. A direct fit using a volume-weighted least-squares method was applied to obtain the coefficients of the fundamental plane, which implicitly corrects for the Malmquist bias. We achieved an accuracy of 15% for the fundamental plane as a distance indicator. We provide a detailed discussion on the calibrations and their influence on the resulting fits. These re-calibrated fundamental plane relations form a well-suited anchor for large-scale peculiar-velocity studies in the nearby universe. In addition to the fundamental plane, we discuss the redshift distribution of the elliptical galaxies and their global parameters.

Key words. galaxies: elliptical and lenticular, cD – galaxies: distances and redshifts – galaxies: fundamental parameters – galaxies: statistics – galaxies: structure

1. Introduction

The fundamental plane is an empirical relation between three global parameters of elliptical galaxies: the central velocity dispersion σ_0, the physical effective radius R_0, and the mean surface brightness μ_0 within the effective radius. The last parameter is usually expressed as I_0, which is a renormalised surface brightness (see Equation 17). The functional form of the fundamental plane reads

$$\log_{10}(R_0) = a \cdot \log_{10}(\sigma_0) + b \cdot \log_{10}(I_0) + c. \qquad (1)$$

Historically, the fundamental plane of elliptical galaxies was first mentioned in Terlevich et al. (1981). It was defined and discussed in more detail in Dressler et al. (1987) and Djorgovski & Davis (1987). As part of an extensive study on elliptical galaxies (Bernardi et al. 2003a,b,c,d), the first work on the fundamental plane using SDSS data was done in Bernardi's paper (Bernardi et al. 2003c). Afterwards considerable work was done on the fundamental plane by a wide range of scientists e.g. D'Onofrio et al. (2008), La Barbera et al. (2008), Gargiulo et al. (2009), Hyde & Bernardi (2009), La Barbera et al. (2010a), Fraix-Burnet et al. (2010), and Magoulas et al. (2012).

The central velocity dispersion as well as the mean surface brightness are distance-independent quantities. Consequently, one can use the fundamental plane as a distance indicator by comparing the predicted effective radius with the observed one. We plan to use this standard-candle property of the fundamental plane in future work on the peculiar-velocity field in the nearby universe.

According to Bernardi et al. (2003c), a direct fit is the most suitable type of fit to obtain the fundamental plane coefficients if one plans on using them as a distance indicator, because it minimises the scatter in the physical radius R_0. Other types of fits also have their advantages, when using the fundamental plane for different applications (such as investigating the global properties of elliptical galaxies). In Table 1, we collect the results for the fundamental plane coefficient of previous literature work. As Bernardi et al. (2003c) already pointed out, the coefficients depend on the fitting method. Table 1 shows that the coefficient a is typically smaller for direct fits than for orthogonal fits.

On theoretical grounds, it is clear that virial equilibrium predicts interrelations between the three parameters R_0, σ_0, and I_0. The coefficients of the fundamental plane can be compared with these expectations from virial equilibrium, and a luminosity-independent mass-to-light (M/L) ratio for all elliptical galaxies. Virial equilibrium and constant M/L predicts $a = 2$ and $b = -1$. Any deviation (usually lower values for a and higher values for b) of these values is referred to as tilt in the literature. From Table 1 it is clear that the actual coefficients of the fundamental plane deviate from these simplified assumptions (e.g. a~1 instead of 2). The physical reasons that give rise to this deviation are obviously a matter of substantial debate in the literature since it provides fundamental information about galaxy evolution (Ciotti et al. 1996; Busarello et al. 1997, 1998; Graham & Colless 1997; Trujillo et al. 2004; D'Onofrio et al. 2006; Cappellari et al. 2006) or its environment dependence (Lucey et al. 1991; Jorgensen et al. 1996; Pahre et al. 1998; de Carvalho & Djorgovski 1992; La Barbera et al. 2010b). The empirical re-

1

parameter	condition
SpecObj.z	> 0
SpecObj.z	< 0.5
SpecObj.zWarning	$= 0$
zooVotes.p_el	> 0.8
zooVotes.nvote_tot	> 10
SpecObj.veldisp	> 100
SpecObj.veldisp	< 420
SpecObj.snMedian	> 10
SpecObj.class	=’GALAXY’
PhotoObj.deVAB_u	> 0.3
PhotoObj.deVAB_g	> 0.3
PhotoObj.deVAB_r	> 0.3
PhotoObj.deVAB_i	> 0.3
PhotoObj.deVAB_z	> 0.3
PhotoObj.lnLDeV_u	$> PhotoObj.lnLExp\_u$
PhotoObj.lnLDeV_g	$> PhotoObj.lnLExp\_g$
PhotoObj.lnLDeV_r	$> PhotoObj.lnLExp\_r$
PhotoObj.lnLDeV_i	$> PhotoObj.lnLExp\_i$
PhotoObj.lnLDeV_z	$> PhotoObj.lnLExp\_z$

Table 2. Selection criteria given in the language of the SDSS CAS-job queries. As a direct consequence of these requirements, we demand that there must be spectroscopic data for every galaxy in our sample. Hereby, we impose the target limit for galaxy spectroscopy of SDSS on our sample, which is a minimum Petrosian magnitude in the r band of 17.77 mag (Strauss et al. 2002).

lation as such is very well documented and is often used as a distance indicator.

There are several two-dimensional relations that can be derived from the fundamental plane: the Faber-Jackson relation (Faber & Jackson 1976) between the luminosity and the velocity dispersion, and the Kormendy relation (Kormendy 1977) between the luminosity and effective radius and the $D - \sigma$-relation (Dressler et al. 1987), which connects the photometric parameter D with the velocity dispersion σ.

In this paper, we provide a calibration of the fundamental plane for usage as a distance indicator, using a sample of about 93000 elliptical galaxies from the eighth data release of the Sloan Digital Sky Survey (SDSS DR8) (Aihara et al. 2011). This doubles the sample of the most extensive FP calibration in the present literature (Hyde & Bernardi 2009). We assumed a Λ-CDM cosmology with a relative dark-energy density of $\Omega_\Lambda = 0.7$ and and a relative matter density of $\Omega_M = 0.3$ as well as a present-day Hubble parameter of $H_0 = 70 \, \mathrm{km \, s^{-1} \, Mpc^{-1}}$. One can use the parameter h_{70} to rescale the results for any other choice of the Hubble parameter.

2. Sample

2.1. Definition

Our starting sample consisted of 100427 elliptical galaxies from SDSS DR8 (Aihara et al. 2011). These galaxies were selected by the following criteria, as also summarised in Table 2:

The redshift z has to be between 0 and 0.5. Furthermore, to ensure that the redshift measurements were trustworthy, the *SpecObj.zWarning* flag had to be 0. For the morphological selection we made use of the citizen science project GalaxyZoo (Lintott et al. 2008), in which volunteers on the internet classify SDSS galaxies in a simplified manner (no scientific background required). The results of these visual classifications (Lintott et al. 2011) were integrated into the SDSS query form. To obtain a

Figure 1. Randomly selected subsample of 12 galaxies of our selected sample with a redshift lower than 0.1. All of them were classified to be elliptical galaxies by our selection criteria, which is confirmed by their morphology.

reasonable sample of elliptical galaxies with only a small number of misclassification, we demanded that the probability that a galaxy is an elliptical is greater than 0.8 and that at least ten GalaxyZoo users classified it. This probability is the fraction of all users who classified the given galaxy as elliptical. It would make no sense to set the parameter to 1 in the query because this would exclude too many galaxies since many users occasionally misclassify a galaxy by accident or trolling. Based on criterion, GalaxyZoo provided 170234 candidates for elliptical galaxies within the given redshift range of 0 and 0.5.

To reduce the number of misqualifications and to ensure the quality of our data set, we applied the following criteria. The signal-to-noise ratio of the spectra had to be higher than 10 and the central velocity dispersion of every galaxy in our sample had to be higher than 100 km/s and lower than 420 km/s. In general, velocity dispersion measurements of SDSS are only recommended to be used if they are between 70 and 420 km/s. Our choice of 100 km/s as lower limit is an additional precaution to avoid contamination of our sample by misclassification, because we found that a significant number of galaxies with a low central velocity dispersion (<100 km/s) are misclassified as elliptical galaxies by GalaxyZoo, although most of them actually are bulge-dominated spiral galaxies, as we found be taking a small random sample and visually inspecting the imaging and spectroscopic data. Furthermore, the spectrum has to be identified by the SDSS pipeline to be of a galaxy, and the likelihood

2

band	a	b	c	σ_{dist} [%]	N_{gal}	type of fit	authors
B	1.39 ± 0.14	-0.90 ± 0.09	-	20	106	2-step inverse R	Djorgovski & Davis (1987)
B	1.33 ± 0.05	-0.83 ± 0.03	-	20	97	inverse R	Dressler et al. (1987)
V+R	1.43 ± 0.03	-0.84 ± 0.02	-7.995 ± 0.021	21	694	inverse R	Smith et al. (2001)
R	1.38 ± 0.04	-0.82 ± 0.03	-	21	352	inverse R	Hudson et al. (1997)
R	1.37 ± 0.05	-0.84 ± 0.03	-	21	428	inverse R	Gibbons et al. (2001)
V	1.26 ± 0.07	-0.82 ± 0.09	-	13	66	forward R	Lucey et al. (1991)
V	1.14	-0.79	-	17	37	forward R	Guzman et al. (1993)
r	1.24 ± 0.07	-0.82 ± 0.02	-	17	226	orthogonal R	Jorgensen et al. (1996)
R	1.25	-0.87	-	19	40	orthogonal R	Müller et al. (1998)
V	1.21 ± 0.05	-0.80 ± 0.01	-	-	-	orthogonal R	D'Onofrio et al. (2008)
r	1.42 ± 0.05	-0.76 ± 0.008	-	28	1430	orthogonal R	La Barbera et al. (2008)
K	1.53 ± 0.04	-0.77 ± 0.01	-	29	1430	orthogonal R	La Barbera et al. (2008)
R	1.35 ± 0.11	-0.81 ± 0.03	-	21	91	orthogonal R	Gargiulo et al. (2009)
g	1.40 ± 0.02	-0.76 ± 0.02	-8.858	31	46410	orthogonal R	Hyde & Bernardi (2009)
r	1.43 ± 0.02	-0.79 ± 0.02	-8.898	30	46410	orthogonal R	Hyde & Bernardi (2009)
i	1.46 ± 0.02	-0.80 ± 0.02	-8.891	29	46410	orthogonal R	Hyde & Bernardi (2009)
z	1.47 ± 0.02	-0.83 ± 0.02	-9.032	29	46410	orthogonal R	Hyde & Bernardi (2009)
g	1.38 ± 0.02	-0.788 ± 0.002	-9.13 ± 0.08	29	4467	orthogonal R	La Barbera et al. (2010a)
r	1.39 ± 0.02	-0.785 ± 0.002	-8.84 ± 0.06	26	4478	orthogonal R	La Barbera et al. (2010a)
i	1.43 ± 0.02	-0.780 ± 0.002	-8.76 ± 0.05	-	4455	orthogonal R	La Barbera et al. (2010a)
z	1.42 ± 0.02	-0.793 ± 0.002	-8.74 ± 0.07	-	4319	orthogonal R	La Barbera et al. (2010a)
Y	1.47 ± 0.02	-0.785 ± 0.002	-8.53 ± 0.06	-	4404	orthogonal R	La Barbera et al. (2010a)
J	1.53 ± 0.02	-0.795 ± 0.002	-8.57 ± 0.06	26	4317	orthogonal R	La Barbera et al. (2010a)
H	1.56 ± 0.02	-0.795 ± 0.002	-8.42 ± 0.08	27	4376	orthogonal R	La Barbera et al. (2010a)
K	1.55 ± 0.02	-0.790 ± 0.002	-8.24 ± 0.08	28	4350	orthogonal R	La Barbera et al. (2010a)
K	1.53 ± 0.08	-0.79 ± 0.03	-	21	251	orthogonal R	Pahre et al. (1998)
V	1.31 ± 0.13	-0.86 ± 0.10	-	14	30	orthogonal R	Kelson et al. (2000)
R	1.22 ± 0.09	-0.84 ± 0.03	-	20	255	orthogonal ML	Colless et al. (2001)
g	1.45 ± 0.06	-0.74 ± 0.01	-8.779 ± 0.029	25	5825	orthogonal ML	Bernardi et al. (2003c)
r	1.49 ± 0.05	-0.75 ± 0.01	-8.778 ± 0.020	23	8228	orthogonal ML	Bernardi et al. (2003c)
i	1.52 ± 0.04	-0.78 ± 0.01	-8.895 ± 0.021	23	8022	orthogonal ML	Bernardi et al. (2003c)
z	1.51 ± 0.04	-0.77 ± 0.01	-8.707 ± 0.023	22	7914	orthogonal ML	Bernardi et al. (2003c)
J	1.52 ± 0.03	-0.89 ± 0.008	-	30	8901	orthogonal ML	Magoulas et al. (2012)
H	1.47 ± 0.02	-0.88 ± 0.008	-	29	8568	orthogonal ML	Magoulas et al. (2012)
K	1.46 ± 0.02	-0.86 ± 0.008	-	29	8573	orthogonal ML	Magoulas et al. (2012)
g	1.08 ± 0.05	-0.74 ± 0.01	-8.033 ± 0.024	-	5825	direct ML	Bernardi et al. (2003c)
r	1.17 ± 0.04	-0.75 ± 0.01	-8.022 ± 0.020	-	8228	direct ML	Bernardi et al. (2003c)
i	1.21 ± 0.04	-0.77 ± 0.01	-8.164 ± 0.019	-	8022	direct ML	Bernardi et al. (2003c)
z	1.20 ± 0.04	-0.76 ± 0.01	-7.995 ± 0.021	-	7914	direct ML	Bernardi et al. (2003c)
g	1.12 ± 0.02	-0.74 ± 0.02	-8.046	-	46410	direct R	Hyde & Bernardi (2009)
r	1.17 ± 0.02	-0.76 ± 0.02	-8.086	-	46410	direct R	Hyde & Bernardi (2009)
i	1.20 ± 0.02	-0.76 ± 0.02	-8.048	-	46410	direct R	Hyde & Bernardi (2009)
z	1.23 ± 0.02	-0.78 ± 0.02	-8.216	-	46410	direct R	Hyde & Bernardi (2009)
I	1.25 ± 0.02	-0.79 ± 0.03	-	20	109	direct R	Scodeggio et al. (1998)
R	1.13 ± 0.03	-0.84 ± 0.01	8.53 ± 0.1	-	699	direct R	Fraix-Burnet et al. (2010)
u	0.798 ± 0.030	-0.700 ± 0.008	-7.53 ± 0.10	16.5	92953	direct R	this paper
g	$0.966 \pm \pm0.030$	-0.740 ± 0.013	-7.75 ± 0.13	15.6	92953	direct R	this paper
r	1.034 ± 0.030	-0.753 ± 0.013	-7.77 ± 0.13	15.3	92953	direct R	this paper
i	1.062 ± 0.030	-0.757 ± 0.013	-7.75 ± 0.13	15.0	92953	direct R	this paper
z	1.108 ± 0.030	-0.763 ± 0.013	-7.81 ± 0.13	14.8	92953	direct R	this paper

Table 1. A list of previous publications (we do not claim completeness) of fundamental plane coefficients, based on the list of Magoulas et al. (2012), which is itself based on the lists of Bernardi et al. (2003c) and Colless et al. (2001). It is sorted by method (note: R=regression, ML=maximum likelihood) and date of publication. Some of the values in the list cannot be found in the same form due to slightly different definitions in the referenced papers. We sometimes had to renormalise the coefficient b, when the fundamental plane was defined using with the mean surface brightness μ_0 instead of the parameter $\log_{10}(I_0)$. Furthermore, the coefficient c, if available, is always given for a Hubble parameter of $H_0 = 70\,\mathrm{km}\,\mathrm{s}^{-1}\,\mathrm{Mpc}^{-1}$ here, therefore we had to rescale it if other values of H_0 were used in the referenced paper. In addition to the fundamental plane coefficients a, b and if available c, the distance error σ_{dist} and the number of galaxies N_{gal} in the sample is given. Furthermore, we also list the type of fit (R = regression, ML = maximum likelihood), which was used to obtain the fundamental plane coefficient, because it is known that the coefficients not only depend on the wavelength, but also on the fitting method.

of a de Vaucouleurs fit on a galaxy has to be higher than the likelihood of an exponential fit, in all five SDSS filters. We also demanded the axis ratio derived from the de Vaucouleurs fit to be higher than 0.3 (which excludes all early-type galaxies later than E7) in all filters, thereby removing very elongated ellipti-cal and lenticular galaxies from our sample. In Figures 1 and 2, randomly selected SDSS colour thumbnails of our selected sample are shown. Their morphologies are all consistent with being ellipticals (some artificial apparent green/red granulation can occur in the colour composite), without obvious spiral/disk pat-
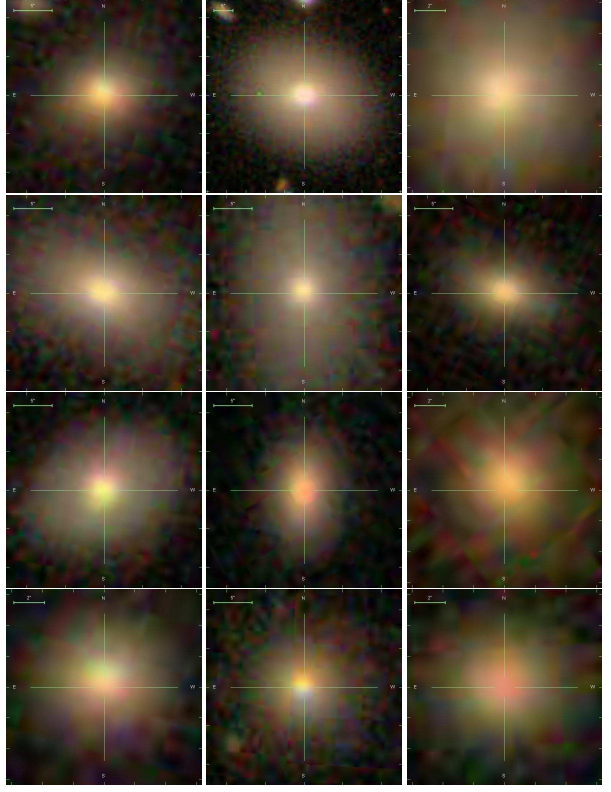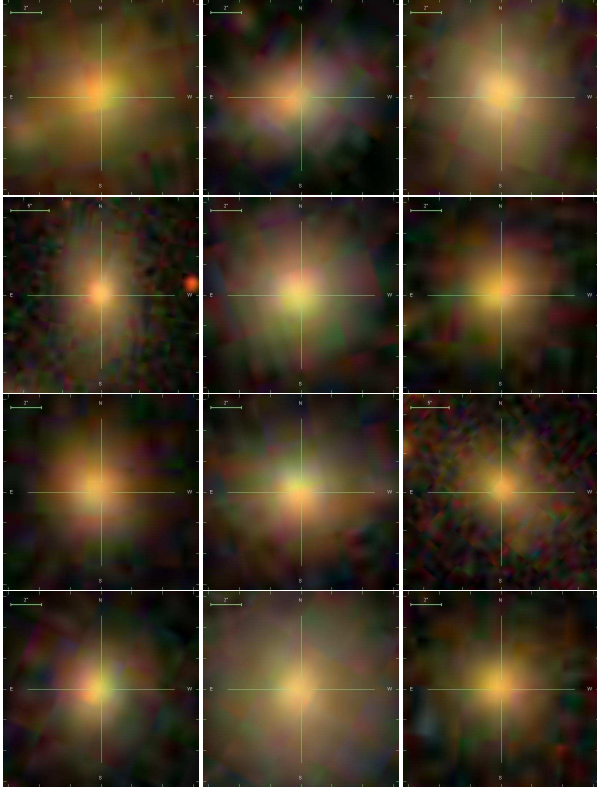
3

Figure 2. Randomly selected subsample of 12 galaxies of our selected sample with a redshift range of [0.1,0.2]. All of them were classified to be elliptical galaxies by our selection criteria, which is confirmed by their morphology.
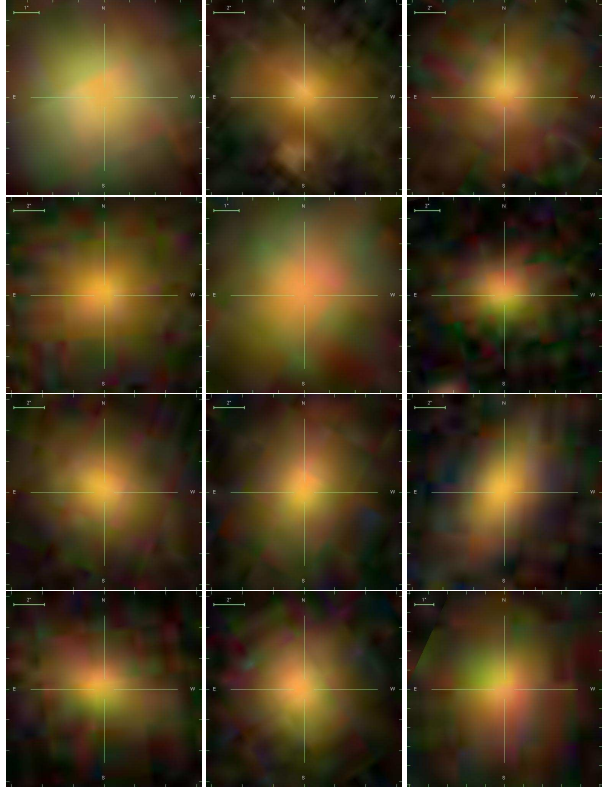

Figure 3. Randomly selected subsample of 12 galaxies of our extended sample (limited to a redshift lower than 0.2 for our main analysis) with a redshift higher than 0.2. All of them were classified to be elliptical galaxies by our selection criteria, which is confirmed by their morphology. Note that for some of the sources with the smallest angular extent, the SDSS colour-composite image becomes imprecise, causing the apparent rainbow-like colour structure.

terns, and overall smoothness. We thus conclude that our sample is sufficiently clean. For redshifts higher than 0.2, our set of criteria still yields a pretty clean sample as one can see in Figure 3. However, in Subsection 2.2 that our criteria create an additional bias at redshifts higher than 0.2, because an increasing fraction of galaxies is rejected due to uncertain classification.

There are 100427 galaxies in SDSS DR8 that fulfil all these requirements; they form our basic sample [1]. We downloaded the galactic coordinates *PhotoObj.b* and *PhotoObj.l*, the redshift *SpecObj.z* and its error *SpecObj.zErr*, the central velocity dispersion *SpecObj.veldisp* and its error *SpecObj.veldispErr*, the axis ratio of the de Vaucouleurs fit *PhotoObj.deVAB_filter*, the scale radius of the de Vaucouleurs fit *PhotoObj.deVRad_filter* and its error *PhotoObj.deVRadErr_filter*, the model magnitude of the de Vaucouleurs fit *PhotoObj.deVMag_filter* and its error *PhotoObj.deVMagErr_filter*, the magnitude of the composite model fit *PhotoObj.cModelMag_filter* and its error *PhotoObj.cModelMagErr_filter*, the scale radius of the Petrosian fit *PhotoObj.petroRad_filter* and its error *PhotoObj.petroRadErr_filter*, the model magnitude of the Petrosian fit *PhotoObj.petroMag_filter* and its error *PhotoObj.petroMagErr_filter* and the extinction values *PhotoObj.extinction_filter*, which are based on Schlegel maps (Schlegel et al. 1998), for all five SDSS filters (if a parameter is

---

[1] finer cuts in redshift and colours as well as a rejection of outliers will reduce this to about 93000 galaxies in the end, see next sections

available for different filters, the wild card *filter* is placed there, which can stand for either u, g, r, i, or z) and all galaxies in our basic sample. The SDSS filters have a central wavelength of 355.1 nm for u, 468.6 nm for g, 616.6 nm for r, 748.0 nm for i, and 893.2 nm for z (Stoughton et al. 2002).

In Figure 4, we consider the overall redshift distribution of our basic sample. In this Figure 4, we use redshifts corrected for the Milky Way's motion relative to the CMB, but note that the impact of the correction on the Figure is insignificant. Figure 4 shows that there are no galaxies in our sample with redshifts greater than 0.3. Furthermore, the number density decreases rapidly after a redshift of 0.15. We adopt a final cut at redshift of 0.2, since beyond that the sample is heavily biased towards only the most luminous galaxies. Quantitative motivation for the cut at a redshift of 0.2 comes from considering the Malmquist bias in detail, see Section 4.1. Moreover, we introduced a lower cut at a redshift of 0.01 to remove the galaxies for which peculiar velocities can notably distort the Hubble flow. The limitation of our sample to a redshift interval of [0.01,0.2] reduces the number of galaxies by roughly 5000. Furthermore, excluding some objects, with unreasonably large or small absolute magnitudes or physical radii removes a handful galaxies more. We also introduce a colour cut by demanding that the galaxies in our sample lie

4

on the red sequence (Chilingarian & Zolotukhin 2012), which is a narrow region in the colour-magnitude diagram where early-type galaxies are located. Since our sample was already relatively clean at this stage, we fitted a second-order polynomial to it in the colour-magnitude diagram. For this end, we used the g-r colours of the apparent magnitudes and the absolute magnitude in the z band. The results of these fits are shown in Figures B.67 to B.69 with their fitting parameters in Table C.6. Using these fits, we perform a 3-σ clipping to remove outliers. Less than 1 % (the exact ratio depends on the choice of the photometric fits, i.e., the composite model, de Vaucouleur or Petrosian (see Section 4 for details on these fits), of the sample is removed by the colour cut. For comparison, applying the same colour cuts on the sample classified only via GalaxyZoo, about 4.5% are removed. The remaining ~95000 galaxies were used for the fundamental plane calibrations and form our selected sample. During the fitting process another about 2000 galaxies were excluded as outliers, which leaves a sample of 93000 galaxies for our final analysis. A set of comparative colour-magnitude diagrams (see Figure 5) illustrates the cleaning process of our sample all the way from the 852173 SDSS galaxies with proper spectroscopic data to our selected sample of about 95000 galaxies.
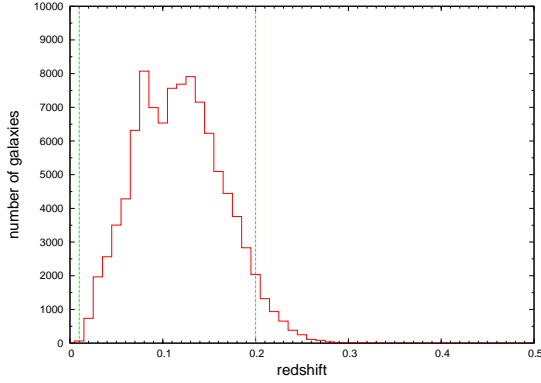

Figure 5. Selection of our sample illustrated using colour-magnitude diagrams. This set of g-r colour versus z band absolute magnitude diagrams shows that with our constraints only the red sequence remains in the selected sample (top left panel) of about 95000 galaxies, which is used to fit the fundamental plane. The basic sample (top right panel), which consists of 100427 galaxies, is already relatively clean by itself. The 170234 candidates of elliptical galaxies from GalaxyZoo can be found in the bottom left panel. The bottom right panel shows 852173 unclassified galaxies with proper spectroscopic data from the SDSS database and in this plot, other structures in the colour magnitude diagram, such as the blue cloud, are clearly visible as well. The colour-coding in the plots is always relative to the maximum number density per pixel. Red indicates the maximum number density (which can vary from figure to figure) per pixel. Colours between red and orange cover number densities between the maximum and 2/3 of the maximum. Shades from yellow to green cover the range between ~2/3 and ~1/3 of the maximum number density. Shades from cyan to blue indicate less than ~1/3 of the maximum number density. White pixels contain no objects. The same colour scheme is used for all other density map plots in this paper as well.

Figure 4. Redshift distribution of the basic sample. The green vertical lines at z=0.01 and z=0.2 indicate the limitation of the selected sample that was used for fitting the fundamental plane.

2.2. Substructure in the redshift distribution

In this section we discuss the redshift substructure in our sample, identifying three peaks in redshift at which galaxies cluster.

Consider Figure 4 again, in which one may immediately notice two peaks in the galaxy counts. The first one, which appears to be most prominent at z=0.08 in this plot, is associated with the Sloan Great Wall, which is located at a redshift of 0.073 (Gott et al. 2005). The other peak is around a redshift of 0.13 and has been reported previously in Bernardi et al. (2003b), though it was not discussed in detail afterwards.

In the following we describe how we corrected the redshift histogram in Figure 4 for completeness and sampling effects to investigate the redshift substructure of our sample in more detail. First of all, for a volume-limited sample one expects the number of galaxies to increase with the third power of the distance (which is in first-order approximation linearly related to the redshift). Then, due to magnitude limitation, one looses the less lu-
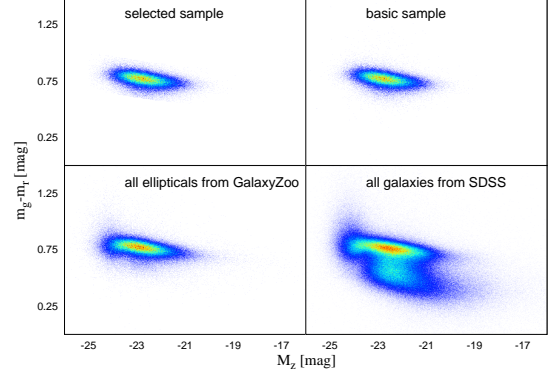
minous part of the sample starting at a certain redshift, and number counts will decrease towards zero at very large distances. The combination of volume sampling and magnitude limitation yield a function that grows as a function of redshift from zero to a peak, and then decreases afterwards to zero again. Our sample in Figure 4 has this overall peak at about z=0.1, close to the two putative sub-peaks.

It is therefore important to remove the signature of magnitude limitation from this histogram, which will allow a clean assessment of the existence of those possible sub-peaks. As a first step (Figure 6), we thus considered the galaxy count per comoving volume instead of the absolute numbers, dividing the number of galaxies in each redshift bin by the comoving volume of the bin. The following equations define the comoving volume of such a redshift bin $V_C(z_1, z_2)$:

$$V_C(z_1, z_2) = \frac{4\pi}{3} \frac{A_{\text{SDSS}}}{A_{\text{sky}}} \left(D_C^3(z_2) - D_C^3(z_1) \right) \qquad (2)$$

$$D_C(z) = D_L(z) \cdot (1 + z)^{-1} \qquad (3)$$

$$D_L(z) = \frac{c \cdot z}{H_0} \left(1 + \left(\frac{z \cdot (1 - q_0)}{\sqrt{1 + 2q_0 \cdot z} + 1 + q_0 \cdot z} \right) \right) \qquad (4)$$

$$q_0 = \frac{\Omega_M}{2} - \Omega_\Lambda. \qquad (5)$$

The comoving volume $V_C(z_1, z_2)$ is derived from the comoving distance $D_C(z)$ and the spectroscopic sky coverage of SDSS

5

DR8 A_{SDSS}, which is 9274 deg^2, normalised to the total size of the sky A_{sky}, which is ~ 41253 deg^2. The comoving distance D_C itself is derived from the luminosity distance D_L, which is given in Equation 4. We assumed a Hubble parameter H_0 of 70 km s^{-1} Mpc^{-1} for our calculations, which can be rescaled to any measured Hubble parameter using h_{70}. The subscript 70 emphasises that this scaling parameter is relative to our chosen value of the Hubble parameter. c denotes the speed of light and q_0 the deceleration parameter of the universe, which is -0.55 for a universe with a relative matter density of $\Omega_M = 0.3$ and relative dark-energy density of $\Omega_\Lambda = 0.7$ according to Equation 5.

In the next step, we corrected for the magnitude limitation. We assumed that we have the same functional shape of the luminosity function of giant elliptical galaxies in every volume element of the universe. For this, we adopted a Gaussian luminosity function with a mean luminosity $\bar{M}$ slowly evolving (evolution parameter Q) as linear function of the redshift, and assumed that the standard deviation σ_M is the same for all redshifts and volume elements. The Gaussian shape of the luminosity function of large elliptical galaxies is discussed in detail in Section 4.2. Although the bulk of the dwarf elliptical galaxies are already too faint at the minimum redshift of our sample, there are still a few bright dwarf elliptical galaxies that do not fall below the magnitude limit. However, these galaxies are not part of the sample, because their light profiles are more exponential than elliptical and therefore, they are already excluded by the sample selection.

Our sample is limited by a fixed apparent magnitude m_{limit} (basically the spectroscopy limit of SDSS), which will cut into the elliptical galaxy luminosity function more and more as redshift/distance increases, biasing our sample towards intrinsically brighter luminosities at high distances. This effect is also known as Malmquist bias.

We can now express the expected space density of ellipticals in our sample with Equation 6:

$$\rho_{obs}(z) = \frac{\rho_0}{2}\left(1 + \mathrm{erf}\left(\frac{\Delta m + Q \cdot z - 5 \cdot \log_{10}(D_L/\mathrm{pc}) + 5}{\sqrt{2} \cdot \sigma_M}\right)\right). \tag{6}$$

$$m_{app} - M_{abs} = 5 \cdot \log_{10}(D_L/\mathrm{pc}) - 5 \tag{7}$$

In these equations, we defined a new parameter $\Delta m = m_{limit} - \bar{M}$, which denotes the difference between limit magnitude m_{limit} and the mean luminosity of the luminosity function at redshift zero $\bar{M}$. To represent the Malmquist bias we made use of the distance modulus (see Equation 7), which defines the difference between the apparent magnitude m_{app} and the absolute magnitude M_{abs} in dependence on the luminosity distance D_L.

We then fitted this 4-parameter function for the observed galaxy density $\rho_{obs}(z)$ to the redshift distribution in Figure 6. The four varied parameters are the density of elliptical galaxies ρ_0, the evolution parameter Q, the standard deviation of the luminosity function σ_M, and the parameter Δm. We used a modified simplex algorithm to perform the first fit to obtain the galaxy densities. After inverting the error function in Equation 6, we used a least-squares fit to obtain the other parameters. For mathematical reasons, we had to exclude the first five bins, which form the plateau of the function, for the least-squares fit. However, since the height of the plateau was already fixed by the simplex fit, which uses these bins, no information is lost. The results of this fit are shown as a dashed (green) line in Figure 6. Our best fit yields an average density of elliptical galaxies in the universe ρ_0 (which fulfil the requirements of our sample) of $7 \cdot 10^{-4}$ galaxies per (Mpc $\cdot h_{70}^{-1}$)^3. Furthermore, we derived a mild redshift evolution Q of 1.07 mag (per z). Our values for Δm and σ_M are $(38.3 - 5 \cdot \log_{10}(h_{70}))$ mag and 0.89 mag, respectively.
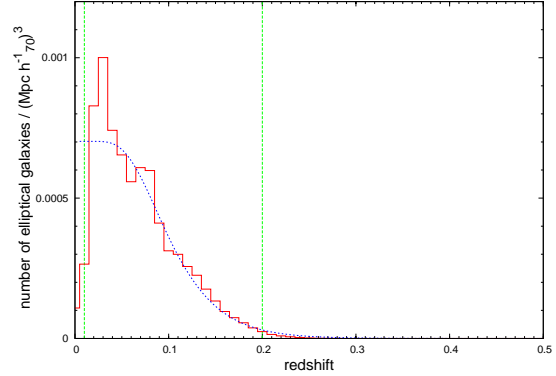

Figure 6. Redshift distribution of the number density of elliptical galaxies in our sample. The measured density of elliptical galaxies is given by the red solid line of the histogram. We divided our sample into redshift bins with a width of 0.01. The blue dashed line represents our best-fit model to the data. The green dashed vertical lines indicate the limits of the sample, which were used for the fundamental plane fitting.

To analyse overdensities, we subtracted the fit function from our data in Figure 6 and normalised it to the fit function's values. The result of this exercise is shown in Figure 7. One notices three overdensities, two of which can be identified with known large-scale structures. There are the CfA2-Great Wall between a redshift of 0.0167 and 0.0333 with a median redshift of 0.029 (Geller & Huchra 1989) and the Sloan Great Wall between a redshift of 0.0509 and 0.0876 with a median redshift of 0.073 (Gott et al. 2005). Furthermore, we found another (so far not investigated) overdensity between 0.12 and 0.15 with a peak around 0.13. This overdensity was previously mentioned in Bernardi et al. (2003b), who noticed two overdensities in their (SDSS-based) sample of elliptical galaxies: one at a redshift of 0.08 (their paper was published before the Sloan Great Wall was discovered at a similar redshift) and another one at 0.13, which we can now confirm. Identifying any large-scales structures, which might be associated with this over-density, would exceed the scope of this paper and is left open for future investigations.

When looking at Figure 7, one will also notice some significant underdensities at very low and at relatively high redshifts. The underdensity at low redshifts is due to a selection effect in SDSS and GalaxyZoo. Very nearby galaxies are sometimes not included in the SDSS spectroscopic sample because they are too bright. Previously well-classified nearby galaxies were not included in GalaxyZoo as well. These two selection effects cause the apparent deficiency of elliptical galaxies at low redshifts. At high redshifts (z>0.2), we encounter a similar problem. Galaxies at this distance are already rather small and difficult to classify. Therefore, we excepted fewer galaxies that were clearly identified as ellipticals by GalaxyZoo. These two findings strengthen our previous considerations to cut our sample at redshifts lower than 0.01 and higher than 0.2 before using them for the fundamental plane fitting.

3. Method

The fitting procedure of fundamental plane coefficients was performed individually for each SDSS filter to derive independent results. The first matter that needs to be taken into account is galactic extinction:
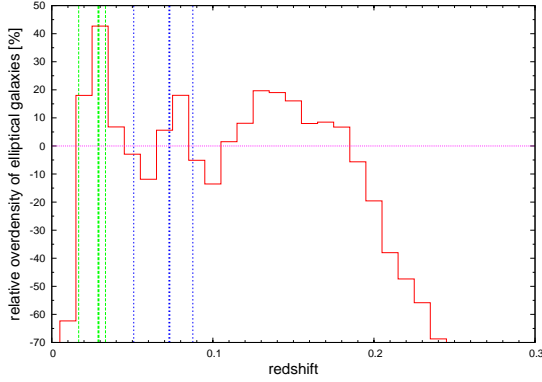
6

Figure 7. Redshift distribution of the relative number density of elliptical galaxies. The red solid line shows the relative overdensity of the galaxies in our sample compared with the model predictions. Two known large-scale structures are indicated by the green and blue dashed vertical lines. The thin lines are the lower and upper limit of these structures, while the thick line indicates their median redshift. The green lines denote the CfA2 Great Wall and the blue lines denote the Sloan Great Wall.

$$m_{\mathrm{extcor}} = m_{\mathrm{sdss}} - A_{\mathrm{Schlegel}}. \tag{8}$$

We corrected the SDSS model magnitudes m_{sdss} for extinction A_{Schlegel} according to the Schlegel maps (Schlegel et al. 1998). The values for extinction were obtained from the SDSS database, in which they can be found for every photometric object based on its coordinates.

We also applied a K-correction to m_{extcor}, to correct for the effect of the redshift on the spectral profile across the filters,

$$K(z, m_{f_1} - m_{f_2}) = \sum_{i,j} B_{ij} z^i (m_{f_1} - m_{f_2})^j \tag{9}$$

$$m'_{\mathrm{app}} = m_{\mathrm{extcor}} - K(z, m_{f_1} - m_{f_2}). \tag{10}$$

The K-correction is calculated using the (extinction-corrected) colour $m_{f_1} - m_{f_2}$ and the redshift z of the galaxy. We used the recent model of Chilingarian et al. (2010) with updated coefficients as shown in Tables C.1 to C.5. This K-correction model uses a two-dimensional polynomial with coefficients B_{ij} that depend on the filter. One obtains the K-corrected apparent magnitude m'_{app} by a simple subtraction of the K-correction term $K(z, m_{f_1} - m_{f_2})$. The subscripts f_1 and f_2 stand for two different filters, which one can choose for calculating the correction.

The next step was to renormalise the measured model radius from the SDSS data r_{sdss} to take into account the different ellipticities of the elliptical galaxies in our sample,

$$r_{\mathrm{cor}} = r_{\mathrm{sdss}} \sqrt{q_{b/a}}. \tag{11}$$

This can be done according to Bernardi et al. (2003c) by using the minor semi-axis to mayor semi-axis ratio $q_{b/a}$ from SDSS. The corrected radius r_{cor} enables us to directly compare all types of elliptical galaxies.

The velocity dispersions also need to be corrected for. Because SDSS uses a fixed fibre size, the fibres cover different physical areas of galaxies at different distances. This affects the measured velocity dispersion. Suitable aperture corrections for

early-type galaxies were calculated by Jorgensen et al. (1995) and Wegner et al. (1999), see the following equation:

$$\sigma_0 = \sigma_{\mathrm{sdss}} \cdot \left(\frac{r_{\mathrm{fiber}}}{r_{\mathrm{cor}}/8} \right)^{0.04}. \tag{12}$$

The radius of the SDSS fibres r_{fiber} is 1.5 arcseconds for all releases up to and including DR8 [2]. σ_0 is typically about 10% higher than the measured value σ_{sdss}.

We also corrected the measured redshifts z for the motion of our solar system relative to the cosmic microwave background (CMB), because we intend to calculate redshift-based distances afterwards. The corrected redshift z_{cor} for the CMB rest frame can be calculated using some basic mathematics as demonstrated in Appendix A.

Since we need distances to obtain the physical radii R_0 of our elliptical galaxies, we calculated angular diameter distances $D_A(z_{\mathrm{cor}})$:

$$D_A(z_{\mathrm{cor}}) = D_L(z_{\mathrm{cor}}) \cdot (1 + z_{\mathrm{cor}})^{-2}. \tag{13}$$

They are derived from the luminosity distances D_L, which have been defined in Equation 4. The physical radius is given in Equation 14:

$$R_0 = D_A(z_{\mathrm{cor}}) \cdot \tan(r_{\mathrm{cor}}). \tag{14}$$

Another aspect needs to be considered, the passive evolution of elliptical galaxies

$$m_{\mathrm{app}} = m'_{\mathrm{app}} + Q \cdot z_{\mathrm{cor}}. \tag{15}$$

The K- and extinction-corrected apparent m'_{app} of a sample of elliptical galaxies changes as a function of look-back time due to stellar evolution. We corrected for this effect using an evolutionary parameter Q. This parameter was derived by fitting Equation 6 to the overall redshift distribution of our sample, as done in Subsection 2.2. The fit assumes a passive evolution of the elliptical galaxies that is linear and proportional to the redshift within the sample's redshift range. Using this parameter, one can to calculate the fully (extinction-, K-, and evolution-) corrected apparent magnitude m_{app}.

A final correction was applied to the measured surface brightness:

$$\mu_0 = m_{\mathrm{app}} + 2.5 \cdot \log_{10}\left(2\pi \cdot r_{\mathrm{cor}}^2\right) - 10 \cdot \log_{10}(1 + z_{\mathrm{cor}}). \tag{16}$$

The mean surface brightness μ_0 within the effective radius r_{cor} is defined by the equation above. The last term corrects for cosmological dimming of surface brightnesses, which is proportional to $(1 + z_{\mathrm{cor}})^4$ in any Friedmann-Lemaître-Robertson-Walker metric-based universe (Tolman 1930; Hubble & Tolman 1935; Sandage & Perelmuter 1990a,b, 1991; Pahre et al. 1996).

$$\log_{10}(I_0) = -\frac{\mu_0}{2.5} \tag{17}$$

To be consistent with Bernardi et al. (2003c), we used $\log_{10}(I_0)$ instead of the surface brightness, although they only differ by a factor.

In the final step, we used the angular diameter distance to determine the physical radius R_0 of the galaxies in our sample. With this, we have all parameters at hand that are required for the fundamental plane.

We now briefly discuss our options for fitting it. One first has to take into account is the Malmquist bias. There are several

---

[2] Afterwards the SDSS-telescope was refitted with new smaller (1 arcsecond radius) fibres for BOSS (Ahn et al. 2012).

7

methods to correct for it, and first we tried to use a maximum-likelihood method to fit the fundamental plane, as done in Bernardi et al. (2003b,c). We found that the extrema landscape of the likelihood function of the multivariate Gaussian (see Bernardi et al. (2003b) for more details) is unsuitable for the method, since small variations in the initial conditions of our simplex fit led to significantly different results. Other more advanced methods for minimising the likelihood function were considered, but rejected because of their unreasonably high computational costs.

As a consequence, we decided to use a less complex, yet efficient method to account for the Malmquist bias: volume-weighting (Sheth & Bernardi 2012). One assigns statistical weights to the galaxies based on the volume in which a galaxy with its luminosity is still visible. To do this, one has to know the exact limits imposed by the bias on one's sample:

$$\log_{10}(D_{L,\text{limit}}) = k_{\text{fit}} \cdot M_{\text{abs}} + d_{\text{fit}} \qquad (18)$$

$$m_{\text{limit}} = 5 \cdot d_{\text{fit}} - 5. \qquad (19)$$

Owing to the nature of the bias, one expects a linear cut in the sample when plotting the logarithm of the luminosity distance D_L versus the absolute magnitude M_{abs}. The fit parameter d_{fit} is directly connected to the limiting magnitude m_{limit} of the sample. We can perform a simple linear fit (see Equation 18) to this cut, but since we know that it originates in a Malmquist bias, we are able to fix the slope k_{fit} to -0.2 and only have to vary the offset d_{fit}. This is done in a way that 99.7% (equivalent to 3σ) of the data points are located on one side of the fitted line. The fit parameter d_{fit} is directly connected to the limiting magnitude m_{limit} of the sample (equation 19). In the next step, we used this fit to determine the maximum distance $D_{L,\text{limit}}$ at which a galaxy with a certain absolute magnitude is still visible. Subsequently, we transformed this luminosity distance into a comoving distance D_C (see Equation 3) for which we derived the redshift z_{limit} from the limiting luminosity distance $D_{L,\text{limit}}$. An inversion of Equation 4 yields,

$$z = \frac{1}{c^2}\left(c^2 q_0 - c^2 + c\,D_L H_0 q_0 + \right. \qquad (20)$$

$$\left. \sqrt{c^2 q_0^2 - 2c^4 q_0 + c^4 + 2c^3 D_L H_0 q_0^2 - 4c^3 D_L H_0 q_0 + 2c^3 D_L H_0}\right),$$

which can be used to derive the limiting redshift to determine the limiting comoving distance and consequently the corresponding comoving volume V_C (see Equation 2),

$$w_{\text{vol},i} = \frac{(V_{C,i})^{-1}}{\sum_j (V_{C,j})^{-1}}. \qquad (21)$$

The normalised volume weights $w_{\text{vol},i}$ for every galaxy i are defined by Equation 21 according to Sheth & Bernardi (2012). With the volume weights at hand, one can compute the coefficients a, b, and c of the fundamental plane (see Equation 1) using a multiple regression based on weighted least-squares. These volume weights correct for the Malmquist bias (see Figure 8), which affects our magnitude-limited sample. One has to solve the following set of equations:

$$\begin{pmatrix} A_{11} & A_{12} & A_{13} \\ A_{12} & A_{22} & A_{23} \\ A_{13} & A_{23} & A_{33} \end{pmatrix} \cdot \begin{pmatrix} a \\ b \\ c \end{pmatrix} = \begin{pmatrix} V_1 \\ V_2 \\ V_3 \end{pmatrix}, \qquad (22)$$

with

$$A_{11} = \sum_{i=1}^{n} \left((\log_{10}(\sigma_{0,i}))^2 \cdot \bar{w}_{\text{vol},i}\right) \qquad (23)$$

$$A_{12} = \sum_{i=1}^{n} (\log_{10}\sigma_{0,i} \cdot \log_{10}(I_{0,i}) \cdot \bar{w}_{\text{vol},i}) \qquad (24)$$

$$A_{13} = \sum_{i=1}^{n} (\log_{10}(\sigma_{0,i}) \cdot \bar{w}_{\text{vol},i}) \qquad (25)$$

$$A_{22} = \sum_{i=1}^{n} \left((\log_{10}(I_{0,i}))^2 \cdot \bar{w}_{\text{vol},i}\right) \qquad (26)$$

$$A_{23} = \sum_{i=1}^{n} (\log_{10}(I_{0,i}) \cdot \bar{w}_{\text{vol},i}) \qquad (27)$$

$$A_{33} = n \qquad (28)$$

$$V_1 = \sum_{i=1}^{n} (\log_{10}(R_{0,i}) \cdot \log_{10}(\sigma_{0,i}) \cdot \bar{w}_{\text{vol},i}) \qquad (29)$$

$$V_2 = \sum_{i=1}^{n} (\log_{10}(R_{0,i}) \cdot \log_{10}(I_{0,i}) \cdot \bar{w}_{\text{vol},i}) \qquad (30)$$

$$V_3 = \sum_{i=1}^{n} (\log_{10}(R_{0,i}) \cdot \bar{w}_{\text{vol},i}), \qquad (31)$$

which is done using Cramer's rule. It should be noted that $\bar{w}_{\text{vol},i} = w_{\text{vol},i} \cdot n$ are renormalized volume weights that were only multiplied by the number of galaxies n used for the fit.

$$s_\varepsilon = \sqrt{\frac{\sum_{i=1}^{n} \bar{w}_{\text{vol},i}\left(a\log_{10}(\sigma_{0,i}) + b\log_{10}(I_{0,i}) + c - \log_{10}(R_{0,i})\right)^2}{n}} \qquad (32)$$

$$\sigma_a = \sqrt{\frac{A_{22}A_{33} - (A_{23})^2}{\det(A)}} \qquad (33)$$

$$\sigma_b = \sqrt{\frac{A_{11}A_{33} - (A_{13})^2}{\det(A)}} \qquad (34)$$

$$\sigma_c = \sqrt{\frac{A_{11}A_{22} - (A_{12})^2}{\det(A)}} \qquad (35)$$

We also computed the root mean square s_ε and the standard errors σ_a, σ_b, and σ_c of the coefficients a, b, and c, where A denotes the matrix from Equation 22.

We performed an iterative 3σ-clipping after the fitting process, which was repeated until all outliers were eliminated. With the entire set of calibration and tools at hand, we then determined the coefficients of the fundamental plane.

4. Results

For the photometric parameters of our model galaxies we used the three available sets of models in SDSS: the c model, the dV model, and the p model. The c model uses *cModelMag*[3] and *de-VRad* (since SDSS does not provide a composite scale radius

---

[3] Actually *PhotoObj.cModelMag_filter*, to be consistent with Subsection 2.1, but we use this short notation and similar abbreviations here.

8

fit). The dV model uses *deVMag* and *deVRad*. The p model uses *petroMag* and *petroRad*, and all filters independently.

The following equations define the various parameters:

$$I(r) = I_0 \cdot \exp\left(-7.67 \left(\frac{r}{r_e}\right)^{\frac{1}{4}}\right) \tag{36}$$

$$I(r) = I_0 \cdot \exp\left(-1.68 \frac{r}{r_e}\right) \tag{37}$$

$$\mathcal{R}_P(r) = \frac{\int_{0.8r}^{1.25r} d\bar{r} \; \bar{r} \cdot I(\bar{r})}{(1.25^2 - 0.8^2) \cdot \int_0^r d\bar{r} \; \bar{r} \cdot I(\bar{r})} \tag{38}$$

$$F_P = \int_0^{N_P \cdot r_P} d\bar{r} \; 2\pi \cdot \bar{r} \cdot I(\bar{r}). \tag{39}$$

The *cModelMag* are based on a simple weighted adding (depending on the likelihood of the two fits) of the fluxes from de Vaucouleurs fits (see Equation 36) and the pure exponential fit (see Equation 37). The *deVMag* are the magnitudes derived directly from the de Vaucouleurs fit given in Equation 36. The Petrosian magnitudes *petroMag* are slightly more complicated. Firstly, one has to calculate the Petrosian ratio $\mathcal{R}_P(r)$ according to Equation 38, where $I(r)$ stands for the azimuthally averaged surface brightness profile. The Petrosian radius r_P, which is denoted with *petroRad*, is the radius for which the Petrosian ratio $\mathcal{R}_P(r_P)$ is equal to a defined value (0.2 for the SDSS). The Petrosian flux F_P is given by Equation 39, where the parameter N_P is defined to be 2 (for the SDSS). SDSS also provides *fibreMag*, but since they are by definition calculated for fixed apertures (diameter of the SDSS-fibre), we found them not to be useful for studying a sample of galaxies at different distances. Therefore, we did not construct a model based on them.
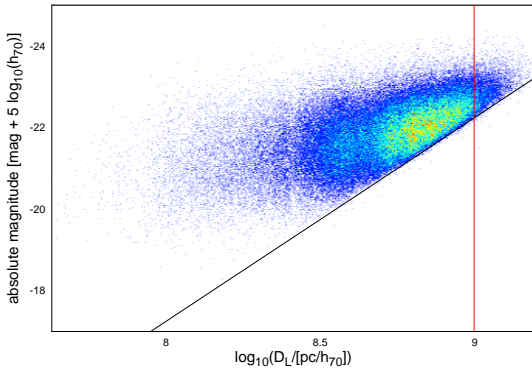

Figure 8. Malmquist bias affecting the magnitude-distance distribution of our sample. Taking the example of the r band for the dV model parameters, one can see a deviation of the pure Malmquist bias (indicated by the black solid line) at large distances. The red solid line indicates a distance corresponding to a redshift of 0.2, which is the limit of our selected sample.

4.1. Malmquist bias

The first stop on our way to proper results is quantifying the Malmquist bias in our sample (see Figure 8). Owing to the physical nature of this bias, it is best to plot the logarithm of the luminosity distance D_L versus the absolute magnitude for the sample.

models	$m_{\text{limit,u}}$	$m_{\text{limit,g}}$	$m_{\text{limit,r}}$	$m_{\text{limit,i}}$	$m_{\text{limit,z}}$
c model	20.61	18.54	17.78	17.46	17.22
dV model	20.59	18.54	17.78	17.46	17.22
p model	20.77	18.59	17.80	17.47	17.23

Table 3. Limiting magnitude $m_{\text{limit,filter}}$, which was derived from the coefficients $d_{\text{fit,filter}}$ of the fit on the Malmquist bias according to Equation 19, for every filter and for every model.

Then one fits a straight line to the cut, which is introduced by the Malmquist bias, in the distribution (see Figures B.1 to B.15). This fit is given by Equation 18, and its result is listed in Table 3. Since the parameter d_{fit} is directly connected to the limiting magnitude m_{limit}, which has a higher physical significance than the fit parameter itself, by Equation 19, we display this limiting magnitude in Table 3. It is assuring to see that the limiting magnitude is almost independent of the model and only depends on the filter. Because spectroscopic data are required for every galaxy in our sample, the limiting magnitudes from Table 19 are driven by the spectroscopic limit of SDSS, which is the (uncorrected) Petrosian magnitude in the r band of 17.77 (Strauss et al. 2002). This value is almost the same limiting magnitude for the same model and filter, as we found. It is not surprising that the limiting magnitude is fainter in the bluer filter than in the redder ones, since elliptical galaxies are more luminous in the red, as one can see in Subsection 4.2.

The fit results shown in Table 3 were used to calculate the volume weights (see Equation 21) to correct for the Malmquist bias in our analysis. We found that our sample is affected by an additional bias for redshifts z ≳ 0.2, which is consistent with our previous findings in Subsection 2.2 (especially Figures 6 and 7): when we extend our plots beyond the luminosity distance corresponding to a redshift of 0.2, there is slight shortage of galaxies just above the fitted line (see Figure 8). This happens for all filters and all models, which is another motivation for removing galaxies above redshift of 0.2 from our sample. A useful review on the Malmquist bias in general can be found in Butkevich et al. (2005).

4.2. Luminosity function

Additional information obtained from the preparations of the calibration of the fundamental plane are the luminosity functions of the galaxies in our sample. We note that the faint-luminosity limit of our sample of $M_r = (-18.66 + 5 \log_{10}(h_{70}))$ mag (corresponding to a 3σ of the mean luminosity of the sample's galaxies in this filter, see Table 4) is brighter than the apparent spectroscopic limit of the SDSS, which is 17.77 Petrosian magnitudes in the r band (Strauss et al. 2002), at the lower redshift limit z=0.01 (distance modulus $m_{\text{app}} - M_{\text{abs}} = (33.16 - 5 \log_{10}(h_{70}))$ mag). The reason for this is the overall surface brightness limit of SDSS (omitting dwarf galaxies), and the restriction of our sample to galaxies that are better fit by a de Vaucouleurs profile than an exponential. The former profile is characteristic of giant ellipticals, whereas an exponential profile corresponds to fainter, mostly dwarf, galaxies. We hereby conclude that our sample is not contaminated by dwarf ellipticals.

We calculated the absolute magnitudes of the galaxies using the distance modulus (see Equation 7) and redshift-based distances (see Equation 4). Since the sample is affected by a Malmquist bias, the luminosity function in different redshift bins is not the same, but shifted to higher luminosity with higher red-
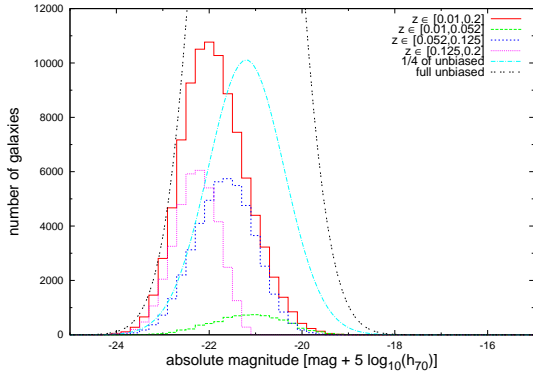
9

Figure 9. Luminosity function for our sample in the r band for the dV model. We split it into different subsamples (within different redshift bins) and compared the expected unbiased luminosity function and the total observed luminosity function. Our sample is complete at the luminous end, but we miss many of the fainter galaxies due to the Malmquist bias.

Figure 10. Distribution of the apparent corrected radius r_{cor} is displayed in different filters for the dV model and the c model (the radii are the same is both models). The vast majority of the measured radii are smaller than 5 arcseconds.

shift. To analyse the luminosity function, we split the data into 0.2 mag bins. We show the resulting luminosity distributions in Figure 9 here as well as in Figures B.16 to B.29.

We also calculated the mean luminosity and its standard deviation for every model and filter. We used these values and the mean galaxy density ρ_0 obtained in Subsection 2.2 to calculate the expected luminosity function assuming that our sample would not suffer from a Malmquist bias (see Figures 9 and B.16 to B.29). In this case, we would have almost 416000 galaxies in our selected sample (between a redshift of 0.01 and 0.2), compared to the about 95 000 that we actually found. The magnitude limitation of the SDSS data set thus reduced the number of galaxies by about 80% for the full redshift range $0.01 < z < 0.2$, compared to an extrapolated volume limited sample. With the volume weights, we then calculated a bias-corrected mean absolute magnitude $\bar{M}_{filter}$ and a standard deviation σ_{filter} for every filter of every model. The results are listed in Table 4. The standard deviations are very similar between all filters and models. The mean absolute magnitude also depends almost entirely on the filter. This again shows that the completeness is entirely constrained by the spectroscopic survey limit, not by photometric limits.

4.3. Parameter distribution

In this subsection, we discuss the properties of the different parameters that define the fundamental plane and their observables. The parameters of the fundamental plane are derived from three observables: the apparent corrected radius r_{cor}, the extinction- and K-corrected apparent magnitude m_{app}, and the central velocity dispersion σ_0, which is already corrected for the fixed aperture size of the SDSS fibres. The three parameters of the fundamental plane are the logarithm of the physical radius $\log_{10}(R_0)$, the logarithm of the central velocity dispersion $\log_{10}(\sigma_0)$, and the mean surface brightness μ_0 in lieu of which as a convention, the parameter $\log_{10}(I_0)$ is used in the fitting process, which only differs by a factor of -2.5.

The distribution of the radii r_{cor} is shown in Figures 10 and B.33. The apparent radius is typically in the order of couple of arcseconds (with its peak about 1.5-2 arcseconds for the c and
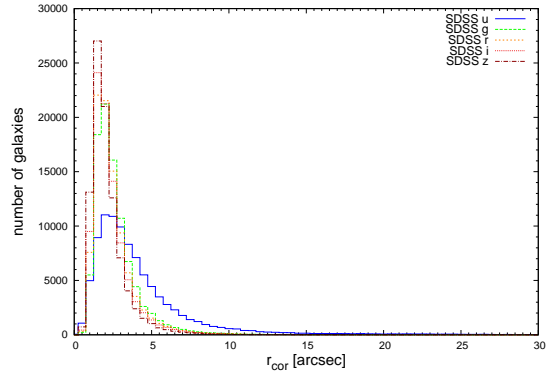
dV models and around 3-4 arcseconds for the p model), but in the case of the SDSS u band, they can be moved to much larger radii (especially for the Petrosian model) because of the known problems with this filter (see the SDSS website[4]). It has been reported in Fathi et al. (2010) that the SDSS fitting algorithm tends to prefer certain sets of values for de Vaucouleurs and exponential fits. We found that this happens for the Petrosian fits as well and that it even is much more prominent there, especially in the u and z band. One can already see some grouping in the plots of the corrected apparent radius r_{cor} against the apparent magnitudes m_{app} (see Figures B.62 and B.64 and compare them with Figure B.63, which is for the r band and does not show any peculiarities). It becomes more prominent in plots of the $\log_{10}(R_0)$ versus redshift, in which one can clearly see band-like structures (see Figures B.65 and B.66). Furthermore, the average apparent radii in all filters are larger for the Petrosian model than for the de Vaucouleurs model (the c model also uses de Vaucouleurs radii). There are some tiny differences (too small to be seen in a plot) between the de Vaucouleurs model and the composite model, which are created by the selection of galaxies (because of limits in the magnitudes and the 3-σ clipping).

In Table C.8, the averages and standard deviations of all previously mentioned parameters are displayed for all filters and all models. For the p model, there is a suspiciously high standard deviation for the u band and for the z band though to a smaller extent there. There is obviously a problem with the measured radii in the u band, which is most likely due to the known problem of scattered light in this filter, and it is much worse for Petrosian fits, for which the z band is also affected. The distribution of the apparent magnitude m_{app} for different models is displayed in Figures B.36 to B.38. The distributions show very steep cut-offs around the limiting magnitudes, which is exactly the expected behaviour for a magnitude-limited sample.

In Figures B.34 and B.35, one can see that the corrected central velocity dispersion barely depends on the filter. This is not surprising since the correction (see Equation 12) only mildly depends on the apparent corrected radius r_{cor}, which is different for different filters. Therefore, as a spectroscopic observable,

---

[4] http://www.sdss.org/dr7/start/aboutdr7.html#imcaveat

10

models	$\bar{M}_u$ [mag + 5 $\log_{10}(h_{70})$]	σ_u [mag]	$\bar{M}_g$ [mag + 5 $\log_{10}(h_{70})$]	σ_g [mag]	$\bar{M}_r$ [mag + 5 $\log_{10}(h_{70})$]	σ_r [mag]	$\bar{M}_i$ [mag + 5 $\log_{10}(h_{70})$]	σ_i [mag]	$\bar{M}_z$ [mag + 5 $\log_{10}(h_{70})$]	σ_z [mag]
c model	-18.82	0.79	-20.47	0.80	-21.20	0.82	-21.55	0.82	-21.78	0.83
dV model	-18.84	0.80	-20.48	0.80	-21.20	0.82	-21.55	0.82	-21.79	0.83
p model	-18.55	1.04	-20.38	0.80	-21.12	0.82	-21.48	0.82	-21.74	0.83

Table 4. Bias- and evolution-corrected absolute magnitudes $\bar{M}_{\text{filter}}$ and the corresponding standard deviation σ_{filter} can be found in this table for all models and all filters.

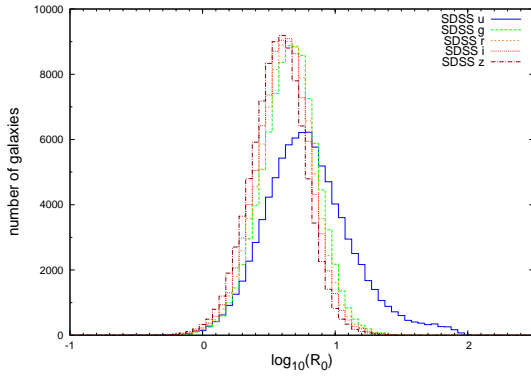one will not notice any significant differences depending on the model either.

Figure 11. Distributions of the logarithm of the physical radius $\log_{10}(R_0)$ in different filters for the dV model can be well described by sharp Gaussian with their peaks almost exactly at the same value. Only the u band shows some digressive behaviour. In this case the peak is smaller and set apart from the other. Furthermore, the distribution is wider and it shows a small bump at the larger end.

The three parameters $\log_{10}(R_0)$, $\log_{10}(\sigma_0)$, and $\log_{10}(I_0)$ enter directly into the fit of the fundamental plane. Therefore, the distribution of these parameter is especially important. The distribution of the logarithm of the physical radius R_0 is shown in Figures 11, B.41, and B.42. They show for almost all filters in all models sharp Gaussians with their peaks very close together for almost all filters and with comparable standard deviations (see Table C.8 for details). Nevertheless, the problems in u band, which we already encountered for the apparent corrected radius r_{cor}, are propagated and are even more striking here. In the case of the c model (Figure B.41) and the dV model (Figure 11), the distribution of $\log_{10}(R_0)$ is widened in the u band compared with the other filters. Moreover, its peak is shifted and the distribution shows a clear deviation from a Gaussian shape at its high end. For the p model (Figure B.42), one can clearly see a two peaked distribution for the u band and also for the z band to some smaller extent. For these particular models and filters, one has to introduce a cut (or another method) to handle the second peak during the least-squares fitting to avoid unwanted offsets.

Since the mean surface brightnesses μ_0 are derived from r_{cor} (see Equation 16), one expects similar problems from them. Indeed, there are similar sharp Gaussians for all filters, but for the u for all models and for the p model, one may notice a double-peaked distribution for the z band as well (see Figures 12, B.39 and B.40).
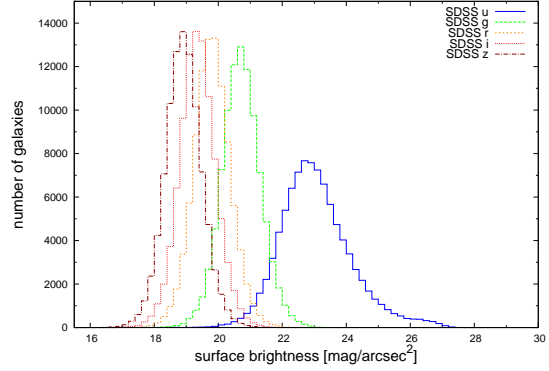

Figure 12. Distribution of the surface brightness μ_0 in different filters for the dV model is close to a Gaussian shape. For the u band, the distribution is wider and shows a small bump at the faint end.
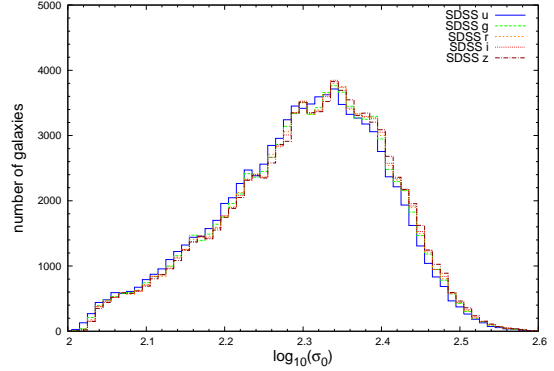
Figure 13. Distributions of the logarithm of the central velocity dispersion $\log_{10}(\sigma_0)$ in different filters for the c model and the dV model are almost exactly the same for all filters.

The logarithm of the central velocity dispersion σ_0 shows the same behaviour as the central velocity dispersion itself, as one can see in Figures 13 and B.43. The shape of the distribution of $\log_{10}(\sigma_0)$ is not a perfect Gaussian, in contrast to the distributions of the previous parameters, but this does not have to be the case for the velocity dispersion distribution. Yet, the distributional shape is sufficiently regular (no double peaks or other strange features) to be used in a least-squares fit without concerns.

11

models and filters	a	b	c	s_ε	$\bar{\sigma}_{\mathrm{dist}}$ [%]
c model					
u	0.809 ± 0.030	-0.696 ± 0.008	-7.53 ± 0.10	0.0947	16.5
g	0.975 ± 0.030	-0.736 ± 0.013	-7.73 ± 0.13	0.0933	15.6
r	1.041 ± 0.030	-0.750 ± 0.013	-7.76 ± 0.13	0.0933	15.3
i	1.068 ± 0.030	-0.755 ± 0.013	-7.75 ± 0.13	0.0918	15.0
z	1.113 ± 0.030	-0.760 ± 0.013	-7.80 ± 0.13	0.0947	14.8
dV model					
u	0.798 ± 0.030	-0.700 ± 0.008	-7.53 ± 0.10	0.0941	16.5
g	0.966 ± 0.030	-0.740 ± 0.013	-7.75 ± 0.13	0.0934	15.6
r	1.034 ± 0.030	-0.753 ± 0.013	-7.77 ± 0.13	0.0933	15.3
i	1.062 ± 0.030	-0.757 ± 0.013	-7.75 ± 0.13	0.0918	15.0
z	1.108 ± 0.030	-0.763 ± 0.013	-7.81 ± 0.13	0.0941	14.8
p model					
u	0.852 ± 0.030	-0.550 ± 0.005	-6.36 ± 0.08	0.1098	19.4
g	0.987 ± 0.030	-0.697 ± 0.013	-7.58 ± 0.13	0.0970	16.5
r	1.055 ± 0.030	-0.718 ± 0.013	-7.69 ± 0.14	0.0956	16.1
i	1.080 ± 0.030	-0.711 ± 0.013	-7.58 ± 0.13	0.0946	15.9
z	1.106 ± 0.030	-0.638 ± 0.010	-6.96 ± 0.11	0.1098	16.7
u (cut)	0.849 ± 0.034	-0.539 ± 0.009	-6.25 ± 0.12	0.1110	19.5
z (cut)	1.126 ± 0.031	-0.688 ± 0.012	-7.41 ± 0.13	0.1102	16.0

Table 5. The results of the best fits for the fundamental-plane coefficients in all filters and for all models using redshift evolution, volume weights, and 3-σ clipping.

4.4. Coefficients of the fundamental plane

We performed a volume-weighted least-squares fit in three dimensions (see Equation 22) to obtain the coefficients a, b, and c of the fundamental plane. The results for all parameters, filters, and models, are shown in Table 5. By definition (see Equation 1), the fundamental plane relates the logarithm of the physical radius $\log_{10}(R_0)$, the logarithm of the central velocity dispersion $\log_{10}(\sigma_0)$, and the renormalized surface brightness $\log_{10}(I_0)$ (see Equation 17 for the relation between I_0 and the surface brightness μ_0). We determined its coefficients and their standard errors as well as the root mean square s_ε. Furthermore, we determined an upper limit $\bar{\sigma}_{\mathrm{dist}}$ for the average distance error σ_{dist} by comparing the distances obtained with the fundamental plane to the redshift-based calibration distances.

The error obtained by this comparison is a combination of the true average distance error σ_{dist}, a scatter afflicted by peculiar motions, and the finite measurement precision. Consequently, $\bar{\sigma}_{\mathrm{dist}}$ is an upper limit to the average distance error, with the true distance error expected to be up to a few percent lower. To estimate the contribution of peculiar motions to the average distance error, we made use of additional data. The catalogue of Tempel et al. (2012) provides redshifts to galaxies in groups and clusters, which are corrected for the Finger-of-God effect. We picked a subsample that overlaps with our sample and in which every (elliptical) galaxy that we used, is in a group of at least 20 members to have a solid corrected redshift. By comparing the average distance errors of this subsample of 5013 galaxies, once using the redshifts of Tempel et al. (2012) and once the ones from SDSS, we noticed that there is no difference in the relevant digits between the fits using the Finger-of-God corrected redshifts and those from SDSS. This agrees with a simple estimate one can make using the mean redshift of our entire sample, which corresponds to a velocity of about 34000 km/s. The typical peculiar velocities of galaxies are on the order of 400 km/s (Masters et al. 2006). The average scatter on the sample inflicted due to peculiar motions is on the order of 1%. Using the propagation of uncertainty, this 1% does not significantly contribute to the overall ~ 15% error in the distance measurement.

For the fitting we used a recursive 3-σ clipping to optimise the results. This reduced the number of galaxies in our selected sample by about 2000 galaxies to 92994 for the c Model, to 92953 for the dV Model and to 92801 for the p model. Because of the problem with double peak in the distribution of the physical radii in the u and z band for the p model, we refitted the coefficients using a cut at $\log_{10}(R_0)$ of 1.5. This value corresponds to a physical radius R_0 of slightly more than 30 kpc h_{70}^{-1} and is motivated by the bimodal distribution in Figure B.42. The results of these refits are given in Table 5. As a consequence of this cut, we only used 73914 galaxies for the u band and 91187 galaxies for the z band.
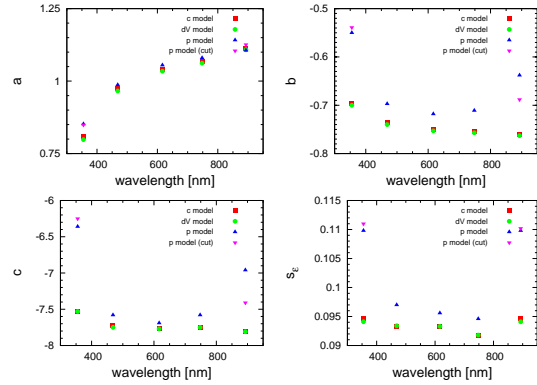

Figure 14. Comparison of the coefficients a (upper left panel), b (upper right panel), and c (lower left panel) and the root mean square s_ε (lower right panel) of the fundamental plane for all models and wavelengths. There are two additional data points for the p model, because we included the refitted coefficients after a cut in $\log_{10}(R_0)$ to remove wrong data points caused by problems discussed earlier in this paper. In general, the behaviour of the coefficients is similar for all models and only depends on the wavelength (notable exception the z band of the p model).

12

A general comparison of the fit parameters and the distance error in Table 5 shows that the c model and the dV model are clearly better than the p model. Moreover, the upper limit of the average distance error $\bar{\sigma}_{dist}$ is almost exactly the same for the c model and the dV model, and so are the fitting parameters a, b, and c. We found only small differences beyond the relevant digits. Furthermore, we found that though the root mean square s_ε is smallest in the i band, the average distance error decreases with longer wavelengths and is smallest in the z band. In addition to that, the coefficients of the fundamental plane show clear tendencies correlated with the wavelength. The coefficient a increases with long wavelengths, while the other coefficients b and c in general decrease with longer wavelengths. These dependencies are illustrated for all models in Figure 14 and hold quite well, save for the two problematic filters u and z in the p model. Figures 15, 16, and B.44 to B.56 show projections of the fundamental plane for all filters and all models. In Figure B.52, one can see a split distribution of two clouds, which is also due to the problems with the p model and the u filter as well. A similar, but smaller, problem occurs for the z filter of the p model (see Figure B.56), too.
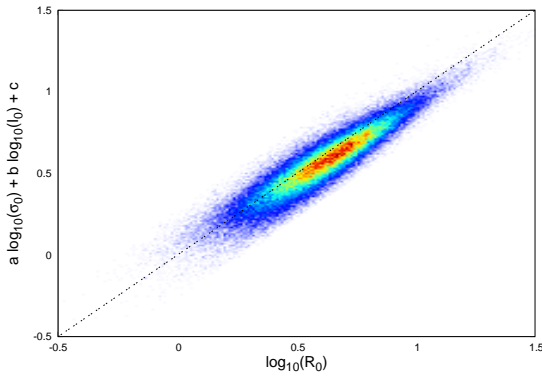

Figure 16. Projection of the fundamental plane for the z band of the dV model. The averaged distance error is smallest for this particular filter and model.

Figure 15. Projection of the fundamental plane for the i band of the dV model. The root mean square is smallest for this particular filter and model.

5. Discussion

5.1. Comparison with alternative fits

In addition to the main fit (for the resulting coefficients see Table 5), which considered redshift evolution and made use of volume weights to correct for the Malmquist bias and a recursive 3-σ clipping, we performed additional fits to test features of the code and assumptions we made. A visual comparison of the different fundamental plane fits of the i band for the dV model is shown in Figure 17.

We provide in Table C.9 the fitting results obtained without a 3-σ clipping. The change in values of the coefficient is marginal, and the quality of the fit (not surprisingly) is a little poorer than with clipping. Removing outliers is important for the calibrations, because we do not want our coefficients to be influenced by them.

We also considered the case without corrections for the Malmquist bias: Table C.10 shows the results of the fitting process with the volume weights turned off. Although the root mean
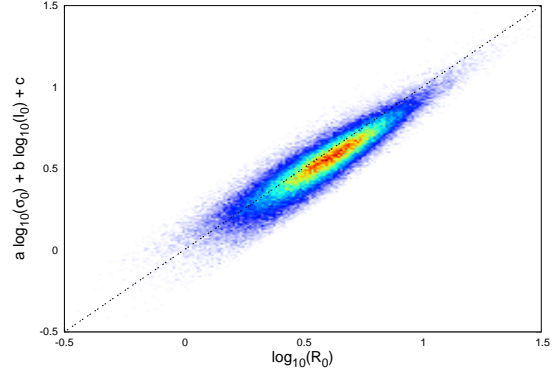
square decreases and the fundamental plane appears to be narrower, its quality as a distance indicator clearly decreases when not correcting for the Malmquist bias. It can be seen in Figure 17 that the fit of the fundamental plane lies directly in the centre of the cloud of data points, if the Malmquist bias is not corrected for by volume weights, while in all other cases (except in the volume-limited sample, which is not affected by a Malmquist bias by definition) the best fit is always slightly above the centre of the cloud.

To test the Malmquist-bias correction further, we calculated the fundamental-plane coefficients for a volume-limited subsample that does not require any corrections. Making use of Equation 6 and the results of the corresponding fit, we calculated the redshift distance for which our sample is still to ~95.45% complete (corresponding to 2-σ). This is the case up to a redshift of $z = 0.0513$, which significantly reduces the number of galaxies in the sample. The c model contains only 7259 galaxies after fitting the fundamental-plane coefficients, the dV model only 7257, and the p model only 7267. We note that the average distance error is by about 2.5 percentage point larger than for the main fit. Although the best fit is going through the centre of the cloud of data points in the same way as for the Malmquist-biased fit (see Figure 17), the coefficients (see Table C.14) are clearly less tilted than those of the Malmquist biased fit (see Table C.10). In fact, the coefficients of the volume-limited sample are relatively close (though in general slightly less tilted) than those of the main fit using the Malmquist bias correction (see Table 5). This correspondence suggests that the Malmquist bias is handled well by the correction, and therefore our magnitude-limited sample can be used with the correction like a volume-limited sample.

In contrast to the smaller volume-limited sample, we extended our sample to a redshift of 0.3, despite the additional bias beyond $z = 0.2$, which we found in Subsection 4.1. We used 97341 galaxies for the c model, 97309 for the dV model, and 97050 for the p model. The results of the fit are listed in Table C.15. We found that the quality of this fit is only marginally poorer than of the main fit (sometimes beyond the relevant digits). However, since the number of additional galaxy in the redshift range between 0.2 and 0.3 is rather small (slightly more than 4000) compared with the sample size, and because these galaxies are the most luminous part of the sample and therefore have relatively small statistic weights, it is not surprising that the
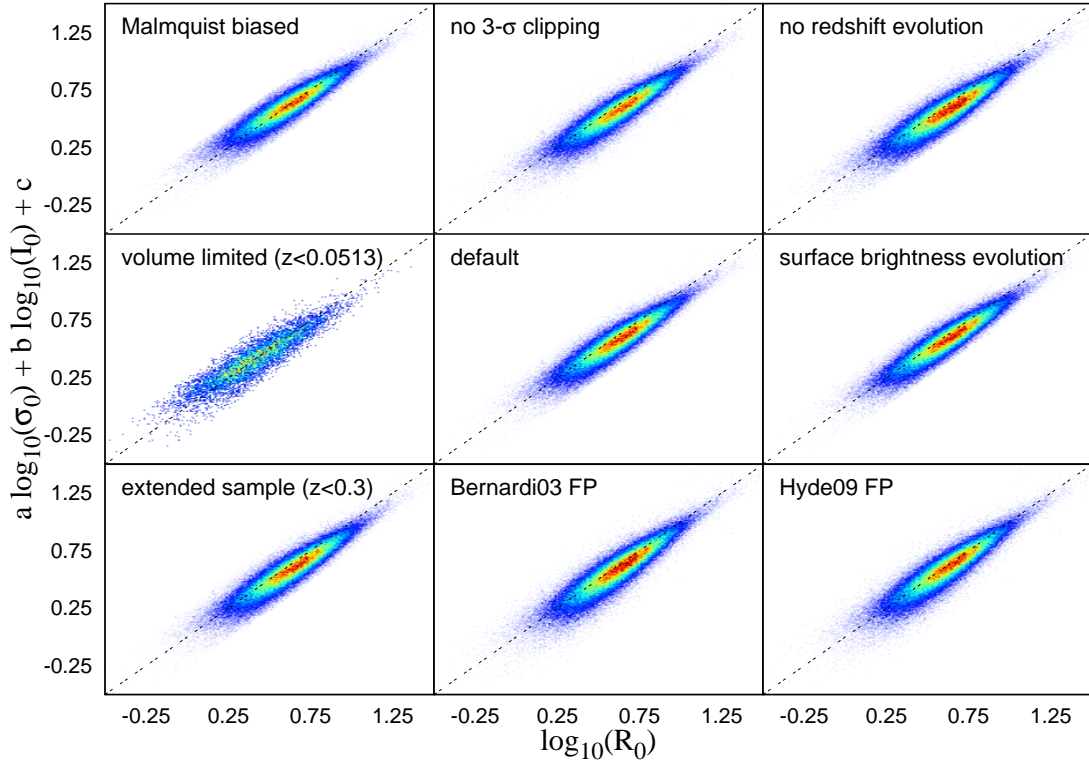
Figure 17. Results for the fundamental plane in the i band for the dV model using our alternatives fits. The plot in the top-left panel does not include the Malmquist bias. We did not perform a 3-σ clipping for the plot in the top-middle panel. The plot in the top-right panel excludes the redshift evolution. The results of the volume-limited sample ($z < 0.0513$) can be found in the central-left panel. The central-middle panel contains a plot of the default i band fit for the dV model for comparison. We are considering the surface brightness evolution instead of the redshift evolution derived form galaxy number densities in the central-right panel. In the bottom-left panel, the results are shown for an extended sample up to $z = 0.3$. The fundamental plane plotted using the coefficients of Bernardi et al. (2003c), but with our sample data is displayed in the bottom-middle panel. A similar plot using the coefficients of Hyde & Bernardi (2009) can be found in the bottom-right panel.

differences between the main fit and this are so small, in spite of the additional bias.

The correction for the redshift evolution that we used for the main fit simply takes the evolutionary parameter Q, whose value was derived in Subsection 2.2. This is 1.07 mag per z, and this value is only based on the redshift distribution of the observed galaxy number density. Therefore, it is independent of any filter. However, we investigated how the coefficients of the fundamental plane and the quality of the fit changed without considering redshift evolution. The results are listed in Table C.11. We found that the upper limit of the average distance error $\bar{\sigma}_{dist}$ is about one percentage point higher for the non-evolution-corrected fit than for the main fit. However, the coefficients of the fundamental plane are less tilted for the non-evolution-corrected fit, therefore it is possible that the details of handling the passive evolution of elliptical galaxies might contribute to the slightly less tilted coefficients (compared with our main fit) in the literature (see Table 1).

We also considered an alternative method of deriving the redshift evolution. For this, we analysed the redshift distribution of the surface brightness in our sample. The surface brightness (if properly corrected for the cosmological dimming) should be a distance, and consequently redshift-independent quantity. However, if the galaxies evolve, one expects different mean

surface brightnesses in different redshift bins. We performed a Malmquist-bias-corrected fit to the redshift distribution of the (non-evolution-corrected) surfaces brightness in all filters and for all models. The results are listed in Table C.13, and a set of graphic examples of the redshift evolution (for the dV model) is shown in Figures B.57 to B.61. These evolutionary parameters are surface brightnesses per redshift and not magnitudes per redshift, but they enter the calibration at a point at which these two are mathematically equivalent. The numeric value of these new Q parameters is at least twice as high as of the one derived by galaxy number densities, since this evolution does not only take into account changes of the absolute magnitude of the galaxies over time, but also possible changes in the radial extension of the galaxies. Furthermore, these values are different for every filter, which is more realistic because one may expect some changes not only in the luminosities, but in the colours of the galaxies. The results of the fundamental plane fit using these Q parameters from Table C.13 can be found in Table C.12. We found that the coefficient of this fit indicates a slightly more tilted fundamental plane than for the main fit. However, the average distance error is smaller by about half a percentage point for all filters and models for the surface brightness evolution fit.
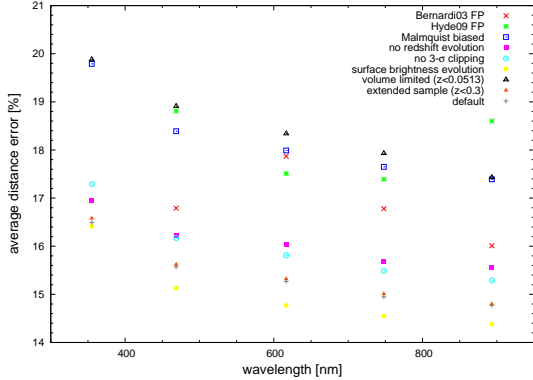
14

Figure 18. Comparison of the upper limits of the average distance error for all performed fits for all filters of the dV model.

5.2. Comparison with the literature

We compared our results with those from the literature. To this end, we used our selected sample of about 95000 galaxies and the derived fundamental-plane parameters $\log_{10}(R_0)$, $\log_{10}(\sigma_0)$, and $\log_{10}(I_0)$ and see how well the fundamental plane with coefficients from the literature fits them. We used the direct-fit coefficients from the two works that best match our own, which are Bernardi et al. (2003c) and Hyde & Bernardi (2009), and derived the root mean square s_ε and the distance error $\bar\sigma_{\mathrm{dist}}$ from our sample and their coefficients. The results of this analysis can be found in Table C.7. Our newly derived coefficients are shown to provide a by a distance estimate couple of percentage points better than the previous ones. We point out that we used the same redshift evolutions for their samples as were given in the references. Furthermore, one can see in Figure 17 that the location of the fundamental plane in Bernardi et al. (2003c) and Hyde & Bernardi (2009) is similarly slightly above the centre of the cloud of data points, as in our fits. As already mentioned before, this is due to the Malmquist-bias correction.

An overall visual comparison between the different fits of the fundamental plane performed by us can be found in Figure 17. Furthermore, we compare the upper limit of the average distance error of each fit or recalculation (Bernardi et al. (2003c) and Hyde & Bernardi (2009) coefficients) in Figure 18.

In addition to the fits of the fundamental plane, we studied the redshift distribution of the elliptical galaxies. We found a comoving number density of elliptical galaxies in the universe of $7 \cdot 10^{-4}$ per $(\mathrm{Mpc} \cdot h_{70}^{-1})^3$, which is about 35% of the value derived in Bernardi et al. (2003b), who reported $(2.0\pm0.1)\cdot10^{-3}$ per $(\mathrm{Mpc} \cdot h_{70}^{-1})^3$. We attribute this difference to the different underlying selection functions of the two samples. If we were to accept all 170962 candidates for elliptical galaxies obtained from GalaxyZoo as true ellipticals, our average comoving number density would increase by about 85% to $1.3\cdot10^{-3}$ per $(\mathrm{Mpc}\cdot h^{-1})^3$ in Figure 6, which is closer to, albeit still clearly below, the value of Bernardi et al. (2003b). When comparing the fractions of SDSS galaxies with spectroscopic data that are classified as ellipticals, our overall selection criteria including GalaxyZoo are slightly stricter than those of Bernardi et al. (2003a). Our selected sample consists of ~95000 galaxies taken from a total of ~852000 SDSS DR8 galaxies with proper spectroscopic data. This yields a fraction of about 11%, somewhat lower than the about 14% obtained by Bernardi et al. (2003a), who classi-

fied ~9000 galaxies as ellipticals of a total of ~65000 galaxies, for which spectroscopic and photometric data was provided by SDSS at that time. We thus conclude that differences in selection strictness work towards closing the gap between the higher density estimate by Bernardi et al. (2003b) and our data, even though they cannot directly explain the full difference. We note that our value is consistent with the luminosity function analysis in Subsection 4.2.

We found the same overdensities in the number counts by redshift as Bernardi et al. (2003b). We identify one as being associated with the CfA2-Great Wall around a redshift of 0.029 (Geller & Huchra 1989) and another related to the Sloan Great Wall around a redshift of 0.073 (Gott et al. 2005). In addition to that, we confirm a peak in the number count of elliptical galaxies around 0.13, which has previously been reported in Bernardi et al. (2003b), but was not investigated in detail. Another result we obtained by analysing the redshift distribution of sample is the evolution parameter Q. The parameter derived just from the galaxy number densities within the sample should be an averaged estimate for all bands. Our fit yields a Q of 1.07 mag (per z), which is similar to the values of Bernardi et al. (2003b). In an alternative approach on deriving the redshift evolution, we used the redshift distribution of the surface brightnesses of the galaxies in our sample, which yielded significantly higher values (see Table C.13) than our first approach and the values of Bernardi et al. (2003b) and Hyde & Bernardi (2009).
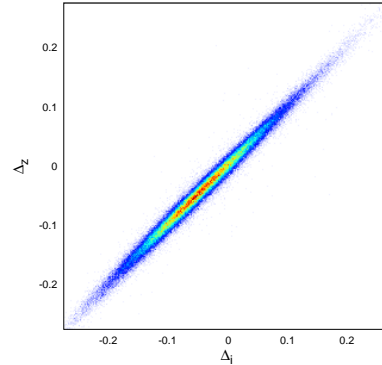
Figure 19. Tight correlation between the residuals of the fundamental plane in the i band Δ_i and of those in the z band Δ_z can be easily seen in this plot. This plot uses the fundamental-plane fit for the dV model.

5.3. Correlations of the residuals

The fundamental plane was fitted independently in every filter. One does not necessarily expect any correlation between the residuals Δ_f (see Equation 40 for the definition) of the fundamental plane for different filters f due to our methodology. However, a significant correlation between the residuals of different filters may still exist if the thickness of the fundamental plane is mainly caused by real deviations of the parameters and not by errors in the measurement of these parameters,

$$\Delta = a \cdot \log_{10}(\sigma_0) + b \cdot \log_{10}(I_0) + c - \log_{10}(R_0). \quad (40)$$

The strength of the correlation between the residuals of the fundamental plane in different filters is strikingly important, especially when one plans on using the fundamental plane as distance

15

36

indicator. If the correlation between the residuals in different filters is found to be low, one will be able to treat the distances obtained by the fundamental plane in different filters as independent measurements and will be able to achieve a better distance estimate by combining them than by using just data from one filter. We can quantify the correlation strength by calculating the linear correlation coefficients r_{f_1,f_2} for all possible combinations of filters.

$$r_{f_1,f_2} = \sqrt{\frac{\left(\left(\sum_j \left(\Delta_{f_1} - \bar{\Delta}_{f_1}\right)\right) \cdot \left(\sum_j \left(\Delta_{f_2} - \bar{\Delta}_{f_2}\right)\right)\right)^2}{\left(\sum_j \left(\Delta_{f_1} - \bar{\Delta}_{f_1}\right)^2\right) \cdot \left(\sum_j \left(\Delta_{f_2} - \bar{\Delta}_{f_2}\right)^2\right)}}. \quad (41)$$

The linear correlation coefficient r_{f_1,f_2} for the two filters f_1 and f_2 can be calculated using the residuals of the fundamental plane Δ_f and their averages $\bar{\Delta}_f$ of the corresponding filters f. For perfectly linearly correlated data points, the coefficient r_{f_1,f_2} is equal to one and for totally uncorrelated data points, it is zero. We found that the residuals of the fundamental plane of different filters are strongly correlated, as illustrated in Figure 19 using the example of the i and z band residuals of the dV model. The corresponding plots for all other combinations of filters for the same model are displayed in Figures B.70 to B.78. The linear correlation coefficients for all filters and models are listed in Table 6. The values are very close to one, which indicates tight correlations. The correlations are slightly weaker, yet very strong for the p model, because the parameters of the fundamental plane have a larger scatter in this model and consequently the larger random errors dampen the correlation somewhat. The same is true for the correlation between the u band and any other filter. Therefore, relative values of the linear correlation coefficients agree with our previous findings about the u band and the p model parameters.

Furthermore, the correlation coefficients decrease with greater differences in the wavelength of two filters, which is not surprising, because one may expect lower correlation the more different the bands are. We found that the correlation between the filters is too strong to enhance the quality of the distance measurement by combining different filters. In fact, every possible combination of the fundamental plane distances obtained by two and more filters yields a greater average distance error than using the best filter (z band) alone. This means that on average, if the parameters of a galaxy are located away from the fundamental plane in one filter, they are most likely similarly displaced in all other filters as well. This shows that the width of the fundamental plane does not primarily originate in measurement uncertainties of the required parameter, but in the intrinsic properties of the elliptical galaxies. The origin of this scatter is widely discussed in the literature. The theoretical derivation of the fundamental plane assumes a primary pressure-supported system. Nevertheless, it is known that elliptical galaxies are partially rotation-supported (Burkert et al. 2008), too, and a variation in the fraction of pressure and rotational support can lead to inaccuracies in the mass estimates, which finally manifest themselves in the scatter of the fundamental plane. However, this effect alone does not seem to be sufficient to explain the entire scatter (Prugniel & Simien 1996; Oñorbe et al. 2005). Other explanations or contributing factors are the age (Forbes et al. 1998) and variations in the stellar population parameters (Gargiulo et al. 2009), which are also considered as an explanation for the tilt of the fundamental plane by some authors (La Barbera et al. 2008; Trujillo et al. 2004), and the merger history (Hopkins et al. 2008). An extensive study on the details of

filters	c model	dV model	p model
$r_{i,z}$	0.9909	0.9918	0.9259
$r_{r,z}$	0.9836	0.9852	0.9268
$r_{g,z}$	0.9635	0.9653	0.9140
$r_{u,z}$	0.8584	0.8637	0.8190
$r_{r,i}$	0.9933	0.9939	0.9812
$r_{g,i}$	0.9788	0.9798	0.9643
$r_{u,i}$	0.8768	0.8823	0.7979
$r_{g,r}$	0.9904	0.9905	0.9808
$r_{u,r}$	0.8865	0.8913	0.8029
$r_{u,g}$	0.9099	0.9155	0.8191

Table 6. Linear correlation coefficients of the fundamental-plane residuals for all possible combinations of the five SDSS filters.

the origin of the scatter and the tilt of the fundamental plane is beyond the scope of this paper.

6. Summary and Conclusions

We analysed a sample of about 93000 elliptical galaxies taken from SDSS DR8. It forms the largest sample used for the calibration of the fundamental plane so far (roughly twice as large as the previous largest sample of Hyde & Bernardi (2009)). Furthermore, we used the high-quality K-corrections by Chilingarian et al. (2010). We also used GalaxyZoo data (Lintott et al. 2011) to classify SDSS galaxies. A direct fit using a volume-weighted least-squares method was applied to obtain the coefficients of the fundamental plane because we plan on using the fundamental plane as a distance indicator in the subsequent work. We achieved an accuracy in the distance measurement of about 15%. In addition to the fundamental plane, we studied the redshift distribution of the elliptical galaxies and the distribution of their global parameters such as the luminosity function.

We found a comoving number density of $7 \cdot 10^{-4}$ per $(\text{Mpc} \cdot h_{70}^{-1})^3$ for elliptical galaxies that qualify for our sample. Furthermore, in the analysis of the redshift distribution of the galaxies in our sample, we detected the same overdensities in the number counts by redshift as Bernardi et al. (2003b). One was identified as being associated with the CfA2-Great Wall (Geller & Huchra 1989) and another is related to the Sloan Great Wall (Gott et al. 2005). In addition to these two well-known overdensities, we confirm a peak in the number count of elliptical galaxies around 0.13, which has previously been reported in Bernardi et al. (2003b), but was not investigated in detail. Moreover, we derived an evolution parameter Q for elliptical galaxies of 1.07 mag (per z), which is similar to the values of Bernardi et al. (2003b).

In addition to the results of our main fit, which are listed in Table 5, we provided a detailed analysis of the calibrations we made and their influence on the quality of the fitting process. We studied the effects of neglecting the Malmquist-bias correction, the 3-σ clipping, or the redshift evolution correction. We also investigated changes in the parameters after using an alternative redshift evolution, a volume-limited sample, or an extended sample.

To compare our calibrations with the literature, we calculated the root mean square and the upper limit of the average distance error using the coefficients and evolution parameters of Bernardi et al. (2003c) and Hyde & Bernardi (2009), but with the galaxies and parameters of our sample. We picked these two papers, because their work is the most similar to our own. The results can be found in Table C.7, and one can easily see that our main fit

16

(see Table 5) provides a better distance indicator by a couple of percentage points.

We investigated the correlation between the fundamental-plane residuals and found that they correlated too strongly to use a combination of the five independent fits (one for every filter) to reduce the overall scatter by combining two or more of them.

We found that in general the quality of the fundamental plane as a distance indicator increases with the wavelength, although the root mean square has its minimum in the SDSS i band. The upper limit of the average distance error is in general lowest in the z band, as one can see in Figure 18. Furthermore, we found that the tilt of the fundamental plane (for the c and dV model) becomes smaller in the redder filters, as illustrated in Figure 14. In our analysis, we learned that the dV model did best when considering the root mean square and the average distance error. It uses the pure de Vaucouleurs-magnitudes and radii. The c model (using composite magnitudes of a de Vaucouleurs and an exponential fit) only performed insignificantly worse, which indicates that the galaxies in our sample are very well described by de Vaucouleurs profiles. This finding is an expected feature of elliptical galaxies and tells us that our sample is very clean (the contamination by non-elliptical galaxies is insignificantly low). By comparing them to the results of the p model, we can instantly see that the Petrosian magnitudes and radii in SDSS provide poorer fits and cause a larger scatter. Therefore, we recommend only using the pure de Vaucouleurs magnitudes and radii together with our coefficients for them (see Table 5) and, if possible, the z or i band for applications of the fundamental plane. Moreover, we strongly discourage the use of the u band due to known problems and the resulting lower quality of the results for this filter.

We also found that our coefficients are similar to other direct fits of the fundamental plane of previous authors (see Table 1) (though the a coefficient is slightly lower in our case, therefore the fundamental plane is more tilted), but due to our larger sample, we managed to achieve a yet unmatched accuracy.

In future work, we plan on using the fundamental plane to obtain redshift-independent distances for a large sample of elliptical galaxies from the SDSS. We will use those distances in combination with redshift data to derive peculiar velocities, which will form the basis of a cosmological test outlined in Saulder et al. (2012). We will investigate the dependence of the Hubble parameter of individual galaxies or clusters on the line of sight mass density towards these objects, and compare this with predictions of cosmological models.

Acknowledgments

Appendix A: Redshift correction for the motion relative to the CMB

The observed redshift z is in the rest frame of our solar system, but for cosmological and extragalactic application, one requires a corrected redshift z_{cor}, which is in the same rest frame as the CMB.

$$z_{cmb,x} = \frac{v_{cmb}}{c}\cos(b_{cmb})\cos(l_{cmb})$$
$$z_{cmb,y} = \frac{v_{cmb}}{c}\cos(b_{cmb})\sin(l_{cmb}) \qquad (A.1)$$
$$z_{cmb,z} = \frac{v_{cmb}}{c}\sin(b_{cmb})$$

The solar system moves into the direction of $l_{cmb} = 263.99° \pm 0.14°$ $b_{cmb} = 48.26° \pm 0.03°$ (galactic coordinates) with a velocity of $v_{cmb} = (369.0 \pm 0.9)\,km\,s^{-1}$ (Hinshaw et al. 2009). The first step required for this correction is to calculate the redshift space vector of our motion relative to the CMB $z_{cmb} = \left(z_{cmb,x}, z_{cmb,y}, z_{cmb,z}\right)$.

$$z_x = z\cos(b)\cos(l)$$
$$z_y = z\cos(b)\sin(l) \qquad (A.2)$$
$$z_z = z\sin(b)$$

Then we translate the coordinates (l,b,z) of the observed galaxies into Cartesian coordinates into redshift space $z = \left(z_x, z_y, z_z\right)$. In the next step, we perform a vector addition,

$$z_\Sigma = z + z_{cmb}. \qquad (A.3)$$

$$z_{cor} = z_{\Sigma,x}\cos(b)\cos(l) + z_{\Sigma,y}\cos(b)\sin(l) + z_{\Sigma,z}\sin(b) \quad (A.4)$$

Now we project the vector $z_\Sigma = \left(z_{\Sigma,x}, z_{\Sigma,y}, z_{\Sigma,z}\right)$ onto the line of sight and obtain the corrected (for our motion relative to the CMB) redshift z_{cor}. The corrected redshifts z_{cor} are in the same rest frame as the CMB and can be used to calculate distances using the Hubble relation.

Appendix B: Additional figures
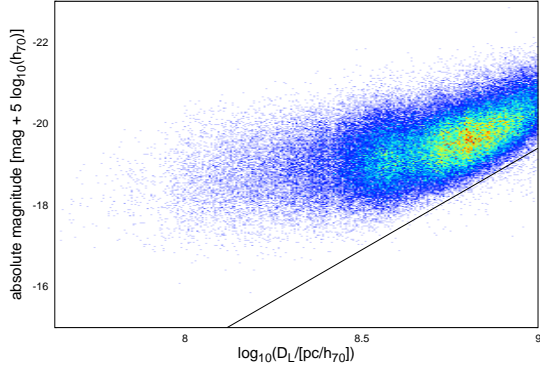
Figure B.1. Malmquist bias in the u band for the c model parameters is indicated by the black solid line of our fit. Due to the larger scatter in the u band, the fit is not as tight as for the other filters.

Figure B.2. Malmquist bias in the g band for the c model parameters is indicated by the black solid line of our fit.
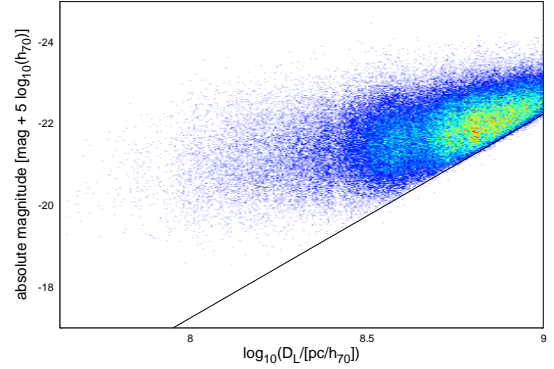
Figure B.3. Malmquist bias in the r band for the c model parameters is indicated by the black solid line of our fit.
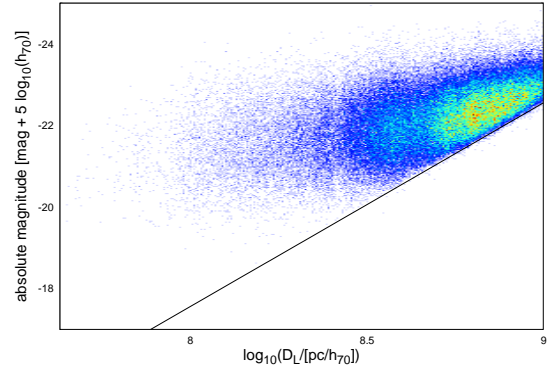
Figure B.4. Malmquist bias in the i band for the c model parameters is indicated by the black solid line of our fit.
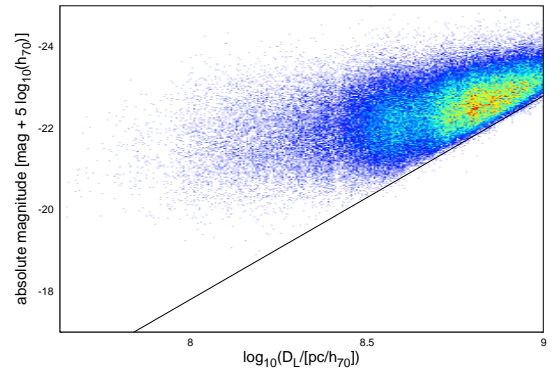
Figure B.5. Malmquist bias in the z band for the c model parameters is indicated by the black solid line of our fit.

18
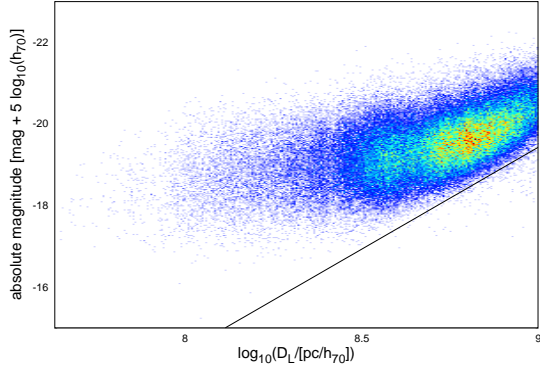
Figure B.6. Malmquist bias in the u band for the dV model parameters is indicated by the black solid line of our fit. Due to the larger scatter in the u band, the fit is not as tight as for the other filters.
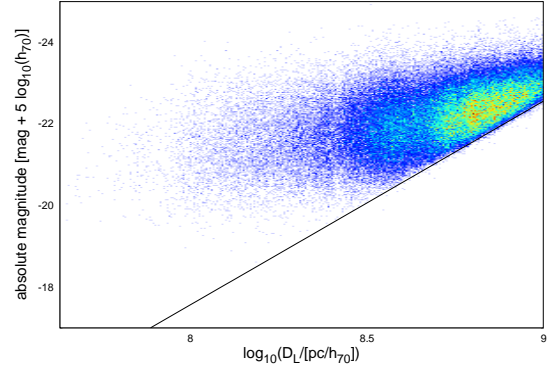
Figure B.9. Malmquist bias in the i band for the dV model parameters is indicated by the black solid line of our fit.
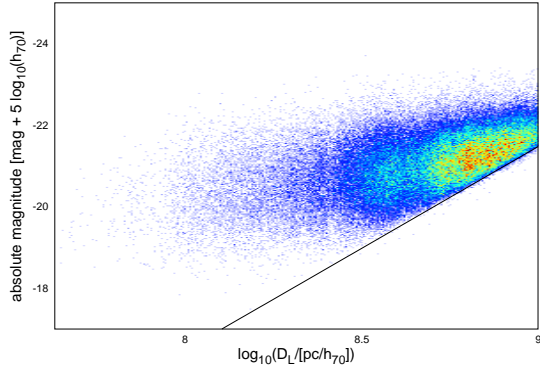
Figure B.7. Malmquist bias in the g band for the dV model parameters is indicated by the black solid line of our fit.
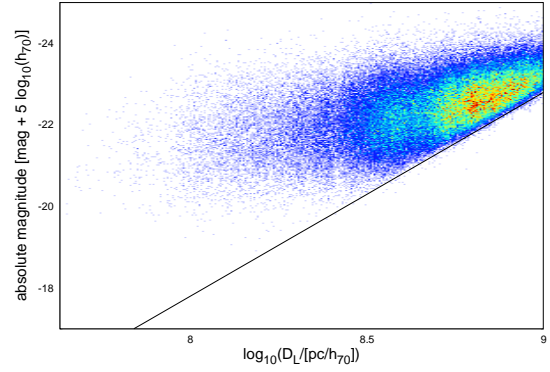
Figure B.10. Malmquist bias in the z band for the dV model parameters is indicated by the black solid line of our fit.
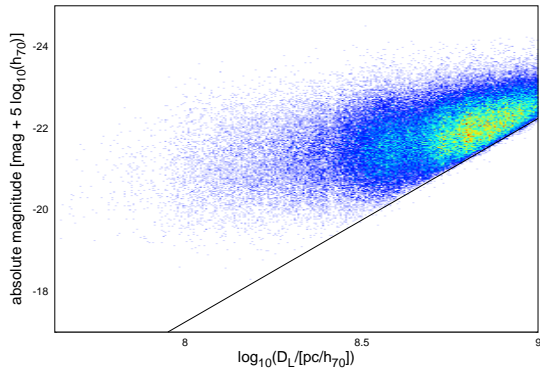
Figure B.8. Malmquist bias in the r band for the dV model parameters is indicated by the black solid line of our fit.
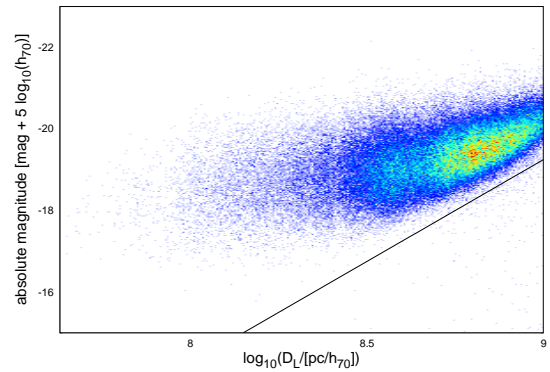
Figure B.11. Malmquist bias in the u band for the p model parameters is indicated by the black solid line of our fit. Due to the larger scatter in the u band, the fit is not as tight as for the other filters.

19
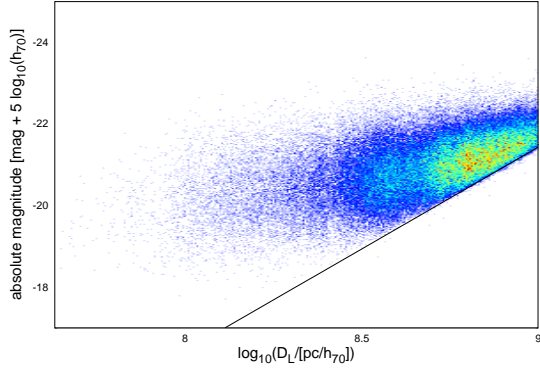
Figure B.12. Malmquist bias in the g band for the p model parameters is indicated by the black solid line of our fit.
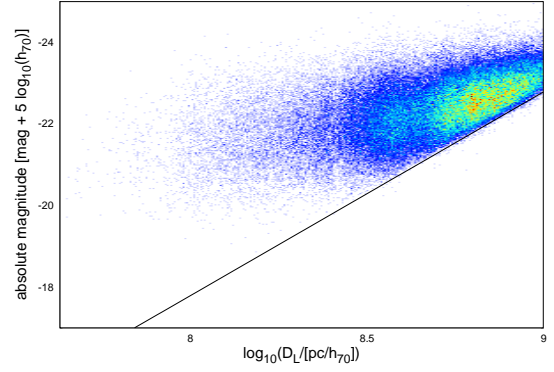
Figure B.15. Malmquist bias in the z band for the p model parameters is indicated by the black solid line of our fit.
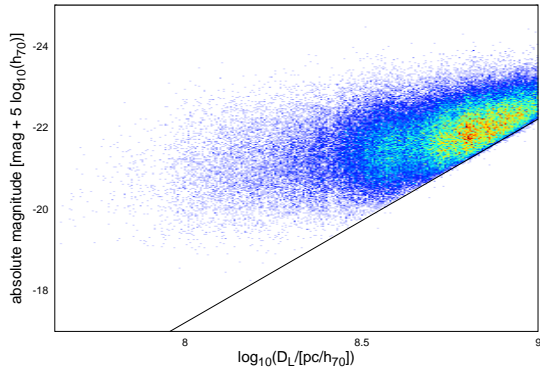
Figure B.13. Malmquist bias in the r band for the p model parameters is indicated by the black solid line of our fit.
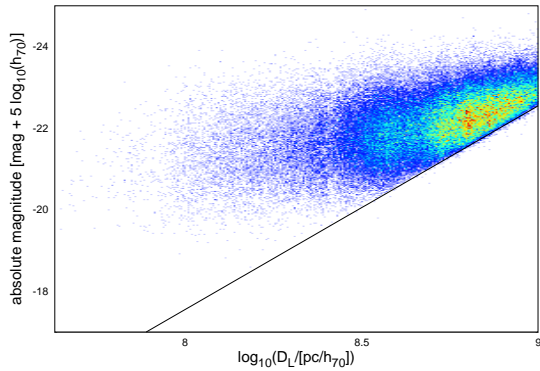
Figure B.14. Malmquist bias in the i band for the p model parameters is indicated by the black solid line of our fit.

Figure B.16. Luminosity function for our sample in the u band for the c model. We split it into different subsamples (within different redshift bins) and compared the expected unbiased luminosity function and the total observed luminosity function. Our sample is almost complete at the luminous end, but we are missing many of the fainter galaxies due to the Malmquist bias.

20
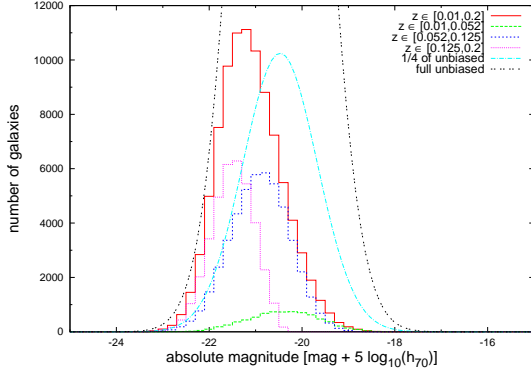
Figure B.17. Luminosity function for our sample in the g band for the c model. We split it into different subsamples (within different redshift bins) and compared the expected unbiased luminosity function and the total observed luminosity function. Our sample is almost complete at the luminous end, but we are missing many of the fainter galaxies due to the Malmquist bias.
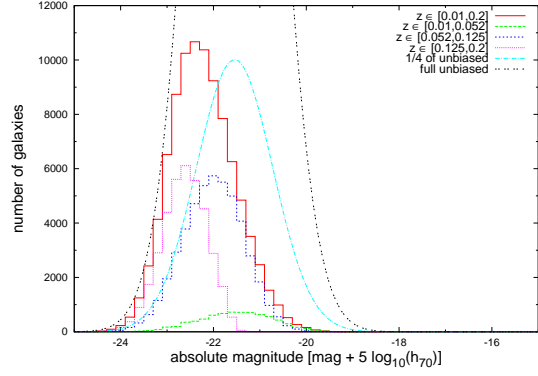
Figure B.19. Luminosity function for our sample in the i band for the c model. We split it into different subsamples (within different redshift bins) and compared the expected unbiased luminosity function and the total observed luminosity function. Our sample is almost complete at the luminous end, but we are missing many of the fainter galaxies due to the Malmquist bias.
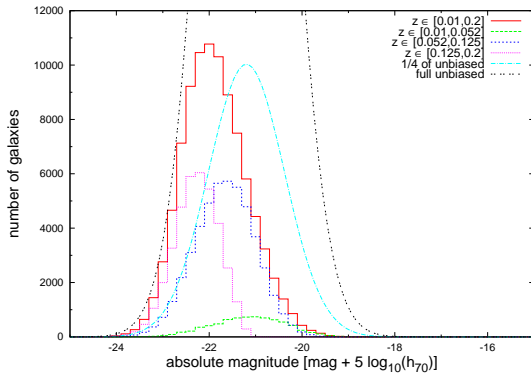
Figure B.18. Luminosity function for our sample in the r band for the c model. We split it into different subsamples (within different redshift bins) and compared the expected unbiased luminosity function and the total observed luminosity function. Our sample is almost complete at the luminous end, but we are missing many of the fainter galaxies due to the Malmquist bias.
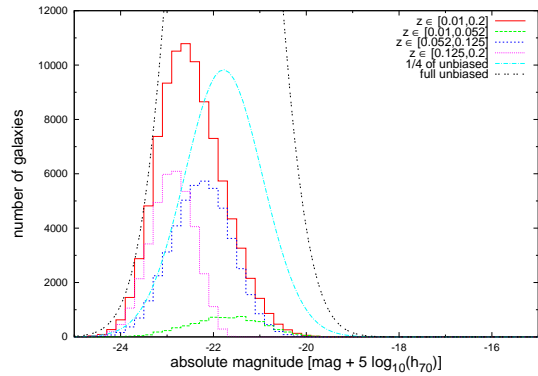
Figure B.20. Luminosity function for our sample in the z band for the c model. We split it into different subsamples (within different redshift bins) and compared the expected unbiased luminosity function and the total observed luminosity function. Our sample is almost complete at the luminous end, but we are missing many of the fainter galaxies due to the Malmquist bias.

21
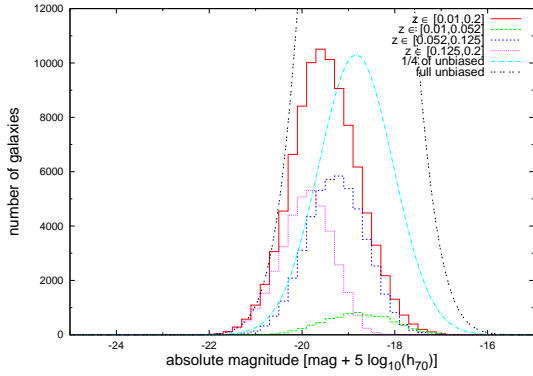
Figure B.21. Luminosity function for our sample in the u band for the dV model. We split it into different subsamples (within different redshift bins) and compared the expected unbiased luminosity function and the total observed luminosity function. Our sample is almost complete at the luminous end, but we are missing many of the fainter galaxies due to the Malmquist bias.
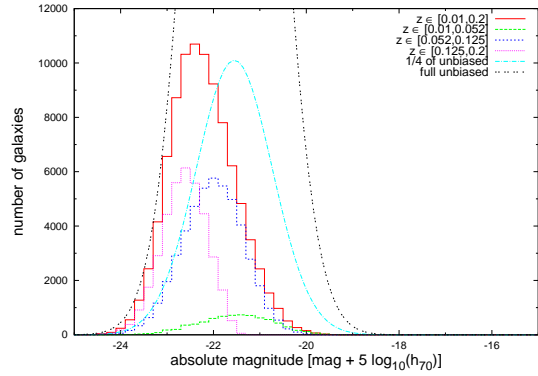
Figure B.23. Luminosity function for our sample in the i band for the dV model. We split it into different subsamples (within different redshift bins) and compared the expected unbiased luminosity function and the total observed luminosity function. Our sample is almost complete at the luminous end, but we are missing many of the fainter galaxies due to the Malmquist bias.
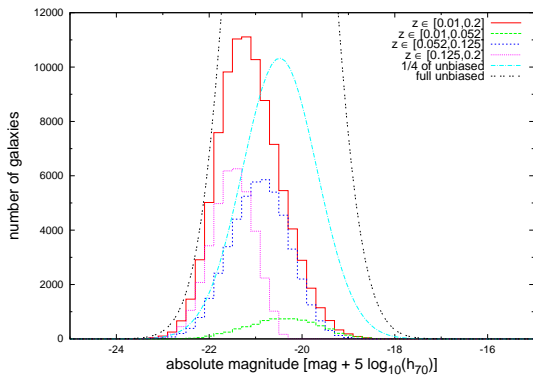
Figure B.22. Luminosity function for our sample in the g band for the dV model. We split it into different subsamples (within different redshift bins) and compared the expected unbiased luminosity function and the total observed luminosity function. Our sample is almost complete at the luminous end, but we are missing many of the fainter galaxies due to the Malmquist bias.
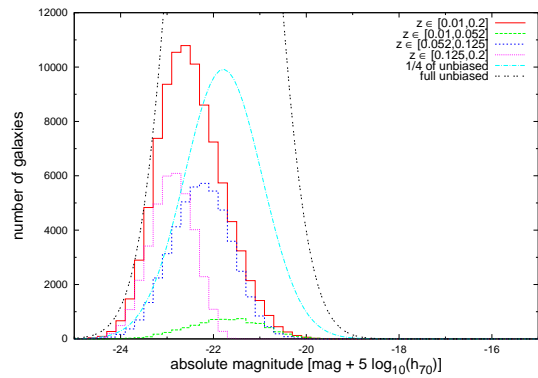
Figure B.24. Luminosity function for our sample in the z band for the dV model. We split it into different subsamples (within different redshift bins) and compared the expected unbiased luminosity function and the total observed luminosity function. Our sample is almost complete at the luminous end, but we are missing many of the fainter galaxies due to the Malmquist bias.

22
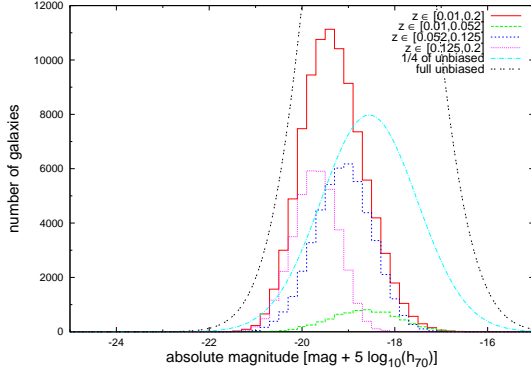
Figure B.25. Luminosity function for our sample in the u band for the p model. We split it into different subsamples (within different redshift bins) and compared the expected unbiased luminosity function and the total observed luminosity function. Our sample is almost complete at the luminous end, but we are missing many of the fainter galaxies due to the Malmquist bias.
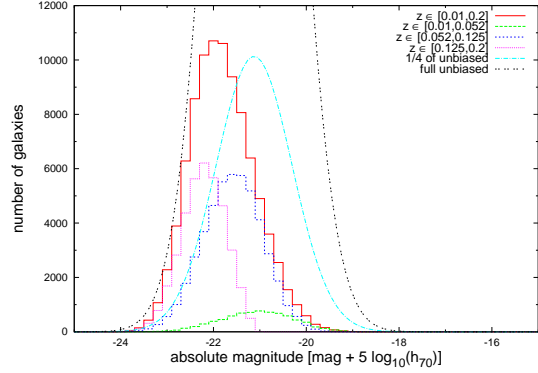
Figure B.27. Luminosity function for our sample in the r band for the p model. We split it into different subsamples (within different redshift bins) and compared the expected unbiased luminosity function and the total observed luminosity function. Our sample is almost complete at the luminous end, but we are missing many of the fainter galaxies due to the Malmquist bias.
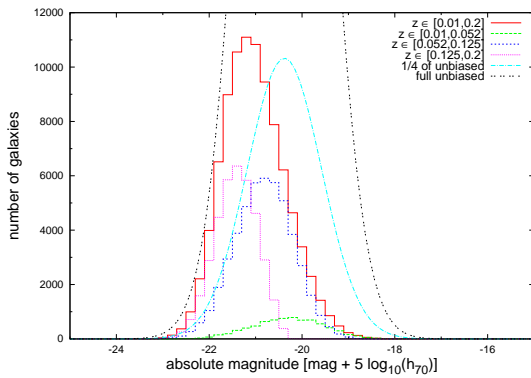
Figure B.26. Luminosity function for our sample in the g band for the p model. We split it into different subsamples (within different redshift bins) and compared the expected unbiased luminosity function and the total observed luminosity function. Our sample is almost complete at the luminous end, but we are missing many of the fainter galaxies due to the Malmquist bias.
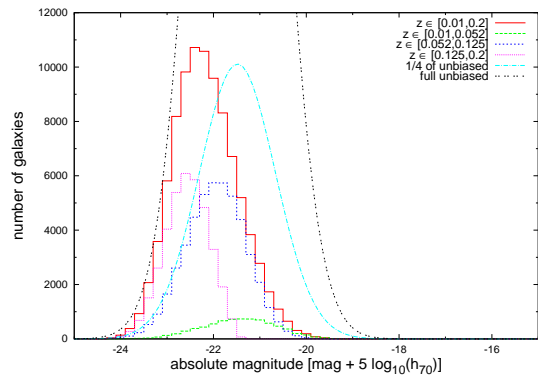
Figure B.28. Luminosity function for our sample in the i band for the p model. We split it into different subsamples (within different redshift bins) and compared the expected unbiased luminosity function and the total observed luminosity function. Our sample is almost complete at the luminous end, but we are missing many of the fainter galaxies due to the Malmquist bias.
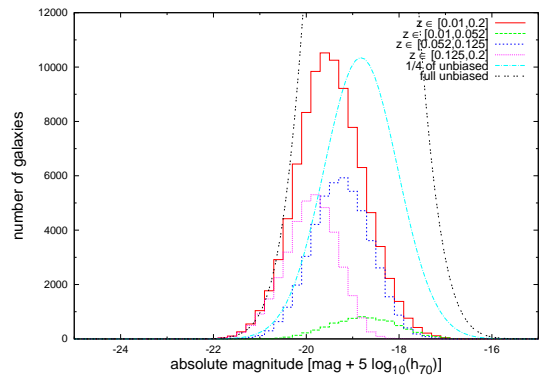
23
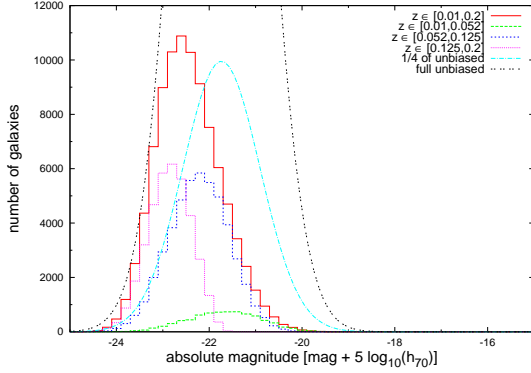
Figure B.29. Luminosity function for our sample in the z band for the p model. We split it into different subsamples (within different redshift bins) and compared the expected unbiased luminosity function and the total observed luminosity function. Our sample is almost complete at the luminous end, but we are missing many of the fainter galaxies due to the Malmquist bias.
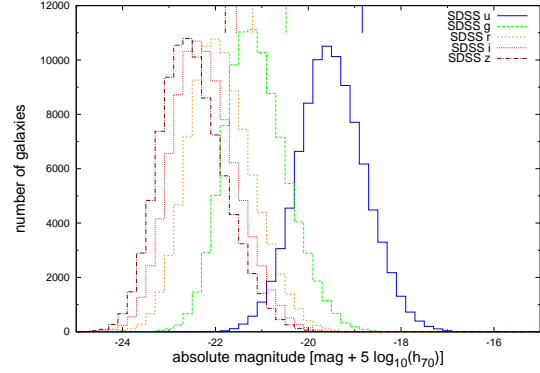

Figure B.31. Comparison of the luminosity functions in different filters for the dV model. Although their shapes stay approximately the same, the peaks move to higher luminosities with redder filters. The short lines in the upper part of the plot indicate the Malmquist-bias-corrected mean magnitudes of our sample in the corresponding filters.
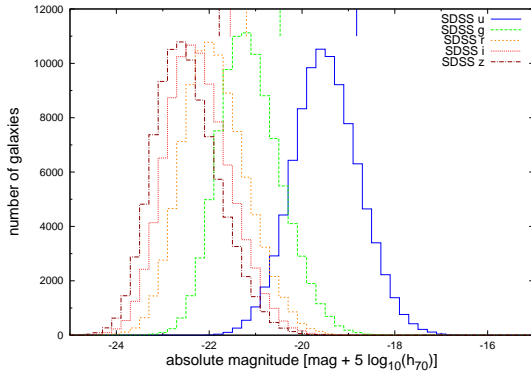
Figure B.30. Comparison of the luminosity functions in different filters for the c model. Although their shapes stay approximately the same, the peaks move to higher luminosities with redder filters. The short lines in the upper part of the plot indicate the Malmquist-bias-corrected mean magnitudes of our sample in the corresponding filters.
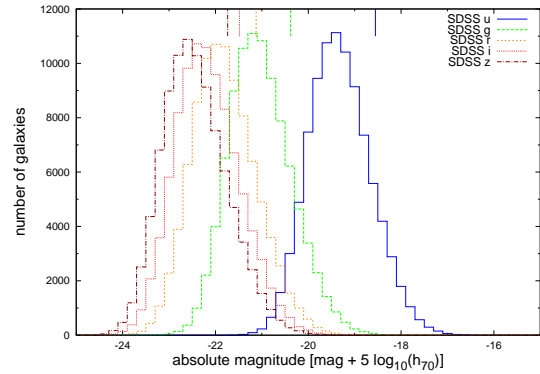
Figure B.32. Comparison of the luminosity functions in different filters for the p model. Although their shapes stay approximately the same, the peaks move to higher luminosities with redder filters. The short lines in the upper part of the plot indicate the Malmquist-bias-corrected mean magnitudes of our sample in the corresponding filters.

24
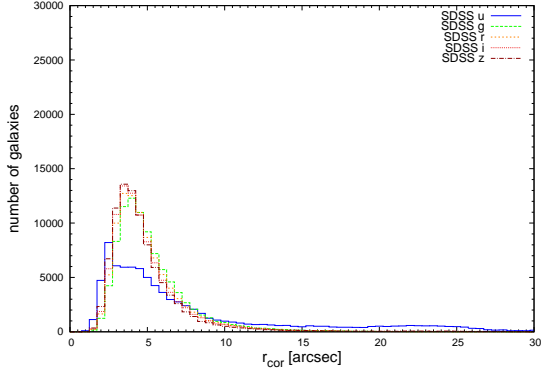
Figure B.33. Distribution of the apparent corrected radius r_{cor} is displayed in different filters for the p model. The measured radii of this model are clearly larger than those of the dV model. Furthermore, the distribution is extremely spread out in the u band due to known problems in this filter.
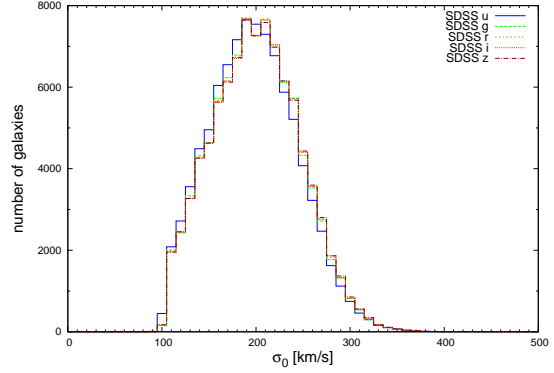
Figure B.35. Central velocity dispersion σ_0 for different filters (only slightly different in all of them due to the small correction for the fixed fibre diameters) for the p model. One can clearly see the cut-off of at 100 km/s, which has been introduced to avoid the contamination of our sample.
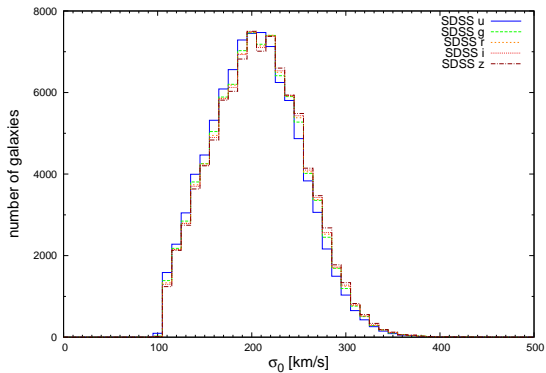
Figure B.34. Central velocity dispersion σ_0 for different filters (only slightly different in all of them due to the small correction for the fixed fibre diameters) for the c and the dV model. One can clearly see the cut-off of at 100 km/s, which has been introduced to avoid the contamination of our sample.
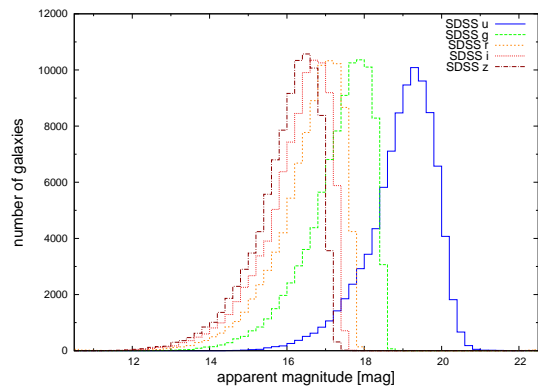
Figure B.36. Distribution of extinction- and K-corrected apparent magnitudes m_{app} in different filters for the c model, showing a steady increase in numbers until the steep cut-off at the sample's limiting magnitudes, which are listed in Table 3.

25
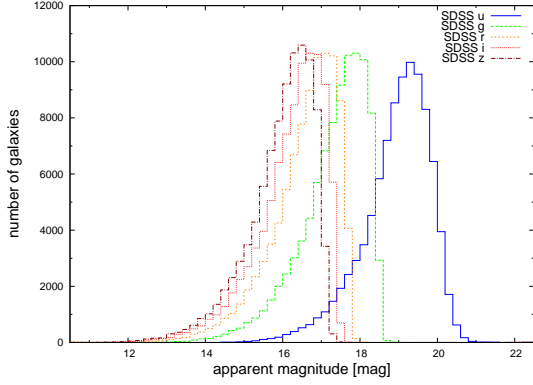
Figure B.37. Distribution of extinction- and K-corrected apparent magnitudes m_{app} in different filters for the dV model, showing a steady increase in numbers until the steep cut-off at the sample's limiting magnitudes, which are listed in Table 3.
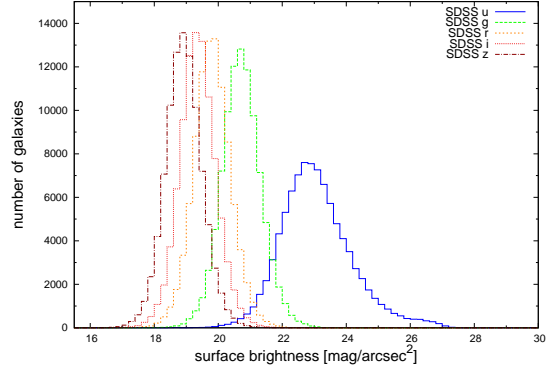
Figure B.39. Distribution of the surface brightness μ_0 in different filters for the c model showing an almost Gaussian shape. For the u band, the distribution is wider and shows a small bump at the faint end.
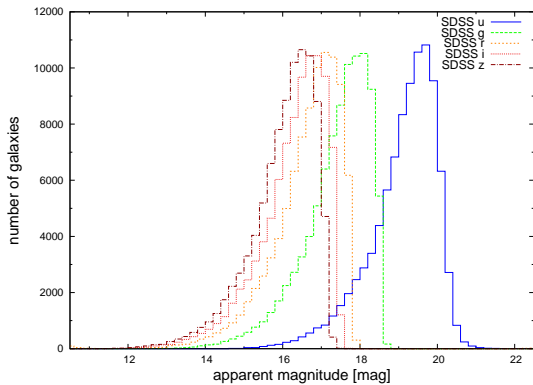
Figure B.38. Distribution of extinction- and K-corrected apparent magnitudes m_{app} in different filters for the p model, showing a steady increase in numbers until the steep cut-off at the sample's limiting magnitudes, which are listed in Table 3.
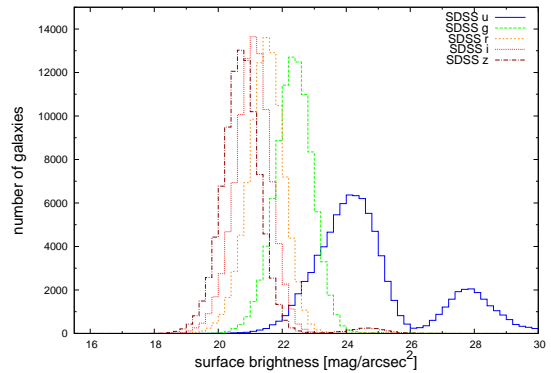
Figure B.40. Distribution of the surface brightness μ_0 in different filters for the p model shows some peculiar features in the u band and to some smaller extent in z band as well. In these two filters, one can see a clear second peak on the faint side of the main Gaussian.

26
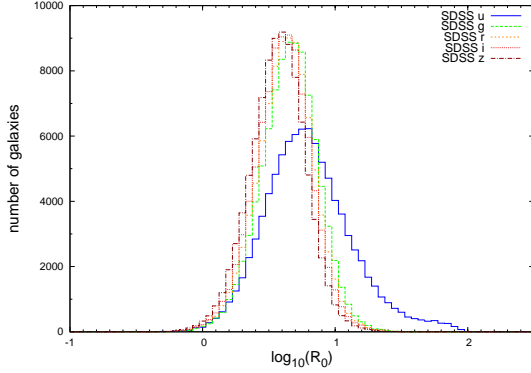
Figure B.41. Distributions of the logarithm of the physical radius $\log_{10}(R_0)$ in different filters for the c model are well described by sharp Gaussian with their peaks almost exactly at the same value. Only the u band shows some digressive behaviour. In this case the peak is smaller and set apart from the other. Furthermore, the distribution is wider and shows a small bump at the larger end.
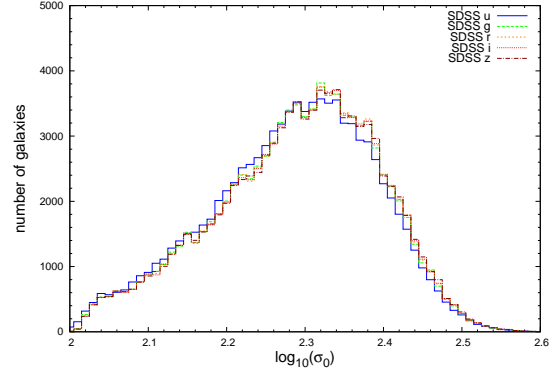
Figure B.43. Distributions of the logarithm of the central velocity dispersion $\log_{10}(R_0)$ in different filters for the p model are almost exactly the same for all filters. They show an general abundance (compared with a perfect Gaussian) of galaxies at the lower end, which might indicate some residual contamination of the sample.
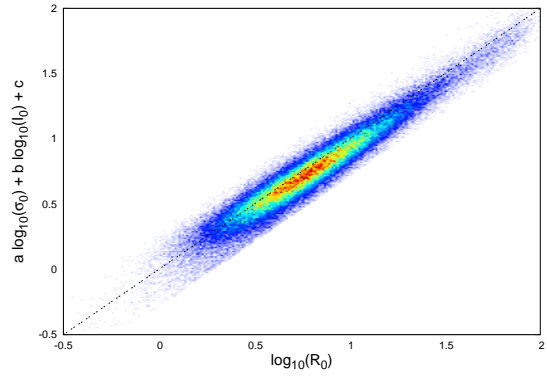
Figure B.44. Projection of the fundamental plane for the u band of the c model.
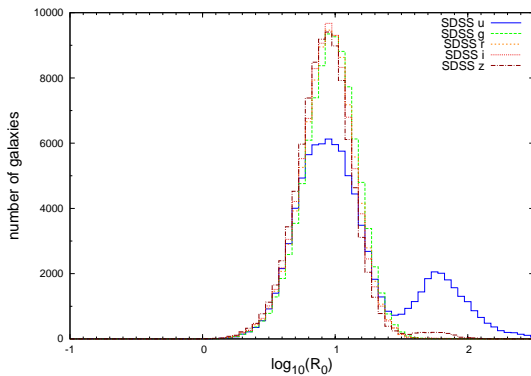
Figure B.42. Distributions of the logarithm of the physical radius $\log_{10}(R_0)$ in different filters for the p model are well described by sharp Gaussian with their peaks almost exactly at the same value. However, the u band shows a peculiar second peak aside the consequently smaller (in comparison to the other filters) main one. In addition to this deviation, the z band distribution has a small bump at its larger end.
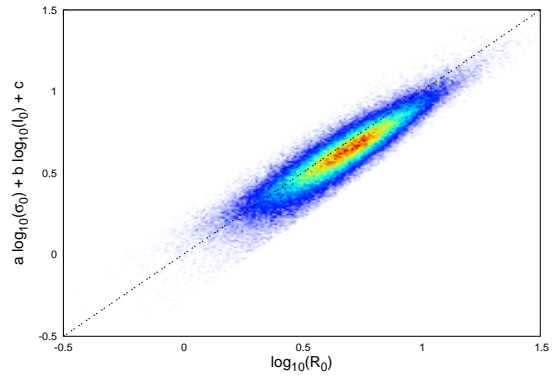
Figure B.45. Projection of the fundamental plane for the g band of the c model.

27
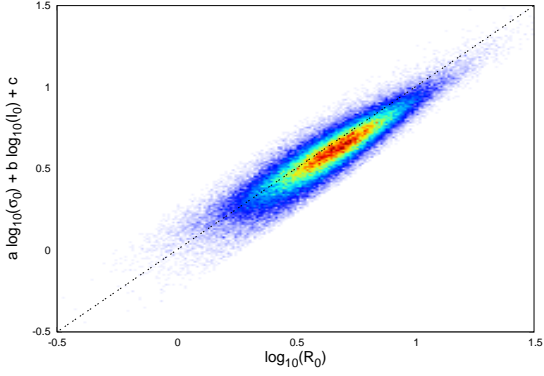
Figure B.46. Projection of the fundamental plane for the r band of the c model.
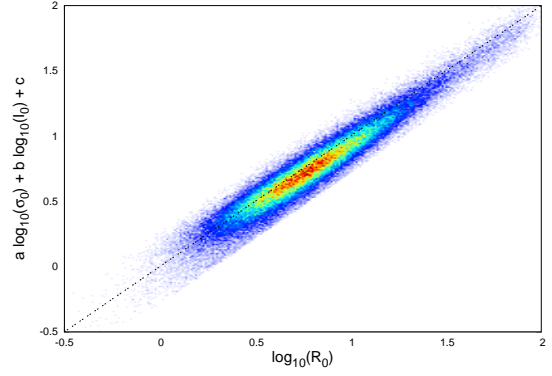
Figure B.49. Projection of the fundamental plane for the u band of the dV model.
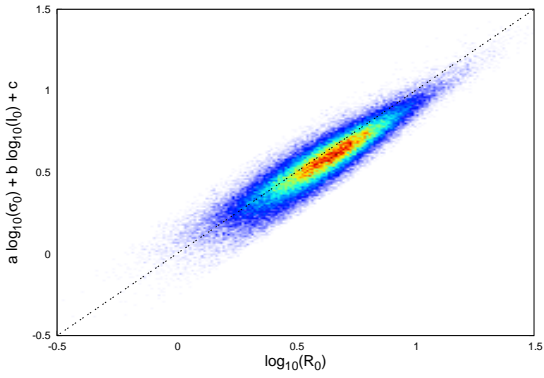
Figure B.47. Projection of the fundamental plane for the i band of the c model.
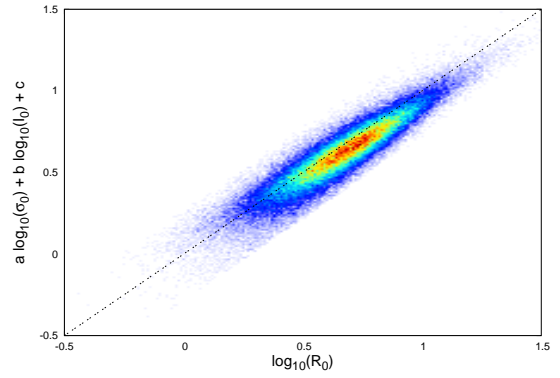
Figure B.50. Projection of the fundamental plane for the g band of the dV model.
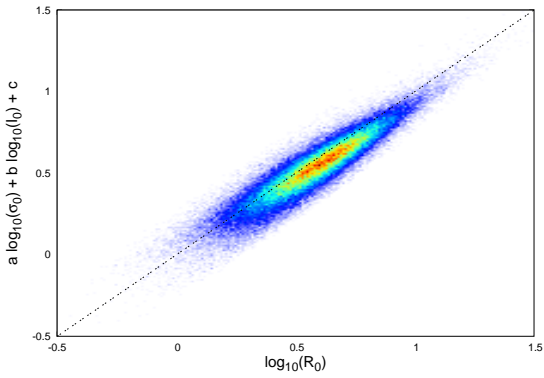
Figure B.48. Projection of the fundamental plane for the z band of the c model.
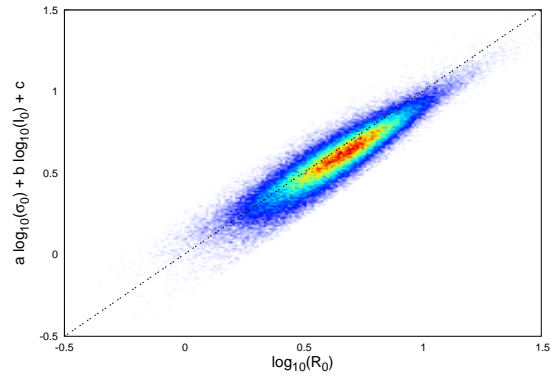
Figure B.51. Projection of the fundamental plane for the r band of the dV model.

28
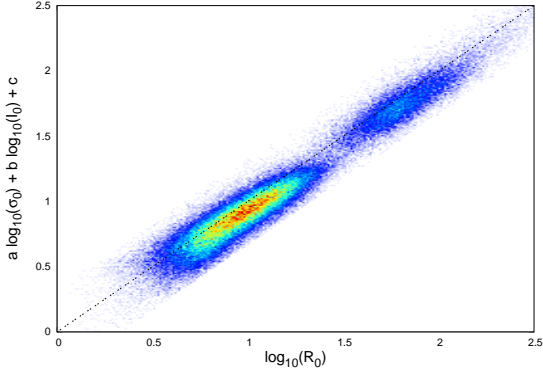
Figure B.52. Projection of the fundamental plane for the u band of the p model.

Figure B.53. Projection of the fundamental plane for the g band of the p model.

Figure B.54. Projection of the fundamental plane for the r band of the p model.
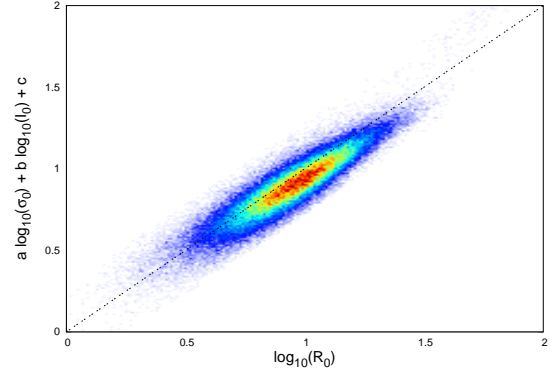
Figure B.55. Projection of the fundamental plane for the i band of the p model.
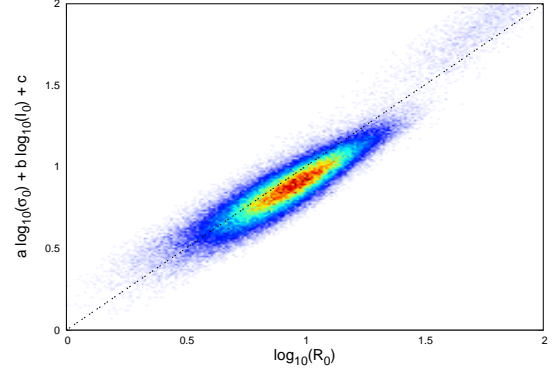
Figure B.56. Projection of the fundamental plane for the z band of the p model.
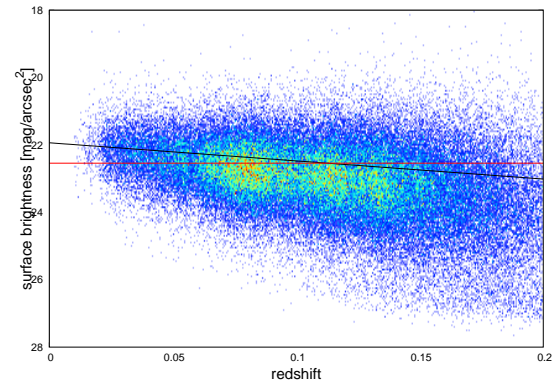
Figure B.57. Redshift evolution of the surface brightness in the u band of dV model indicated by the solid black line. The solid red line shows the Malmquist-bias-corrected average value of the surface brightness for this particular filter and model.

29
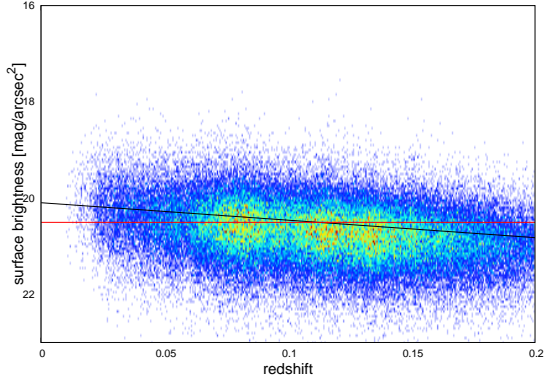
Figure B.58. Redshift evolution of the surface brightness in the g band of dV model indicated by the solid black line. The solid red line shows the Malmquist-bias-corrected average value of the surface brightness for this particular filter and model.
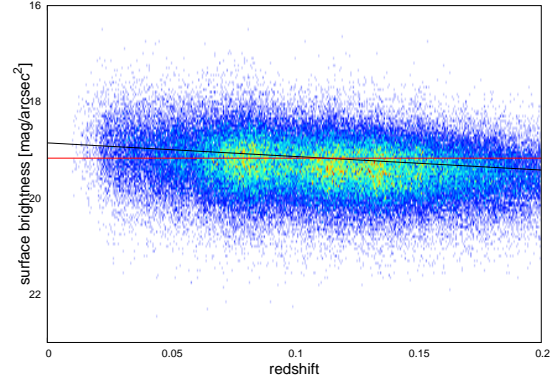
Figure B.60. Redshift evolution of the surface brightness in the i band of dV model indicated by the solid black line. The solid red line shows the Malmquist-bias-corrected average value of the surface brightness for this particular filter and model.
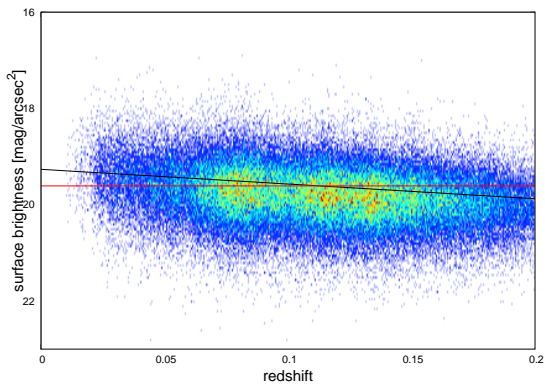
Figure B.59. Redshift evolution of the surface brightness in the r band of dV model indicated by the solid black line. The solid red line shows the Malmquist-bias-corrected average value of the surface brightness for this particular filter and model.
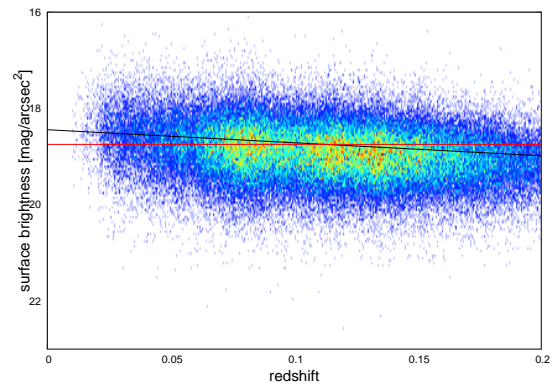
Figure B.61. Redshift evolution of the surface brightness in the z band of dV model indicated by the solid black line. The solid red line shows the Malmquist-bias-corrected average value of the surface brightness for this particular filter and model.

30
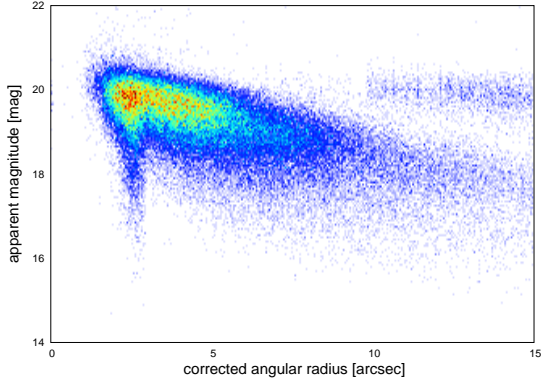
Figure B.62. Corrected angular radii plotted against the apparent magnitudes, showing some grouping in the u band for the p model.

Figure B.63. Corrected angular radii plotted against the apparent magnitudes, not showing any peculiar features in the r band for the p model.

Figure B.64. Corrected angular radii plotted against the apparent magnitudes, showing some small grouping in the z band for the p model.

Figure B.65. Logarithm of the physical radii against the redshift, clearly showing band-like structures in the u band for the p model.
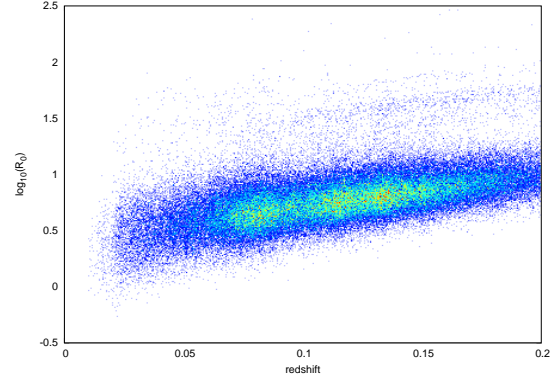
Figure B.66. Logarithm of the physical radii against the redshift, showing band-like structures in the z band for the p model.
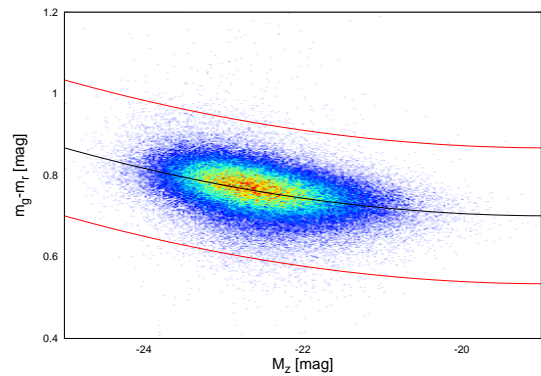
Figure B.67. Colour-magnitude diagram of the red sequence for the c model. The solid black line represents our best fit and the two solid red lines indicate the 3-σ confidence limits beyond which we clipped the sample.

31
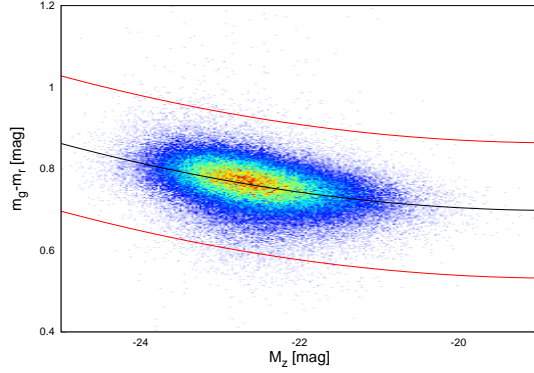
Figure B.68. Colour-magnitude diagram of the red sequence for the dV model. The solid black line represents our best fit and the two solid red lines indicate the 3-σ confidence limits beyond which we clipped the sample.
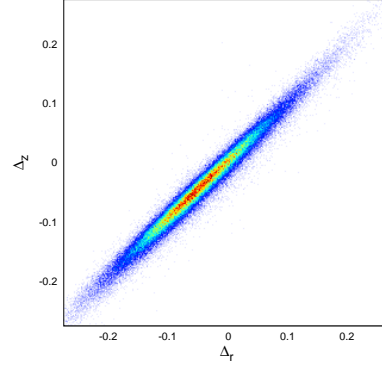
Figure B.70. Tight correlation between the residuals of the fundamental plane in the r band Δ_r and of those in the z band Δ_z. This plot uses the fundamental-plane fit for the dV model.
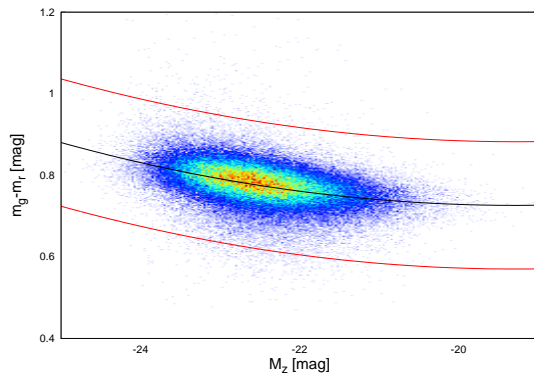
Figure B.69. Colour-magnitude diagram of the red sequence for the p model. The solid black line represents our best fit and the two solid red lines indicate the 3-σ confidence limits beyond which we clipped the sample.
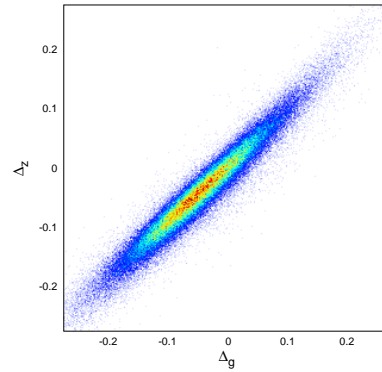
Figure B.71. Strong correlation between the residuals of the fundamental plane in the g band Δ_g and of those in the z band Δ_z, however the correlation is visible weaker than for previous plots, due to the larger difference in the wavelength between the two filters. This plot uses the fundamental-plane fit for the dV model.

32
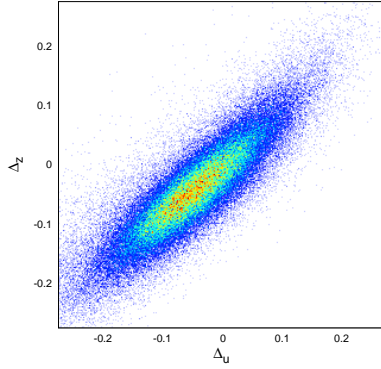
Figure B.72. Correlation between the residuals of the fundamental plane in the u band Δ_u and of those in the z band Δ_z. Due to the larger scatter in the u band, the correlation is significantly weaker than for all other filters. This plot uses the fundamental-plane fit for the dV model.
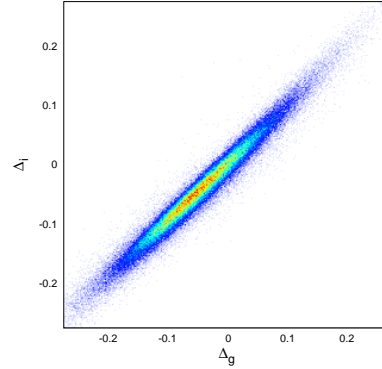
Figure B.74. Strong correlation between the residuals of the fundamental plane in the g band Δ_g and of those in the i band Δ_i. This plot uses the fundamental-plane fit for the dV model.
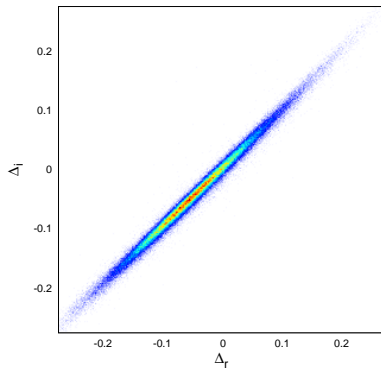
Figure B.73. Tight correlation between the residuals of the fundamental plane in the r band Δ_r and of those in the z band Δ_i. This plot uses the fundamental-plane fit for the dV model.
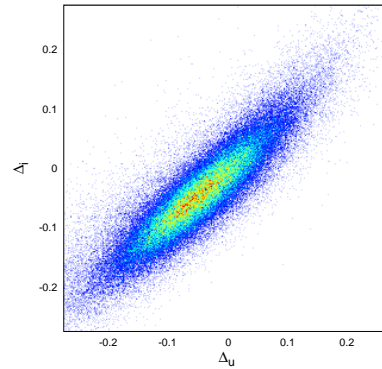
Figure B.75. Correlation between the residuals of the fundamental plane in the u band Δ_u and of those in the i band Δ_i. Due to the larger scatter in the u band, the correlation is significantly weaker than for all other filters. This plot uses the fundamental-plane fit for the dV model.

33
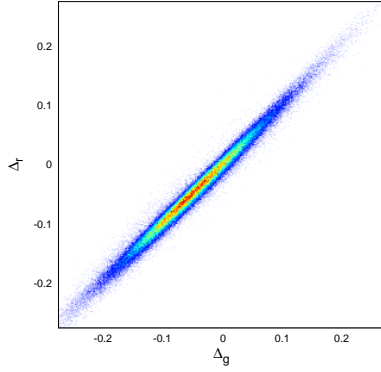
Figure B.76. Strong correlation between the residuals of the fundamental plane in the g band Δ_g and of those in the r band Δ_r. This plot uses the fundamental-plane fit for the dV model.
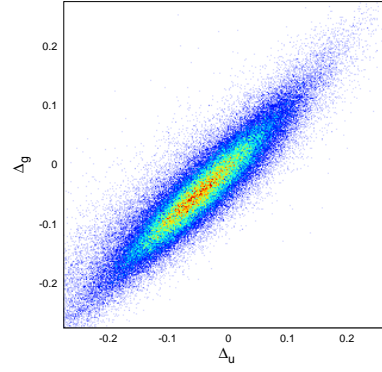
Figure B.78. Correlation between the residuals of the fundamental plane in the u band Δ_u and of those in the g band Δ_g. Due to the larger scatter in the u band, the correlation is significantly weaker than for all other filters. This plot uses the fundamental-plane fit for the dV model.

Appendix C: Additional Tables

	$(u-r)^0$	$(u-r)^1$	$(u-r)^2$	$(u-r)^3$
z^0	0	0	0	0
z^1	10.3686	-6.12658	2.58748	-0.299322
z^2	-138.069	45.0511	-10.8074	0.95854
z^3	540.494	-43.7644	3.84259	0
z^4	-1005.28	10.9763	0	0
z^5	710.482	0	0	0

Table C.1. Coefficients for the K-correction in the u band using u-r colours.

	$(g-r)^0$	$(g-r)^1$	$(g-r)^2$	$(g-r)^3$
z^0	0	0	0	0
z^1	-2.45204	4.10188	10.5258	-13.5889
z^2	56.7969	-140.913	144.572	57.2155
z^3	-466.949	222.789	-917.46	-78.0591
z^4	2906.77	1500.8	1689.97	30.889
z^5	-10453.7	-4419.56	-1011.01	0
z^6	17568	3236.68	0	0
z^7	-10820.7	0	0	0

Table C.2. Coefficients for the K-correction in the g band using g-r colours.

Figure B.77. Correlation between the residuals of the fundamental plane in the u band Δ_u and of those in the r band Δ_r. Due to the larger scatter in the u band, the correlation is significantly weaker than for all other filters. This plot uses the fundamental-plane fit for the dV model.

	$(g-r)^0$	$(g-r)^1$	$(g-r)^2$	$(g-r)^3$
z^0	0	0	0	0
z^1	1.83285	-2.71446	4.97336	-3.66864
z^2	-19.7595	10.5033	18.8196	6.07785
z^3	33.6059	-120.713	-49.299	0
z^4	144.371	216.453	0	0
z^5	-295.39	0	0	0

Table C.3. Coefficients for the K-correction in the r band using g-r colours.

34

models	c_2	c_1	c_0	rms
c Model	0.0045	0.1681	2.2878	0.0555
dV Model	0.0042	0.1555	2.1523	0.0553
p Model	0.0047	0.1816	2.4768	0.0520

Table C.6. Coefficients and the root mean square of the best fit for the red sequence using our sample. The polynomial for these coefficients is of the shape $(m_g - m_r) = c_2 \cdot M_z^2 + c_1 \cdot M_z + c_0$.

	$(g\text{-}i)^0$	$(g\text{-}i)^1$	$(g\text{-}i)^2$	$(g\text{-}i)^3$
z^0	0	0	0	0
z^1	-2.21853	3.94007	0.678402	-1.24751
z^2	-15.7929	-19.3587	15.0137	2.27779
z^3	118.791	-40.0709	-30.6727	0
z^4	-134.571	125.799	0	0
z^5	-55.4483	0	0	0

Table C.4. Coefficients for the K-correction in the i band using g-i colours.

	$(g\text{-}z)^0$	$(g\text{-}z)^1$	$(g\text{-}z)^2$	$(g\text{-}z)^3$
z^0	0	0	0	0
z^1	0.30146	-0.623614	1.40008	-0.534053
z^2	-10.9584	-4.515	2.17456	0.913877
z^3	66.0541	4.18323	-8.42098	0
z^4	-169.494	14.5628	0	0
z^5	144.021	0	0	0

Table C.5. Coefficients for the K-correction in the z band using g-z colours.

filters	s_ε	$\bar{\sigma}_{\text{dist}}$ [%]
Bernardi et al. (2003c)		
g	0.1056	16.8
r	0.1054	17.9
i	0.1028	16.8
z	0.1134	16.0
Hyde & Bernardi (2009)		
g	0.1063	18.8
r	0.1042	17.5
i	0.1031	17.4
z	0.1087	18.6

Table C.7. Quality of the fundamental plane as a distance indicator using our selected sample of 94922 elliptical galaxies, but with the direct-fit coefficients of Bernardi et al. (2003c) or Hyde & Bernardi (2009), respectively (the coefficients are listed in Table 1 of this paper). We found that our best-fit coefficients (see Table 5) are better by a few percent than those of our esteemed colleagues.

SDSS-filter	u	g	r	i	z
$\bar{r}_{cor}$ (c model) [arcsec]	2.95	2.29	2.13	2.04	1.89
$\bar{r}_{cor}$ (dV model) [arcsec]	2.93	2.28	2.13	2.03	1.88
$\bar{r}_{cor}$ (p model) [arcsec]	9.35	4.67	4.44	4.37	4.54
$\sigma_{r_{cor}}$ (c model) [arcsec]	2.13	1.26	1.16	1.12	1.02
$\sigma_{r_{cor}}$ (dV model) [arcsec]	2.12	1.25	1.16	1.12	1.01
$\sigma_{r_{cor}}$ (p model) [arcsec]	15.26	2.33	2.11	2.25	3.69
$\bar{m}_{app}$ (c model) [mag]	19.02	17.33	16.58	16.24	15.98
$\bar{m}_{app}$ (dV model) [mag]	19.01	17.32	16.58	16.24	15.97
$\bar{m}_{app}$ (p model) [mag]	19.14	17.40	16.64	16.28	16.01
$\sigma_{m_{app}}$ (c model) [mag]	0.92	0.87	0.87	0.87	0.87
$\sigma_{m_{app}}$ (dV model) [mag]	0.92	0.88	0.87	0.87	0.87
$\sigma_{m_{app}}$ (p model) [mag]	0.90	0.87	0.86	0.87	0.86
$\bar{\sigma}_0$ (c model) [km/s]	180.1	177.7	176.8	176.8	177.0
$\bar{\sigma}_0$ (dV model) [km/s]	180.4	177.9	176.9	176.9	177.1
$\bar{\sigma}_0$ (p model) [km/s]	173.5	171.9	170.9	170.6	170.1
σ_{σ_0} (c model) [km/s]	46.0	45.3	45.1	45.1	45.4
σ_{σ_0} (dV model) [km/s]	46.0	45.4	45.1	45.1	45.4
σ_{σ_0} (p model) [km/s]	44.4	43.9	43.7	43.6	43.7
$\overline{\log_{10}(R_0)}$ (c model) [$\log_{10}$(kpc)]	0.564	0.483	0.449	0.431	0.394
$\overline{\log_{10}(R_0)}$ (dV model) [$\log_{10}$(kpc)]	0.562	0.482	0.448	0.430	0.394
$\overline{\log_{10}(R_0)}$ (p model) [$\log_{10}$(kpc)]	0.950	0.801	0.777	0.770	0.765
$\sigma_{\log_{10}(R_0)}$ (c model) [$\log_{10}$(kpc)]	0.305	0.235	0.231	0.228	0.228
$\sigma_{\log_{10}(R_0)}$ (dV model) [$\log_{10}$(kpc)]	0.304	0.235	0.231	0.228	0.228
$\sigma_{\log_{10}(R_0)}$ (p model) [$\log_{10}$(kpc)]	0.399	0.229	0.225	0.226	0.250
$\bar{\mu}_0$ (c model) [mag/arcsec^2]	22.57	20.52	19.62	19.18	18.75
$\bar{\mu}_0$ (dV model) [mag/arcsec^2]	22.54	20.50	19.61	19.17	18.75
$\bar{\mu}_0$ (p model) [mag/arcsec^2]	24.60	22.19	21.32	20.93	20.65
σ_{μ_0} (c model) [mag/arcsec^2]	0.99	0.65	0.62	0.61	0.62
σ_{μ_0} (dV model) [mag/arcsec^2]	0.98	0.64	0.62	0.61	0.61
σ_{μ_0} (p model) [mag/arcsec^2]	1.72	0.64	0.62	0.64	0.83
$\overline{\log_{10}(\sigma_0)}$ (c model) [$\log_{10}$(km/s)]	2.24	2.24	2.23	2.23	2.23
$\overline{\log_{10}(\sigma_0)}$ (dV model) [$\log_{10}$(km/s)]	2.24	2.24	2.23	2.23	2.23
$\overline{\log_{10}(\sigma_0)}$ (p model) [$\log_{10}$(km/s)]	2.23	2.22	2.22	2.22	2.22
$\sigma_{\log_{10}(\sigma_0)}$ (c model) [$\log_{10}$(km/s)]	0.11	0.11	0.11	0.11	0.11
$\sigma_{\log_{10}(\sigma_0)}$ (dV model) [$\log_{10}$(km/s)]	0.11	0.11	0.11	0.11	0.11
$\sigma_{\log_{10}(\sigma_0)}$ (p model) [$\log_{10}$(km/s)]	0.11	0.11	0.11	0.11	0.11

Table C.8. Mean values and standard deviations of several different parameters that have to be calculated or measured for the calibration of the fundamental plane. These values are given for all models and all filters. $\bar{r}_{cor}$ stands for the mean value of the apparent corrected radius r_{cor}, and $\sigma_{r_{cor}}$ is the corresponding standard deviation. $\bar{m}_{app}$ denotes the mean value of the apparent magnitude m_{app}, and $\sigma_{m_{app}}$ its standard deviation. The mean value of the central velocity dispersion σ_0 is given by $\bar{\sigma}_0$ and the corresponding standard deviation by σ_{σ_0}. $\overline{\log_{10}(R_0)}$ denotes the mean value of logarithm of the physical radius R_0, and $\sigma_{\log_{10}(R_0)}$ the corresponding standard deviation. $\bar{\mu}_0$ is the mean value of the mean surface brightness μ_0, and σ_{μ_0} is its standard deviation. The mean value of the logarithm of the central velocity dispersion σ_0 is given by $\overline{\log_{10}(\sigma_0)}$ and the corresponding standard deviation by $\sigma_{\log_{10}(\sigma_0)}$.

models and filters	a	b	c	s_ε	$\bar{\sigma}_{\text{dist}}$ [%]
c model					
u	0.806 ± 0.029	-0.683 ± 0.008	-7.41 ± 0.10	0.1026	17.2
g	0.972 ± 0.030	-0.722 ± 0.012	-7.62 ± 0.12	0.1011	16.2
r	1.038 ± 0.030	-0.738 ± 0.013	-7.66 ± 0.12	0.1010	15.8
i	1.065 ± 0.030	-0.744 ± 0.013	-7.66 ± 0.13	0.9979	15.5
z	1.113 ± 0.030	-0.753 ± 0.013	-7.74 ± 0.13	0.1026	15.3
dV model					
u	0.823 ± 0.029	-0.669 ± 0.008	-7.31 ± 0.10	0.1079	17.3
g	0.964 ± 0.030	-0.727 ± 0.012	-7.63 ± 0.12	0.1012	16.2
r	1.031 ± 0.030	-0.742 ± 0.013	-7.67 ± 0.13	0.1011	15.8
i	1.059 ± 0.030	-0.747 ± 0.013	-7.66 ± 0.13	0.0998	15.5
z	1.107 ± 0.030	-0.757 ± 0.013	-7.76 ± 0.13	0.1079	15.3
p model					
u	0.623 ± 0.029	-0.494 ± 0.005	-5.32 ± 0.08	0.1729	23.1
g	0.992 ± 0.030	-0.676 ± 0.012	-7.41 ± 0.13	0.1054	17.0
r	1.058 ± 0.030	-0.713 ± 0.013	-7.66 ± 0.13	0.1029	16.5
i	1.081 ± 0.030	-0.670 ± 0.012	-7.24 ± 0.13	0.1048	16.5
z	1.106 ± 0.030	-0.621 ± 0.009	-6.817 ± 0.110	0.1729	17.1

Table C.9. Best fits for the fundamental-plane coefficients in all filters and for all models with the 3-σ clipping disabled.

models and filters	a	b	c	s_ε	$\bar{\sigma}_{\text{dist}}$ [%]
c model					
u	0.720 ± 0.031	-0.681 ± 0.007	-7.14 ± 0.10	0.0859	19.7
g	0.890 ± 0.032	-0.701 ± 0.013	-7.20 ± 0.13	0.0800	18.4
r	0.955 ± 0.032	-0.724 ± 0.014	-7.31 ± 0.13	0.0787	18.0
i	0.977 ± 0.032	-0.735 ± 0.014	-7.34 ± 0.13	0.0768	17.6
z	1.003 ± 0.032	-0.738 ± 0.014	-7.33 ± 0.13	0.0859	17.4
dV model					
u	0.708 ± 0.031	-0.684 ± 0.007	-7.13 ± 0.10	0.0860	19.8
g	0.882 ± 0.032	-0.707 ± 0.013	-7.23 ± 0.13	0.0802	18.4
r	0.948 ± 0.032	-0.729 ± 0.014	-7.33 ± 0.13	0.0787	18.0
i	0.973 ± 0.032	-0.739 ± 0.014	-7.36 ± 0.13	0.0768	17.6
z	0.999 ± 0.032	-0.743 ± 0.014	-7.36 ± 0.14	0.0860	17.4
p model					
u	0.796 ± 0.031	-0.538 ± 0.004	-6.04 ± 0.09	0.0996	22.4
g	0.903 ± 0.031	-0.659 ± 0.013	-6.99 ± 0.14	0.0842	19.2
r	0.973 ± 0.031	-0.690 ± 0.014	-7.21 ± 0.15	0.0819	18.7
i	0.997 ± 0.032	-0.688 ± 0.014	-7.14 ± 0.14	0.0807	18.5
z	1.018 ± 0.032	-0.611 ± 0.010	-6.48 ± 0.12	0.0996	18.9

Table C.10. Best fits for the fundamental-plane coefficients in all filters and for all models with the volume weights disabled. Consequently, these results suffer from a Malmquist bias.

models and filters	a	b	c	s_ε	$\bar{\sigma}_{\text{dist}}$ [%]
c model					
u	0.865 ± 0.030	-0.699 ± 0.008	-7.66 ± 0.10	0.0998	17.0
g	1.036 ± 0.030	-0.738 ± 0.013	-7.87 ± 0.13	0.0995	16.2
r	1.103 ± 0.030	-0.751 ± 0.013	-7.89 ± 0.13	0.0997	16.1
i	1.131 ± 0.030	-0.757 ± 0.014	-7.87 ± 0.13	0.0982	15.7
z	1.176 ± 0.030	-0.763 ± 0.014	-7.93 ± 0.13	0.0998	15.6
dV model					
u	0.852 ± 0.030	-0.704 ± 0.009	-7.68 ± 0.10	0.0990	16.9
g	1.028 ± 0.030	-0.743 ± 0.013	-7.89 ± 0.13	0.0995	16.2
r	1.096 ± 0.030	-0.755 ± 0.013	-7.90 ± 0.13	0.0997	16.0
i	1.125 ± 0.030	-0.759 ± 0.014	-7.88 ± 0.13	0.0981	15.7
z	1.171 ± 0.030	-0.766 ± 0.014	-7.94 ± 0.13	0.0990	15.5
p model					
u	0.893 ± 0.030	-0.552 ± 0.005	-6.45 ± 0.08	0.1149	20.1
g	1.042 ± 0.030	-0.705 ± 0.013	-7.74 ± 0.14	0.1028	17.2
r	1.112 ± 0.030	-0.725 ± 0.014	-7.85 ± 0.14	0.1015	16.8
i	1.137 ± 0.030	-0.718 ± 0.013	-7.74 ± 0.14	0.1004	16.6
z	1.157 ± 0.030	-0.642 ± 0.010	-7.09 ± 0.12	0.1149	17.5

Table C.11. Best fits for the fundamental-plane coefficients in all filters and for all models with the correction for redshift evolution completely disabled.

models and filters	a	b	c	s_ε	$\bar{\sigma}_{\text{dist}}$ [%]
c model					
u	0.643 ± 0.030	-0.671 ± 0.008	-7.01 ± 0.09	0.0850	16.4
g	0.880 ± 0.030	-0.720 ± 0.012	-7.43 ± 0.12	0.08592	15.2
r	0.974 ± 0.030	-0.742 ± 0.013	-7.58 ± 0.12	0.0875	14.8
i	1.012 ± 0.030	-0.749 ± 0.013	-7.60 ± 0.13	0.0872	14.6
z	1.061 ± 0.030	-0.755 ± 0.013	-7.66 ± 0.13	0.0850	14.5
dV model					
u	0.626 ± 0.030	-0.672 ± 0.008	-6.98 ± 0.09	0.0840	16.4
g	0.869 ± 0.030	-0.725 ± 0.012	-7.45 ± 0.12	0.0853	15.1
r	0.965 ± 0.030	-0.747 ± 0.013	-7.59 ± 0.12	0.0868	14.8
i	1.005 ± 0.030	-0.752 ± 0.013	-7.61 ± 0.13	0.0865	14.5
z	1.056 ± 0.030	-0.759 ± 0.013	-7.68 ± 0.13	0.0840	14.4
p model					
u	0.641 ± 0.030	$-0.536 \, pm 0.004$	-5.84 ± 0.08	0.0938	17.7
g	0.840 ± 0.030	-0.661 ± 0.012	-6.99 ± 0.12	0.0867	15.9
r	0.928 ± 0.030	-0.689 ± 0.013	-7.21 ± 0.13	0.0867	15.4
i	0.955 ± 0.030	-0.683 ± 0.012	-7.12 ± 0.13	0.0861	15.4
z	0.966 ± 0.030	-0.615 ± 0.009	-6.507 ± 0.11	0.0938	15.7

Table C.12. Best fits for the fundamental-plane coefficients in all filters and for all models with volume weights and 3-σ clipping and a filter-dependend redshift evolution derived from the redshift evolution of the surface brightness (see Table C.13).

models and filters	Q_u[mag/arcsec^2]	Q_g [mag/arcsec^2]	Q_r [mag/arcsec^2]	Q_i [mag/arcsec^2]	Q_z [mag/arcsec^2]
c model	4.26	2.69	2.18	1.96	1.87
dV model	4.40	2.72	2.20	1.97	1.88
p model	6.03	3.78	3.29	3.24	3.73

Table C.13. Redshift evolution derived from changes in the surface brightness using non-evolution-corrected magnitudes.

38

models and filters	a	b	c	s_ε	$\bar{\sigma}_{\mathrm{dist}}$ [%]
c model					
u	0.847 ± 0.106	-0.688 ± 0.040	-7.53 ± 0.45	0.0989	19.9
g	0.994 ± 0.107	-0.723 ± 0.046	-7.67 ± 0.46	0.0942	19.0
r	1.058 ± 0.107	-0.742 ± 0.047	-7.74 ± 0.47	0.0914	18.4
i	1.102 ± 0.107	-0.758 ± 0.048	-7.85 ± 0.47	0.0895	18.0
z	1.126 ± 0.108	-0.762 ± 0.048	-7.84 ± 0.47	0.0989	17.5
dV model					
u	0.832 ± 0.106	-0.705 ± 0.041	-7.64 ± 0.46	0.0988	19.9
g	0.987 ± 0.107	-0.731 ± 0.047	-7.72 ± 0.47	0.0939	18.9
r	1.052 ± 0.107	-0.747 ± 0.048	-7.76 ± 0.47	0.0911	18.3
i	1.097 ± 0.107	-0.763 ± 0.048	-7.87 ± 0.47	0.0892	17.9
z	1.122 ± 0.108	-0.768 ± 0.049	-7.87 ± 0.47	0.0988	17.4
p model					
u	0.833 ± 0.106	-0.553 ± 0.020	-6.34 ± 0.32	0.1081	22.0
g	0.988 ± 0.106	-0.656 ± 0.043	-7.21 ± 0.47	0.0989	20.1
r	1.059 ± 0.107	-0.681 ± 0.045	-7.37 ± 0.49	0.0956	19.4
i	1.093 ± 0.107	-0.688 ± 0.044	-7.40 ± 0.47	0.0941	19.1
z	1.111 ± 0.109	-0.640 ± 0.040	-6.99 ± 0.45	0.1081	19.3

Table C.14. Fundamental-plane coefficients in all filters and for all models derived from the volume-limited subsample, which is to 95,45% (2-σ) completed. This condition limits the sample to a redshift of 0.0513. Owing to its completeness, the Malmquist-bias correction was disabled.

models and filters	a	b	c	s_ε	$\bar{\sigma}_{\mathrm{dist}}$ [%]
c model					
u	0.820 ± 0.029	-0.697 ± 0.008	-7.56 ± 0.10	0.0952	16.6
g	0.987 ± 0.029	-0.738 ± 0.013	-7.78 ± 0.12	0.0937	15.6
r	1.054 ± 0.029	-0.752 ± 0.013	-7.81 ± 0.12	0.0936	15.3
i	1.080 ± 0.029	-0.757 ± 0.013	-7.79 ± 0.12	0.0922	15.0
z	1.124 ± 0.029	-0.762 ± 0.013	-7.84 ± 0.13	0.0952	14.8
dV model					
u	0.809 ± 0.029	-0.701 ± 0.008	-7.57 ± 0.10	0.0946	16.6
g	0.979 ± 0.029	-0.742 ± 0.012	-7.79 ± 0.12	0.0937	15.6
r	1.047 ± 0.029	-0.755 ± 0.013	-7.81 ± 0.12	0.0936	15.3
i	1.075 ± 0.029	-0.759 ± 0.013	-7.79 ± 0.12	0.0922	15.0
z	1.120 ± 0.029	-0.766 ± 0.013	-7.85 ± 0.13	0.0946	14.8
p model					
u	0.871 ± 0.029	-0.551 ± 0.004	-6.41 ± 0.08	0.11099	19.7
g	1.001 ± 0.029	-0.700 ± 0.012	-7.63 ± 0.13	0.0977	16.6
r	1.070 ± 0.029	-0.720 ± 0.013	-7.74 ± 0.13	0.0962	16.1
i	1.095 ± 0.029	-0.713 ± 0.013	-7.63 ± 0.13	0.0952	16.0
z	1.121 ± 0.029	-0.639 ± 0.010	-6.99 ± 0.11	0.1110	16.7

Table C.15. Fundamental-plane coefficients in all filters and for all models derived from an extended sample up to a redshift of 0.3. However, it already suffers from an additional bias beyond the Malmquist bias at these distances.

39

References

Ahn, C. P., Alexandroff, R., Allende Prieto, C., et al. 2012, *ApJS*, 203, 21

Aihara, H., Allende Prieto, C., An, D., et al. 2011, *ApJS*, 193, 29

Bernardi, M., Sheth, R. K., Annis, J., et al. 2003a, *AJ*, 125, 1817

Bernardi, M., Sheth, R. K., Annis, J., et al. 2003b, *AJ*, 125, 1849

Bernardi, M., Sheth, R. K., Annis, J., et al. 2003c, *AJ*, 125, 1866

Bernardi, M., Sheth, R. K., Annis, J., et al. 2003d, *AJ*, 125, 1882

Burkert, A., Naab, T., Johansson, P. H., & Jesseit, R. 2008, *ApJ*, 685, 897

Busarello, G., Capaccioli, M., Capozziello, S., Longo, G., & Puddu, E. 1997, *A&A*, 320, 415

Busarello, G., Lanzoni, B., Capaccioli, M., et al. 1998, *Mem. Soc. Astron. Italiana*, 69, 217

Butkevich, A. G., Berdyugin, A. V., & Teerikorpi, P. 2005, *MNRAS*, 362, 321

Cappellari, M., Bacon, R., Bureau, M., et al. 2006, *MNRAS*, 366, 1126

Chilingarian, I. V., Melchior, A., & Zolotukhin, I. Y. 2010, *MNRAS*, 405, 1409

Chilingarian, I. V. & Zolotukhin, I. Y. 2012, *MNRAS*, 419, 1727

Ciotti, L., Lanzoni, B., & Renzini, A. 1996, *MNRAS*, 282, 1

Colless, M., Saglia, R. P., Burstein, D., et al. 2001, *MNRAS*, 321, 277

de Carvalho, R. R. & Djorgovski, S. 1992, *ApJ*, 389, L49

Djorgovski, S. & Davis, M. 1987, *ApJ*, 313, 59

D'Onofrio, M., Fasano, G., Varela, J., et al. 2008, *ApJ*, 685, 875

D'Onofrio, M., Valentinuzzi, T., Secco, L., Caimmi, R., & Bindoni, D. 2006, New A Rev., 50, 447

Dressler, A., Lynden-Bell, D., Burstein, D., et al. 1987, *ApJ*, 313, 42

Faber, S. M. & Jackson, R. E. 1976, *ApJ*, 204, 668

Fathi, K., Allen, M., Boch, T., Hatziminaoglou, E., & Peletier, R. F. 2010, *MNRAS*, 406, 1595

Forbes, D. A., Ponman, T. J., & Brown, R. J. N. 1998, *ApJ*, 508, L43

Fraix-Burnet, D., Dugué, M., Chattopadhyay, T., Chattopadhyay, A. K., & Davoust, E. 2010, *MNRAS*, 407, 2207

Gargiulo, A., Haines, C. P., Merluzzi, P., et al. 2009, *MNRAS*, 397, 75

Geller, M. J. & Huchra, J. P. 1989, Science, 246, 897

Gibbons, R. A., Fruchter, A. S., & Bothun, G. D. 2001, *AJ*, 121, 649

Gott, III, J. R., Jurić, M., Schlegel, D., et al. 2005, *ApJ*, 624, 463

Graham, A. & Colless, M. 1997, *MNRAS*, 287, 221

Guzman, R., Lucey, J. R., & Bower, R. G. 1993, *MNRAS*, 265, 731

Hinshaw, G., Weiland, J. L., Hill, R. S., et al. 2009, *ApJS*, 180, 225

Hopkins, P. F., Cox, T. J., & Hernquist, L. 2008, *ApJ*, 689, 17

Hubble, E. & Tolman, R. C. 1935, *ApJ*, 82, 302

Hudson, M. J., Lucey, J. R., Smith, R. J., & Steel, J. 1997, *MNRAS*, 291, 488

Hyde, J. B. & Bernardi, M. 2009, *MNRAS*, 396, 1171

Jorgensen, I., Franx, M., & Kjaergaard, P. 1995, *MNRAS*, 276, 1341

Jorgensen, I., Franx, M., & Kjaergaard, P. 1996, *MNRAS*, 280, 167

Kelson, D. D., Illingworth, G. D., van Dokkum, P. G., & Franx, M. 2000, *ApJ*, 531, 184

Kormendy, J. 1977, *ApJ*, 218, 333

La Barbera, F., Busarello, G., Merluzzi, P., et al. 2008, *ApJ*, 689, 913

La Barbera, F., de Carvalho, R. R., de La Rosa, I. G., & Lopes, P. A. A. 2010a, *MNRAS*, 408, 1335

La Barbera, F., Lopes, P. A. A., de Carvalho, R. R., de La Rosa, I. G., & Berlind, A. A. 2010b, *MNRAS*, 408, 1361

Lintott, C., Schawinski, K., Bamford, S., et al. 2011, *MNRAS*, 410, 166

Lintott, C. J., Schawinski, K., Slosar, A., et al. 2008, *MNRAS*, 389, 1179

Lucey, J. R., Bower, R. G., & Ellis, R. S. 1991, *MNRAS*, 249, 755

Magoulas, C., Springob, C. M., Colless, M., et al. 2012, *MNRAS*, 427, 245

Masters, K. L., Springob, C. M., Haynes, M. P., & Giovanelli, R. 2006, *ApJ*, 653, 861

Müller, K. R., Freudling, W., Watkins, R., & Wegner, G. 1998, *ApJ*, 507, L105

Oñorbe, J., Domínguez-Tenreiro, R., Sáiz, A., Serna, A., & Artal, H. 2005, *ApJ*, 632, L57

Pahre, M. A., Djorgovski, S. G., & de Carvalho, R. R. 1996, *ApJ*, 456, L79

Pahre, M. A., Djorgovski, S. G., & de Carvalho, R. R. 1998, *AJ*, 116, 1591

Prugniel, P. & Simien, F. 1996, *A&A*, 309, 749

Sandage, A. & Perelmuter, J.-M. 1990a, *ApJ*, 350, 481

Sandage, A. & Perelmuter, J.-M. 1990b, *ApJ*, 361, 1

Sandage, A. & Perelmuter, J.-M. 1991, *ApJ*, 370, 455

Saulder, C., Mieske, S., & Zeilinger, W. W. 2012, ArXiv e-prints

Schlegel, D. J., Finkbeiner, D. P., & Davis, M. 1998, *ApJ*, 500, 525

Scodeggio, M., Gavazzi, G., Belsole, E., Pierini, D., & Boselli, A. 1998, *MNRAS*, 301, 1001

Sheth, R. K. & Bernardi, M. 2012, *MNRAS*, 422, 1825

Smith, R. J., Lucey, J. R., Schlegel, D. J., et al. 2001, *MNRAS*, 327, 249

Stoughton, C., Lupton, R. H., Bernardi, M., et al. 2002, *AJ*, 123, 485

Strauss, M. A., Weinberg, D. H., Lupton, R. H., et al. 2002, *AJ*, 124, 1810

Tempel, E., Tago, E., & Liivamägi, L. J. 2012, *A&A*, 540, A106

Terlevich, R., Davies, R. L., Faber, S. M., & Burstein, D. 1981, *MNRAS*, 196, 381

Tolman, R. C. 1930, Proceedings of the National Academy of Science, 16, 511

Trujillo, I., Burkert, A., & Bell, E. F. 2004, *ApJ*, 600, L39

Wegner, G., Colless, M., Saglia, R. P., et al. 1999, *MNRAS*, 305, 259

40

Chapter 5

Dozens of compact and high velocity-dispersion, early-type galaxies in Sloan Digital Sky Survey

The content of this paper is complementary to the main goal of my thesis. We identify a certain group of extreme early-type galaxies that deviate from the fundamental plane, for further follow up study. The results and analysis performed in this paper help to further improve my calibration of the fundamental plane and provide again the largest sample ever used to calibrate this relation. The new coefficients are presented in Appendix A of this paper and will be used in the subsequent work. Furthermore, this paper illustrates that the huge amount of data calibrated and analysed in the process can spawn other interesting scientific investigations aside the main aim of my thesis.

The paper "Dozens of compact and high velocity-dispersion, early-type galaxies in Sloan Digital Sky Survey" was published in Astronomy & Astrophysics, Volume 578, id.A134, 36 pp [1]. As the first author of this paper, I wrote the majority of the text. The introduction of this paper was co-written with Remco van den Bosch. The basic idea of searching for extreme galaxies in the data of my previous paper was suggested by Remco van den Bosch. I developed it further leading to the results presented in this paper. Steffen Mieske helped me with the initial set-up of this project. I also acknowledge the help of my two collaborators in proof-reading and structuring this paper.

---

[1]More information is available on ADS: `http://adsabs.harvard.edu/abs/2015A%26A...578A.134S`

Dozens of compact and high velocity-dispersion, early-type galaxies in Sloan Digital Sky Survey

Christoph Saulder[1,4], Remco C. E. van den Bosch[2], and Steffen Mieske[3]

[1] European Southern Observatory, Karl-Schwarzschild-Straße 2, 85748 Garching bei München, Germany
e-mail: christoph.saulder@equinoxomega.net

[2] Max-Planck-Institut für Astronomie, Königstuhl 17, 69117 Heidelberg, Germany

[3] European Southern Observatory, Alonso de Córdova 3107, Vitacura, Casilla 19001, Santiago, Chile

[4] Department of Astrophysics, University of Vienna, Türkenschanzstraße 17, 1180 Vienna, Austria

Abstract

Context. Passive galaxies at high redshift are much smaller than equally massive early types today. If this size evolution is caused by stochastic merging processes, then a small fraction of the compact galaxies should persist until today. Up to now it has not been possible to systematically identify the existence of such objects in SDSS.
Aims. We aim at finding potential survivors of these compact galaxies in SDSS, as targets for more detailed follow-up observations.
Methods. From the virial theorem, it is expected that for a given mass, compact galaxies have stellar velocity dispersion higher than the mean owing to their smaller sizes. Therefore velocity dispersion, coupled with size (or mass), is an appropriate method of selecting relics, independent of the stellar population properties. Based on these considerations, we designed a set of criteria the use the distribution of early-type galaxies from SDSS on the $\log_{10}(R_0)$-$\log_{10}(\sigma_0)$ plane to find the most extreme objects on it. We thus selected compact massive galaxy candidates by restricting them to high velocity dispersions $\sigma_0 >$323.2 km s^{-1} and small sizes $R_0 <$2.18 kpc.
Results. We find 76 galaxies at $0.05 < z < 0.2$, which have properties that are similar to the typical quiescent galaxies at high redshift. We discuss how these galaxies relate to average present-day early-type galaxies. We study how well these galaxies fit on well-known local universe relations of early-type galaxies, such as the fundamental plane, the red sequence, or mass-size relations. As expected from the selection criteria, the candidates are located in an extreme corner of the mass-size plane. However, they do not extend as deeply into the so-called zone of exclusion as some of the red nuggets found at high redshift, since they are a factor 2-3 less massive on a given intrinsic scale size. Several of our candidates are close to the size resolution limit of SDSS, but are not so small that they are classified as point sources. We find that our candidates are systematically offset on a scaling relation compared to the average early-type galaxies, but still within the general range of other early-type galaxies. Furthermore, our candidates are similar to the mass-size range expected for passive evolution of the red nuggets from their high redshift to the present.
Conclusions. The 76 selected candidates form an appropriate set of objects for further follow-up observations. They do not constitute a separate population of peculiar galaxies, but form the extreme tail of a continuous distribution of early-type galaxies. We argue that selecting a high-velocity dispersion is the best way to find analogues of compact high redshift galaxies in the local universe.

Key words. galaxies: elliptical and lenticular, cD – surveys – galaxies: fundamental parameters – galaxies: peculiar

1. Introduction

Compact massive early-type galaxies are common at high redshifts ($z > 1$) (Trujillo et al. 2006; van Dokkum et al. 2008). At those epochs, an average 10^{11} M$_\odot$ passive galaxy has a size of 1 kpc, whereas today's early-type galaxies are three to ten times larger (Taylor et al. 2010), indicating that galaxies undergo a significant amount of size evolution (van der Wel et al. 2014a). If a small fraction of those early galaxies, which are also called red nuggets, evolve completely passively, without any mergers, then some of them must have remained compact until today. Those objects would be pristine relics, which would allow direct insight into how these objects formed long ago. It is therefore interesting to find out if any of those systems still remain today.

Several studies have been done to find such objects using the SDSS photometry with varying success. Taylor et al. (2010)

found no analogues of the $z \sim 2$ early-type galaxies. Similarly, Trujillo et al. (2009) found few objects, but those turned out to be young with ages of 2 Gyr. Damjanov et al. (2009) found nine objects – some of which were old – indicating that some of the relics must exist. Damjanov et al. (2014) found several object in the BOSS survey and measured a space density of 10^{-6} galaxies Mpc^{-3}, which is consistent with expectations from semi-analytic models (Quilis & Trujillo 2013). In contrast to this, there are also claims of detecting high number densities of these compact massive early-type galaxies in cluster environments (Valentinuzzi et al. 2010), and even in the field (Poggianti et al. 2013), that are in tension with the upper limits of the model predictions (Damjanov et al. 2014). The results from Valentinuzzi et al. (2010) have been debated, and various inconsistencies with other works are pointed out in Taylor et al. (2010).

1

The virial theorem (and its observational projection, the fundamental plane) predicts that these small galaxies must have high-velocity dispersions. This has been directly confirmed with deep spectroscopy of a handful of these objects (van Dokkum et al. 2009; van de Sande et al. 2013; Toft et al. 2012). This makes the dispersion a very good discriminator for finding these very dense objects in the local universe because measuring dispersion is much easier at low redshift. The other advantage is that such a selection is independent of uncertainties in photometric stellar masses. The stellar velocity dispersion was used in van den Bosch et al. (2012) as a discriminator and found six compact objects – including NGC 1277 – in the HETMGS survey (van den Bosch et al. 2015). These objects appear to be consistent with being relics, given their size, mass, and velocity dispersion (van den Bosch et al. 2012). In particular, NGC 1277 has a high dynamical mass-to-light ratio (Emsellem 2013; Yıldırım et al. submitted). Subsequently, Trujillo et al. (2014) revealed that its photometry is similar to the nuggets and the stellar population has a uniformly old age. The galaxies of van den Bosch et al. (2012) are lenticular, which agrees well with most compact massive high redshift galaxies being disc-dominated (van der Wel et al. 2011; Chevance et al. 2012).

This begs the question of whether relics of such compact high-z nuggets can be found as high-dispersion galaxies in SDSS. The starting point of our investigation is [BHF2008] 19, which is the galaxy with ID number 19 on the list of the highest dispersion galaxies in SDSS by Bernardi et al. (2008). It is a very compact and massive early-type galaxy with a size of R_e=2.17 kpc and mass of 10^{11} M$_\odot$. We refer to this object as b19 in this paper. It was investigated in great detail in Läsker et al. (2013) and it was found that b19 has a high stellar mass-to-ratio of ~ 7 $M_\odot/L_{\odot,i}$ and probably a bottom-heavy initial mass function[1]. The object is located at a redshift $z = 0.1166$ and is considered to be one of the most compact galaxies for its given mass in the local universe.

In this paper, we performed a systematic search in SDSS to find objects similar to b19, so as to have a broader basis for future investigations of compact, high-dispersion, massive early-type galaxies. The other object, NGC 1277, could not be used for this, because it is not in the main SDSS survey[2].

While this paper is primarily a sample selection for follow-up observations, we also touch on the following important questions. Is b19 the most extreme (in the sense of mass and compactness) early-type galaxy in the local universe? Do objects like b19 just form the compact-massive tail of the general distribution of elliptical galaxies, or are they outliers known scaling relations for early-type galaxies? In which aspects do b19-like objects differ from other present-day, early-type galaxies, and are they related to red nuggets from the early universe?

We used selection criteria based on size and central velocity dispersion to find potential red nuggets in the local universe. This is different from what was done by other authors, such as Trujillo et al. (2009) and Taylor et al. (2010), who used selection criteria based on size and stellar mass. It is difficult to measure stellar masses without additional follow-up on the SDSS, and the uncertainties are high with at least 0.1 dex statistical and 0.2 dex systematic error for the stellar masses of Blanton &

Roweis (2007), which were used by Trujillo et al. (2009): about 0.1 dex for the stellar masses used by Taylor et al. (2010), which were based on method of Kauffmann et al. (2003) and Salim et al. (2007), and 0.15 dex for the stellar masses of Mendel et al. (2014), which we used in this paper. To avoid these uncertainties in our sample definition, we selected with more directly measured quantities, such as the physical radii and the central velocity dispersion. The galaxies of van den Bosch et al. (2012) and b19 are usually assumed to be relics of the red nuggets and if this is the case, there might be more galaxies with similar properties, and some of them may have the same origins. Our method is additionally motivated by the fact that at least a subgroup of red nuggets possess high central velocity dispersions (Newman et al. 2010; Bezanson et al. 2013) and that the stellar-to-dynamical mass-to-light ratio decreases slightly over time (van de Sande et al. 2013). We set out to find them and provide a new selection method that is capable of discovering possible remnants of compact massive red galaxies from the early universe that would have been missed in previous investigations that used different selection criteria. Our goal is to define a sample to be used for follow-up observations to determine whether there is a systematic variation in the initial mass function, such as the bottom-heavy initial mass function of b19 (Läsker et al. 2013), and if they host over-massive central black hole such as the one in NGC 1277 (van den Bosch et al. 2012). Furthermore, follow-up observation will also be required to clean the sample from high central velocity dispersion galaxies that are superpositions of two or more galaxies, which is a known issue with this kind of galaxies in SDSS (Bernardi et al. 2008).

In Section 2, we describe the basic sample used for this investigation. After it is calibrated as explained in Section 3, we discuss the selection of our candidates in Section 4 using various cuts, which are defined there. We investigate the global properties of our candidates and their relation to the basic sample in Section 5. We discuss our candidates and their relation to other samples of potential red nugget galaxies in Section 6. In Section 7, we provide a summary and some concluding remarks on our work. We supplement our paper with three appendices that provide updated fundamental-plane coefficients in Appendix A, additional tables of other samples and their cross-matches with our candidates in Appendix C, and an alternative candidate sample using Sersic profiles instead of the de Vaucouleurs profile in Appendix B.

Throughout this paper, we assume a Λ-CDM cosmology with the following parameters: relative dark energy density $\Omega_\Lambda = 0.7$, relative matter density $\Omega_M = 0.3$, and a Hubble parameter $H_0 = 70$ km s^{-1} Mpc^{-1}.

2. Basic sample

As the baseline sample of our search for b19 analogues, we made broad use of the Sloan Digital Sky Surveys (SDSS) and especially of its tenth (Ahn et al. 2014) and seventh (Abazajian et al. 2009) data releases (DR10 and DR7). Furthermore, we used GalaxyZoo (Lintott et al. 2008, 2011) for our galaxy classifications, the refits of SDSS DR7 using Sersic profiles done by Simard et al. (2011), and the stellar masses from Mendel et al. (2014), which is itself based on the previous work of Simard et al. (2011). For comparison, we also used the list of 63 compact massive galaxies from Taylor et al. (2010), which is based on SDSS DR7 as well as a list of 29 compact massive galaxies from Trujillo et al. (2009), which is based on the NYU Value-Added Galaxy Catalog (Blanton et al. 2005) and covers a sub-sample of SDSS.

---

[1] A large black hole could not be ruled out by the observations, but even if this system has a large black hole, then the dynamical and stellar population models still work better with a bottom heavy initial mass function.

[2] NGC 1277 was observed by SDSS as part of a auxiliary Perseus survey.

parameter	condition
SpecObj.z	> 0
SpecObj.z	< 0.5
SpecObj.zWarning	$= 0$
SpecObj.veldisp	> 100
SpecObj.snMedian	> 10
SpecObj.class	$=$'GALAXY'
(*P.flags_r* & 0x40000)	$= 0$

Table 1. Selection criteria given in the language of the SDSS CAS-job queries.

We selected all galaxies from the SDSS database that fulfil the following criteria, which are summarized in Table 1: spectroscopic data has to be available and redshifts have to be reliably obtained (*zWarning*-flag set to zero). We required that the measured redshifts lie between 0 and 0.5. By using spectroscopic data from SDSS, we implicitly introduced the selection criteria of SDSS spectroscopy on our data, which are a minimum apparent magnitude in the r band of 17.77 mag (Strauss et al. 2002) and a saturation limit, which corresponds to a maximum magnitude of either 13 mag in the u band, 14 mag in the g, r, or i band, or 12 mag in the z band. The central velocity dispersion has to be higher than 100 km s^{-1}, the signal-to-noise for spectra has to be better than 10, and the automatic spectral classification has to confirm that the object is a galaxy. To ensure reliable photometric measurements, we required that there are no saturated objects in our sample (*P.flags_r* not set to *SATURATED*). As a direct consequence of these requirements, we required that there must be spectroscopic data for every galaxy in our sample. We imposed the target limit for galaxy spectroscopy of SDSS on our sample, which is a minimum Petrosian magnitude in the r band of 17.77 mag (Strauss et al. 2002) and saturation limit of 13 mag in the u band, 14 mag in the g, r, or i band, or 12 mag in the z band.

With these criteria, we found 393 033 galaxies in SDSS DR10. For these galaxies, we downloaded the SDSS DR10 object ID, the galactic and equatorial coordinates, the redshift, the central velocity dispersion, and the following photometric quantities for the g, r, i, and z filters each: the axis-ratios, the de Vaucouleurs radii, the de Vaucouleurs model magnitudes, the galactic extinction, the likelihoods for a de Vaucouleurs profile and for an exponential profile, and the probability of its being an early-type galaxy based on GalaxyZoo.

We used the Sersic fit radii and magnitudes, as well as the Sersic indices from the catalogue by Simard et al. (2011). This catalogue is based on SDSS DR7, and it only provides the SDSS DR7 ID, which differs from the SDSS DR10 object IDs, to identify the galaxies in the catalogue, but no coordinates to do a direct cross-match. We could revert to SDSS DR7, but we prefer to take advantage of the updated photometry of SDSS DR10 (Ahn et al. 2014). We solved this problem by using a complete set of all SDSS DR7 galaxies with object IDs, equatorial coordinates, and redshifts to create a bridge between our data and the catalogue, which allows for direct cross-identification between them.

We used the stellar masses of SDSS galaxies based on the dusty models of the catalogue by Mendel et al. (2014). Their estimates for stellar masses were derived using a stellar population synthesis based on the code of Conroy et al. (2009) with spectral energy distributions based on the SDSS broadband photometry. We cross-matched this catalogue with the one of Simard et al. (2011) and our DR10 sample. Since the Mendel et al. (2014)

catalogue has stricter redshift limits than our SDSS DR10 sample, the measured redshifts of the combined sample have to lie between 0.005 and 0.4[3] now. This also removed all galaxies that might be blended with a nearby star (Mendel et al. 2014). We used the SDSS DR7 Object ID (to cross-match the catalogue with the other samples) and the logarithm of the stellar masses derived from the Sersic profiles and the composite profiles of the Mendel et al. (2014) catalogue. After all these cross-matching, we ended up with a sample of 370 159 galaxies.

Additional constraints were applied to the data after the calculation of several parameters from the observed values. Galaxies with a velocity dispersion of higher than 420 km s^{-1} were removed from the sample, because these values would be outside the trusted margin of SDSS algorithm for measuring the central velocity dispersion. We checked that dropping this upper dispersion limit would only contribute galaxies with unreasonably high central velocity dispersions. Furthermore, we eliminated all galaxies with an absolute magnitude either brighter than -25 mag or fainter than -15 mag in any of the used filters. A handful of galaxies with physical radii of more than $10^{2.5}$ kpc were also removed to avoid contamination from incorrectly measured radii.

Furthermore, the selected galaxies must have been identified as an elliptical galaxy with a probability greater than 0.5 based on GalaxyZoo. We carefully investigated the effect of different values of the criterion on our sample and on the candidates we want to find (see Section 4). Values higher than 0.5 will remove too many promising candidates from our sample, while for values below 0.5, the candidates in our sample will be heavily contaminated by galaxies that are superimposed on another galaxy in the line of sight or near neighbours, galaxies close to a very bright foreground star, and star-burst galaxies. We required that the likelihood for a de Vaucouleurs profile is greater than the likelihood for an exponential profile in every filter except the u band, owing to known problems[4] with this filter. This criterion was necessary because we used parameters, such as the radii and magnitudes obtained by de Vaucouleurs fits in this paper. If the likelihood for another profile is indeed higher, it would result in poorly derived values for our parameters.

In light of our comparison with other samples of compact massive galaxies in the local universe (see Section 5 for details), we found that the vast majority of these galaxies in the literature are within our basic sample and therefore best described by a de Vaucouleurs profile. Since we were searching for potential survivors of the red nuggets, we limited our sample to red sequence galaxies. We did this by removing all galaxies bluer than the lower 3-σ limit of the red sequence fit performed in Saulder et al. (2013). After this filtering, there were 233 833 galaxies between a redshift of 0.005 and 0.4 left (about 59.5% of the first selection and 63% of the cross-matched sample). Those form the basic sample that were used for the further analysis in this paper.

3. Method

One has to carefully calibrate the parameters obtained from the SDSS database and the refits done by Simard et al. (2011) before using them to classify and characterize the galaxies. The follow-

---

[3] The reduced upper redshift limit is no concern to us, since we do not expect to detect any intrinsically small galaxies at redshifts higher than 0.2 anyway.

[4] See: https://www.sdss3.org/dr10/imaging/caveats.php#usky.

ing quantities are calculated for all sources in every band used and for every set of fit parameters.

One starts off by considering the galactic extinction by using the Schlegel maps (Schlegel et al. 1998):

$$m_{\text{extcor}} = m_{\text{sdss}} - A_{\text{Schlegel}}, \tag{1}$$

where m_{extcor} denotes the extinction correct magnitude, m_{sdss} the observed apparent magnitude, and A_{Schlegel} the extinction according to Schlegel maps.

The K-correction used in this paper,

$$K(z_{obs}, m_{f_1} - m_{f_2}) = \sum_{i,j} B_{ij} z_{obs}^i (m_{f_1} - m_{f_2})^j \tag{2}$$

follows the model of Chilingarian et al. (2010), but with updated coefficients B_{ij} from Saulder et al. (2013). It requires the extinction-corrected magnitudes, m_{f_1} and m_{f_2}, of two different filters, f_1 and f_2, and the observed redshift z_{obs}.

In the next step, one obtains the fully corrected rest-frame magnitude m_{app} by considering the K correction $K(z_{obs}, m_{f_1} - m_{f_2})$:

$$m_{\text{cor}} = m_{\text{extcor}} - K(z_{obs}, m_{f_1} - m_{f_2}). \tag{3}$$

The redshift z is corrected for our motion relative to the cosmic microwave background (CMB).

The measured model semi-major from the SDSS data a_{sdss} has to be renormalized to account for the different ellipticities of the galaxies in the following way:

$$r_{\text{circ}} = a_{\text{sdss}} \sqrt{q_{b/a}}. \tag{4}$$

We follow Bernardi et al. (2003) and get a comparable quantity for all types of elliptical galaxies, the circularized radius r_{circ}, with the help of the minor semi-axis to the major semi-axis ratio $q_{b/a}$.

Because of the fixed fibre size of SDSS, an additional correction on the measured central velocity dispersion σ_{sdss} is required and we take advantage of the work of Jorgensen et al. (1995) and Wegner et al. (1999) to use

$$\sigma_0 = \sigma_{\text{sdss}} \cdot \left(\frac{a_{\text{fiber}}}{r_{\text{circ}}/8} \right)^{0.04}, \tag{5}$$

where σ_0 denotes the corrected central velocity dispersion and a_{fiber} stands for the radius of the SDSS fibres, which is 1.5 arcseconds for the galaxies in our sample. Here, σ_0 is typically about 10% higher than the measured value σ_{sdss} (Saulder et al. 2013).

For the following calculations, one requires the luminosity distance D_L, which is given by

$$D_L(z) = \frac{c \cdot z}{H_0} \left(1 + \left(\frac{z \cdot (1 - q_0)}{\sqrt{1 + 2 q_0 \cdot z} + 1 + q_0 \cdot z} \right) \right) \tag{6}$$

with H_0 being the present day Hubble parameter and $q_0 = \frac{\Omega_M}{2} - \Omega_\Lambda$ the current declaration parameter, which depends on the cosmological parameters Ω_M and Ω_Λ.

With the luminosity distance at hand, the angular diameter distance is given by

$$D_A(z) = D_L(z) \cdot (1 + z)^{-2}. \tag{7}$$

The physical radius R_0 of the galaxy is obtained using simple trigonometry:

$$R_0 = D_A(z) \cdot \tan(r_{\text{circ}}). \tag{8}$$

The measured surface brightness μ_0 is defined in the following way:

$$\mu_0 = m_{\text{cor}} + 2.5 \cdot \log_{10} \left(2\pi \cdot r_{\text{circ}}^2 \right) - 10 \cdot \log_{10} (1 + z) + Q \cdot z \tag{9}$$

with the term $-10 \cdot \log_{10}(1 + z)$ correcting for cosmological dimming of surface brightnesses. Since we only intend to use the surface brightness, we include a parameter that corrects for the secular evolution evolution of early-type galaxies, when applying or calculating the fundamental plane (see Appendix A and Saulder et al. (2013)). The evolution parameter $Q = 1.07$ mag per z was derived in Saulder et al. (2013) for early-type galaxies.

Another quantity that is required for our investigations is the absolute magnitude M_{abs}, which is calculated using the distance module:

$$m_{\text{cor}} - M_{\text{abs}} = 5 \cdot \log_{10}(D_L/\text{pc}) - 5. \tag{10}$$

The dynamical mass is given by

$$M_{\text{dyn}} = \frac{\beta(n)\sigma_0^2 \cdot R_0}{G} \tag{11}$$

with G being the gravitational constant. The function $\beta(n_S)$ is defined by:

$$\beta(n) = 8.87 - 0.831 \cdot n_S + 0.0241 \cdot n_S^2 \tag{12}$$

according to Cappellari et al. (2006), based on results from Bertin et al. (2002). It depends on the Sersic-index n_S, if a Sersic profile was used to obtain the effective radius. For de Vaucouleurs profiles, which are Sersic profiles with Sersic-indices $n_S = 4$, one would expect a β of 5.953; however, it has been found by observations (Cappellari et al. 2006) that a β of five works better. Cappellari et al. (2006) argue that this deviation is due to differences between the idealised simulation Equation 12 is based on and real observational data. Belli et al. (2014) find that the equations works well for spherical systems, but has problems if discs are present. We therefore decided to use the $\beta(n_S)$ from Equation 12, when using a Sersic profile, but we adopt a β of 5, when using a de Vaucouleurs profile in our analysis.

With all the equations and definitions given in this section, we now proceed to the selection and analysis of galaxies similar to b19.

4

Internal ID	SDSS DR10 ID	ra [°]	dec [°]	z	$m_{sdss,r}$ [mag]	a_{sdss} [arcsec]	σ_{sdss} [km/s]	$q_{b/a}$	$\mathcal{L}_{ETG}$
1	1237648721255596242	236.8072	-0.1422	0.1138	17.18 ± 0.00	1.17 ± 0.02	315± 14	0.67	0.88
2	1237648703523520846	229.4240	-0.7049	0.1166	17.04 ± 0.00	1.25 ± 0.02	336± 12	0.67	0.81
3	1237651191892607189	125.5691	48.2553	0.1276	17.56 ± 0.01	1.39 ± 0.02	351± 14	0.46	0.75
4	1237651753466462236	164.0158	1.9983	0.1153	17.72 ± 0.01	0.95 ± 0.03	297± 22	0.66	0.82
5	1237652934037536913	327.3491	-8.6752	0.1014	17.39 ± 0.01	0.81 ± 0.03	320± 16	0.88	0.70
6	1237652900773298301	58.0541	-5.8611	0.1137	17.25 ± 0.01	1.03 ± 0.02	306± 14	0.38	0.66
7	1237652629102067836	8.1716	-10.6661	0.1557	17.60 ± 0.01	1.00 ± 0.03	355± 18	0.63	1.00
8	1237651252589363420	247.9117	46.2683	0.1321	17.67 ± 0.01	0.78 ± 0.01	311± 14	0.30	0.76
9	1237655502424769160	256.4241	33.4779	0.1022	17.33 ± 0.01	1.51 ± 0.02	326± 16	0.52	0.77
10	1237651539246186637	167.7205	66.7862	0.1362	17.57 ± 0.01	1.09 ± 0.02	350± 14	0.29	0.59
11	1237651735773708418	218.3124	1.5053	0.1096	17.33 ± 0.01	0.96 ± 0.02	291± 16	0.68	0.74
12	1237659329240236080	243.4534	41.1059	0.1381	17.66 ± 0.01	0.85 ± 0.03	290± 17	0.56	0.78
13	1237666339727671425	20.8205	0.2955	0.0928	17.10 ± 0.00	1.11 ± 0.02	296± 11	0.73	0.88
14	1237651714798125236	248.3287	47.1274	0.1229	17.63 ± 0.01	0.60 ± 0.02	335± 12	0.85	0.66
15	1237658206124507259	193.5474	50.8170	0.1209	17.22 ± 0.00	1.17 ± 0.01	341± 16	0.41	0.80
16	1237652944786424004	1.1323	16.0719	0.1144	17.58 ± 0.01	0.91 ± 0.01	291± 15	0.29	0.55
17	1237662267540570526	235.5841	4.7666	0.1105	17.15 ± 0.01	1.20 ± 0.02	302± 10	0.56	0.77
18	1237652948530102500	10.3768	-9.2352	0.0538	15.24 ± 0.00	3.09 ± 0.02	310± 5	0.33	0.53
19	1237656241159995854	331.7753	12.0459	0.1607	17.91 ± 0.01	1.00 ± 0.03	306± 16	0.57	0.89
20	1237656243317113067	354.1646	15.8222	0.1179	17.56 ± 0.01	1.16 ± 0.02	290± 16	0.41	0.73
21	1237655474503024820	245.6049	44.7856	0.0716	15.84 ± 0.00	1.86 ± 0.02	333± 8	0.61	0.81
22	1237657596224209238	123.8014	38.6793	0.1259	17.16 ± 0.00	1.26 ± 0.02	333± 13	0.48	0.89
23	1237662264318034136	217.8880	8.9225	0.1108	17.09 ± 0.01	1.46 ± 0.02	384± 15	0.53	0.72
24	1237665569297203655	254.5120	41.8378	0.0375	15.37 ± 0.00	1.62 ± 0.01	303± 7	0.48	0.64
25	1237654605857751221	148.8860	4.3722	0.0937	16.41 ± 0.00	1.48 ± 0.01	352± 9	0.39	0.52
26	1237655465916170402	184.8400	63.5358	0.1039	17.46 ± 0.01	0.76 ± 0.01	292± 14	0.39	0.52
27	1237657628456190055	187.6884	51.7060	0.1517	17.61 ± 0.01	0.90 ± 0.01	307± 14	0.43	0.62
28	1237660025032081578	340.4373	-0.8113	0.1293	17.68 ± 0.01	0.63 ± 0.02	373± 22	0.86	0.77
29	1237661064411349290	138.3286	8.1161	0.0934	16.82 ± 0.00	1.41 ± 0.01	295± 9	0.28	0.61
30	1237661849849430137	156.3195	40.3153	0.0682	16.57 ± 0.00	1.53 ± 0.02	317± 10	0.78	0.58
31	1237663277928022281	0.6027	0.5352	0.0784	17.56 ± 0.01	0.64 ± 0.02	331± 17	0.68	0.77
32	1237661383314702588	160.1959	39.9311	0.1394	17.77 ± 0.01	0.86 ± 0.02	324± 15	0.36	0.69
33	1237662697568796852	226.2857	30.1184	0.1450	17.24 ± 0.01	0.86 ± 0.02	314± 9	0.73	0.71
34	1237661812272857187	180.2528	12.2175	0.1295	17.73 ± 0.01	1.00 ± 0.03	291± 17	0.52	0.81
35	1237665532252520624	223.1388	22.5927	0.1551	17.66 ± 0.01	1.32 ± 0.02	318± 16	0.34	0.54
36	1237662224087974057	238.7278	25.4691	0.1556	17.84 ± 0.01	1.18 ± 0.02	308± 17	0.45	0.76
37	1237664130483618005	166.7737	13.3182	0.1188	17.10 ± 0.00	1.40 ± 0.02	328± 13	0.49	0.76
38	1237664669510074510	158.0224	37.4689	0.1043	16.60 ± 0.00	0.99 ± 0.01	385± 12	0.63	0.71
39	1237665549429899544	223.0734	22.4871	0.1165	17.39 ± 0.01	0.78 ± 0.01	335± 13	0.29	0.62
40	1237667209978380503	149.1117	23.9641	0.1193	17.33 ± 0.01	0.95 ± 0.02	356± 25	0.81	0.68
41	1237663278461944053	353.8668	1.0467	0.0827	16.35 ± 0.00	1.71 ± 0.02	320± 9	0.55	0.80
42	1237662340012638220	239.5694	27.2367	0.0896	17.01 ± 0.00	0.81 ± 0.01	296± 12	0.55	0.75

Internal ID	SDSS DR10 ID	ra [°]	dec [°]	z	$m_{\text{sdss},r}$ [mag]	a_{sdss} [arcsec]	σ_{sdss} [km/s]	$q_{b/a}$	$\mathcal{L}_{\text{ETG}}$
43	1237664667887140986	128.6548	24.3250	0.0705	16.42 ± 0.00	1.22 ± 0.02	296± 9	0.71	0.77
44	1237664093432119636	121.7265	20.7624	0.1247	17.64 ± 0.01	0.93 ± 0.02	299± 14	0.44	0.66
45	1237661850400260193	199.4989	43.6141	0.1140	17.76 ± 0.01	0.64 ± 0.02	287± 16	0.59	0.62
46	1237664852035174654	219.1545	31.3943	0.0850	16.14 ± 0.00	1.46 ± 0.01	331± 9	0.36	0.77
47	1237667429035540562	178.7061	26.4323	0.1108	17.05 ± 0.00	1.12 ± 0.01	316± 12	0.62	0.67
48	1237673808655221213	121.7151	19.4664	0.1242	18.05 ± 0.01	0.69 ± 0.03	294± 19	0.62	0.73
49	1237664854715727968	210.0376	35.9503	0.1494	17.76 ± 0.01	1.01 ± 0.03	317± 14	0.66	0.65
50	1237665535469486145	243.3042	17.8080	0.0374	14.72 ± 0.00	3.44 ± 0.01	316± 7	0.44	0.68
51	1237663478723969457	338.0784	-0.4059	0.0865	17.04 ± 0.00	1.23 ± 0.02	327± 17	0.54	0.80
52	1237665440978698364	194.2722	28.9814	0.0686	15.45 ± 0.00	2.19 ± 0.01	340± 8	0.57	0.78
53	1237667910055100586	181.7985	23.8744	0.0775	16.55 ± 0.00	1.21 ± 0.02	328± 11	0.77	0.86
54	1237667734526492801	227.3075	16.4333	0.1159	17.56 ± 0.01	1.02 ± 0.02	310± 17	0.49	0.61
55	1237662619725005006	240.2092	29.2028	0.0913	16.65 ± 0.00	1.40 ± 0.01	327± 11	0.62	0.84
56	1237664869745230095	128.9418	34.2085	0.1978	18.43 ± 0.01	0.68 ± 0.04	316± 24	0.77	0.65
57	1237665429169242591	209.7906	27.9501	0.0811	17.16 ± 0.00	0.63 ± 0.01	287± 10	0.46	0.62
58	1237665440975224988	185.1490	29.2998	0.0908	16.49 ± 0.00	1.45 ± 0.02	332± 13	0.74	0.85
59	1237668299281662070	194.2881	20.8064	0.0868	16.76 ± 0.00	1.17 ± 0.01	307± 9	0.51	0.56
60	1237668349753950509	232.0499	12.1307	0.1225	17.63 ± 0.01	1.16 ± 0.02	311± 14	0.38	0.81
61	1237668271372501042	227.9714	14.2653	0.1221	17.70 ± 0.01	0.92 ± 0.02	291± 16	0.54	0.75
62	1237648721758978188	160.3022	0.2285	0.1300	17.60 ± 0.01	1.24 ± 0.02	305± 15	0.37	0.64
63	1237664671640715458	191.2284	36.1838	0.0877	17.64 ± 0.01	0.47 ± 0.01	293± 15	0.65	0.68
64	1237667735062708393	225.9192	17.2367	0.1505	17.73 ± 0.01	1.07 ± 0.03	309± 17	0.56	0.74
65	1237662335717015837	236.8248	33.1773	0.1265	17.74 ± 0.01	0.84 ± 0.03	296± 16	0.64	0.78
66	1237668310021440087	245.6255	9.3970	0.2018	17.70 ± 0.01	0.85 ± 0.02	302± 13	0.51	0.79
67	1237661358617067696	181.3091	48.4216	0.0648	15.89 ± 0.00	2.01 ± 0.02	311± 8	0.54	0.71
68	1237668298203070641	182.4650	20.0535	0.1116	17.58 ± 0.01	1.02 ± 0.02	293± 12	0.56	0.72
69	1237662336794820961	245.8542	28.0910	0.1233	17.01 ± 0.00	1.01 ± 0.02	306± 11	0.73	0.65
70	1237667917032980629	189.9670	21.1529	0.1085	16.78 ± 0.00	1.43 ± 0.01	321± 9	0.51	0.74
71	1237662224614490342	214.0046	35.9910	0.1271	17.52 ± 0.01	1.12 ± 0.02	300± 14	0.54	0.78
72	1237661950244945934	162.5130	11.8190	0.0812	16.56 ± 0.00	1.75 ± 0.02	340± 11	0.46	0.88
73	1237663333640810655	225.5537	14.6343	0.0697	16.62 ± 0.00	0.95 ± 0.01	351± 14	0.58	0.52
74	1237662236410577091	226.1287	6.6601	0.1439	17.76 ± 0.01	0.82 ± 0.03	316± 17	0.78	0.80
75	1237662302971691136	214.9301	49.2366	0.0260	14.54 ± 0.00	3.59 ± 0.02	378± 2	0.93	0.51
76	1237667917030555837	184.0304	21.1393	0.1278	17.04 ± 0.00	1.24 ± 0.02	389± 16	0.53	0.79

Table 2. List of the basic parameters of our candidate galaxies. First column: internal IDs, which are used to identify the galaxies. The numbering is essentially random and only based on the order the galaxies were drawn from the basic sample. The galaxy b19 has the internal ID 2. Second column: object ID used by SDSS DR10. Third and fourth column: equatorial coordinates of the galaxies. Fifth column: redshift z, already corrected for our motion relative to the CMB. Sixth, seventh, and eighth columns: observed uncorrected refitted SDSS parameters in the following order: observed apparent magnitude m_{sdss}, angular semi-major axis a_{sdss}, central velocity dispersion σ_{sdss}. Ninth column: axis ratio $q_{b/a}$. Tenth column: GalaxyZoo probability $\mathcal{L}_{\text{ETG}}$ of the galaxy being classified as an early-type.

internal ID	R_r [kpc]	σ_0 [km s^{-1}]	μ_r [$\frac{\text{mag}}{\text{arcsec}^2}$]	M_r [mag]	$(M_g - M_r)$ [mag]	M_z [mag]	$\log_{10}(M_{\text{dyn}})$ [$\log_{10}(M_\odot)$]	$\log_{10}(M_*)$ [$\log_{10}(M_\odot)$]	Υ_{dyn} [$M_\odot/L_{\odot,r}$]	Υ_* [$M_\odot/L_{\odot,r}$]
1	2.00 ± 0.04	348± 16	18.38 ± 0.04	-21.81 ± 0.01	0.83 ± 0.01	-22.46 ± 0.01	11.45 ± 0.02	11.04 ± 0.15	6.95 ± 0.37	2.71 ± 1.12
2	2.17 ± 0.05	371± 13	18.43 ± 0.05	-21.95 ± 0.01	0.80 ± 0.01	-22.61 ± 0.01	11.54 ± 0.02	11.15 ± 0.15	7.55 ± 0.35	3.06 ± 1.26
3	2.17 ± 0.05	389± 16	18.78 ± 0.05	-21.60 ± 0.01	0.77 ± 0.02	-22.31 ± 0.01	11.58 ± 0.02	10.98 ± 0.15	11.39 ± 0.61	2.85 ± 1.18

internal ID	R_r [kpc]	σ_0 [km s^{-1}]	μ_r [$\frac{mag}{arcsec^2}$]	M_r [mag]	$(M_g - M_r)$ [mag]	M_z [mag]	$\log_{10}(M_{\mathrm{dyn}})$ [$\log_{10}(M_\odot)$]	$\log_{10}(M_*)$ [$\log_{10}(M_\odot)$]	Υ_{dyn} [$M_\odot/L_{\odot,r}$]	Υ_* [$M_\odot/L_{\odot,r}$]
4	1.62 ± 0.06	332± 25	18.60 ± 0.07	-21.15 ± 0.01	0.77 ± 0.02	-21.83 ± 0.02	11.32 ± 0.03	10.77 ± 0.15	9.41 ± 0.83	2.64 ± 1.09
5	1.44 ± 0.05	358± 18	18.29 ± 0.08	-21.18 ± 0.01	0.62 ± 0.01	-22.00 ± 0.01	11.33 ± 0.03	10.83 ± 0.15	9.44 ± 0.61	2.99 ± 1.23
6	1.32 ± 0.04	344± 15	17.50 ± 0.06	-21.79 ± 0.01	0.77 ± 0.01	-22.46 ± 0.01	11.26 ± 0.02	10.95 ± 0.15	4.54 ± 0.26	2.23 ± 0.92
7	2.18 ± 0.09	395± 20	18.41 ± 0.09	-22.01 ± 0.01	0.78 ± 0.02	-22.80 ± 0.02	11.60 ± 0.03	11.16 ± 0.15	8.13 ± 0.55	2.97 ± 1.23
8	1.02 ± 0.03	355± 16	17.27 ± 0.06	-21.48 ± 0.01	0.83 ± 0.01	-22.19 ± 0.01	11.18 ± 0.02	11.00 ± 0.15	5.01 ± 0.28	3.32 ± 1.37
9	2.05 ± 0.05	358± 17	19.02 ± 0.05	-21.22 ± 0.01	0.84 ± 0.02	-21.89 ± 0.01	11.49 ± 0.02	10.85 ± 0.15	13.02 ± 0.77	3.00 ± 1.24
10	1.42 ± 0.05	395± 16	17.81 ± 0.08	-21.66 ± 0.01	0.83 ± 0.01	-22.39 ± 0.02	11.41 ± 0.02	10.99 ± 0.15	7.28 ± 0.43	2.75 ± 1.14
11	1.58 ± 0.04	324± 18	18.26 ± 0.06	-21.42 ± 0.01	0.73 ± 0.02	-22.06 ± 0.01	11.29 ± 0.03	10.88 ± 0.15	6.80 ± 0.45	2.65 ± 1.09
12	1.59 ± 0.07	327± 19	18.10 ± 0.09	-21.62 ± 0.01	1.10 ± 0.02	-22.16 ± 0.02	11.29 ± 0.03	11.01 ± 0.15	5.78 ± 0.44	2.97 ± 1.23
13	1.66 ± 0.03	327± 13	18.54 ± 0.04	-21.22 ± 0.01	0.76 ± 0.01	-21.87 ± 0.01	11.31 ± 0.03	10.78 ± 0.15	8.76 ± 0.41	2.58 ± 1.07
14	1.24 ± 0.03	379± 14	17.88 ± 0.06	-21.29 ± 0.01	0.59 ± 0.01	-21.91 ± 0.01	11.31 ± 0.02	10.66 ± 0.15	8.23 ± 0.39	1.82 ± 0.75
15	1.65 ± 0.03	381± 18	18.09 ± 0.04	-21.70 ± 0.01	0.83 ± 0.01	-22.39 ± 0.01	11.45 ± 0.02	11.00 ± 0.15	7.60 ± 0.41	2.74 ± 1.13
16	1.03 ± 0.03	331± 17	17.46 ± 0.05	-21.29 ± 0.01	0.81 ± 0.02	-22.01 ± 0.01	11.12 ± 0.02	10.85 ± 0.15	5.21 ± 0.31	2.80 ± 1.16
17	1.83 ± 0.04	335± 11	18.33 ± 0.05	-21.66 ± 0.01	0.83 ± 0.01	-22.33 ± 0.01	11.38 ± 0.02	10.95 ± 0.15	6.72 ± 0.30	2.51 ± 1.04
18	1.85 ± 0.02	334± 6	18.15 ± 0.02	-21.82 ± 0.01	0.82 ± 0.01	-22.51 ± 0.01	11.38 ± 0.01	11.04 ± 0.15	5.89 ± 0.14	2.69 ± 1.11
19	2.13 ± 0.07	342± 18	18.44 ± 0.07	-21.94 ± 0.01	0.85 ± 0.02	-22.69 ± 0.02	11.46 ± 0.03	11.15 ± 0.15	6.35 ± 0.42	3.07 ± 1.27
20	1.60 ± 0.04	324± 18	18.26 ± 0.05	-21.45 ± 0.01	0.80 ± 0.02	-22.18 ± 0.01	11.29 ± 0.03	10.88 ± 0.15	6.69 ± 0.43	2.64 ± 1.09
21	2.00 ± 0.02	362± 9	18.34 ± 0.02	-21.81 ± 0.01	0.81 ± 0.01	-22.46 ± 0.01	11.48 ± 0.01	11.02 ± 0.15	7.54 ± 0.24	2.57 ± 1.06
22	2.00 ± 0.04	370± 14	18.27 ± 0.05	-21.94 ± 0.01	0.82 ± 0.01	-22.63 ± 0.01	11.50 ± 0.02	11.14 ± 0.15	6.99 ± 0.34	3.01 ± 1.24
23	2.17 ± 0.04	423± 17	18.70 ± 0.04	-21.67 ± 0.01	0.82 ± 0.02	-22.42 ± 0.03	11.66 ± 0.02	11.02 ± 0.15	12.70 ± 0.64	2.96 ± 1.22
24	0.84 ± 0.01	333± 7	17.39 ± 0.02	-20.83 ± 0.01	0.82 ± 0.01	-21.59 ± 0.01	11.03 ± 0.01	10.60 ± 0.15	6.53 ± 0.20	2.42 ± 1.00
25	1.62 ± 0.02	390± 10	17.72 ± 0.03	-22.00 ± 0.01	0.82 ± 0.01	-22.73 ± 0.01	11.46 ± 0.01	11.11 ± 0.15	5.94 ± 0.19	2.68 ± 1.11
26	0.92 ± 0.02	333± 16	17.37 ± 0.05	-21.12 ± 0.01	0.82 ± 0.01	-21.86 ± 0.01	11.07 ± 0.02	10.77 ± 0.15	5.49 ± 0.31	2.74 ± 1.13
27	1.58 ± 0.04	346± 16	17.81 ± 0.05	-21.91 ± 0.01	0.83 ± 0.01	-22.60 ± 0.01	11.34 ± 0.02	11.06 ± 0.15	4.96 ± 0.27	2.58 ± 1.06
28	1.36 ± 0.05	421± 25	17.83 ± 0.07	-21.53 ± 0.01	0.77 ± 0.02	-22.23 ± 0.02	11.45 ± 0.03	10.93 ± 0.15	8.88 ± 0.65	2.73 ± 1.13
29	1.29 ± 0.02	329± 10	17.65 ± 0.03	-21.57 ± 0.01	0.81 ± 0.01	-22.29 ± 0.01	11.21 ± 0.01	10.85 ± 0.15	4.99 ± 0.19	2.15 ± 0.89
30	1.76 ± 0.03	346± 11	18.91 ± 0.04	-20.96 ± 0.01	0.66 ± 0.01	-21.57 ± 0.01	11.39 ± 0.02	10.57 ± 0.15	13.21 ± 0.53	1.99 ± 0.82
31	0.78 ± 0.02	375± 19	17.76 ± 0.06	-20.35 ± 0.01	0.74 ± 0.02	-21.00 ± 0.02	11.10 ± 0.02	10.41 ± 0.15	11.99 ± 0.82	2.40 ± 0.99
32	1.29 ± 0.05	368± 17	17.73 ± 0.08	-21.54 ± 0.01	0.82 ± 0.02	-22.27 ± 0.01	11.31 ± 0.02	10.96 ± 0.15	6.41 ± 0.40	2.90 ± 1.20
33	1.89 ± 0.06	351± 10	17.95 ± 0.07	-22.16 ± 0.01	0.79 ± 0.01	-22.71 ± 0.01	11.43 ± 0.02	11.15 ± 0.15	4.87 ± 0.22	2.51 ± 1.04
34	1.68 ± 0.06	326± 19	18.41 ± 0.08	-21.43 ± 0.01	0.83 ± 0.02	-22.18 ± 0.02	11.32 ± 0.03	10.94 ± 0.15	7.28 ± 0.53	3.05 ± 1.26
35	2.09 ± 0.07	355± 18	18.36 ± 0.07	-21.97 ± 0.01	0.86 ± 0.02	-22.75 ± 0.01	11.49 ± 0.02	11.18 ± 0.15	6.51 ± 0.41	3.22 ± 1.33
36	2.16 ± 0.06	343± 19	18.53 ± 0.06	-21.88 ± 0.01	0.82 ± 0.02	-22.54 ± 0.02	11.47 ± 0.03	11.09 ± 0.15	6.86 ± 0.47	2.88 ± 1.19
37	2.13 ± 0.04	363± 15	18.57 ± 0.04	-21.77 ± 0.01	0.77 ± 0.01	-22.39 ± 0.01	11.51 ± 0.02	10.96 ± 0.15	8.32 ± 0.39	2.33 ± 0.96
38	1.51 ± 0.02	429± 13	17.61 ± 0.03	-21.97 ± 0.01	0.78 ± 0.01	-22.62 ± 0.01	11.51 ± 0.01	11.06 ± 0.15	6.88 ± 0.27	2.44 ± 1.01
39	0.89 ± 0.02	383± 15	16.94 ± 0.05	-21.50 ± 0.01	0.80 ± 0.01	-22.20 ± 0.01	11.18 ± 0.02	10.87 ± 0.15	4.96 ± 0.25	2.45 ± 1.01
40	1.87 ± 0.05	395± 27	18.48 ± 0.06	-20.35 ± 0.01	0.66 ± 0.02	-22.23 ± 0.01	11.53 ± 0.03	10.80 ± 0.15	10.44 ± 0.79	1.94 ± 0.80
41	1.97 ± 0.02	350± 10	18.38 ± 0.03	-21.75 ± 0.01	0.81 ± 0.01	-22.50 ± 0.01	11.45 ± 0.01	11.09 ± 0.15	7.33 ± 0.25	3.21 ± 1.33
42	1.01 ± 0.02	334± 13	17.41 ± 0.05	-21.27 ± 0.01	0.84 ± 0.01	-22.04 ± 0.01	11.12 ± 0.02	10.88 ± 0.15	5.28 ± 0.26	3.05 ± 1.26
43	1.39 ± 0.02	327± 10	18.09 ± 0.03	-21.27 ± 0.01	0.79 ± 0.01	-21.91 ± 0.01	11.24 ± 0.01	10.84 ± 0.15	7.01 ± 0.27	2.79 ± 1.15
44	1.40 ± 0.03	336± 15	18.01 ± 0.05	-21.42 ± 0.01	0.78 ± 0.01	-22.17 ± 0.01	11.26 ± 0.02	10.91 ± 0.15	6.49 ± 0.36	2.87 ± 1.19
45	1.03 ± 0.04	326± 18	17.72 ± 0.08	-21.03 ± 0.01	0.77 ± 0.02	-21.78 ± 0.01	11.10 ± 0.03	10.71 ± 0.15	6.42 ± 0.46	2.61 ± 1.08

internal ID	R_r [kpc]	σ_0 [km s^{-1}]	μ_r [$\frac{mag}{arcsec^2}$]	M_r [mag]	$(M_g - M_r)$ [mag]	M_z [mag]	$\log_{10}(M_{dyn})$ [$\log_{10}(M_\odot)$]	$\log_{10}(M_*)$ [$\log_{10}(M_\odot)$]	Υ_{dyn} [$M_\odot/L_{\odot,r}$]	Υ_* [$M_\odot/L_{\odot,r}$]
46	1.39 ± 0.01	368± 11	17.45 ± 0.02	-21.93 ± 0.01	0.80 ± 0.01	-22.63 ± 0.01	11.34 ± 0.01	11.04 ± 0.15	4.86 ± 0.17	2.43 ± 1.00
47	1.80 ± 0.03	350± 14	18.28 ± 0.04	-21.68 ± 0.01	0.76 ± 0.01	-22.24 ± 0.01	11.41 ± 0.02	10.90 ± 0.15	7.12 ± 0.33	2.21 ± 0.91
48	1.22 ± 0.06	333± 21	18.11 ± 0.11	-21.02 ± 0.01	0.86 ± 0.02	-21.57 ± 0.02	11.20 ± 0.03	10.70 ± 0.15	8.01 ± 0.68	2.54 ± 1.05
49	2.17 ± 0.07	352± 16	18.70 ± 0.08	-21.71 ± 0.01	0.85 ± 0.02	-22.39 ± 0.01	11.50 ± 0.02	11.05 ± 0.15	8.50 ± 0.51	3.04 ± 1.26
50	1.69 ± 0.01	338± 7	18.18 ± 0.01	-21.56 ± 0.01	0.84 ± 0.01	-22.22 ± 0.01	11.35 ± 0.01	10.91 ± 0.15	6.96 ± 0.21	2.55 ± 1.05
51	1.48 ± 0.03	363± 18	18.32 ± 0.05	-21.19 ± 0.01	0.77 ± 0.02	-21.86 ± 0.02	11.35 ± 0.02	10.74 ± 0.15	9.88 ± 0.62	2.43 ± 1.00
52	2.17 ± 0.02	368± 9	18.22 ± 0.02	-22.10 ± 0.01	0.84 ± 0.01	-22.80 ± 0.01	11.53 ± 0.01	11.10 ± 0.15	6.43 ± 0.19	2.37 ± 0.98
53	1.57 ± 0.03	361± 12	18.30 ± 0.03	-21.33 ± 0.01	0.76 ± 0.01	-21.91 ± 0.01	11.38 ± 0.02	10.85 ± 0.15	9.11 ± 0.39	2.70 ± 1.12
54	1.52 ± 0.05	347± 19	18.31 ± 0.07	-21.30 ± 0.01	0.82 ± 0.02	-21.97 ± 0.02	11.33 ± 0.03	10.86 ± 0.15	8.44 ± 0.58	2.87 ± 1.19
55	1.89 ± 0.03	360± 12	18.39 ± 0.03	-21.66 ± 0.01	0.79 ± 0.01	-22.30 ± 0.01	11.45 ± 0.02	10.92 ± 0.15	8.07 ± 0.33	2.34 ± 0.97
56	2.00 ± 0.14	356± 27	18.38 ± 0.15	-21.90 ± 0.01	1.04 ± 0.03	-22.49 ± 0.02	11.47 ± 0.04	11.28 ± 0.15	6.67 ± 0.71	4.27 ± 1.77
57	0.66 ± 0.01	328± 12	16.93 ± 0.04	-20.81 ± 0.01	0.79 ± 0.01	-21.47 ± 0.01	10.92 ± 0.02	10.58 ± 0.15	5.09 ± 0.23	2.36 ± 0.98
58	2.12 ± 0.03	364± 15	18.55 ± 0.03	-21.75 ± 0.01	0.77 ± 0.01	-22.39 ± 0.01	11.51 ± 0.02	10.97 ± 0.15	8.51 ± 0.40	2.45 ± 1.01
59	1.37 ± 0.02	342± 11	17.92 ± 0.04	-21.41 ± 0.01	0.80 ± 0.01	-22.15 ± 0.01	11.27 ± 0.01	10.88 ± 0.15	6.59 ± 0.26	2.67 ± 1.10
60	1.59 ± 0.04	348± 16	18.29 ± 0.05	-21.42 ± 0.01	0.79 ± 0.02	-22.20 ± 0.02	11.35 ± 0.02	10.96 ± 0.15	7.95 ± 0.47	3.27 ± 1.35
61	1.50 ± 0.04	326± 18	18.27 ± 0.05	-21.31 ± 0.01	0.78 ± 0.02	-21.96 ± 0.01	11.27 ± 0.03	10.86 ± 0.15	7.25 ± 0.47	2.80 ± 1.16
62	1.77 ± 0.05	341± 16	18.32 ± 0.06	-21.63 ± 0.01	0.84 ± 0.02	-22.36 ± 0.01	11.38 ± 0.02	11.00 ± 0.15	6.97 ± 0.41	2.90 ± 1.20
63	0.62 ± 0.01	337± 17	17.12 ± 0.05	-20.51 ± 0.01	0.80 ± 0.02	-21.14 ± 0.01	10.91 ± 0.02	10.45 ± 0.15	6.71 ± 0.40	2.32 ± 0.96
64	2.14 ± 0.08	344± 19	18.58 ± 0.08	-21.95 ± 0.01	0.81 ± 0.02	-22.46 ± 0.01	11.47 ± 0.03	11.06 ± 0.15	7.33 ± 0.52	2.87 ± 1.18
65	1.54 ± 0.06	332± 18	18.30 ± 0.08	-21.34 ± 0.01	0.79 ± 0.02	-22.07 ± 0.02	11.29 ± 0.03	10.80 ± 0.15	7.46 ± 0.54	2.38 ± 0.99
66	2.06 ± 0.08	340± 15	17.66 ± 0.09	-22.69 ± 0.01	0.80 ± 0.02	-23.36 ± 0.01	11.44 ± 0.03	11.27 ± 0.15	3.03 ± 0.19	2.05 ± 0.84
67	1.83 ± 0.02	338± 9	18.39 ± 0.03	-21.57 ± 0.01	0.78 ± 0.01	-22.25 ± 0.01	11.39 ± 0.01	10.89 ± 0.15	7.52 ± 0.26	2.38 ± 0.98
68	1.56 ± 0.05	328± 13	18.46 ± 0.07	-21.19 ± 0.01	0.75 ± 0.01	-21.88 ± 0.01	11.29 ± 0.02	10.79 ± 0.15	8.45 ± 0.46	2.69 ± 1.11
69	1.94 ± 0.04	339± 12	18.06 ± 0.05	-22.07 ± 0.01	0.62 ± 0.01	-22.66 ± 0.01	11.41 ± 0.02	10.96 ± 0.15	5.02 ± 0.22	1.77 ± 0.73
70	2.03 ± 0.03	355± 10	18.26 ± 0.03	-21.95 ± 0.01	0.80 ± 0.01	-22.70 ± 0.01	11.47 ± 0.01	11.17 ± 0.15	6.40 ± 0.23	3.23 ± 1.33
71	1.90 ± 0.04	334± 15	18.57 ± 0.05	-21.52 ± 0.01	0.80 ± 0.02	-22.12 ± 0.01	11.39 ± 0.02	10.91 ± 0.15	7.93 ± 0.43	2.61 ± 1.08
72	1.83 ± 0.03	373± 12	18.53 ± 0.03	-21.43 ± 0.01	0.77 ± 0.01	-22.13 ± 0.01	11.47 ± 0.01	10.87 ± 0.15	10.33 ± 0.41	2.62 ± 1.08
73	0.97 ± 0.01	393± 15	17.56 ± 0.03	-21.01 ± 0.01	0.76 ± 0.01	-21.64 ± 0.01	11.24 ± 0.02	10.61 ± 0.15	8.94 ± 0.42	2.08 ± 0.86
74	1.85 ± 0.07	353± 19	18.41 ± 0.09	-21.65 ± 0.01	0.80 ± 0.02	-22.36 ± 0.01	11.43 ± 0.03	10.99 ± 0.15	7.70 ± 0.55	2.80 ± 1.15
75	1.81 ± 0.01	397± 3	19.07 ± 0.02	-20.81 ± 0.04	0.73 ± 0.06	-21.39 ± 0.04	11.52 ± 0.00	10.59 ± 0.15	20.56 ± 2.13	2.42 ± 1.03
76	2.08 ± 0.04	432± 18	18.22 ± 0.04	-22.07 ± 0.01	0.79 ± 0.01	-22.77 ± 0.01	11.65 ± 0.02	11.10 ± 0.15	8.76 ± 0.44	2.47 ± 1.02

Table 3. List of the derived parameters based on the de Vaucouleurs fits from SDSS for our candidate galaxies. First column: internal IDs of our galaxies. Second column: scale radius R_r of the galaxies measured in the SDSS r band (in kpc). Third column: corrected central velocity dispersion σ_0 (in km/s). Fourth column: surface brightness μ_r measured in the SDSS r band (in mag/arcsec^2). Fifth column: absolute magnitude in r band M_r. Sixth column: g-r colour $(M_g - M_r)$ (in mag). Seventh column: logarithm of the dynamical mass M_{dyn} (in solar masses). Eighth column: logarithm of the stellar mass M_* (in solar masses). Ninth column: dynamical mass-to-light ratio Υ_{dyn} (in solar units $M_\odot/L_{\odot,r}$). Tenth column: stellar mass-to-light ratio Υ_* (in solar units $M_\odot/L_{\odot,r}$).

4. Candidate selection
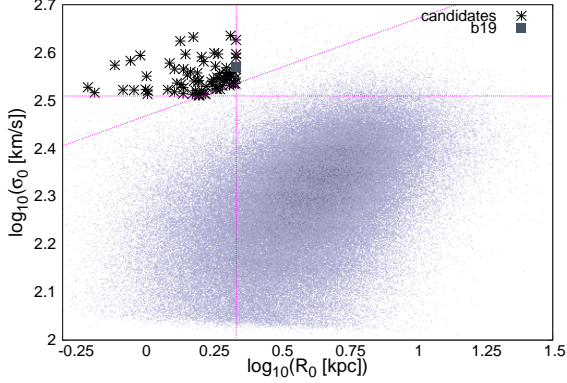
Figure 1. Selection criteria for our compact and massive galaxy candidates indicated by the dashed magenta lines. The black stars represent the 75 new candidates for galaxies with similar properties in de Vaucouleurs fit parameters as b19, while b19 itself is represented by a grey filled square in the plot.

The main idea behind this paper is to find galaxies with properties comparable to b19 (Läsker et al. 2013) and NGC 1277 (van den Bosch et al. 2012) and to investigate whether they are unique objects or not. B19 is characterized by a relatively small scale radius, but a relatively high central velocity dispersion that implies a high dynamical mass for its given radius.

In the following we define a set of criteria that provides us with galaxies in the same region of the $\log_{10}(R_0)$-$\log_{10}(\sigma_0)$ diagram as b19. The selection criteria have to be restrictive enough that only the most massive and most compact galaxies are included, but still generous enough to include b19. To avoid too much arbitrariness, we used the samples averages and standard deviations as a basis for our definitions. We adopted the following selection criteria:

– $\log_{10}(R_0) < \overline{\log_{10}(R_0)} - \sigma_{\log_{10}(R_0)}$
– $\log_{10}(\sigma_0) > \overline{\log_{10}(\sigma_0)} + 2\,\sigma_{\log_{10}(\sigma_0)}$
– $\log_{10}(\sigma_0) - k_{R\sigma} \cdot \log_{10}(R_0) < d_{R\sigma} + 3\,s_{\epsilon,R\sigma}$.

The first criterion means that the logarithm of the physical radius R_0 has to be smaller than the sample's average $\overline{\log_{10}(R_0)}$ by at least one standard deviation $\sigma_{\log_{10}(R_0)}$, which provides us with an upper limit for R_0 of 2.18 kpc for the de Vaucouleurs fit parameters. The lower limit for the central velocity dispersion σ_0 is requiring by demanding it to be at least two standard deviation $\sigma_{\log_{10}(\sigma_0)}$ higher than the mean of the logarithm of the central velocity dispersion $\overline{\log_{10}(\sigma_0)}$. This yields a lower limit of $\sigma_0 = 323.2$ km s^{-1}. The last criterion ensures that all candidates are more than three root mean square $s_{\epsilon,R\sigma}$ off from the $\log_{10}(R_0) - \log_{10}(\sigma_0)$ relation: $\log_{10}(\sigma_0) = k_{R\sigma} \cdot \log_{10}(R_0) + d_{R\sigma}$, for which the coefficients $k_{R\sigma}$ and $d_{R\sigma}$ were obtained by a linear fit to the data points of the basic sample. The selection criteria are illustrated in Figure 1.

By applying the above selection criteria to the basic sample, one finds 76 galaxies. All candidates are listed with their basic parameters in Table 2 and their derived parameters in Table 3. B19 itself has the internal ID 2. The others are new compact massive galaxies similar to b19, whose global properties will be investigated over the course of this paper. A set of SDSS thumbnail images for all our candidates is provided in Figure 2.

In Appendix B, we provide an alternative sample of candidates using the Sersic fit parameters from Simard et al. (2011) instead of the de Vaucouleurs fit directly from SDSS.

9
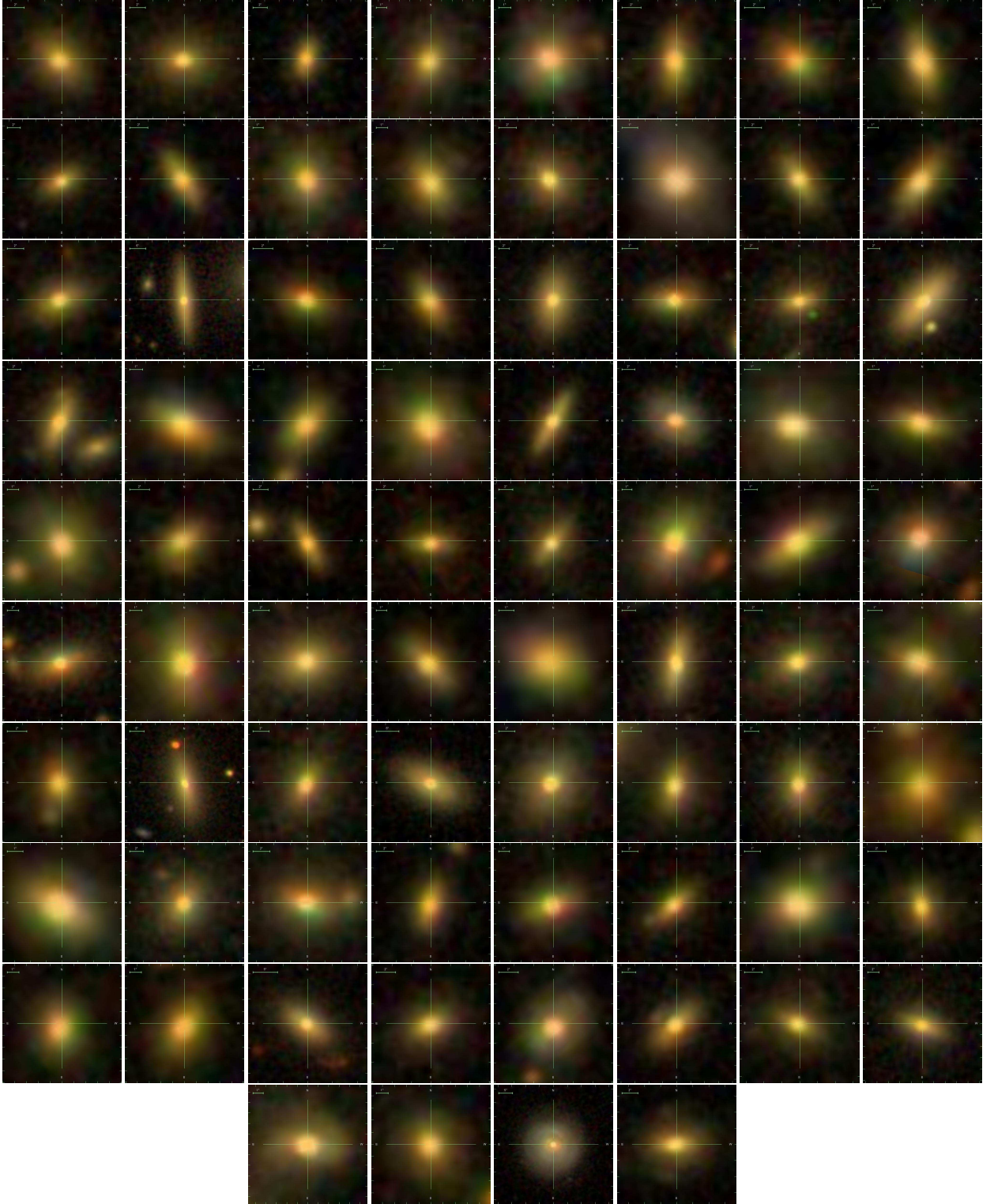
Figure 2. SDSS DR10 colour thumbnails for our 76 compact massive galaxy candidates. They are arranged by their internal ID with galaxy 1 in upper left corner and then in ascending order from left to right and top to bottom. B19 is the second galaxy in the top row. The thumbnails show an square area with a side length corresponding to 12 $a_{\rm sdss}$ of the displayed galaxy. There is also a small scale in the top left corner of each image.

10

5. Results

In this section, we discuss the distribution of our candidates along known scaling relations for early-type galaxies. We compare our sample to the work of Taylor et al. (2010), who listed 63 compact massive red-sequence galaxies in a similar redshift range. When cross-matching their sample with our data, we find 60 of their galaxies that are in our basic sample. Another sample of possible low-redshift, compact, massive red-sequence galaxies is the sample of Trujillo et al. (2009), which contains 29 such galaxies, of which we detect 23 in our basic sample. All samples are based on SDSS. In the following, we compare our compact galaxy sample of 76 galaxies to the 60 galaxies that are in both our basic sample and the Taylor et al. (2010) sample, as well as to the 23 galaxies, which are in both our basic sample and the Trujillo et al. (2009) sample. For simplicity, we call the 60 galaxies of Taylor et al. (2010), which are in our basic sample, the Ta10 sample from here on, and they are listed with their basic and derived parameters from SDSS in Tables C.2 and C.3. The 23 galaxies of the Trujillo et al. (2009), which are in our basic sample, are called the Tr09 sample from here, and they are listed with their basic and derived parameters from SDSS in Tables C.4 and C.5.

A comparison of the Ta10 sample with our compact galaxy sample reveals that they only have five galaxies in common (see Table C.1). It is surprising to only find so few galaxies in common with a sample that should be similar to our own. The difference between our candidate sample and the Tr09 is even more striking, since they do not share a single galaxy. Aside from local samples, we compare our candidates also to various samples of intermediate- and high redshift data (see Figs.5 and following). We used the recent intermediate redshift sample of Zahid et al. (2015), the classic high redshift sample of Damjanov et al. (2009), the new high redshift sample of Belli et al. (2014), and the catalogue of van de Sande et al. (2013), which contains a composition of various high redshift samples, such as Bezanson et al. (2013), van Dokkum et al. (2009), Onodera et al. (2012), Cappellari et al. (2009), Newman et al. (2010), van der Wel et al. (2008), Blakeslee et al. (2006), Toft et al. (2012), and their own work. We cannot perform a comparison with these datasets in every figure, because sometimes some samples do not contain the required parameters.

5.1. The fundamental plane

As illustrated in Figure 3, the fundamental plane is a tight relation for early-type galaxies and a good starting point for our investigation. According to Läsker et al. (2013), b19 is a clear outlier of the fundamental plane of Bernardi et al. (2003). In contrast to this, we found that b19 is only slightly more than 1-σ off the fundamental plane using the new coefficients listed in Appendix A, which are based on the work of Saulder et al. (2013). Furthermore, all candidate galaxies can be found clearly within 3-σ of the fundamental plane (see Figure 3). Almost all of them are located on the same side above the fundamental plane and are grouped in a similar region. The Ta10 sample is much more distributed over the fundamental plane than our sample. Some galaxies in the Ta10 sample are even beyond the 3-σ boundary on the opposite side to the clustering of our candidates. The Tr09 sample forms a relatively tight group around and beyond the 3-σ boundary at the opposite side of our candidate sample on the fundamental plane. The Ta10 sample appears to be distributed between the Tr09 sample and our sample, which are opposite extremes of the Ta10 sample distribution.
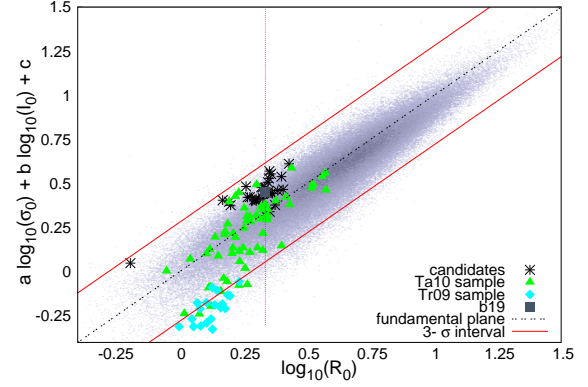
Figure 3. Location of the candidate galaxies on the fundamental plane. The candidates are indicated by black stars. The galaxies belonging to the Ta10 sample are represented using filled green triangles, and the Tr09 sample is denoted by filled cyan diamonds. B19, the starting point of our investigation, is indicated by a filled grey square. The magenta dotted lines show the limiting physical radius used in the sample sample selection. The black dashed lines are the fundamental plane fits from Appendix A with their corresponding 3-σ confidence intervals shown as red solid lines. The fit appears to be slightly offset due to the volume weights used to correct the Malmquist bias in the fitting process.

5.2. The colour-magnitude diagram
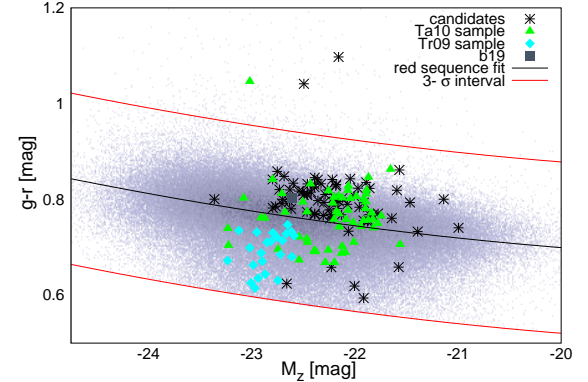
Figure 4. Distribution of the candidate galaxies in a colour-magnitude diagram. The galaxies belonging to the Ta10 sample are represented using filled green triangles, and the Tr09 sample is denoted by filled cyan diamonds. B19 is indicated by a filled grey square. The black dashed line represents the fit on the red sequence performed in Saulder et al. (2013) with the corresponding 3-σ confidence intervals shown as solid red lines.

In Figure 4, we plot the z band absolute magnitudes vs. the g-r colours. Galaxies in the colour-magnitude plane can generally be divided into two main groups: the red sequence and the blue cloud (Chilingarian & Zolotukhin 2012), which are only connected by a relatively sparsely populated 'green valley'. While the blue cloud is mainly composed of late-type galaxies, the red sequence mainly consists of early-type galaxies, such as the galaxies discussed in this paper. The selection criteria of our basic sample reduces the galaxies used in this paper to the red se-

11

quence. In Figure 4 we indicate the red sequence fit from Saulder et al. (2013) in the g-r colour vs. the absolute z band magnitude plane.

At a given absolute magnitude M_z, the galaxies of our candidate sample are systematically redder than the average red sequence galaxy by about 0.05 mag in g-r. At the same time, except for two outliers, all galaxies are well within 3-σ limits of the overall distribution, and there are only a few galaxies, which are blue than the average red sequence galaxy. Most of the galaxies of the Ta10 sample are also redder than the average and are associated to the grouping of galaxies from the candidates (see Figure 4). The systematic offset of our sample towards redder colours is consistent with a higher stellar metallicity than that of the average early-type galaxy at the same luminosity. All galaxies of the Tr09 sample are bluer than the average red sequence galaxy, which contrasts with our candidate sample.

5.3. The mass-size relations

In Figures 5 and 6, we plot the stellar masses and the dynamical masses, respectively, against the physical radii of the galaxies. Relations between the size and the mass of dynamically hot stellar systems are frequently used to distinguish them into different classes, as done, for example, in Misgeld & Hilker (2011) for dwarf galaxies vs. star clusters. Also bulges, large elliptical galaxies and similar objects can be found in very distinct areas of a mass-size diagram. The galaxies in which we are interested in this paper are early-type galaxies with small radii and relatively high masses. These galaxies are located on the edge of the so-called zone of exclusion (Burstein et al. 1997; Misgeld & Hilker 2011; Norris et al. 2014). This zone is empirically defined by a limit of stellar mass beyond which (most) hot stellar systems cannot grow at fixed sizes.

In Figure 5, one finds, in contrast to the previous figures, that there seems to be rough overall agreement on the distribution of our galaxies and the galaxies from Taylor et al. (2010) as well as our galaxies and the galaxies from Trujillo et al. (2009). We found that the galaxies from the Ta10 sample tend to contain less stellar mass for their sizes than our candidates. In contrast, the galaxies of the Tr09 sample tend to be more compact for their stellar masses than most of our galaxies. Almost all galaxies are at the edge of the distribution, as expected. When plotting the dynamical mass instead of the stellar mass against the scale radius (see Figure 6), the Ta10 and the Tr09 samples are detached from our candidates again. Since Figure 6 is basically a rescaled and tilted version of the selection criteria (see Figure 1), because of the definition of the dynamical mass (see Equation 11), it highlights the differences in the sample selection between this work and Taylor et al. (2010) as well as Trujillo et al. (2009), who used stellar masses, when compared to Figure 5. Over the course of this paper, we found that our selection criteria yield a more cohesive sample than the Ta10 sample or the Tr09 sample. The sample of Zahid et al. (2015) apparently contains many galaxies with larger radii than the low redshift samples. Most galaxies in the various high redshift samples can be found in areas close to our candidates and the other low redshift sample. They are located close to the edge of the zone of exclusion. A more detailed discussion of the differences between our sample and the samples of various other authors can be found in Sections 6.4 and 6.5.

5.4. The mass-to-light ratio

Since the starting point of our investigation, b19, is said (Läsker et al. 2013) to have a bottom-heavy initial mass function, the mass-to-light ratio Υ will contain valuable information for us. We investigated both the dynamical mass-to-light ratio Υ_{dyn} and the stellar mass-to-light ratio Υ_*. The dynamical mass-to-light ratio is derived directly from measured SDSS parameters using Equation 11, while the stellar mass-to-light ratio requires some additional modelling to derive the stellar masses, which was done by Mendel et al. (2014). They used a stellar population synthesis to derive the stellar masses from spectral energy distributions based on the SDSS broadband photometry.
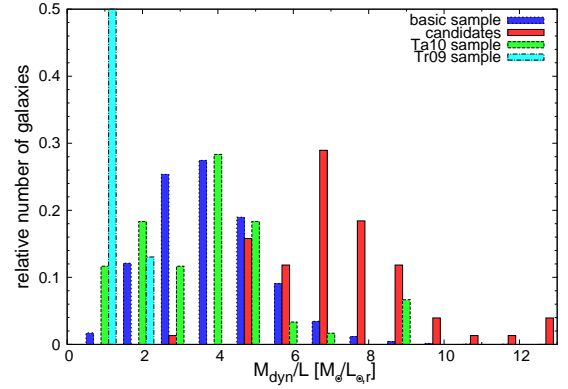
Figure 7. Distribution of the dynamical mass-to-light ratios Υ_{dyn}. The blue histogram corresponds to our basic sample, which consists of early-type galaxies alone. The green histogram represents the Ta10 sample, while the cyan histogram corresponds to Tr09 sample. The red histogram indicates our 76 candidates.
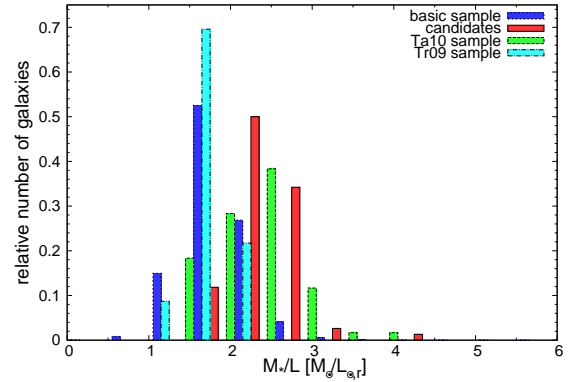
Figure 8. Distribution of the stellar mass-to-light ratios Υ_*. The blue histogram corresponds to our basic sample, which consists of early-type galaxies alone. The green histogram represents the Ta10 sample, while the cyan histogram corresponds to Tr09 sample. The red histogram indicates our 76 candidates.

Figures 7 and 8 illustrate the distribution of the r band dynamical and stellar mass-to-light ratios, respectively, for our candidate sample, the Ta10 sample, the Tr09 sample, and the ba-

12

Figure 5. Stellar mass-size relation for our basic sample and several other samples of compact massive early-type galaxies from the literature in comparison to our own data. The blueish cloud indicates the early-type galaxies of our basic sample. The black stars represent the candidates of our sample. The galaxies of the Ta10 sample are shown using filled green triangles and the galaxies of the Tr09 sample are denoted by filled cyan diamonds. The galaxies from Taylor et al. (2010), using the values of their paper, are indicated by open dark green triangles. The open blue diamonds represent the galaxies of Trujillo et al. (2009). Orange crosses mark the catalogue of various high redshift samples by van de Sande et al. (2013). The high redshift sample of Belli et al. (2014) is indicated by red Xs. Open brown nabla symbols mark the high redshift galaxies of Damjanov et al. (2009). Open magenta circles indicate the intermediate redshift sample of Zahid et al. (2015). NGC 1277 of van den Bosch et al. (2012), which is the only galaxy of their sample for which we have a stellar mass is represented by an filled violet circle. b19 using our calibration of SDSS data is shown by a filled grey square and b19 using the calibration of Läsker et al. (2013) is indicated by an open grey square. Because we use the values available in the literature to mark the positions of the galaxies in this plot, one has to consider potential systematics, especially in the effective radius R_0, which was measured in different filters by different authors. The dashed magenta line marks the limiting scaling radius for our sample selection.

sic sample. Comparing the mass-to-light ratios of our candidates to the basic sample, we found them clearly elevated. The average dynamical mass-to-light of the basic sample is 3.75 ± 0.46 $M_\odot/L_{\odot,r}$, and the average stellar mass-to-light of the basic sample is 2.07 ± 0.20 $M_\odot/L_{\odot,r}$. The average dynamical mass-to-light ratio of our candidate sample is 7.60 ± 2.45 $M_\odot/L_{\odot,r}$, which is about twice the number of the average of the basic sample. Also the average stellar mass-to-light ratio of our candidates is with, 2.66 ± 0.38 $M_\odot/L_{\odot,r}$, notably higher than the one of the basic sample. The average mass-to-light ratios of the Ta10 sample are, however, relatively close to the averages of the basic sample with a Υ_{dyn} of 3.81 ± 1.98 $M_\odot/L_{\odot,r}$ and a Υ_* of 2.27 ± 0.51 $M_\odot/L_{\odot,r}$. The average mass-to-light ratios of the Tr09 sample are extremely low: $\Upsilon_{dyn} = 1.15 \pm 0.31$ $M_\odot/L_{\odot,r}$ and $\Upsilon_* = 1.60 \pm 0.24$ $M_\odot/L_{\odot,r}$.

Conroy et al. (2013) show that there is an increasing difference between the dynamical and the stellar mass-to-light ratio for compact galaxies with higher central velocity dispersion using the same data (fits from Simard et al. (2011) and stellar masses from Mendel et al. (2014)). They argue that this indicates a systematic variation in the initial mass function. In Figure 9, we plot the ratio of dynamical over stellar mass against velocity dispersion. The increase in this ratio with increasing velocity dispersion is clearly visible. The area in Figure 9 below a logarithm of the dynamical-mass-to-stellar-mass ratio of zero is only sparsely populated, and most galaxies in that region are consistent with a log ratio of 0 thanks to measurement uncertainties (0.15 dex for the stellar masses according to Mendel et al. (2014)). The Ta10 sample is scattered widely over the general distribution with some galaxies even in the forbidden area,

while our candidates form the high end in Figure 9 owing to our selection criteria. We found that the galaxies of our sample have a M_{dyn} to M_* ratio as one might expect for galaxies with such high σ_0, following the general trend of the galaxy distribution in Figure 9. Galaxies of the basic sample with a central velocity dispersion between 323.2 and 400.0 km/s have $\log_{10}(M_{dyn}/M_*) = 0.432$, which is almost the same value as our candidates with $\log_{10}(M_{dyn}/M_*) = 0.441$. The vast majority of the Tr09 sample have M_{dyn} to M_* ratios below one and are thus located in a zone of exclusion, indicating possible problems in the measurement of the stellar masses of these galaxies. Although the galaxies of the various intermediate and high redshift samples are scattered widely the distribution of our basic sample, there is a tendency toward higher central velocity dispersion, but few of them reach values as high as our candidates.

In Figure 10, we plot the distribution of our sample in the dynamical mass vs. stellar mass plane. The difference between our own sample and the Ta10 sample becomes very clear in Figure 10. While the Ta10 sample has several objects with lower dynamical to stellar mass-to-light ratios, our galaxies are in general more massive in both dynamical and stellar mass, and they show a tendency for elevated dynamical mass compared to their stellar mass, as already shown in Figure 9. The Tr09 sample is again concentrated in what is normally a zone of exclusion, with formally higher stellar than dynamical masses.

13
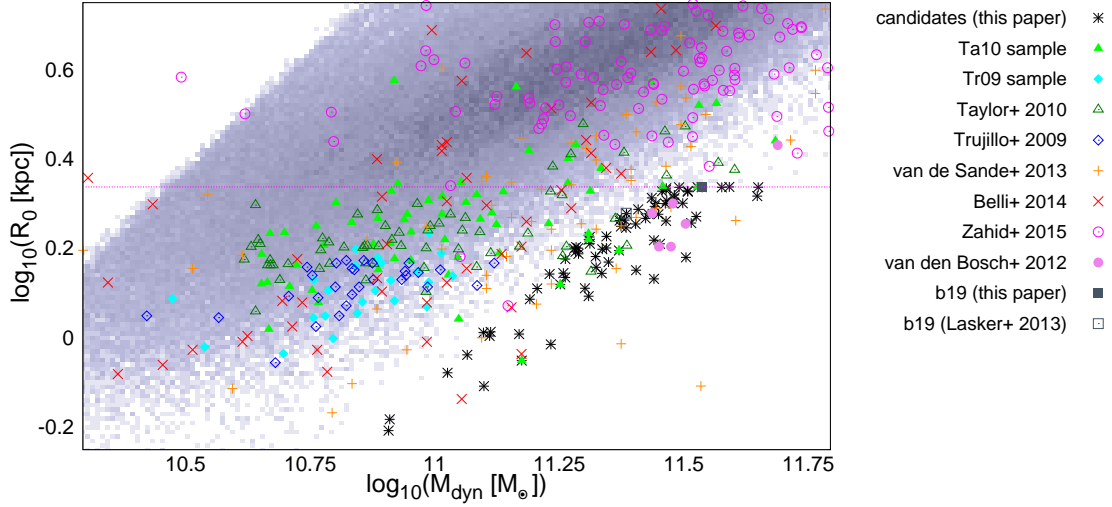
Figure 6. Dynamical mass-size relation for our basic sample and several other samples of compact massive early-type galaxies from the literature in comparison to our own data. The blueish cloud indicates the early-type galaxies of our basic sample. The black stars represent the candidates of our sample. The galaxies of the Ta10 sample are shown using filled green triangles and the g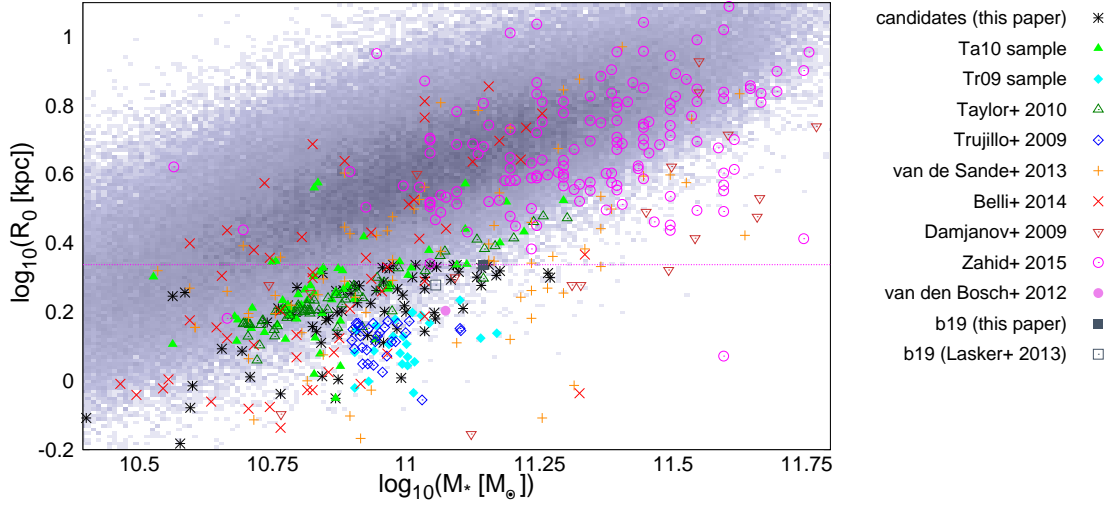alaxies of the Tr09 sample are marked by filled cyan diamonds. The galaxies from Taylor et al. (2010) using the values of their paper are indicated by open dark green triangles. The open blue diamonds represent the galaxies of Trujillo et al. (2009). Orange crosses mark the catalogue of various high redshift samples by van de Sande et al. (2013). The high redshift sample of Belli et al. (2014) is indicated by red Xs. We do not have dynamical masses for the high-redshift sample of Damjanov et al. (2009). However we can calculate dynamical masses for the intermediate-redshift sample of Zahid et al. (2015), which is indicated by open magenta circles. The six galaxies of van den Bosch et al. (2012) are represented by filled violet circles. b19 using our calibration of SDSS data is shown by a filled grey square and b19 using the calibration of Läsker et al. (2013) is indicated by an open grey square. Because we use the values available in the literature to mark the positions of the galaxies in this plot, one has to consider potential systematics, especially in the effective radius R_0, which was measured in different filters by different authors. The dashed magenta line denotes the limiting scaling radius for our sample selection.

5.5. Sersic indices

Thanks to the SDSS refits from Simard et al. (2011), we have Sersic profiles for almost all SDSS galaxies. In Figure 11, we compare the Sersic indices of different samples. It should be pointed out that the algorithm used by Simard et al. (2011) only allows a maximum Sersic index n=8, so we have some clustering around this value for all samples. In Figure 11 there is a clear difference between our basic sample, which only consists of red sequence galaxies because of the colour cut and GalaxyZoo classification (Lintott et al. 2011) used in its selection, and the sample of all SDSS DR7 galaxies, that qualified for the refits done by Simard et al. (2011), which thereby consists of a mixed population. The early-type galaxies have clearly higher Sersic indices than the full SDSS DR7 sample. The Ta10 sample and our 76 candidates do not show any significant peculiarities compared to the distribution of the Sersic indices of the basic sample, except for a less smooth distribution due to small number statistics and a weak trend toward higher Sersic indices. The Tr09 sample shows an outstanding peak in its distribution around a Sersic index of 4.5, but is otherwise in agreement with our basic sample. The sample of Belli et al. (2014) shows a preference for lower Sersic indices in contrast to all other samples.

5.6. Semi-axis ratios

We investigate the distribution of the semi-minor to semi-major axis ratios $q_{b/a}$ of our sample and the samples that we used for comparison. A ratio of 1 indicates a perfectly round galaxy, and the value decreases to zero for increasing ellipticity of

the galaxy. Our candidates are clearly more elongated than the galaxies of our basic sample. The Ta10 sample appears to be rounder than the basic sample, but the Tr09 contains several galaxies with high ellipticity (higher than our sample), but also a larger number of very round galaxies than our sample. The sample of Belli et al. (2014) seems to contain on average rounder galaxies than our candidate sample.

6. Discussion

We started our investigation with b19, which is known to be a very compact massive elliptical galaxy in SDSS in the local universe (Läsker et al. 2013). In this paper, we identify a sample of 76 galaxies (including b19) that have similar global properties, with dispersions of $\sigma_0 > 323.2$ km s^{-1} and sizes smaller than $R_0 < 2.18$ kpc. These selection criteria, which are described in detail in section 4, place these objects at the edge of the $\log_{10}(R_0)$-$\log_{10}(\sigma_0)$.

6.1. Global properties

Our candidate sample forms a relatively homogeneous group in most of the scaling relations and parameter spaces we investigated. The observed parameters (see Table 2), such as the observed apparent magnitude m_{sdss}, the angular semi-major axis a_{sdss}, and the central velocity dispersion σ_{sdss}, are in a range where SDSS measurements are reliable (statistical error of less than 4%).

We found that all our candidate galaxies are located within the 3-σ limits of the fundamental plane using the new coeffi-

14
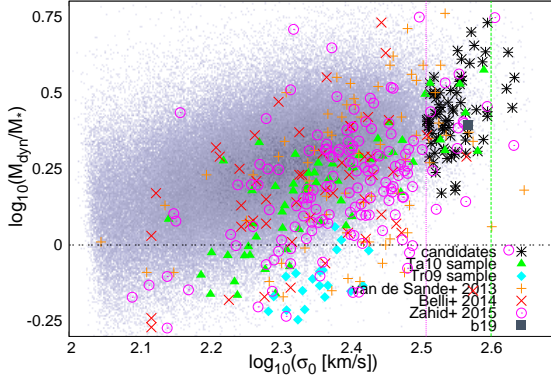
Figure 9. Dependence of the dynamical mass M_{dyn} to stellar mass M_* ratio on central velocity dispersion σ_0. The candidates are indicated by black stars. The galaxies belonging to the Ta10 sample are represented using filled green triangles, and the Tr09 sample is indicated by filled cyan diamonds. Orange crosses indicate the catalogue of various high redshift samples by van de Sande et al. (2013). The high redshift sample of Belli et al. (2014) is indicated by red Xs. The intermediate redshift sample of Zahid et al. (2015) is indicated by open magenta circles. B19 is indicated by a filled grey square. The magenta dashed line marks the limiting scaling central velocity dispersion for our sample selection. The green dashed line indicates a central velocity dispersion of 400 km/s. The area below the black dashed line is considered to be unphysical, because M_* would exceed M_{dyn}.
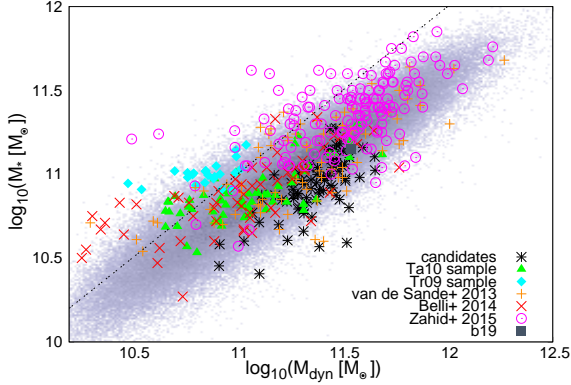
Figure 10. Distribution of the sample's galaxies in the dynamical mass M_{dyn} vs. stellar mass M_* plane. The candidates are indicated by black stars. The galaxies belonging to the Ta10 sample are represented using filled green triangles, and the Tr09 sample is indicated by filled cyan diamonds. Orange crosses indicate the catalogue of various high redshift samples by van de Sande et al. (2013). The high redshift sample of Belli et al. (2014) is indicated by red Xs. The intermediate redshift sample of Zahid et al. (2015) is indicated by open magenta circles. B19 is indicated by a filled grey square. The magenta dashed line marks the limiting scaling central velocity dispersion for our sample selection. The black dashed line marks the limit of the M_{dyn} to M_* ratio, which is still considered to be physical, because above it M_* would exceed M_{dyn}.

cients listed in Appendix A. They occupy the same corner of the overall distribution of the galaxies on the fundamental plane (see Figure 3), indicating that our candidates are more compact than the average galaxy with similar surface brightness and central velocity dispersion.
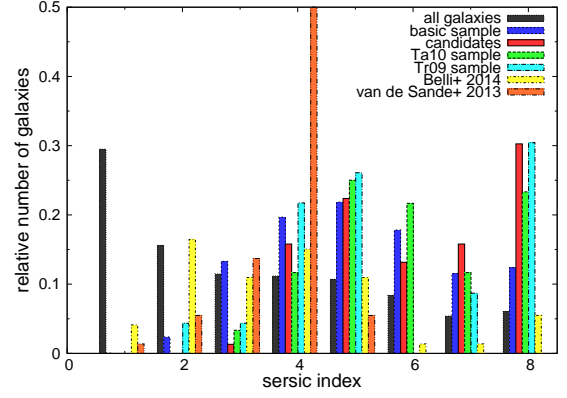
Figure 11. Distribution of the Sersic indices of different samples of galaxies. The black histogram corresponds to all galaxies in SDSS DR7 for which Simard et al. (2011) did their refits. The blue histogram corresponds to our basic sample, which consists of early-type galaxies alone. The green histogram represents the Ta10 sample, and the cyan histogram the Tr09 sample. The yellow histogram corresponds to sample of Belli et al. (2014) and the orange histogram indicated the distribution of the sample of van de Sande et al. (2013). The red histogram shows our 76 candidates.
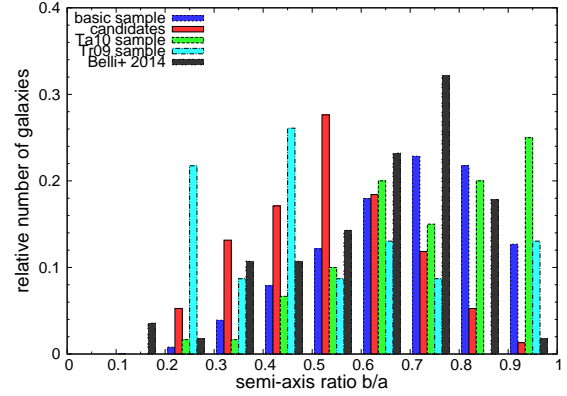
Figure 12. Distribution of the semi-minor to semi-major axis ratios $q_{b/a}$ of different samples of galaxies. The blue histogram corresponds to our basic sample. The green histogram represents the Ta10 sample, and the cyan histogram the Tr09 sample. The black histogram corresponds to sample of Belli et al. (2014). The red histogram shows our 76 candidates.

Our candidates are also redder than the average early-type galaxies, suggesting metallicity enhancements compared to less compact galaxies at the same luminosity. The vast majority of them can be found above our fit on the red sequence in the CMD diagram (see Figure 4), but still within the 3-σ limits (except for two very red outliers).

When analysing the mass-size relations, we found that the galaxies of the candidate sample are located within or close to the zone of exclusion (Burstein et al. 1997; Misgeld & Hilker 2011; Norris et al. 2014). This is a direct consequence of the sample's definition, because we were looking specifically for galaxies in this area. We wanted the most massive galaxies for their given small sizes, and Figures 5 and 6 illustrate nicely that we got them. One should keep in mind that the sizes may carry

15

an additional systematic uncertainty, because the intrinsic angular sizes of our galaxies are close to the size of the SDSS PSF.

We found that both the stellar and the dynamical mass-to-light ratios of our candidates are elevated compared to the rest of the sample. Figure 9 illustrates that there is an increasing difference between the stellar masses and the dynamical masses with increasing central velocity dispersion σ_0 as reported in Conroy et al. (2013). Since we specifically selected for high central velocity dispersion galaxies, the candidates belong to the high σ_0 tip of this correlation. Our galaxies have not only high stellar and dynamical masses for their small sizes, but also high dynamical masses for their given stellar mass as illustrated in Figure 10.

As shown in Figure 11, our sample does not have any significant difference in their Sersic indices compared to regular early-type galaxy. Figure 12 shows that our candidate galaxies have a higher ellipticity than the galaxies of the basic sample. In the context of the SAURON results (Krajnović et al. 2008; Cappellari et al. 2007; Emsellem et al. 2007), we interpret these results such that most of our our candidates are lenticular galaxies that host a significant disc component. This result is consistent with the observation that red nuggets are disc-dominated (van der Wel et al. 2011; Chevance et al. 2012).

6.2. Comparison to the Ta10 sample

The most important difference between our candidate sample and the sample of Taylor et al. (2010) is the way in which it was selected. Taylor et al. (2010) selected their sample using a colour cut demanding that their galaxies be redder than than 2.5 in $^{0.1}(u\text{-}r)$[5], and they also restricted their sample to have a minimum stellar mass of $10^{10.7} M_\odot$. Furthermore, their galaxies have to be located between the redshifts of 0.066 and 0.12, while our candidate sample allows redshifts up to 0.4, although we did only detect one galaxy beyond 0.2. When cross-matching their 63 galaxies with our own basic sample, we found 60 galaxies. These 60 galaxies, the so-called Ta10 sample, are listed with their parameters in Tables C.2 and C.3. There are only five galaxies that are shared between the Ta10 sample and our candidate sample (see Table C.1), the galaxies with the internal IDs 6, 13, 39, 52, and 53. We attribute the difference between our candidates and the Ta10 sample to the different selection criteria and want to point out that most of our galaxies tend to contain more stellar mass and definitely more dynamical mass for their sizes than the galaxies of the Ta sample.

In general, we found that the galaxies of the Ta10 sample occupy different regions in the various considered scaling relations and diagrams than our candidate galaxies. Furthermore, they are a less homogeneous sample than the galaxies presented in this paper. In a stellar mass-size diagram (see Figure 5), they occupy a very similar corner to our candidates, although they are less massive for their size than a large portion of our galaxies. Their distribution in this specific diagram is restricted to a small region, which is a consequence of the selection criteria for this sample. Figure 5 also contains the positions in the stellar mass-size plane of all galaxies of Taylor et al. (2010) using the parameters of their paper. They occupy a similar area in that plot. Comparing Figures 5 and 6 highlights the difference between the Ta10 sample and our candidates owing to their selection criteria. We found that the galaxies of the Ta10 sample largely behave like average early-type galaxies, while our candidates always occupy off-average regions in the parameter space, because they are in the extreme tail of the general distribution of early-type

galaxies. We note, though, that there is a small overlap of the parameter range occupied by the Ta10 sample with our sample, as seen in the various plots provided in this paper.

6.3. Comparison to the Tr09 sample

While the Ta10 sample still has a small overlap with the parameter range of our candidates, the Tr09 sample behaves totally differently from our candidate sample in most scaling relations. The Tr09 does not have a single galaxy in common with our sample or the Ta10 sample.

The galaxies of the Tr09 are bluer than almost all our candidates (see Figure 4), related to their indeed being bluer than the average red sequence galaxies, and some are close to the green valley. This is certainly connected to the younger stellar ages that Trujillo et al. (2009) derived for their sample of 29 "superdense massive galaxies".

The Tr09 sample occupies a different region on the fundamental plane (see Figure 3) around and beyond the $3 - \sigma$ limit, rendering their galaxies outliers on the opposite side to our sample. The galaxies of Tr09 sample have stellar masses comparable to our galaxies (see Figure 5), but lower dynamical masses (see Figure 6), which are comparable to those of the Ta10 sample. This and the fact that they have very low mass-to-light ratios (see Figures 7 and 8) indicate a potential problem. As illustrated in Figure 9 and more clearly in Figure 10, the galaxies of the Tr09 sample appear to contain more stellar mass than dynamical mass, which hints at stellar population peculiarities in these objects. The stellar masses that we used have uncertainties of about 40%. We know that these galaxies are very young (about 2 Gyr (Trujillo et al. 2009)). It seems reasonable to assume that the contrast between the young Tr09 sample and our candidate galaxies may indicate that our sample contains old objects, which are true survivors of the red nuggets from the early universe.

6.4. Comparison to other local samples

Aside from the comparison to the Ta10 and the Tr09 samples, we cross-matched our data with other samples of compact massive early-type galaxies as well. A visual comparison of the location of compact massive early-type galaxies from different authors on the stellar mass-size plane is provided in Figure 5. We only have the stellar mass of one galaxy in the sample of van den Bosch et al. (2012), namely NGC 1277, which is located next to the bulk of our sample and b19 in the plot, and it is even one of the denser objects of our sample. None of our candidates has been covered by the HETMGS (van den Bosch et al. 2015). The other samples using galaxies from the local universe (ours, Trujillo et al. (2009), and Taylor et al. (2010)) occupy a distinct region in the stellar mass-size plane at the edge or within the zone of exclusion (Burstein et al. 1997; Misgeld & Hilker 2011; Norris et al. 2014), but with only a small overlap between the individual samples.

As a visual comparison of the different samples in the dynamical mass-size plane, Figure 6 shows that the samples of Taylor et al. (2010) (the Ta10 sample and the one with the parameters from their paper) and Trujillo et al. (2009) (the Tr09 sample and the one with the parameters from their paper) are distributed in a large area of the plot partially overlapping. Although small, they are clearly less massive than the galaxies of our sample. The six galaxies of van den Bosch et al. (2012) are within the compact distribution of our candidates in the dynamical mass-size

---

[5] This denotes the SDSS u-r band colour at a redshift of 0.1

plane, which agrees with our intention to find galaxies similar to them and b19. In Figures 5 and 6, there may be small systematic deviations between the different samples because the effective radii were measured in different filters. While our sample and the Ta10 samples uses the r band, the sample of Taylor et al. (2010) was measured in the i band, the sample of Trujillo et al. (2009) was measured in the z band and the Tr09 sample uses the r band, and the sample of van den Bosch et al. (2012) was measured in the K band. Our candidates in the redder SDSS bands are smaller than what we measured in the r band by an average of 0.30 kpc ($\sim$ 14%) in the z band and 0.11 kpc ($\sim$ 5%) in the i band. This suggests that at least the points of the samples of Taylor et al. (2010) and Trujillo et al. (2009) are shifted downwards a little bit in relation to the r band measured points of our sample, the Ta10 sample, and the Tr09 sample in Figures 5 and 6.

Since b19 was first analysed in Bernardi et al. (2008), we have cross-matched our candidate sample with their list of 43 massive early-type galaxies. Although they also selected their sample by high central velocity dispersion, the only other galaxy in common with our candidate sample, aside from b19, is b17, which has the internal ID 3. However, they do not impose any restriction on the effective radii of their sample, and only a fraction of our sample can match their minimum σ_0 of 350 km/s. Furthermore, the redshifts of most of their galaxies are higher than of the galaxies in our sample, and small galaxies will not be resolved and detected any more at this distance. The sample of Bernardi et al. (2008) is also a subset of SDSS DR1 (Abazajian et al. 2003), which covered a much smaller area of the sky than SDSS DR10, which we used. An interesting result of their paper was that almost half (20 out of 43) of their sample of high-σ_0 galaxies are either superposition of two or more galaxies, which is something to consider in the light of follow-up observations.

6.5. Comparison to intermediate and high redshift samples

We compared our candidates and the other low redshift samples to various intermediate and high redshift samples. We found quite some difference between them and the local samples, but also between the different high redshift samples themselves. Our candidate sample corresponds best to the subsample of the catalogue of van de Sande et al. (2013) with high dynamical masses.

We used a very recent sample of compact massive galaxies at intermediate redshifts of Zahid et al. (2015), which is based on COSMOS results (Damjanov et al. 2015). Their galaxies are in general more massive, but also less compact than ours. A large number of them are located at the edge of or within the zone of exclusion, as can been seen in comparison to our basic sample in Figure 5. They seem to form an extension of our sample and the other low redshift sample, but restricted to higher masses and larger radii. As illustrated in Figure 6, the intermediate redshift sample of Zahid et al. (2015) contains galaxies of similar (and also higher) dynamical masses to our candidates, but they are generally less compact than our galaxies or other low redshift samples. In Figure 10, the galaxies of Zahid et al. (2015) tend to be more massive than ours and behave like the more massive galaxies of the basic sample. In Figure 9, they show a tendency to higher central velocity dispersion than does the basic sample, but few of them reach values that are as high as ours.

We used a variety of high redshift samples for comparison, such as the classic high redshift sample of Damjanov et al. (2009), the new high redshift sample of Belli et al. (2014), and the catalogue of van de Sande et al. (2013), which contains a composition of various high redshift samples, such as Bezanson

et al. (2013), van Dokkum et al. (2009), Onodera et al. (2012), Cappellari et al. (2009), Newman et al. (2010), van der Wel et al. (2008), Blakeslee et al. (2006), Toft et al. (2012), and their own work. In the size-stellar mass plane (see Figure 5), all the high redshift samples are distributed along the edge of the zone of exclusion with some objects deeper in to it than any of the low redshift samples. The sample of Belli et al. (2014) consists of more compact and lower mass objects to which the low redshift samples match best. Although the van de Sande et al. (2013) sample is distributed over a wider range of masses, a significant fraction of it shares the same areas with our low redshift samples. The sample of Damjanov et al. (2009) mainly consists of higher mass galaxies, which are on average deeper in the zone of exclusion than the other high redshift samples. Things look differently in the size-dynamical mass plane (see Figure 6). The galaxies of Belli et al. (2014) take less extreme positions than our candidates in this diagram. However, the Belli et al. (2014) galaxies agree well with the low redshift samples of Taylor et al. (2010) and Trujillo et al. (2009). The sample of van de Sande et al. (2013) contains galaxies with higher dynamical masses and many of its most massive and most compact members agree well with our candidate sample and the sample of van den Bosch et al. (2012).

When analysing Figure 10, we get a similar result. The sample of Belli et al. (2014) agrees well with Ta10 sample, while a large number of galaxies from the van de Sande et al. (2013) catalogue can be found around our candidates. We have to bear in mind that van de Sande et al. (2013) report a decrease in $M_*/M_{\rm dyn}$ over time, which would explain the shift of our candidates in relation to most of the high redshift sample. In Figure 9, the high redshift samples are all over the place. There are some tendencies towards higher central velocity dispersions for them, but only a few galaxies (from the van de Sande et al. (2013) sample) posses as high values as our candidates. The distribution of the Sersic indices of the Belli et al. (2014) sample is different from the low redshift sample, since it favours lower values for the Sersic indices as illustrated in Figure 11. The Sersic indices of the van de Sande et al. (2013) catalogue strongly peak at four, which is the value for de Vaucouleurs profiles. Since the van de Sande et al. (2013) catalogue is a composite of various high redshift samples, where not all of them performed a Sersic model fit, but only a de Vaucouleurs fit, this result is not surprising. As illustrated in Figure 12, the galaxies of the high redshift sample of Belli et al. (2014) are also slightly rounder than our candidates or the Tr09 sample, but not as round as the galaxies of the Ta10 sample.

After this comprehensive analysis, we conclude that the various high redshift samples do not form a very uniform group and that there are differences between the various samples, which raises the question of whether this is due to systematic differences between selection and fitting methods applied to the samples (discussed in van de Sande et al. (2013)) or to the red nuggets themselves being a relatively diverse population. Furthermore, none of the low redshift samples agrees in every aspect with the high redshift data. However, one has to keep in mind that ten billion years lie between them, in which the red nuggets may have undergone significant changes.

We explored the connections of our candidate sample to compact galaxies at higher redshifts in Figure 13 further, where for reasons of comparability, we plot only galaxies whose stellar masses lie between $10^{10.75} M_\odot$ and $10^{11.25} M_\odot$. It is highlighted in the plot that our candidates are indeed amongst the most compact galaxies of the stellar mass range in SDSS and indeed border the resolution limit of SDSS. We adopt a value of 0.50 arcsec for the observed Vaucouleurs radii in the SDSS r band as resolu-

17
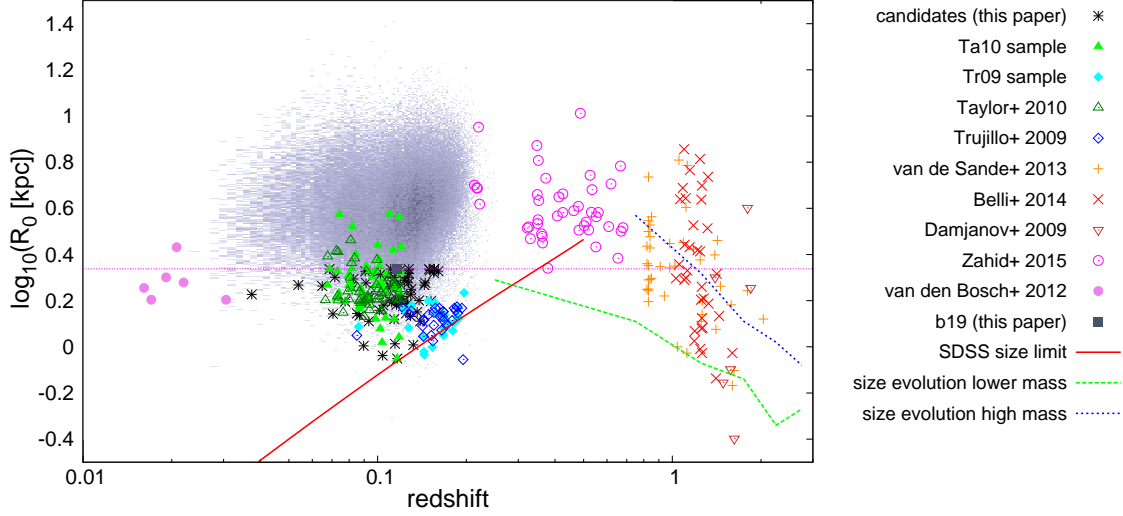
Figure 13. Redshift vs. size distribution for galaxies of different samples within a stellar mass range between $10^{10.75} M_\odot$ and $10^{11.25} M_\odot$. The blueish cloud in the background represents all galaxies of the basic sample with stellar masses greater than $10^{10.75} M_\odot$ and less than $10^{11.25} M_\odot$. The black stars represent the candidates of our sample. The galaxies of the Ta10 sample are shown using filled green triangles and the galaxies of the Tr09 sample are indicated by filled cyan diamonds. The galaxies from Taylor et al. (2010) using the values of their paper are indicated by open dark green triangles. The open blue diamonds represent the galaxies of Trujillo et al. (2009). Orange crosses denote the catalogue of various high redshift samples by van de Sande et al. (2013). The high redshift sample of Belli et al. (2014) is indicated by red Xs. Open brown nabla symbols indicate the high redshift galaxies of Damjanov et al. (2009). Open magenta circles indicate the intermediate redshift sample of Zahid et al. (2015). The six galaxies of van den Bosch et al. (2012) are represented by filled violet circles. Using our calibration of SDSS data, b19 is shown by a filled grey square. The magenta dashed line denotes the limiting scaling radius for our sample selection. The red solid line corresponds to the angular resolution limit of SDSS of 0.50 arcsec. The green dashed line denotes the 16-percentile range of the redshift evolution of an early-type galaxy with a stellar masses of $10^{10.75} M_\odot$ according to Table A1 of van der Wel et al. (2014b) and the blue dotted line indicates the 16-percentile range of the redshift evolution of an early-type galaxy with a stellar masses of $10^{11.25} M_\odot$ based on the same work.

tion limit, which is the lower lower 3-σ-limit of all angular sizes (de Vaucouleurs radii) of early-type galaxies in SDSS. The Ta10 sample and the original values of Taylor et al. (2010) can both be found in the same region of the plot as our candidates, but at slightly lower redshifts. The Trujillo et al. (2009) sample (and naturally the Tr09 sample) appears to be around and partly even beyond the resolution limits of SDSS.

The galaxies of van den Bosch et al. (2012) are much nearer than the galaxies of any other sample and would be beyond the saturation limit of SDSS. The nearest galaxies of our candidate sample can be found close to them. The new intermediate redshift sample of Zahid et al. (2015) mainly contains larger galaxies than the other samples, but their most compact objects are on the expected evolutionary path of the most compact high redshift objects on the way to our candidates. The high redshift samples of Damjanov et al. (2009), Belli et al. (2014), and van de Sande et al. (2013) contain many galaxies that are as compact as the most compact galaxies in the local universe, while containing more mass at the same time. We included the redshift evolution of early-type galaxies of the two highest mass bins from van der Wel et al. (2014b) in our plot. The 16-percentile range of the redshift evolution of an early-type galaxy with a stellar masses of $10^{10.75} M_\odot$ (only 16% of all early-type galaxies at this mass range are more compact than indicated by the line) shows a connection between the two of the most compact galaxies of various high redshift samples, the most compact galaxies of the intermediate redshift sample of Zahid et al. (2015), and our candidates (if extrapolated to the redshift ranges of our sample).

The 16-percentile range of the redshift evolution of an early-type galaxy with a stellar masses of $10^{11.25} M_\odot$ only extends

down to a redshift of 0.75 in van der Wel et al. (2014b), because for some unknown reason, the value at a redshift of 0.25 for this percentile and mass is missing in their table for circularized radii, but an educated guess based on the other values and other tables would yield a value of $\log_{10}(R_0) \sim 0.6$. The stellar masses of almost all of our candidates range between $10^{10.75} M_\odot$ and $10^{11.25} M_\odot$ (we only plotted those within that range in Figure 13), which means that when comparing with the extrapolation of the redshift evolution of van der Wel et al. (2014b), we found that our candidates are clearly amongst the most compact galaxies of their mass range and that they may be relics of the red nuggets.

6.6. Space density

We calculated the space density of candidate sample considering the Malmquist-bias and a resolution limit of 0.50 arcsec (lower 3-σ-limit). The value that we obtained this way is $4 \cdot 10^{-7}$ galaxies/Mpc^3, which is about 400 times lower than the space density of red nuggets at $z = 2$ (Quilis & Trujillo 2013). However, when comparing space densities of different samples, one has to be aware of the selection criteria used to define them and biases affecting them. Our sample only contains one galaxy above a redshift of 0.2, while the rest are clearly below it. This is a consequence of the selection bias from using spectroscopic data from SDSS. Galaxies with very small angular sizes (below the resolution limit mentioned above) are not included in the basic sample, which explains the dearth of compact galaxies at higher redshifts in our sample. Most samples (Trujillo et al. 2009; Taylor et al. 2010; Quilis & Trujillo 2013) use stellar

18

masses as a selection criterion. We tried to derive more comparable quantities by considering additional selection criteria for our candidate galaxies, which are similar to the selection criteria of other authors. We restricted our candidate sample to dynamical masses greater than $8 \cdot 10^{10} M_\odot$ and physical radii of less than 2 kpc to be better comparable with the predication for old (formed before a redshift of 2) compact massive galaxies by Damjanov et al. (2014). Fifty-eight of 76 galaxies in the candidate sample fulfil this condition, and they obtain a space density of $3.6 \cdot 10^{-7}$ galaxies/Mpc^3 for our sample, which is located at redshifts below 0.2. The lowest redshift interval considered in Damjanov et al. (2014) is 0.2 to 0.3, and they predict a space density of $2.6^{1.2}_{2.4} \cdot 10^{-7}$ galaxies/Mpc^3, which is about seven times higher than ours.

For our comparison with the space density of Trujillo et al. (2009), we applied the same restriction as they do on our candidate sample. The stellar masses have to be higher than $8 \cdot 10^{10} M_\odot$, and the z band physical radii smaller than 1.5 kpc. This reduces our candidate sample to merely 16 galaxies, and we obtained a space density for them of $5.9 \cdot 10^{-8}$ galaxies/Mpc^3, which is by more than a factor of two lower than the upper limit of the space density of Trujillo et al. (2009), which is $1.3 \cdot 10^{-7}$ galaxies/Mpc^3 (Quilis & Trujillo 2013). Comparing to space densities to the Taylor et al. (2010) is more difficult due to their definition. We only considered their restriction that the stellar masses have to be higher than $10^{10.7} M_\odot$. Hence the space density, which we derived using a subsample of 67 galaxies of our candidates, is an upper limit. We obtained a value of $2.7 \cdot 10^{-7}$ galaxies/Mpc^3, which is almost an order of magnitude higher than the value of Taylor et al. (2010) of $3 \cdot 10^{-8}$ galaxies/Mpc^3 (Quilis & Trujillo 2013). We thus found that the space densities we derived are comparable within an order of magnitude to those of other samples in the local (and intermediate redshift) universe, but we refrain from a strong interpretation of our numbers compared to the high redshift universe given the dominating influence of selection effects on the results.

6.7. Individual galaxies

Although the candidate galaxies form a very homogeneous group in all their properties, one can identify particularly peculiar objects by focusing on some individual galaxies. There are seven galaxies in our sample with radii less than a kpc. The smallest one has the internal ID 63 and a physical radius of $R_0 = (0.62 \pm 0.01)$ kpc. At its redshift of 0.0877, this means that the observed angular semi-major axis a_sdss is only (0.47 ± 0.01) arcsec and therefore at the limit of SDSS resolution. Galaxy 63 also happens to be the second faintest object of our sample, with an r-band absolute magnitude of (-20.51 ± 0.01), and it has the lowest surface brightness with (17.12 ± 0.05) mag/arcsec^2 in the r band. The galaxy also stands out by its mass: it possesses the lowest dynamical mass of our candidates with $M_\mathrm{dyn} = (8.13 \pm 0.38) \, 10^{10} M_\odot$ and the second lowest stellar mass of our sample with $M_* = (2.82 \pm 1.16) \, 10^{10} M_\odot$. By being a peculiarly compact and faint, but also relatively low mass object in our sample, we consider galaxy 63 as one of the most interesting objects for our follow-up observations.

The other extremely small objects in our sample show similar properties to galaxy 63. The faintest object with an absolute r-band magnitude of only (-20.35 ± 0.02) is, with a physical radius of $R_0 = (0.78 \pm 0.02)$ kpc, also the third smallest galaxy in the candidate sample. It has an internal ID of 31 and is located at a redshift of 0.0784. Galaxy 31 is with an ob-

served angular semi-major axis a_sdss of only (0.64 ± 0.02) arcsec one of the galaxies close to the resolution limit of SDSS. Although this galaxy has the lowest stellar mass of our candidate sample with $M_* = (2.57 \pm 1.06) \, 10^{10} M_\odot$, its dynamical mass $M_\mathrm{dyn} = (1.25 \pm 0.06) \, 10^{11} M_\odot$ is fairly average for our candidate sample. In combination with the fact that it is the faintest galaxy, this results in a relatively high dynamical mass-to-light ratio of $\Upsilon_\mathrm{dyn} = (11.99 \pm 0.82) M_\odot / L_{\odot,\mathrm{r}}$. This makes it a promising object for follow-up observations.

At the other extreme of the angular sizes, we have our three best-resolved galaxies with a_sdss greater than 3 arcsec. The galaxy with an internal ID of 75 is with an angular semi-major axis of (3.59 ± 0.02) arcsec not only the apparently biggest object in the sky of our candidate sample, but also the nearest. It is located at a redshift of 0.0260. Galaxy 75 is also outstanding because it has the by far highest dynamical mass-to-light ratio of our sample with $\Upsilon_\mathrm{dyn} = (20.56 \pm 2.13) M_\odot / L_{\odot,\mathrm{r}}$ and, with 0.51 (which is just over the selection criterion of 0.50), the lowest GalaxyZoo probability $\mathcal{L}_\mathrm{ETG}$ for a galaxy to be classified as an early type within our sample. A visual inspection of the galaxy (see Figure 2) shows a face-on featureless disc, which differs from the other candidate galaxies. A manual analysis of the SDSS classification of its spectrum confirms our suspicion that this galaxy is no regular early-type galaxy, but rather a starburst galaxy. We therefore consider it a false positive in our sample.

The next largest galaxy in angular size has the internal ID 50, which also happens to be, with a redshift of 0.0374, the second nearest candidate galaxy. It possesses a physical radius of $R_0 = (1.69 \pm 0.01)$ kpc and an absolute r-band magnitude of (-21.56 ± 0.01). With a dynamical mass of $M_\mathrm{dyn} = (2.24 \pm 0.05) \, 10^{11} M_\odot$, a stellar mass of $M_* = (8.13 \pm 3.35) \, 10^{10} M_\odot$, and no outstanding mass-to-light ratios, galaxy 50 is an average example of our candidates. Its low redshift allows for easier follow-up observations of this object, so we rank it as one of our priority candidates.

The brightest galaxy in our sample has the internal ID 66 and shines with an absolute magnitude of (-22.69 ± 0.01) mag in the r band. It is located at a redshift of 0.2018[6] and is therefore the most distant galaxy of our candidates. It has a physical radius of $R_0 = (2.06 \pm 0.08)$ kpc and is one of the largest candidates. Galaxy 66 possesses a dynamical mass of $M_\mathrm{dyn} = (2.75 \pm 0.20) \, 10^{11} M_\odot$, and it stands out with the second highest stellar mass of our candidates with $M_* = (1.86 \pm 0.77) \, 10^{11} M_\odot$. Another outstanding property of galaxy 66 is its dynamical mass-to-light ratio of $\Upsilon_\mathrm{dyn} = (3.03 \pm 0.19) M_\odot / L_{\odot,\mathrm{r}}$ is the lowest of our candidate sample, and we found that is also has the fifth lowest stellar mass-to-light ratio with $\Upsilon_* = (2.05 \pm 0.84) M_\odot / L_{\odot,\mathrm{r}}$. We consider galaxy 66 a priority candidate for follow-up observations, although its high redshift will make them more difficult, but on the other hand the high luminosity of the galaxy will help a bit.

The galaxy with the highest stellar mass has the internal ID 56. It has a stellar mass of $M_* = (1.91 \pm 0.79) \, 10^{11} M_\odot$ and a dynamical mass of $M_\mathrm{dyn} = (2.95 \pm 0.28) \, 10^{11} M_\odot$. The galaxy with a physical radius of $R_0 = (2.00 \pm 0.14)$ kpc is also the second most distant candidate with a redshift of 0.1978. It is the second reddest object with a g-r colour of (1.04 ± 0.03) mag, which makes it one of only two outliers of our candidate sample above the upper $3 - \sigma$ limit of the red sequence. Galaxy 56 also stands out for having the highest stellar mass-to-light ratio of our candidate sample with $\Upsilon_* = (4.27 \pm 1.77) M_\odot / L_{\odot,\mathrm{r}}$. This

---

[6] It is also the only galaxy beyond a redshift of 0.2 in our candidate sample.

and its average dynamical mass-to-light ratio of $\Upsilon_{dyn} = (6.67 \pm 0.71) M_\odot/L_{\odot,r}$ contrasts it with the previously discussed galaxy 66. Galaxy 56 is a very interesting object and qualifies as priority target for our follow-up observations.

The galaxy with the highest dynamical mass has the internal ID 23. It contains a stellar mass of $M_* = (1.10 \pm 0.45)\,10^{11} M_\odot$ and a dynamical mass of $M_{dyn} = (4.57 \pm 0.22)\,10^{11} M_\odot$. This is due to its high central velocity dispersion of $\sigma_0 = (423 \pm 17)$ km s^{-1} and its relatively large physical radius $R_0 = (2.17 \pm 0.04)$ kpc, which is close to the limit of our sample selection. Galaxy 23 has the fourth highest dynamical mass-to-light ratio with $\Upsilon_{dyn} = (12.70 \pm 0.64) M_\odot/L_{\odot,r}$ and an average stellar mass-to-light ratio of $\Upsilon_* = (2.96 \pm 1.22) M_\odot/L_{\odot,r}$.

Aside from the troublesome galaxy 75, galaxy 30 has the highest dynamical mass-to-light ratio with $\Upsilon_{dyn} = (13.21 \pm 0.53) M_\odot/L_{\odot,r}$. In contrast to this, its stellar mass-to-light ratio is one of the lowest with only $\Upsilon_* = (1.99 \pm 0.82) M_\odot/L_{\odot,r}$. This agrees with Galaxy 30, which has the third lowest stellar mass of the candidate sample with $M_* = (3.72 \pm 1.53)\,10^{10} M_\odot$. Galaxy 30 has a dynamical mass of $M_{dyn} = (2.45 \pm 0.12)\,10^{11} M_\odot$. It is worth pointing out that it has neither an extraordinarily high central velocity dispersion of $\sigma_0 = (346 \pm 11)$ km s^{-1} nor a large physical radius $R_0 = (1.76 \pm 0.03)$ kpc for the candidate galaxies.

The galaxy with the highest central velocity dispersion is galaxy 76 with $\sigma_0 = (432 \pm 18)$ km s^{-1}. With an absolute r-band magnitude of (-22.07 ± 0.01), this galaxy is one of the brighter objects in our candidate sample. It is also the second most massive galaxy in our sample in terms of dynamical mass with $M_{dyn} = (4.47 \pm 0.21)\,10^{11} M_\odot$.

The reddest galaxy in our candidate sample has the internal ID 12. With a g-r colour of (-1.10 ± 0.02) mag, it is a clear outlier on the red sequence and significantly redder than all galaxies in our candidate sample (except one) and even than most galaxies in the basic sample (see Figure 4). Surprisingly, galaxy 12 is not outstanding in any other parameters than colour, and it appears to be an average member of the candidate sample.

We visually inspected the images of all our candidates (see Figure 2) and find that several have other (foreground or background) objects that are only less than five angular scale radii a_{sdss} from their centre. The galaxies with the internal IDs 18, 24, 25, 33, 35, and 50 have other prominent objects (galaxies or stars) within their immediate vicinity. We have to be careful when using the parameters measured for these galaxy, since there is a chance that their values might suffer from some contamination.

Last but not least, we return to the starting point of our investigation, b19, which has the internal ID 2. It is a member of our candidate sample with rather average properties compared to the other 75 candidates. It is always a central part of the group of data points formed by our candidates in the diagrams. The only feature of b19 that is a little outstanding compared to the other members of the candidate sample is its Sersic parameter n_S, which borders the maximum allowed value of eight by the algorithm used by Simard et al. (2011). This is close to the Sersic index of 6.9 found by Läsker et al. (2013) based on HST/ACS/HRC imaging.

7. Summary and conclusions

Our sample of 76 candidates (including b19) for compact massive early-type galaxies forms an ideal basis for future follow-up observations using high-resolution spectroscopy and imaging. We found that our homogeneous sample, which has been defined as extreme outliers in the $\log_{10}(R_0)$-$\log_{10}(\sigma_0)$ plane does

not behave as do outliers in other relations for early-type galaxies except for those that are directly related to the selection criteria. The candidates seem to form the compact massive tail of the general distribution of early-type galaxies, and are not a separate population of particularly peculiar objects. We confirmed that there is an increase in the dynamical and stellar mass-to-light ratios at higher central velocity dispersions.

Furthermore, we saw the same tendency as Conroy et al. (2013) that the difference between the dynamical mass and the stellar mass derived using simple models (Mendel et al. 2014) increases at higher central velocity dispersions. This is usually considered to be an indication of a systematic variation in the initial mass function of those galaxies. As a result our candidates may have an extremely bottom-heavy initial mass function as proposed for b19 (Läsker et al. 2013). The high central velocity dispersion, which is crucial for determining of the dynamical mass, could also be due to over-massive central black holes (van den Bosch et al. 2012; Mieske et al. 2013; Seth et al. 2014). However, a robust detection of such a black hole is only possible for the nearest objects with high spatial resolution spectroscopy (Läsker et al. 2013; Emsellem 2013; Yıldırım et al. submitted). It is unlikely that all these objects contain such a large black hole.

We also tried to draw a connection between the compact massive galaxies in our sample and even more massive and more compact galaxies from high redshifts. Based on the previous observation of quiescent high-redshift galaxies (Kriek et al. 2006, 2008), van Dokkum et al. (2008) found that there are already fully formed early-type galaxies with scale radii that are much smaller and stellar masses that are much higher than any object known in the local universe. For comparison, we used several samples of these galaxies at high redshifts, such as those of Damjanov et al. (2009), van de Sande et al. (2013), and Belli et al. (2014), and also at intermediate redshifts as in Zahid et al. (2015). Many of these galaxies must have evolved, most likely by mergers, into more regular early-type galaxies. The galaxies in our sample are those that still resemble to a specific subgroup of these red nuggets. Some of these exotic galaxies in the early universe possess high dynamical masses and small sizes. From some local galaxies, such as b19 (Läsker et al. 2013) and NGC 1277, and others (van den Bosch et al. 2012), we know similar features, and they are remnants of red nugget galaxies. It is shown in van de Sande et al. (2015) that although the initial mass function of most red nuggets shows a rather shallow slope, the one for those galaxies with high mass-to-light ratios tend to be bottom-heavy. The galaxy b19 is known for its bottom heavy initial mass function and our candidates have an elevated mass-to-light ratio in comparison to normal early-type galaxies. Therefore, one may suspect that some galaxies of our sample are remnants of these ancient objects or that they are at least somehow related to the subgroup of these objects where the galaxies of Läsker et al. (2013) and van den Bosch et al. (2012) originated. The advantage of our sample is that it is located in the local universe and is thus easier to study than galaxies at high redshifts.

By selecting galaxies based on stellar velocity dispersion, we found 76 compact, massive early-type galaxies below a redshift of $z = 0.2018$. These are excellent targets for further studies of various scientific questions, such as the variation in the initial mass function, over-massive black holes, and potential remnants of exotic galaxies from the early universe. High-resolution imaging data can confirm their sizes and rule out superpositions. Spectroscopy of these objects will enable us to study their dynamical mass distribution and kinematics, and it will allow for (resolved) stellar population analysis.

20

Appendix A: Updated fundamental plane coefficients

The fundamental plane, which was first mentioned in Terlevich et al. (1981) and properly defined and discussed Dressler et al. (1987) and Djorgovski & Davis (1987), is an empirical relation between three global parameters of elliptical galaxies: the central velocity dispersion σ_0, the physical effective radius R_0, and the mean surface brightness μ_0 within the effective radius. The last parameter is usually expressed as I_0, which is a renormalized surface brightness μ_0: $\log_{10}(I_0) = -\frac{\mu_0}{2.5}$. The coefficients a, b, and c are obtained by fitting

$$\log_{10}(R_0) = a \cdot \log_{10}(\sigma_0) + b \cdot \log_{10}(I_0) + c. \tag{A.1}$$

We provide updated values of the fundamental plane coefficients presented in Saulder et al. (2013). The main improvements are that we now use SDSS DR10 (Ahn et al. 2014) instead of SDSS DR8 (Aihara et al. 2011) and that we do not use any constraints on or information about the SDSS u band, which we found to be quite problematic. Therefore, we have 133 107 galaxies instead of 100 427 for our basic sample (for definitions see Saulder et al. (2013)), and after all filtering we end up with 119 085 galaxies instead of the 92 953 that are used for the final fit. This again makes it the largest sample ever used for calibrating the fundamental plane so far. In addition to improved fits, which are based on the de Vaucouleurs fit parameters directly from SDSS, we provide new fits for the g and r bands using the Sersic parameters from Simard et al. (2011). To this end, we use 121 443 galaxies selected after some 3-σ clipping from the basic sample in this paper.

Aside from the extended sample, there are a couple of other minor changes and improvements over the old paper (Saulder et al. 2013). First of all, we corrected a minor mistake in the
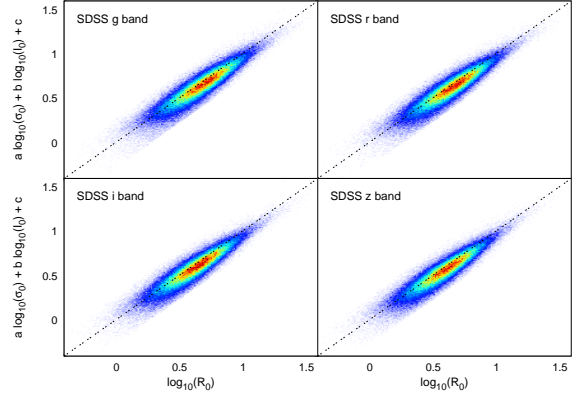
Figure A.1. Edge-on projections of the fundamental plane of elliptical galaxies for four different SDSS filters using the de Vaucouleurs fit parameters. The g band is shown in the top left panel and the r band in the top right panels. The bottom left panel displays the i band and the bottom right the z band. The dashed black lines indicate the fundamental plane fits in the corresponding filters.
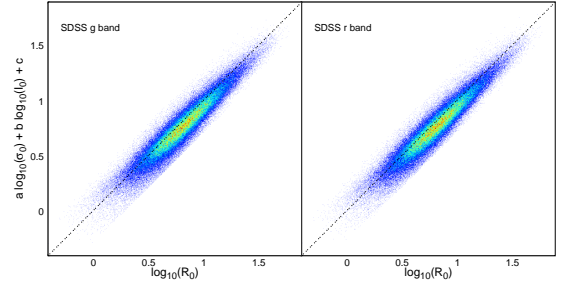
Figure A.2. Edge-on projections of the fundamental plane of elliptical galaxies for the SDSS g band (left panel) and r band (right panel) using Sersic fit parameters. The dashed black lines indicate the fundamental plane fits in the corresponding filters.

calculation of the average distance error. This mistake caused the values of the error estimate in the old paper to be systematically lower by a couple of percentage points than they actually are. Even with the slightly larger error, it is still the best fit of the fundamental plane using a large sample at this wave-length range (Bernardi et al. 2003; Hyde & Bernardi 2009; La Barbera et al. 2010).

Another improvement on the fit is that the volume weights are now considering that the sample only covers a limited redshift from 0.01 to 0.2 (or from 0.05 to 0.4 for the Sersic fits based on the basic sample in this paper). In our previous analysis, the very luminous galaxies were slightly under-represented, because their volume weights assumed a larger volume (the one in which they are theoretically still visible) than the volume of sample (redshift cut at 0.2). We then also subtract the volume corresponding to a redshift of 0.01 from the volume weights, where all galaxies were removed from the sample. The saturation limit of SDSS spectroscopy is also measured and included in the new volume weights by removing the volume associated with it in the same fashion as for the the Malmquest bias limitation. The negligence of these two corrections caused the volume weights of very faint galaxies to be underestimated. Both corrections are relatively tiny, and the new coefficients are only slightly

21

bands	a	b	c	s_ε	$\bar{\sigma}_{\text{dist}}$ [%]
g (dV)	0.999 ± 0.026	-0.754 ± 0.011	-7.93 ± 0.10	0.0942	19.3
r (dV)	1.070 ± 0.026	-0.770 ± 0.011	-7.98 ± 0.11	0.0935	19.0
i (dV)	1.100 ± 0.026	-0.775 ± 0.012	-7.96 ± 0.11	0.0919	18.6
z (dV)	1.145 ± 0.025	-0.781 ± 0.012	-8.02 ± 0.11	0.0920	18.5
g (S)	0.966 ± 0.026	-0.726 ± 0.009	-7.62 ± 0.09	0.0977	20.6
r (S)	1.029 ± 0.026	-0.729 ± 0.009	-7.56 ± 0.09	0.0972	20.4

Table A.1. Results of the best fits for the fundamental plane. The coefficients a, b, and c for 4 SDSS bands using redshift evolution, volume weights, 3-σ clipping, and the radii and magnitudes of de Vaucouleurs (dV) fits are provided in this table. Furthermore, it contains the coefficients for 2 SDSS bands using the same calibration, but the radii and magnitudes from the Sersic (S) fits of Simard et al. (2011). The root mean square s_ε of the fits and the relative distance error $\bar{\sigma}_{\text{dist}}$ of the fundamental plane are also provided.

different from the old ones. In particular, the a coefficient is moderately larger, hence closer to the values from the literature (see Table 1 in Saulder et al. (2013)). The new coefficients are listed in Table A.1, edge-on projects of the fundamental plane for all four bands used for the de Vaucouleurs fit parameters in the calibration can be found in Figure A.1, and the edge-on projects of the fundamental plane for the g and r SDSS bands using the Sersic fit parameters are displayed in Figure A.2.

Appendix B: The Sersic fit sample
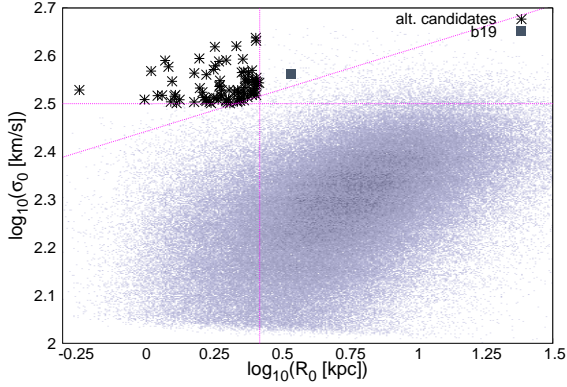
Figure B.1. Selection of the alternative candidates in the R_0-σ_0 plane. The restrictions, which define our alternative candidates, are indicated by the dashed magenta lines. The black stars represent the 85 candidates for galaxies with similar properties in Sersic fit parameters as b19, and b19 itself is represented by a grey filled square in the plot.

In addition to the candidate sample defined using the de Vaucouleurs fit parameters, we provide an alternative sample using the Sersic fit parameters from Simard et al. (2011).

The sample is defined in the same fashion as the main candidate sample, and we find 85 galaxies fulfilling the requirements (listed in Table B.1, together with b19, which was assigned the Sersic ID 1). The logarithm of the physical radius R_0 has to be smaller than the sample's average by at least one standard deviation, which provides us with an upper limit for R_0 of ~2.65 kpc. The lower limit for the central velocity dispersion σ_0 of ~316.6 km s^{-1} is obtained by requiring it to be at least two standard deviations higher than the mean of the logarithm of the central velocity dispersion. The last criterion ensures that all candidates are more than three standard deviations off from the

$\log_{10}(R_0) - \log_{10}(\sigma_0)$ relation, which was obtained by a linear fit to the data points. The selection criteria is illustrated in Figure B.1. We find that b19 fails to fulfil the radial size requirement in the case of the Sersic fit parameters (see Table B.2 for numbers), and it is not included in the 85 alternative candidates. However, we keep on providing its position in the plots and tables. As illustrated in Figures B.2 to B.9, the alternative sample has generally speaking similar properties to the main candidate sample, but it is less cohesive and more scattered. We therefore prefer our main sample to this one. There are 51 galaxies, which the two candidate lists have in common (see Table C.1). We consider these galaxies as candidates with increased priority for any follow-up observations.
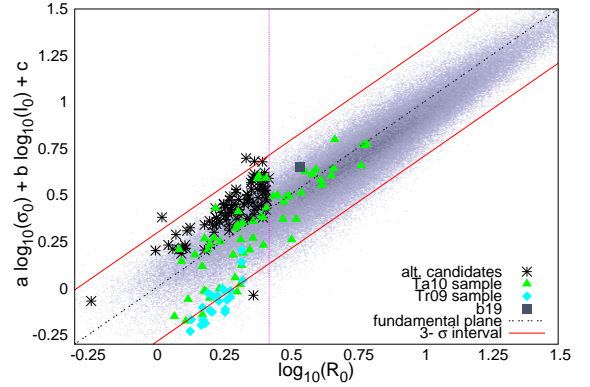
Figure B.2. Location of the candidate galaxies on the fundamental plane using Sersic fit parameters. The candidates are indicated by black stars. The galaxies belonging to the Ta10 sample are represented using filled green triangles, and the Tr09 sample is marked by filled cyan diamonds. The starting point of our investigation, b19, is indicated by a filled grey square. The magenta dotted lines show the limiting physical radius used in the sample sample selection. The black dashed lines are the fundamental plane fits from Appendix A with their corresponding 3-σ confidence intervals shown as red solid lines. The fit appears to be slightly offset owing to the volume weights used to correct the Malmquist bias in the fitting process.
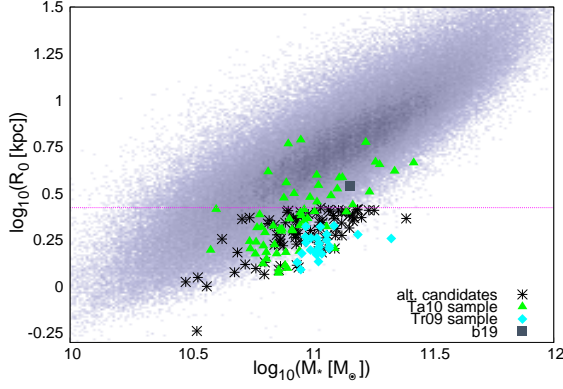
Figure B.3. Stellar mass-size relation for our basic sample using the Sersic fit parameters. The alternative candidates are indicated by black stars. The galaxies belonging to the Ta10 sample are represented using filled green triangles, and the Tr09 sample is indicated by filled cyan diamonds. B19 is indicated by a filled grey square. The magenta dashed line denotes the limiting scaling radius for our sample selection.
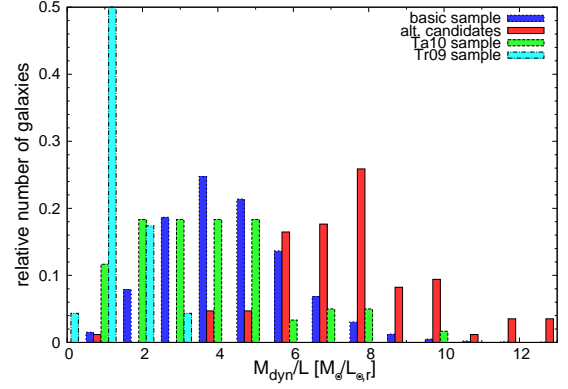
Figure B.5. Distribution of the dynamical mass-to-light ratios Υ_{dyn} using the Sersic fit parameters. The blue histogram corresponds to our basic sample, which only consists of early-type galaxies. The green histogram represents the Ta10 sample, while the cyan histogram corresponds to Tr09 sample. The red histogram denotes our 85 alternative candidates.
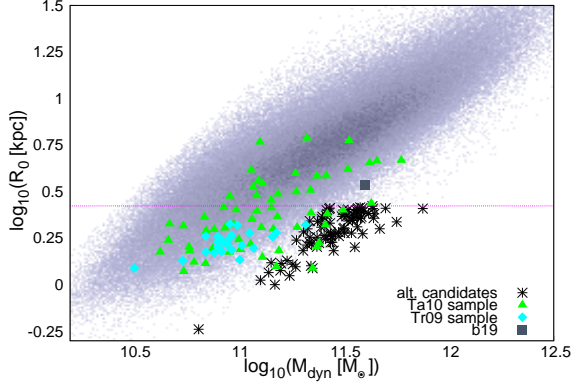
Figure B.4. Dynamical mass-size relation for our basic sample using the Sersic fit parameters. The alternative candidates are indicated by black stars. The galaxies belonging to the Ta10 sample are represented using filled green triangles, and the Tr09 sample is indicated by filled cyan diamonds. B19 is indicated by a filled grey square. The magenta dashed line denotes the limiting scaling radius for our sample selection.
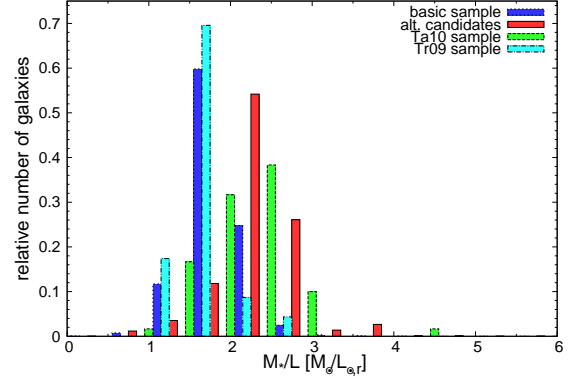
Figure B.6. Distribution of the stellar mass-to-light ratios Υ_* using the Sersic fit parameters. The blue histogram corresponds to our basic sample, which only consists of early-type galaxies. The green histogram represents the Ta10 sample, while the cyan histogram corresponds to Tr09 sample. The red histogram denotes our 85 alternative candidates.

23

86
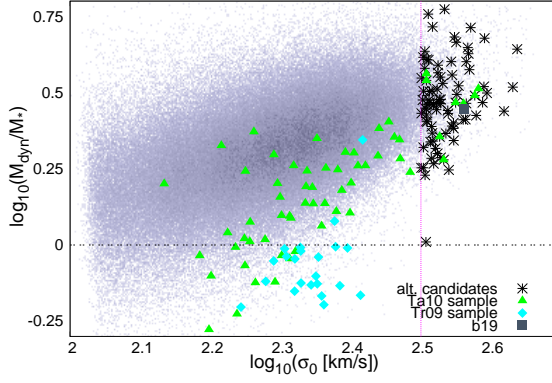
Figure B.7. Dependence of the dynamical mass M_{dyn} to stellar mass M_* ratio on central velocity dispersion σ_0 using the Sersic fit parameters. The alternative candidates are indicated by black stars. The galaxies belonging to the Ta10 sample are represented using filled green triangles and the Tr09 sample is marked by filled cyan diamonds. B19 is indicated by a filled grey square. The magenta dashed line marks the limiting scaling central velocity dispersion for our sample selection. The area below the black dashed line is considered to be unphysical, because M_* would exceed M_{dyn}.
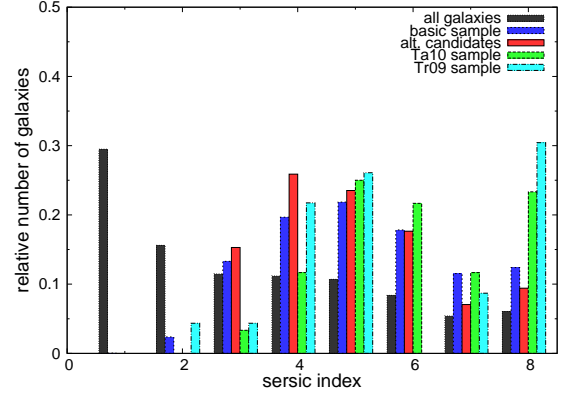
Figure B.9. Distribution of the Sersic indices of different samples of galaxies. The black histogram of the Sersic indices stands for all galaxies in SDSS DR7 for which Simard et al. (2011) did their refits. The blue histogram indicates the distribution of Sersic parameters for our basic sample, which only consists of early-type galaxies. The green histogram represents the Ta10 sample, while the cyan histogram corresponds to Tr09 sample. The red histogram denotes our 85 alternative candidates.
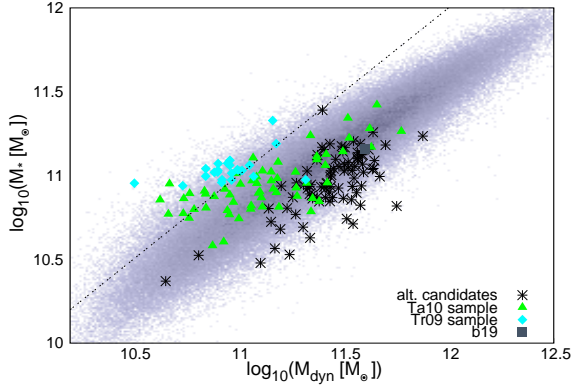
Figure B.8. Distribution of the sample's galaxies in the dynamical mass M_{dyn} vs. stellar mass M_* plane using the Sersic fit parameters. The alternative candidates are indicated by black stars. The galaxies belonging to the Ta10 sample are represented using filled green triangles, and the Tr09 sample is indicated by filled cyan diamonds. B19 is indicated by a filled grey square. The magenta dashed line marks the limiting scaling central velocity dispersion for our sample selection. The black dashed line denotes the limit of the M_{dyn} to M_* ratio, which is still considered to be physical, because M_* would exceed M_{dyn} above it.

24

87

Sersic ID	SDSS DR10 ID	ra [°]	dec [°]	z	$m_{S,r}$ [mag]	a_S [arcsec]	σ_{sdss} [km/s]	n_S	$\mathcal{L}_{ETG}$
1	1237648703523520846	229.4240	-0.7049	0.1166	16.71 ± 0.01	1.62 ± 0.02	336± 12	7.99 ± 0.04	0.81
2	1237651191892607189	125.5691	48.2553	0.1276	17.56 ± 0.03	0.87 ± 0.02	351± 14	2.92 ± 0.30	0.75
3	1237651252557513010	125.0735	48.8830	0.1338	17.44 ± 0.03	1.00 ± 0.03	318± 13	3.22 ± 0.34	0.83
4	1237652934037536913	327.3491	-8.6752	0.1014	17.13 ± 0.02	1.01 ± 0.03	320± 16	3.50 ± 0.19	0.70
5	1237654342254002376	212.1645	61.1317	0.1215	17.19 ± 0.03	1.13 ± 0.02	338± 16	5.66 ± 0.36	0.76
6	1237652900773298301	58.0541	-5.8611	0.1137	17.13 ± 0.03	0.77 ± 0.02	306± 14	4.76 ± 0.37	0.66
7	1237651252589363420	247.9117	46.2683	0.1321	17.61 ± 0.02	0.53 ± 0.01	311± 14	3.79 ± 0.21	0.76
8	1237655502424769160	256.4241	33.4779	0.1022	17.12 ± 0.02	1.32 ± 0.02	326± 16	5.63 ± 0.17	0.77
9	1237651539246186637	167.7205	66.7862	0.1362	17.52 ± 0.02	0.65 ± 0.02	350± 14	3.51 ± 0.13	0.59
10	1237655742944248167	223.0119	5.2335	0.0639	16.05 ± 0.01	1.37 ± 0.02	294± 10	2.51 ± 0.10	0.77
11	1237651714798125236	248.3287	47.1274	0.1229	17.33 ± 0.01	0.81 ± 0.02	335± 12	7.98 ± 0.08	0.66
12	1237660615586611373	175.2231	11.0085	0.0809	16.75 ± 0.02	1.00 ± 0.02	289± 14	4.48 ± 0.23	0.82
13	1237658206124507259	193.5474	50.8170	0.1209	17.07 ± 0.02	0.83 ± 0.01	341± 16	5.70 ± 0.33	0.80
14	1237652944786424004	1.1323	16.0719	0.1144	17.46 ± 0.02	0.62 ± 0.01	291± 15	4.48 ± 0.29	0.55
15	1237658423007707334	138.8689	4.6676	0.1431	17.49 ± 0.03	0.91 ± 0.03	303± 14	3.75 ± 0.38	0.71
16	1237657242435584230	146.2765	47.8321	0.1170	16.99 ± 0.02	1.24 ± 0.03	319± 19	4.25 ± 0.27	0.62
17	1237657856067830007	161.5842	49.4468	0.1306	17.41 ± 0.03	0.88 ± 0.02	286± 14	5.01 ± 0.49	0.71
18	1237654952670003535	253.9937	39.4776	0.1496	17.30 ± 0.02	0.97 ± 0.02	393± 18	2.85 ± 0.20	0.78
19	1237670956787695816	23.2042	-9.1208	0.1336	17.00 ± 0.02	1.09 ± 0.03	318± 9	5.36 ± 0.27	0.79
20	1237652948530102500	10.3768	-9.2352	0.0538	15.05 ± 0.00	2.46 ± 0.02	310± 5	4.38 ± 0.01	0.53
21	1237656243317113067	354.1646	15.8222	0.1179	17.43 ± 0.03	0.79 ± 0.02	290± 16	5.00 ± 0.34	0.73
22	1237657610723655845	158.1494	53.3763	0.1340	17.50 ± 0.04	0.92 ± 0.02	293± 15	3.29 ± 0.46	0.69
23	1237655474503024820	245.6049	44.7856	0.0716	15.65 ± 0.00	1.89 ± 0.02	333± 8	5.46 ± 0.03	0.81
24	1237658424616616162	134.8572	5.6269	0.1625	17.65 ± 0.03	0.79 ± 0.03	288± 16	6.21 ± 0.28	0.72
25	1237657596224209238	123.8014	38.6793	0.1517	17.02 ± 0.02	1.06 ± 0.02	333± 13	4.70 ± 0.17	0.89
26	1237665569297203655	254.5120	41.8378	0.0375	15.18 ± 0.00	1.50 ± 0.01	303± 7	3.54 ± 0.04	0.64
27	1237654605857751221	148.8860	4.3722	0.0937	16.32 ± 0.01	1.07 ± 0.01	352± 9	3.99 ± 0.05	0.52
28	1237653614796865660	143.0592	56.4013	0.1173	16.73 ± 0.01	1.09 ± 0.01	302± 10	5.21 ± 0.12	0.69
29	1237655465916170402	184.8400	63.5358	0.1039	17.33 ± 0.01	0.60 ± 0.01	292± 14	6.00 ± 0.28	0.52
30	1237658204493185306	130.8260	34.6824	0.0658	16.10 ± 0.01	1.79 ± 0.03	301± 11	2.62 ± 0.03	0.86
31	1237657628456190055	187.6884	51.7060	0.1517	17.46 ± 0.02	0.70 ± 0.01	307± 14	4.51 ± 0.22	0.62
32	1237660025032081578	340.4373	-0.8113	0.1293	17.38 ± 0.02	0.78 ± 0.02	373± 22	7.95 ± 0.16	0.77
33	1237661064411349290	138.3286	8.1161	0.0934	16.71 ± 0.01	0.95 ± 0.01	295± 9	4.78 ± 0.14	0.61
34	1237661849849430137	156.3195	40.3153	0.0682	16.36 ± 0.03	1.79 ± 0.02	317± 10	5.30 ± 0.28	0.58
35	1237661069261209757	180.2716	14.5850	0.0831	16.24 ± 0.01	1.29 ± 0.02	291± 9	2.86 ± 0.06	0.57
36	1237662663746060502	221.9296	34.6657	0.0974	17.30 ± 0.02	0.72 ± 0.01	284± 14	6.17 ± 0.38	0.59
37	1237663277928022281	0.6027	0.5352	0.0784	17.30 ± 0.03	0.71 ± 0.02	331± 17	7.97 ± 0.11	0.77
38	1237661383314702588	160.1959	39.9311	0.1394	17.64 ± 0.02	0.68 ± 0.02	324± 15	5.06 ± 0.25	0.69
39	1237662697568796852	226.2857	30.1184	0.1450	16.99 ± 0.02	1.00 ± 0.02	314± 9	7.99 ± 0.04	0.71
40	1237661812272857187	180.2528	12.2175	0.1295	17.60 ± 0.03	0.87 ± 0.03	291± 14	5.55 ± 0.46	0.81
41	1237665532252520624	223.1388	22.5927	0.1551	17.51 ± 0.02	0.94 ± 0.02	318± 16	4.06 ± 0.28	0.54
42	1237667255083991162	170.3135	29.9694	0.1237	17.64 ± 0.02	0.97 ± 0.03	378± 24	3.26 ± 0.18	0.65

Sersic ID	SDSS DR10 ID	ra [°]	dec [°]	z	$m_{S,r}$ [mag]	a_S [arcsec]	σ_{sdss} [km/s]	n_S	$\mathcal{L}_{ETG}$
43	1237667324323758158	166.9049	27.1948	0.1502	17.45 ± 0.04	0.83 ± 0.02	287± 14	6.32 ± 0.69	0.63
44	1237667735054647478	206.9225	20.9708	0.1232	17.41 ± 0.03	0.78 ± 0.01	286± 14	6.30 ± 0.49	0.76
45	1237662193459986552	206.5336	39.4248	0.1297	17.47 ± 0.03	0.80 ± 0.03	289± 15	3.77 ± 0.35	0.68
46	1237667736104861820	149.3027	19.2625	0.0975	17.01 ± 0.03	0.97 ± 0.02	287± 10	3.41 ± 0.26	0.84
47	1237665549429899544	223.0734	22.4871	0.1165	17.29 ± 0.02	0.58 ± 0.01	335± 13	4.63 ± 0.19	0.62
48	1237667209978380503	149.1117	23.9641	0.1193	17.14 ± 0.02	1.06 ± 0.02	356± 25	6.92 ± 0.26	0.68
49	1237663278461944053	353.8668	1.0467	0.0827	16.16 ± 0.02	1.62 ± 0.02	320± 9	5.18 ± 0.24	0.80
50	1237662340012638220	239.5694	27.2367	0.0896	16.81 ± 0.02	0.77 ± 0.01	296± 12	5.82 ± 0.28	0.75
51	1237664667887140986	128.6548	24.3250	0.0705	16.13 ± 0.01	1.63 ± 0.02	296± 9	7.17 ± 0.08	0.77
52	1237664093432119636	121.7265	20.7624	0.1247	17.48 ± 0.02	0.72 ± 0.02	299± 13	5.55 ± 0.53	0.66
53	1237665533335175692	243.8410	16.3942	0.0818	15.72 ± 0.01	1.63 ± 0.01	311± 7	6.03 ± 0.13	0.81
54	1237661850400260193	199.4989	43.6141	0.1140	17.64 ± 0.04	0.65 ± 0.02	287± 16	5.15 ± 0.48	0.62
55	1237664852035174654	219.1545	31.3943	0.0850	16.06 ± 0.01	0.95 ± 0.01	331± 9	3.96 ± 0.04	0.77
56	1237667321652248694	199.8561	25.5487	0.2810	17.48 ± 0.03	0.52 ± 0.01	284± 12	6.49 ± 0.44	0.89
57	1237667730736873763	134.9926	14.7626	0.1008	17.22 ± 0.02	1.07 ± 0.02	291± 14	2.98 ± 0.09	0.57
58	1237662664290402490	239.6933	27.2131	0.0879	16.99 ± 0.01	1.01 ± 0.02	292± 15	3.91 ± 0.11	0.74
59	1237665535469486145	243.3042	17.8080	0.0374	14.57 ± 0.00	2.89 ± 0.01	316± 7	5.76 ± 0.05	0.68
60	1237665016311840908	163.4479	32.8694	0.1307	17.34 ± 0.03	0.97 ± 0.02	332± 14	3.67 ± 0.44	0.64
61	1237667212115050932	124.1550	16.1777	0.1225	17.62 ± 0.02	0.77 ± 0.02	303± 13	2.74 ± 0.19	0.64
62	1237665564997976239	218.1283	20.4259	0.1216	17.28 ± 0.02	1.11 ± 0.03	304± 17	4.62 ± 0.23	0.83
63	1237663478723969457	338.0784	-0.4059	0.0865	16.74 ± 0.02	1.44 ± 0.02	327± 17	7.96 ± 0.10	0.80
64	1237667910055100586	181.7985	23.8744	0.0775	16.27 ± 0.01	1.63 ± 0.02	328± 11	7.99 ± 0.03	0.86
65	1237667734526492801	227.3075	16.4333	0.1159	17.24 ± 0.04	1.21 ± 0.02	310± 17	7.62 ± 0.37	0.61
66	1237670450522816720	137.8481	16.5697	0.0900	16.59 ± 0.01	1.09 ± 0.02	295± 9	4.42 ± 0.08	0.77
67	1237663789032669425	125.7014	59.7435	0.1344	17.34 ± 0.02	0.99 ± 0.03	296± 14	4.86 ± 0.25	0.69
68	1237665429169242591	209.7906	27.9501	0.0811	17.07 ± 0.01	0.65 ± 0.01	287± 10	3.67 ± 0.32	0.62
69	1237668299281662070	194.2881	20.8064	0.0868	16.39 ± 0.03	1.54 ± 0.01	307± 9	7.40 ± 0.52	0.56
70	1237668349753950509	232.0499	12.1307	0.1225	17.56 ± 0.03	0.85 ± 0.02	311± 14	3.77 ± 0.21	0.81
71	1237667783900135493	164.2812	22.2115	0.1206	17.11 ± 0.02	1.01 ± 0.02	303± 14	3.80 ± 0.17	0.77
72	1237668271372501042	227.9714	14.2653	0.1221	17.43 ± 0.03	0.90 ± 0.02	291± 16	6.61 ± 0.40	0.75
73	1237648721758978188	160.3022	0.2285	0.1300	17.45 ± 0.02	0.94 ± 0.02	305± 15	4.40 ± 0.18	0.64
74	1237668495782117442	176.4731	17.3242	0.0928	16.88 ± 0.01	0.72 ± 0.01	285± 9	3.40 ± 0.11	0.59
75	1237664671640715458	191.2284	36.1838	0.0877	17.44 ± 0.02	0.35 ± 0.01	293± 15	7.03 ± 0.49	0.68
76	1237662335717015837	236.8248	33.1773	0.1265	17.53 ± 0.03	0.84 ± 0.03	296± 16	7.01 ± 0.48	0.78
77	1237667782274187688	128.9043	12.6627	0.1054	17.07 ± 0.02	0.98 ± 0.02	297± 12	4.29 ± 0.13	0.71
78	1237661087497126080	132.4080	29.6033	0.1059	16.55 ± 0.01	1.27 ± 0.02	302± 7	3.75 ± 0.12	0.80
79	1237661358617067696	181.3091	48.4216	0.0648	15.80 ± 0.00	1.54 ± 0.02	311± 8	4.09 ± 0.07	0.71
80	1237653651837026391	4.8387	14.9802	0.1277	17.31 ± 0.03	1.10 ± 0.03	303± 14	5.41 ± 0.29	0.74
81	1237668298203070641	182.4650	20.0535	0.1116	17.43 ± 0.02	0.88 ± 0.02	293± 12	4.96 ± 0.30	0.72
82	1237654604796985469	178.6502	4.3536	0.0761	17.50 ± 0.02	0.18 ± 0.01	277± 13	2.66 ± 0.22	0.53
83	1237667917032980629	189.9670	21.1529	0.1085	16.58 ± 0.01	1.17 ± 0.01	321± 9	5.19 ± 0.12	0.74
84	1237661950244945934	162.5130	11.8190	0.0812	16.42 ± 0.01	1.51 ± 0.02	340± 11	5.14 ± 0.16	0.88

Sersic ID	SDSS DR10 ID	ra [°]	dec [°]	z	$m_{S,r}$ [mag]	a_S [arcsec]	σ_{sdss} [km/s]	n_S	$\mathcal{L}_{ETG}$
85	1237668333640810655	225.5537	14.6343	0.0697	16.37 ± 0.01	0.89 ± 0.01	351± 14	8.00 ± 0.02	0.52
86	1237667917030555837	184.0304	21.1393	0.1278	16.79 ± 0.01	1.12 ± 0.02	389± 16	6.35 ± 0.13	0.79

Table B.1. List of the basic parameters of our alternative candidate galaxies using the Sersic fit parameters of Simard et al. (2011) instead of the de Vaucouleurs fit parameters used for our main candidate sample. First column: internal Sersic IDs, which are used to identify the galaxies. The numbering is essentially random and only based on the order the galaxies were drawn from the basic sample. The galaxy b19 has the internal ID 3. Second column: object ID used by SDSS DR10. Third and fourth column: equatorial coordinates of the galaxies. Fifth column: redshift z, already corrected for our motion relative to the CMB. Sixth, seventh, and eighth columns: observed uncorrected refitted SDSS parameters in the following order: observed apparent magnitude m_{sdss}, angular semi-major axis a_{sdss}, central velocity dispersion σ_{sdss}. Ninth column: axis ratio $q_{b/a}$. Tenth column: GalaxyZoo probability $\mathcal{L}_{ETG}$ of the galaxy being classified as an early-type.

Sersic ID	R_r [kpc]	σ_0 [km s^{-1}]	μ_r [$\frac{mag}{arcsec^2}$]	M_r [mag]	$(M_g - M_r)$ [mag]	$\log_{10}(M_{dyn})$ [$\log_{10}(M_\odot)$]	$\log_{10}(M_*)$ [$\log_{10}(M_\odot)$]	Υ_{dyn} [$M_\odot/L_{\odot,r}$]	Υ_* [$M_\odot/L_{\odot,r}$]
1	3.46 ± 0.05	364± 13	19.11 ± 0.01	-22.28 ± 0.01	0.80 ± 0.02	11.60 ± 0.02	11.16 ± 0.15	6.44 ± 0.30	2.31 ± 0.96
2	2.00 ± 0.05	390± 16	18.59 ± 0.03	-21.62 ± 0.03	0.84 ± 0.04	11.67 ± 0.05	10.99 ± 0.15	13.84 ± 1.84	2.90 ± 1.22
3	2.41 ± 0.06	351± 14	18.76 ± 0.03	-21.86 ± 0.03	0.83 ± 0.05	11.65 ± 0.05	11.09 ± 0.15	10.43 ± 1.41	2.89 ± 1.21
4	1.90 ± 0.05	354± 18	18.62 ± 0.02	-21.45 ± 0.02	0.67 ± 0.04	11.54 ± 0.03	10.86 ± 0.15	11.86 ± 1.05	2.46 ± 1.02
5	2.49 ± 0.05	371± 17	18.92 ± 0.03	-21.76 ± 0.03	0.86 ± 0.04	11.60 ± 0.03	11.02 ± 0.15	10.16 ± 1.10	2.70 ± 1.13
6	1.60 ± 0.04	341± 15	17.78 ± 0.03	-21.92 ± 0.03	0.83 ± 0.04	11.37 ± 0.04	11.09 ± 0.15	5.24 ± 0.61	2.76 ± 1.15
7	1.27 ± 0.03	352± 16	17.67 ± 0.02	-21.55 ± 0.02	0.87 ± 0.04	11.35 ± 0.03	10.95 ± 0.15	6.95 ± 0.60	2.76 ± 1.15
8	2.51 ± 0.05	356± 17	19.24 ± 0.02	-21.43 ± 0.02	0.87 ± 0.03	11.56 ± 0.02	10.90 ± 0.15	12.79 ± 0.99	2.76 ± 1.15
9	1.59 ± 0.05	393± 16	18.00 ± 0.03	-21.73 ± 0.03	0.88 ± 0.03	11.55 ± 0.03	11.05 ± 0.15	9.53 ± 0.71	3.02 ± 1.26
10	1.69 ± 0.03	321± 11	18.37 ± 0.01	-21.41 ± 0.01	0.81 ± 0.02	11.45 ± 0.02	10.87 ± 0.15	10.00 ± 0.61	2.63 ± 1.09
11	1.80 ± 0.03	373± 14	18.38 ± 0.01	-21.59 ± 0.01	0.59 ± 0.02	11.34 ± 0.02	10.63 ± 0.15	6.62 ± 0.30	1.28 ± 0.53
12	1.53 ± 0.03	319± 16	18.25 ± 0.02	-21.32 ± 0.02	0.76 ± 0.03	11.31 ± 0.03	10.69 ± 0.15	7.85 ± 0.69	1.90 ± 0.79
13	1.83 ± 0.03	380± 18	18.15 ± 0.02	-21.86 ± 0.02	0.84 ± 0.04	11.48 ± 0.03	11.05 ± 0.15	7.11 ± 0.64	2.67 ± 1.11
14	1.29 ± 0.02	328± 17	17.83 ± 0.02	-21.41 ± 0.02	0.81 ± 0.04	11.26 ± 0.03	10.87 ± 0.15	6.47 ± 0.62	2.64 ± 1.10
15	2.31 ± 0.07	336± 16	18.57 ± 0.03	-21.97 ± 0.03	0.84 ± 0.04	11.57 ± 0.05	11.09 ± 0.15	7.89 ± 1.06	2.63 ± 1.10
16	2.64 ± 0.06	350± 21	18.96 ± 0.02	-21.84 ± 0.02	0.73 ± 0.04	11.64 ± 0.04	11.04 ± 0.15	10.40 ± 1.05	2.60 ± 1.08
17	2.06 ± 0.05	317± 16	18.54 ± 0.03	-21.74 ± 0.03	0.96 ± 0.04	11.41 ± 0.05	11.15 ± 0.15	6.73 ± 0.89	3.76 ± 1.58
18	2.57 ± 0.05	434± 20	18.58 ± 0.02	-22.19 ± 0.02	0.87 ± 0.04	11.88 ± 0.04	11.23 ± 0.15	13.05 ± 1.29	2.97 ± 1.24
19	2.60 ± 0.06	350± 10	18.54 ± 0.02	-22.25 ± 0.02	0.85 ± 0.03	11.58 ± 0.02	11.19 ± 0.15	6.27 ± 0.47	2.55 ± 1.06
20	2.58 ± 0.02	330± 5	18.67 ± 0.00	-22.01 ± 0.01	0.86 ± 0.01	11.57 ± 0.01	11.11 ± 0.15	7.62 ± 0.16	2.65 ± 1.09
21	1.69 ± 0.04	323± 18	18.24 ± 0.03	-21.59 ± 0.03	0.83 ± 0.04	11.34 ± 0.04	10.94 ± 0.15	6.60 ± 0.76	2.60 ± 1.09
22	2.22 ± 0.06	325± 17	18.75 ± 0.04	-21.69 ± 0.04	0.79 ± 0.06	11.54 ± 0.06	10.94 ± 0.15	9.57 ± 1.71	2.36 ± 1.00
23	2.58 ± 0.02	358± 9	18.71 ± 0.00	-21.99 ± 0.01	0.85 ± 0.01	11.59 ± 0.01	11.07 ± 0.15	8.10 ± 0.24	2.43 ± 1.00
24	2.25 ± 0.07	321± 18	18.35 ± 0.03	-22.15 ± 0.03	0.86 ± 0.05	11.40 ± 0.03	11.17 ± 0.15	4.50 ± 0.46	2.65 ± 1.11
25	2.42 ± 0.04	367± 14	18.53 ± 0.02	-22.09 ± 0.02	0.88 ± 0.03	11.62 ± 0.02	11.15 ± 0.15	7.97 ± 0.58	2.73 ± 1.14
26	1.12 ± 0.01	329± 7	17.83 ± 0.00	-21.02 ± 0.01	0.83 ± 0.01	11.24 ± 0.01	10.53 ± 0.15	8.94 ± 0.28	1.72 ± 0.71
27	1.88 ± 0.02	388± 10	17.95 ± 0.01	-22.09 ± 0.01	0.82 ± 0.02	11.59 ± 0.01	11.12 ± 0.15	7.44 ± 0.29	2.53 ± 1.05
28	2.33 ± 0.03	332± 11	18.37 ± 0.01	-22.16 ± 0.01	0.86 ± 0.02	11.49 ± 0.02	11.18 ± 0.15	5.56 ± 0.27	2.68 ± 1.11
29	1.16 ± 0.02	329± 16	17.75 ± 0.01	-21.25 ± 0.01	0.84 ± 0.02	11.14 ± 0.03	10.80 ± 0.15	5.74 ± 0.42	2.62 ± 1.08
30	2.27 ± 0.04	324± 11	19.00 ± 0.01	-21.42 ± 0.01	0.80 ± 0.02	11.58 ± 0.02	10.82 ± 0.15	13.45 ± 0.64	2.35 ± 0.97
31	1.88 ± 0.04	344± 16	18.03 ± 0.02	-22.07 ± 0.02	0.88 ± 0.04	11.46 ± 0.03	11.10 ± 0.15	5.63 ± 0.47	2.42 ± 1.01
32	1.82 ± 0.05	416± 24	18.16 ± 0.02	-21.85 ± 0.02	0.83 ± 0.04	11.44 ± 0.03	11.00 ± 0.15	6.60 ± 0.54	2.40 ± 1.00

Sersic ID	R_r [kpc]	σ_0 [km s^{-1}]	μ_r [$\frac{\text{mag}}{\text{arcsec}^2}$]	M_r [mag]	$(M_g - M_r)$ [mag]	$\log_{10}(M_{dyn})$ [$\log_{10}(M_\odot)$]	$\log_{10}(M_*)$ [$\log_{10}(M_\odot)$]	Υ_{dyn} [$M_\odot/L_{\odot,r}$]	Υ_* [$M_\odot/L_{\odot,r}$]
33	1.66 ± 0.02	326± 10	18.08 ± 0.01	-21.69 ± 0.01	0.78 ± 0.02	11.35 ± 0.02	10.88 ± 0.15	6.17 ± 0.31	2.10 ± 0.87
34	2.34 ± 0.03	342± 11	19.31 ± 0.03	-21.18 ± 0.03	0.73 ± 0.04	11.52 ± 0.03	10.74 ± 0.15	14.47 ± 1.38	2.44 ± 1.02
35	2.02 ± 0.03	318± 10	18.34 ± 0.01	-21.84 ± 0.01	0.85 ± 0.02	11.50 ± 0.02	11.03 ± 0.15	7.64 ± 0.35	2.55 ± 1.06
36	1.31 ± 0.02	317± 16	18.15 ± 0.02	-21.12 ± 0.02	0.77 ± 0.03	11.16 ± 0.03	10.72 ± 0.15	6.69 ± 0.63	2.47 ± 1.03
37	1.06 ± 0.02	370± 19	18.16 ± 0.03	-20.62 ± 0.03	0.78 ± 0.04	11.11 ± 0.02	10.48 ± 0.15	9.42 ± 0.90	2.22 ± 0.93
38	1.69 ± 0.05	364± 17	18.17 ± 0.02	-21.68 ± 0.02	0.85 ± 0.03	11.44 ± 0.03	11.03 ± 0.15	7.62 ± 0.64	2.96 ± 1.23
39	2.58 ± 0.06	347± 10	18.40 ± 0.02	-22.39 ± 0.02	0.74 ± 0.03	11.44 ± 0.01	11.19 ± 0.15	3.96 ± 0.22	2.24 ± 0.93
40	2.04 ± 0.06	323± 19	18.69 ± 0.03	-21.56 ± 0.03	0.85 ± 0.04	11.39 ± 0.04	10.93 ± 0.15	7.70 ± 0.97	2.66 ± 1.11
41	2.57 ± 0.07	353± 17	18.65 ± 0.02	-22.13 ± 0.02	0.89 ± 0.04	11.64 ± 0.04	11.26 ± 0.15	8.00 ± 0.79	3.31 ± 1.38
42	2.18 ± 0.02	417± 26	19.06 ± 0.02	-21.33 ± 0.02	0.75 ± 0.03	11.75 ± 0.03	10.82 ± 0.15	21.75 ± 2.22	2.53 ± 1.05
43	2.19 ± 0.04	319± 16	18.36 ± 0.04	-22.07 ± 0.04	0.84 ± 0.06	11.38 ± 0.05	11.12 ± 0.15	4.61 ± 0.71	2.57 ± 1.09
44	1.74 ± 0.03	319± 16	18.30 ± 0.03	-21.60 ± 0.03	0.80 ± 0.04	11.28 ± 0.04	10.96 ± 0.15	5.66 ± 0.67	2.71 ± 1.14
45	1.87 ± 0.06	322± 17	18.44 ± 0.03	-21.63 ± 0.03	0.85 ± 0.05	11.44 ± 0.04	10.99 ± 0.15	8.01 ± 1.03	2.87 ± 1.20
46	1.76 ± 0.04	317± 11	18.48 ± 0.03	-21.42 ± 0.03	0.83 ± 0.04	11.41 ± 0.03	10.87 ± 0.15	9.22 ± 1.03	2.61 ± 1.09
47	1.23 ± 0.02	378± 15	17.53 ± 0.02	-21.60 ± 0.02	0.82 ± 0.03	11.35 ± 0.02	10.86 ± 0.15	6.74 ± 0.52	2.18 ± 0.91
48	2.30 ± 0.05	392± 27	18.76 ± 0.03	-21.74 ± 0.02	0.60 ± 0.03	11.55 ± 0.03	10.71 ± 0.15	9.22 ± 0.86	1.35 ± 0.56
49	2.54 ± 0.02	346± 9	18.74 ± 0.02	-21.94 ± 0.02	0.88 ± 0.03	11.57 ± 0.02	11.14 ± 0.15	8.11 ± 0.59	3.00 ± 1.25
50	1.30 ± 0.02	330± 13	17.76 ± 0.02	-21.47 ± 0.02	0.89 ± 0.03	11.20 ± 0.03	10.94 ± 0.15	5.38 ± 0.43	2.91 ± 1.21
51	2.20 ± 0.02	321± 10	18.80 ± 0.01	-21.56 ± 0.01	0.83 ± 0.02	11.34 ± 0.01	10.89 ± 0.15	6.79 ± 0.29	2.41 ± 1.00
52	1.63 ± 0.03	334± 15	18.17 ± 0.04	-21.59 ± 0.04	0.84 ± 0.06	11.33 ± 0.04	11.03 ± 0.15	6.39 ± 0.92	3.20 ± 1.36
53	2.52 ± 0.02	337± 7	18.30 ± 0.01	-22.36 ± 0.01	0.78 ± 0.02	11.50 ± 0.01	11.14 ± 0.15	4.67 ± 0.19	2.06 ± 0.85
54	1.35 ± 0.04	323± 18	18.18 ± 0.04	-21.16 ± 0.04	0.84 ± 0.06	11.23 ± 0.04	10.80 ± 0.15	7.65 ± 1.12	2.86 ± 1.22
55	1.53 ± 0.01	367± 10	17.57 ± 0.01	-22.01 ± 0.01	0.81 ± 0.02	11.45 ± 0.01	11.04 ± 0.15	5.84 ± 0.24	2.26 ± 0.93
56	2.32 ± 0.05	322± 14	16.94 ± 0.03	-23.76 ± 0.03	0.71 ± 0.05	11.40 ± 0.03	11.39 ± 0.15	1.03 ± 0.11	1.01 ± 0.42
57	2.00 ± 0.04	321± 15	18.83 ± 0.02	-21.35 ± 0.02	0.86 ± 0.04	11.50 ± 0.02	10.86 ± 0.15	11.92 ± 0.90	2.76 ± 1.15
58	1.67 ± 0.03	322± 17	18.54 ± 0.01	-21.25 ± 0.01	0.85 ± 0.03	11.38 ± 0.02	10.85 ± 0.15	10.05 ± 0.67	2.90 ± 1.20
59	2.14 ± 0.01	335± 7	18.56 ± 0.00	-21.71 ± 0.01	0.84 ± 0.01	11.44 ± 0.01	10.85 ± 0.15	7.41 ± 0.22	1.90 ± 0.79
60	2.28 ± 0.05	368± 16	18.69 ± 0.03	-21.80 ± 0.03	0.85 ± 0.04	11.64 ± 0.05	11.04 ± 0.15	10.91 ± 1.61	2.73 ± 1.14
61	2.05 ± 0.05	338± 14	18.35 ± 0.02	-21.94 ± 0.02	0.86 ± 0.03	11.57 ± 0.03	11.10 ± 0.15	8.07 ± 0.76	2.77 ± 1.15
62	2.46 ± 0.06	335± 19	18.92 ± 0.02	-21.73 ± 0.02	0.80 ± 0.03	11.55 ± 0.03	10.98 ± 0.15	9.42 ± 0.85	2.56 ± 1.07
63	2.35 ± 0.03	356± 18	19.01 ± 0.02	-21.50 ± 0.02	0.85 ± 0.03	11.42 ± 0.02	10.92 ± 0.15	8.58 ± 0.65	2.75 ± 1.15
64	2.40 ± 0.03	355± 12	18.93 ± 0.01	-21.62 ± 0.01	0.87 ± 0.03	11.42 ± 0.01	10.96 ± 0.15	7.79 ± 0.35	2.66 ± 1.10
65	2.55 ± 0.05	340± 19	19.11 ± 0.04	-21.62 ± 0.04	0.81 ± 0.07	11.43 ± 0.03	10.90 ± 0.15	7.97 ± 0.99	2.35 ± 1.00
66	1.84 ± 0.04	325± 10	18.32 ± 0.01	-21.67 ± 0.01	0.82 ± 0.02	11.41 ± 0.02	10.93 ± 0.15	7.19 ± 0.32	2.40 ± 0.99
67	2.39 ± 0.06	327± 15	18.55 ± 0.02	-22.05 ± 0.02	0.88 ± 0.04	11.51 ± 0.03	11.17 ± 0.15	6.32 ± 0.54	2.90 ± 1.21
68	1.00 ± 0.01	323± 11	17.76 ± 0.01	-20.90 ± 0.01	0.79 ± 0.02	11.17 ± 0.04	10.56 ± 0.15	8.48 ± 0.83	2.09 ± 0.86
69	2.52 ± 0.02	333± 10	18.88 ± 0.03	-21.78 ± 0.03	0.82 ± 0.05	11.42 ± 0.03	10.95 ± 0.15	6.64 ± 0.70	2.26 ± 0.95
70	1.89 ± 0.04	346± 16	18.58 ± 0.03	-21.51 ± 0.03	0.91 ± 0.05	11.51 ± 0.03	11.06 ± 0.15	10.45 ± 1.09	3.78 ± 1.58
71	2.22 ± 0.05	334± 15	18.59 ± 0.02	-21.84 ± 0.02	0.84 ± 0.03	11.54 ± 0.03	11.03 ± 0.15	8.37 ± 0.68	2.58 ± 1.07
72	2.00 ± 0.04	322± 18	18.61 ± 0.03	-21.59 ± 0.02	0.84 ± 0.05	11.33 ± 0.03	10.92 ± 0.15	6.43 ± 0.71	2.52 ± 1.06
73	2.20 ± 0.05	338± 16	18.64 ± 0.02	-21.78 ± 0.02	0.85 ± 0.03	11.52 ± 0.03	11.04 ± 0.15	8.39 ± 0.67	2.79 ± 1.16
74	1.25 ± 0.02	319± 10	17.72 ± 0.01	-21.44 ± 0.01	0.78 ± 0.02	11.27 ± 0.02	10.77 ± 0.15	6.53 ± 0.34	2.04 ± 0.84

Sersic ID	R_r [kpc]	σ_0 [km s^{-1}]	μ_r [$\frac{\mathrm{mag}}{\mathrm{arcsec}^2}$]	M_r [mag]	$(M_g - M_r)$ [mag]	$\log_{10}(M_{\mathrm{dyn}})$ [$\log_{10}(M_\odot)$]	$\log_{10}(M_*)$ [$\log_{10}(M_\odot)$]	Υ_{dyn} [$M_\odot/L_{\odot,r}$]	Υ_* [$M_\odot/L_{\odot,r}$]
75	0.58 ± 0.01	338± 17	16.76 ± 0.02	-20.71 ± 0.02	0.83 ± 0.03	10.81 ± 0.04	10.52 ± 0.15	4.38 ± 0.44	2.26 ± 0.94
76	1.92 ± 0.06	329± 18	18.56 ± 0.03	-21.56 ± 0.03	0.82 ± 0.04	11.31 ± 0.04	10.94 ± 0.15	6.32 ± 0.73	2.71 ± 1.14
77	1.91 ± 0.05	328± 13	18.48 ± 0.02	-21.60 ± 0.02	0.81 ± 0.03	11.44 ± 0.02	10.93 ± 0.15	8.24 ± 0.58	2.57 ± 1.07
78	2.49 ± 0.03	330± 8	18.55 ± 0.01	-22.11 ± 0.01	0.84 ± 0.02	11.58 ± 0.02	11.12 ± 0.15	7.19 ± 0.34	2.49 ± 1.03
79	1.92 ± 0.02	338± 9	18.40 ± 0.00	-21.66 ± 0.01	0.83 ± 0.01	11.48 ± 0.01	10.93 ± 0.15	8.50 ± 0.30	2.39 ± 0.99
80	2.54 ± 0.06	333± 16	18.84 ± 0.03	-21.88 ± 0.03	0.86 ± 0.04	11.52 ± 0.03	11.08 ± 0.15	7.67 ± 0.79	2.76 ± 1.16
81	1.80 ± 0.05	326± 13	18.60 ± 0.03	-21.36 ± 0.02	0.83 ± 0.04	11.37 ± 0.03	10.87 ± 0.15	8.84 ± 0.77	2.77 ± 1.15
82	0.26 ± 0.01	328± 15	15.44 ± 0.02	-20.33 ± 0.02	0.76 ± 0.03	10.65 ± 0.04	10.37 ± 0.15	4.37 ± 0.47	2.27 ± 0.94
83	2.35 ± 0.03	353± 10	18.37 ± 0.01	-22.16 ± 0.01	0.89 ± 0.02	11.55 ± 0.02	11.21 ± 0.15	6.29 ± 0.29	2.86 ± 1.18
84	2.32 ± 0.03	369± 12	18.91 ± 0.01	-21.58 ± 0.01	0.85 ± 0.02	11.59 ± 0.02	10.94 ± 0.15	11.79 ± 0.62	2.65 ± 1.10
85	1.19 ± 0.01	389± 15	17.76 ± 0.01	-21.26 ± 0.01	0.79 ± 0.02	11.20 ± 0.02	10.68 ± 0.15	6.46 ± 0.32	1.95 ± 0.81
86	2.58 ± 0.04	428± 17	18.43 ± 0.01	-22.33 ± 0.01	0.83 ± 0.02	11.70 ± 0.02	11.18 ± 0.15	7.67 ± 0.41	2.33 ± 0.96

Table B.2. List of the derived parameters based on the Sersic fits from Simard et al. (2011) for our alternative candidate galaxies. First column: internal Sersic IDs of our galaxies. Second column: scale radius R_r of the galaxies measured in the SDSS r band (in kpc). Third column: corrected central velocity dispersion σ_0 (in km/s). Fourth column: surface brightness μ_r measured in the SDSS r band (in mag/arcsec^2). Fifth column: absolute magnitude in r band M_r. Sixth column: g-r colour $(M_g - M_r)$ (in mag). Seventh column: logarithm of the dynamical mass M_{dyn} (in solar masses). Eighth column: logarithm of the stellar mass M_* (in solar masses). Ninth column: dynamical mass-to-light ratio Υ_{dyn} (in solar units $M_\odot/L_{\odot,r}$). Tenth column: stellar mass-to-light ratio Υ_* (in solar units $M_\odot/L_{\odot,r}$).

Appendix C: The cross-match list and, the Ta10 and Tr09 samples

SDSS DR10 ID	internal ID	Sersic ID	Taylor ID	Trujillo IDNY	SDSS DR10 ID	internal ID	Sersic ID	Taylor ID	Trujillo IDNY
1237648704060129355	-	-	55	-	1237648721255596242	1	-	-	-
1237648703523520846	2	1	-	-	1237651191892607189	3	2	-	-
1237650760782905596	-	-	-	155310	1237651538710167661	-	-	-	225402
1237651252557513010	-	3	-	-	1237651753466462236	4	-	-	-
1237652934037536913	5	4	-	-	1237654880201932994	-	-	-	460843
1237654342254002376	-	5	-	-	1237652900773298301	6	6	49	-
1237652629102067836	7	-	-	-	1237651252589363420	8	7	-	-
1237655502424769160	9	8	-	-	1237656496713892027	-	-	-	685469
1237657401874710721	-	-	62	-	1237651539246186637	10	9	-	-
1237654400765591702	-	-	30	-	1237651735773708418	11	-	-	-
1237655742944248167	-	10	-	-	1237662267538997604	-	-	21	-
1237662501086691600	-	-	38	-	1237659329240236080	12	-	-	-
1237666339727671425	13	-	19	-	1237651714798125236	14	11	-	-
1237660615586611373	-	12	-	-	1237658206124507259	15	13	-	-
1237652943695184336	-	-	-	321479	1237658204522807485	-	-	-	796740
1237652944786424004	16	14	-	-	1237652629104427133	-	-	22	-
1237658423007707334	-	15	-	-	1237660412113912034	-	-	-	929051
1237652629103968326	-	-	18	-	1237662267540570526	17	-	-	-
1237653651308871866	-	-	15	-	1237654400224592070	-	-	-	415405
1237650796219662509	-	-	14	-	1237657242435584230	-	16	-	-

SDSS DR10 ID	internal ID	Sersic ID	Taylor ID	Trujillo IDNY	SDSS DR10 ID	internal ID	Sersic ID	Taylor ID	Trujillo IDNY
1237657856067830007	-	17	-	-	1237654391106896136	-	-	-	411130
1237654952670003535	-	18	-	-	1237662524157460585	-	-	1	-
1237670956787695816	-	19	-	-	1237658300604809510	-	-	-	815852
1237652948530102500	18	20	-	-	1237653665789575334	-	-	-	417973
1237662524694659165	-	-	42	-	1237657590319022174	-	-	-	721837
1237656241159995854	19	-	-	-	1237656243317113067	20	21	-	-
1237657610723655845	-	22	-	-	1237655474503024820	21	23	-	-
1237661070319091925	-	-	8	-	1237658423018389671	-	-	-	824795
1237658424616616162	-	24	-	-	1237657769628926193	-	-	27	-
1237657190367297807	-	-	48	-	1237657596224209238	22	25	-	-
1237622264318034136	23	-	-	-	1237671265496006878	-	-	20	-
1237657401346687209	-	-	36	-	1237665569297203655	24	26	-	-
1237674650998341919	-	-	33	-	1237654605857751221	25	27	-	-
1237655126084157462	-	-	47	-	1237653614796865660	-	28	-	-
1237655463236141124	-	-	9	-	1237655465916170402	26	29	-	-
1237658204493185306	-	30	-	-	1237658206117036087	-	-	26	-
1237659324945072200	-	-	-	896687	1237657628456190055	27	31	-	-
1237657874328715438	-	-	24	-	1237661356460671120	-	-	12	-
1237659153685610726	-	-	37	-	1237660343928750289	-	-	57	-
1237660962936062177	-	-	-	986020	1237660025032081578	28	32	-	-
1237661064411349290	29	33	-	-	1237661064941929079	-	-	45	-
1237659916735397586	-	-	-	890167	1237661068721586383	-	-	61	-
1237661849849430137	30	34	-	-	1237661069261209757	-	35	-	-
1237662663746060502	-	36	-	-	1237663277928022281	31	37	-	-
1237661383314702588	32	38	-	-	1237662619722711187	-	-	50	-
1237662697568796852	33	39	-	-	1237665128542044254	-	-	34	-
1237665531170783414	-	-	56	-	1237661812272857187	34	40	-	-
1237665532252520624	35	41	-	-	1237667255083991162	-	42	-	-
1237673324323758158	-	43	-	-	1237667735054647478	-	44	-	-
1237662193459986552	-	45	-	-	1237667736104861820	-	46	-	-
1237662224087974057	36	-	-	-	1237670965389557929	-	-	39	-
1237664130483618005	37	-	-	-	1237664469510074510	38	-	-	-
1237665549429899544	39	47	35	-	1237672099780380503	40	48	-	-
1237663278461944053	41	49	-	-	1237662340012638220	42	50	-	-
1237662664292630745	-	-	11	-	1237662307269804288	-	-	52	-
1237677781740331285	-	-	41	-	1237664667887140986	43	51	-	-
1237664093432119636	44	52	-	-	1237665533335175692	-	53	54	-
1237661850400260193	45	54	-	-	1237664852035174654	46	55	-	-
1237663543683711270	-	-	43	-	1237665098466656347	-	-	63	-
1237667321652248694	-	56	-	-	1237667429035540562	47	-	-	-
1237664339328172101	-	-	-	1780650	1237673808655221213	48	-	-	-
1237667730736873763	-	57	-	-	1237665373329096903	-	-	10	-

SDSS DR10 ID	internal ID	Sersic ID	Taylor ID	Trujillo IDNY	SDSS DR10 ID	internal ID	Sersic ID	Taylor ID	Trujillo IDNY
1237664853648015625	-	-	3	-	1237664854715727968	49	-	-	-
1237662664290402490	-	58	17	-	1237665535469486145	50	59	-	-
1237665016311840908	-	60	-	-	1237667212115050932	-	61	-	-
1237667442972754078	-	-	53	-	1237665564997976239	-	62	-	-
1237663478723969457	51	63	-	-	1237665440978698364	52	-	59	-
1237667910055100586	53	64	13	-	1237667252924842120	-	-	-	2258945
1237667734526492801	54	65	-	-	1237667782277071029	-	-	46	-
1237670450522816720	-	66	-	-	1237668495245705310	-	-	-	2402259
1237663789032669425	-	67	-	-	1237662619725005006	55	-	-	-
1237664869745230095	56	-	-	-	1237665429169242591	57	68	-	-
1237665440975224988	58	-	-	-	1237668299281662070	59	69	-	-
1237668349753950509	60	70	-	-	1237670449986273410	-	-	31	-
1237661871876669606	-	-	5	-	1237667783900135493	-	71	-	-
1237668271372501042	61	72	-	-	1237648721758978188	62	73	-	-
1237663547440431315	-	-	2	-	1237668625165975629	-	-	23	-
1237668495782117442	-	74	-	-	1237648720716890184	-	-	-	54829
1237674359919363403	-	-	7	-	1237664671640715458	63	75	-	-
1237661356469387315	-	-	60	-	1237665351319552146	-	-	6	-
1237661433237733495	-	-	25	-	1237661139034046601	-	-	-	1044397
1237667735062708393	64	-	-	-	1237662237484646804	-	-	4	-
1237662335717015837	65	76	-	-	1237667782274187688	-	77	-	-
1237661087497126080	-	78	-	-	1237668585969877156	-	-	-	2434587
1237668310021440087	66	-	-	-	1237662195064438832	-	-	-	1173134
1237661358617067696	67	79	-	-	1237648721747378408	-	-	28	-
1237653651837026391	-	80	-	-	1237668298203070641	68	81	-	-
1237662336261685637	-	-	29	-	1237662224621240601	-	-	51	-
1237654604796985469	-	82	-	-	1237662236945088747	-	-	58	-
1237662336794820961	69	-	-	-	1237667917032980629	70	83	-	-
1237662224614490342	71	-	-	-	1237661950244945934	72	84	-	-
1237668333640810655	73	85	-	-	1237662236410577091	74	-	-	-
1237662302971691136	75	-	-	-	1237661971718799467	-	-	40	-
1237667917030555837	76	86	-	-					

Table C.1. Cross-match list of all IDs of all galaxies of used in this investigation. First column: Object IDs used by SDSS DR10. Second column: internal IDs of our candidate sample. Third column: Sersic IDs of the alternative sample based on the parameters from Simard et al. (2011) provided in Appendix B. Fourth column: IDs of Taylor et al. (2010) as listed in their paper. Fifth column: IDNY from Trujillo et al. (2009).

Taylor ID	SDSS DR10 ID	ra [°]	dec [°]	z	$m_{sdss,r}$ [mag]	a_{sdss} [arcsec]	σ_{sdss} [km/s]	$q_{b/a}$	$\mathcal{L}_{ETG}$
55	1237648704060129355	228.8519	-0.3402	0.1001	16.49 ± 0.00	1.62 ± 0.03	359± 11	0.84	0.86
49	1237652900773298301	58.0541	-5.8611	0.1137	17.25 ± 0.01	1.03 ± 0.02	306± 14	0.38	0.66
62	1237657401874710721	121.4479	32.8120	0.1203	16.97 ± 0.01	1.38 ± 0.03	227± 10	0.80	0.78
30	1237654400765591702	178.7375	65.7964	0.1071	16.74 ± 0.00	1.11 ± 0.01	192± 8	0.62	0.75
21	1237662267538997604	231.9958	5.0639	0.0872	16.94 ± 0.00	1.00 ± 0.02	229± 8	0.85	0.88
38	1237662501086691600	253.5743	26.9582	0.1035	17.10 ± 0.00	0.81 ± 0.01	174± 8	0.46	0.67
19	1237666339727671425	20.8205	0.2955	0.0928	17.10 ± 0.00	1.11 ± 0.02	296± 11	0.73	0.88
22	1237652629104427133	13.5572	-10.6207	0.1189	17.70 ± 0.01	0.83 ± 0.04	143± 14	0.91	0.86

Taylor ID	SDSS DR10 ID	ra [°]	dec [°]	z	$m_{\mathrm{sdss},r}$ [mag]	a_{sdss} [arcsec]	σ_{sdss} [km/s]	$q_{b/a}$	$\mathcal{L}_{\mathrm{ETG}}$
18	1237652629103968326	12.4721	-10.7547	0.0983	17.36 ± 0.01	1.06 ± 0.04	184± 12	0.90	0.68
15	1237653651308871866	25.4214	13.6498	0.0724	16.43 ± 0.00	1.25 ± 0.02	183± 6	0.87	0.81
14	1237650796219662509	145.3475	0.0544	0.0913	17.08 ± 0.00	0.95 ± 0.02	163± 7	0.98	0.84
1	1237662524157460585	190.1666	13.8156	0.0865	16.38 ± 0.00	1.02 ± 0.02	160± 6	0.77	0.83
42	1237662524694659165	190.9405	14.1608	0.0877	16.59 ± 0.00	1.43 ± 0.02	231± 8	0.58	0.76
8	1237661070319091925	143.0571	11.7045	0.0821	16.49 ± 0.00	0.90 ± 0.01	166± 6	0.86	0.70
27	1237657769628926193	131.3568	41.5528	0.1015	16.96 ± 0.00	1.19 ± 0.03	192± 8	0.98	0.79
48	1237657190367297807	357.6717	-0.6124	0.0794	16.07 ± 0.00	1.77 ± 0.02	187± 7	0.58	0.68
20	1237671265496006878	191.8619	-1.5344	0.0887	16.89 ± 0.00	1.16 ± 0.02	249± 10	0.64	0.83
36	1237657401346687209	141.6903	45.8730	0.0799	16.53 ± 0.00	1.23 ± 0.02	221± 9	0.98	0.79
33	1237674650998341919	170.7120	0.4215	0.1040	17.18 ± 0.01	1.12 ± 0.02	259± 9	0.70	0.63
47	1237655126084157462	187.1464	5.5812	0.0676	15.30 ± 0.00	1.52 ± 0.01	175± 4	0.87	0.88
9	1237655463236141124	204.6658	59.8185	0.0707	16.43 ± 0.00	1.16 ± 0.01	235± 7	0.78	0.82
26	1237658206117036087	166.7747	49.6303	0.1069	17.17 ± 0.00	1.07 ± 0.03	189± 10	0.96	0.77
24	1237657874328715438	139.8645	40.1167	0.0937	16.73 ± 0.00	1.29 ± 0.03	167± 7	0.89	0.89
12	1237661356460671120	153.4443	42.0479	0.1060	17.03 ± 0.00	0.93 ± 0.01	143± 8	0.71	0.81
37	1237659153685610726	254.3686	26.7014	0.1198	17.66 ± 0.01	1.00 ± 0.04	203± 12	0.92	0.82
57	1237660343928750289	127.0233	30.0714	0.1097	17.13 ± 0.01	1.90 ± 0.06	129± 9	0.96	0.91
45	1237661064941929079	124.0758	5.9420	0.1032	17.00 ± 0.00	1.01 ± 0.02	221± 11	0.98	0.81
61	1237661068721586383	173.8238	13.9530	0.0821	15.61 ± 0.00	2.25 ± 0.02	279± 7	0.89	0.97
50	1237662619722711187	235.1621	32.1894	0.1183	17.18 ± 0.01	2.25 ± 0.04	173± 15	0.56	0.75
34	1237665128542044254	179.5965	35.0486	0.0807	16.69 ± 0.00	1.39 ± 0.02	199± 8	0.79	0.87
56	1237665531170783414	203.4256	25.7488	0.0742	15.59 ± 0.00	2.70 ± 0.02	237± 6	0.96	1.00
39	1237670965389557929	149.4396	16.5398	0.1017	16.72 ± 0.00	1.25 ± 0.02	183± 7	0.64	0.74
35	1237665549429899544	223.0734	22.4871	0.1165	17.39 ± 0.01	0.78 ± 0.01	335± 13	0.29	0.62
11	1237662664292630745	244.4193	24.3831	0.0829	17.20 ± 0.01	1.70 ± 0.04	152± 9	0.57	0.83
52	1237662307269804288	232.0260	32.5324	0.0918	16.49 ± 0.00	1.56 ± 0.02	247± 8	0.68	0.79
41	1237667781740331285	135.7019	14.4294	0.1141	16.97 ± 0.00	0.96 ± 0.02	163± 6	0.82	0.87
54	1237665533335175692	243.8410	16.3942	0.0818	15.87 ± 0.00	1.86 ± 0.01	311± 7	0.58	0.81
43	1237663543683711270	331.9419	0.3080	0.0978	17.05 ± 0.01	1.20 ± 0.03	216± 12	0.94	0.88
63	1237665098466656347	149.9874	30.2277	0.0833	15.61 ± 0.00	2.62 ± 0.03	289± 8	0.66	0.90
10	1237665373329096903	230.2855	24.2198	0.0813	16.75 ± 0.00	1.17 ± 0.02	153± 6	0.98	0.79
3	1237664853648015625	225.3171	30.5827	0.0984	17.05 ± 0.00	0.92 ± 0.01	195± 6	0.70	0.88
17	1237662664290402490	239.6933	27.2131	0.0879	17.04 ± 0.00	1.17 ± 0.02	292± 15	0.79	0.74
53	1237667442972754078	189.3463	27.3214	0.1009	16.61 ± 0.00	1.39 ± 0.02	256± 8	0.84	0.91
59	1237665440978698364	194.2722	28.9814	0.0686	15.45 ± 0.00	2.19 ± 0.01	340± 8	0.57	0.78
13	1237667910055100586	181.7985	23.8744	0.0775	16.55 ± 0.00	1.21 ± 0.02	328± 11	0.77	0.86
46	1237667782277071029	135.2174	14.7181	0.0959	17.63 ± 0.01	1.24 ± 0.04	204± 11	0.82	0.84
31	1237670449986273410	138.7474	16.3422	0.0909	16.88 ± 0.00	1.61 ± 0.03	167± 8	0.65	0.78
5	1237661871876669606	215.4104	40.0323	0.1003	17.51 ± 0.01	1.06 ± 0.02	176± 10	0.42	0.74
2	1237663547440431315	127.0272	55.3799	0.0669	16.42 ± 0.00	1.31 ± 0.03	191± 7	0.93	0.81
23	1237668625165975629	199.4207	17.6978	0.0739	15.97 ± 0.00	1.50 ± 0.01	141± 5	0.65	0.80

Taylor ID	SDSS DR10 ID	ra [°]	dec [°]	z	$m_{sdss,r}$ [mag]	a_{sdss} [arcsec]	σ_{sdss} [km/s]	$q_{b/a}$	$\mathcal{L}_{ETG}$
7	1237674365919363403	118.8170	33.2286	0.0985	17.06 ± 0.00	0.92 ± 0.01	154± 7	0.62	0.67
60	1237661356469387315	180.7761	46.6946	0.0730	15.16 ± 0.00	1.91 ± 0.01	267± 6	0.64	0.93
6	1237665351319552146	222.1299	26.4879	0.1063	16.80 ± 0.00	0.71 ± 0.02	155± 6	0.92	0.68
25	1237661433237733495	195.3300	46.1813	0.0914	16.77 ± 0.00	1.22 ± 0.02	212± 9	0.63	0.80
4	1237662237484646804	227.0853	7.2533	0.0770	16.79 ± 0.00	1.03 ± 0.02	199± 8	1.00	0.76
28	1237648721747378408	133.7980	0.2189	0.1020	16.60 ± 0.00	0.95 ± 0.01	183± 6	0.44	0.72
29	1237662336261685637	252.5918	22.1319	0.1182	17.62 ± 0.01	0.78 ± 0.01	262± 14	0.43	0.73
51	1237662224621240601	230.9765	29.9078	0.1128	17.09 ± 0.01	1.42 ± 0.03	207± 11	0.80	0.88
58	1237662236945088747	220.8522	7.6574	0.0842	15.48 ± 0.00	1.64 ± 0.02	234± 5	0.93	0.87
40	1237661971718799467	176.6058	7.6119	0.0867	16.17 ± 0.01	1.17 ± 0.01	206± 5	0.61	0.74

Table C.2. List of the basic parameters of all galaxies in our basic sample that are also parts of the galaxies provided in Taylor et al. (2010). First column: IDs used in the table in their paper. Second column: object ID used by SDSS DR10. Third and fourth column: equatorial coordinates of the galaxies. Fifth column: redshift z, already corrected for our motion relative to the CMB. Sixth, seventh, and eighth columns: observed uncorrected refitted SDSS parameters in the following order: observed apparent magnitude m_{sdss}, angular semi-major axis a_{sdss}, central velocity dispersion σ_{sdss}. Ninth column: axis ratio $q_{b/a}$. Tenth column: GalaxyZoo probability $\mathcal{L}_{ETG}$ of the galaxy being classified as an early-type.

Taylor ID	R_r [kpc]	σ_0 [km s^{-1}]	μ_r [$\frac{mag}{arcsec^2}$]	M_r [mag]	$(M_g - M_r)$ [mag]	M_z [mag]	$\log_{10}(M_{dyn})$ [$\log_{10}(M_\odot)$]	$\log_{10}(M_*)$ [$\log_{10}(M_\odot)$]	Υ_{dyn} [$M_\odot/L_{\odot,r}$]	Υ_* [$M_\odot/L_{\odot,r}$]
55	2.76 ± 0.05	391± 12	18.80 ± 0.04	-22.08 ± 0.01	0.77 ± 0.01	-22.68 ± 0.01	11.69 ± 0.02	11.12 ± 0.15	9.39 ± 0.40	2.51 ± 1.04
49	1.32 ± 0.04	344± 15	17.50 ± 0.06	-21.79 ± 0.01	0.77 ± 0.01	-22.46 ± 0.01	11.26 ± 0.02	10.95 ± 0.15	4.54 ± 0.26	2.23 ± 0.92
62	2.71 ± 0.06	248± 11	18.81 ± 0.05	-22.05 ± 0.01	0.76 ± 0.01	-22.91 ± 0.01	11.29 ± 0.02	11.23 ± 0.15	3.84 ± 0.21	3.32 ± 1.37
30	1.72 ± 0.02	213± 9	17.99 ± 0.03	-21.87 ± 0.01	0.69 ± 0.01	-22.40 ± 0.01	10.96 ± 0.02	10.91 ± 0.15	2.12 ± 0.10	1.89 ± 0.78
21	1.51 ± 0.03	253± 8	18.29 ± 0.04	-21.27 ± 0.01	0.81 ± 0.01	-21.98 ± 0.01	11.05 ± 0.02	10.80 ± 0.15	4.57 ± 0.19	2.55 ± 1.05
38	1.04 ± 0.03	197± 10	17.15 ± 0.05	-21.62 ± 0.01	0.76 ± 0.01	-22.20 ± 0.01	10.67 ± 0.02	10.83 ± 0.15	1.38 ± 0.08	2.00 ± 0.83
19	1.66 ± 0.03	327± 13	18.54 ± 0.04	-21.22 ± 0.01	0.76 ± 0.01	-21.87 ± 0.01	11.31 ± 0.02	10.78 ± 0.15	8.76 ± 0.41	2.58 ± 1.07
22	1.72 ± 0.08	159± 16	18.62 ± 0.10	-21.25 ± 0.01	0.85 ± 0.02	-21.87 ± 0.02	10.70 ± 0.05	10.87 ± 0.15	2.09 ± 0.24	3.03 ± 1.25
18	1.84 ± 0.07	203± 14	18.90 ± 0.09	-21.10 ± 0.01	0.76 ± 0.02	-21.83 ± 0.01	10.94 ± 0.03	10.82 ± 0.15	4.18 ± 0.34	3.11 ± 1.28
15	1.62 ± 0.03	201± 7	18.33 ± 0.04	-21.37 ± 0.01	0.75 ± 0.01	-22.02 ± 0.01	10.88 ± 0.02	10.78 ± 0.15	2.84 ± 0.12	2.21 ± 0.91
14	1.61 ± 0.04	180± 8	18.39 ± 0.05	-21.31 ± 0.01	0.81 ± 0.01	-21.89 ± 0.01	10.78 ± 0.02	10.79 ± 0.15	2.38 ± 0.13	2.41 ± 1.00
1	1.45 ± 0.02	178± 6	17.71 ± 0.04	-21.76 ± 0.01	0.69 ± 0.01	-22.26 ± 0.01	10.73 ± 0.02	10.76 ± 0.15	1.38 ± 0.06	1.50 ± 0.62
42	1.79 ± 0.03	254± 9	18.34 ± 0.03	-21.59 ± 0.01	0.79 ± 0.01	-22.21 ± 0.01	11.13 ± 0.02	10.88 ± 0.15	4.07 ± 0.17	2.27 ± 0.94
8	1.30 ± 0.01	185± 7	17.72 ± 0.03	-21.51 ± 0.01	0.69 ± 0.01	-22.09 ± 0.01	10.71 ± 0.02	10.69 ± 0.15	1.69 ± 0.07	1.59 ± 0.66
27	2.23 ± 0.05	210± 9	18.85 ± 0.05	-21.56 ± 0.01	0.74 ± 0.01	-22.15 ± 0.01	11.06 ± 0.02	10.76 ± 0.15	3.54 ± 0.18	1.78 ± 0.74
48	2.03 ± 0.02	204± 8	18.31 ± 0.03	-21.88 ± 0.01	0.71 ± 0.01	-22.46 ± 0.01	10.99 ± 0.02	11.01 ± 0.15	2.28 ± 0.10	2.36 ± 0.98
20	1.55 ± 0.03	276± 11	18.30 ± 0.04	-21.31 ± 0.01	0.80 ± 0.01	-21.91 ± 0.01	11.14 ± 0.02	10.79 ± 0.15	5.32 ± 0.26	2.39 ± 0.99
36	1.84 ± 0.03	242± 9	18.56 ± 0.04	-21.42 ± 0.01	0.80 ± 0.01	-22.12 ± 0.01	11.10 ± 0.02	10.89 ± 0.15	4.40 ± 0.20	2.72 ± 1.12
33	1.80 ± 0.03	286± 10	18.53 ± 0.04	-21.43 ± 0.01	0.80 ± 0.01	-22.04 ± 0.01	11.23 ± 0.02	10.83 ± 0.15	6.02 ± 0.26	2.39 ± 0.99
47	1.85 ± 0.02	190± 5	17.74 ± 0.02	-22.24 ± 0.00	0.70 ± 0.01	-22.74 ± 0.01	10.89 ± 0.01	10.97 ± 0.15	1.30 ± 0.04	1.56 ± 0.64
9	1.38 ± 0.02	259± 7	18.15 ± 0.03	-21.20 ± 0.01	0.77 ± 0.01	-21.84 ± 0.01	11.03 ± 0.01	10.74 ± 0.15	4.67 ± 0.16	2.38 ± 0.98
26	2.07 ± 0.06	209± 11	18.81 ± 0.06	-21.46 ± 0.01	0.76 ± 0.01	-22.08 ± 0.01	11.02 ± 0.02	10.84 ± 0.15	3.59 ± 0.22	2.38 ± 0.98
24	2.13 ± 0.05	183± 8	18.74 ± 0.05	-21.57 ± 0.01	0.74 ± 0.01	-22.15 ± 0.01	10.92 ± 0.02	10.85 ± 0.15	2.56 ± 0.13	2.18 ± 0.90
12	1.54 ± 0.03	160± 9	18.06 ± 0.04	-21.55 ± 0.01	0.69 ± 0.01	-22.13 ± 0.01	10.66 ± 0.03	10.68 ± 0.15	1.42 ± 0.09	1.51 ± 0.62
37	2.09 ± 0.08	225± 13	18.91 ± 0.08	-21.38 ± 0.01	0.82 ± 0.02	-22.07 ± 0.02	11.09 ± 0.03	10.89 ± 0.15	4.50 ± 0.32	2.81 ± 1.16

Taylor ID	R_r [kpc]	σ_0 [km s^{-1}]	μ_r [$\frac{mag}{arcsec^2}$]	M_r [mag]	$(M_g - M_r)$ [mag]	M_z [mag]	$\log_{10}(M_{dyn})$ [$\log_{10}(M_\odot)$]	$\log_{10}(M_*)$ [$\log_{10}(M_\odot)$]	Υ_{dyn} [$M_\odot/L_{\odot,r}$]	Υ_* [$M_\odot/L_{\odot,r}$]
57	3.76 ± 0.12	139± 10	19.96 ± 0.07	-21.61 ± 0.01	0.67 ± 0.01	-22.20 ± 0.01	10.92 ± 0.03	10.84 ± 0.15	2.50 ± 0.20	2.06 ± 0.85
45	1.90 ± 0.04	244± 12	18.52 ± 0.05	-21.56 ± 0.01	0.81 ± 0.01	-22.16 ± 0.01	11.12 ± 0.02	10.98 ± 0.15	4.11 ± 0.24	2.95 ± 1.22
61	3.31 ± 0.03	299± 7	18.83 ± 0.02	-22.42 ± 0.01	1.05 ± 0.01	-23.02 ± 0.01	11.54 ± 0.01	11.19 ± 0.15	4.83 ± 0.14	2.19 ± 0.90
50	3.64 ± 0.09	187± 16	19.75 ± 0.05	-21.74 ± 0.01	0.77 ± 0.01	-22.18 ± 0.01	11.17 ± 0.04	10.83 ± 0.15	3.86 ± 0.35	1.78 ± 0.74
34	1.89 ± 0.03	218± 9	18.78 ± 0.03	-21.26 ± 0.01	0.79 ± 0.01	-21.89 ± 0.01	11.02 ± 0.02	10.83 ± 0.15	4.29 ± 0.20	2.74 ± 1.13
56	3.74 ± 0.03	252± 7	19.37 ± 0.02	-22.14 ± 0.01	0.81 ± 0.01	-22.71 ± 0.01	11.44 ± 0.01	11.12 ± 0.15	5.00 ± 0.15	2.37 ± 0.98
39	1.89 ± 0.04	202± 8	18.24 ± 0.04	-21.81 ± 0.01	0.69 ± 0.01	-22.38 ± 0.01	10.95 ± 0.02	10.90 ± 0.15	2.19 ± 0.10	1.93 ± 0.80
35	0.89 ± 0.02	383± 15	16.94 ± 0.05	-21.50 ± 0.01	0.80 ± 0.01	-22.20 ± 0.01	11.18 ± 0.02	10.87 ± 0.15	4.96 ± 0.25	2.45 ± 1.01
11	2.00 ± 0.06	166± 9	19.22 ± 0.06	-20.95 ± 0.01	0.71 ± 0.01	-21.56 ± 0.02	10.81 ± 0.03	10.53 ± 0.15	3.51 ± 0.23	1.86 ± 0.77
52	2.22 ± 0.03	270± 9	18.60 ± 0.03	-21.80 ± 0.01	0.83 ± 0.01	-22.43 ± 0.01	11.27 ± 0.02	10.99 ± 0.15	4.67 ± 0.19	2.45 ± 1.01
41	1.81 ± 0.03	181± 6	18.11 ± 0.04	-21.87 ± 0.01	0.72 ± 0.01	-22.47 ± 0.01	10.84 ± 0.02	10.87 ± 0.15	1.62 ± 0.07	1.75 ± 0.72
54	2.18 ± 0.02	339± 7	18.14 ± 0.02	-22.21 ± 0.01	0.76 ± 0.01	-22.87 ± 0.01	11.46 ± 0.01	11.12 ± 0.15	4.97 ± 0.14	2.25 ± 0.93
43	2.12 ± 0.05	238± 13	18.78 ± 0.05	-21.52 ± 0.01	0.77 ± 0.01	-22.15 ± 0.01	11.14 ± 0.02	10.88 ± 0.15	4.47 ± 0.27	2.42 ± 1.00
63	3.34 ± 0.05	310± 9	18.85 ± 0.03	-22.42 ± 0.01	0.80 ± 0.01	-23.08 ± 0.01	11.57 ± 0.01	11.30 ± 0.15	5.22 ± 0.18	2.80 ± 1.15
10	1.78 ± 0.03	168± 6	18.60 ± 0.03	-21.31 ± 0.01	0.78 ± 0.01	-21.90 ± 0.01	10.77 ± 0.02	10.80 ± 0.15	2.30 ± 0.10	2.49 ± 1.03
3	1.42 ± 0.02	218± 7	18.06 ± 0.04	-21.37 ± 0.01	0.74 ± 0.01	-21.94 ± 0.01	10.89 ± 0.02	10.71 ± 0.15	2.88 ± 0.11	1.92 ± 0.79
17	1.71 ± 0.03	322± 17	18.64 ± 0.04	-21.19 ± 0.01	0.82 ± 0.01	-21.89 ± 0.01	11.31 ± 0.02	10.82 ± 0.15	9.00 ± 0.54	2.88 ± 1.19
53	2.39 ± 0.04	280± 9	18.70 ± 0.03	-21.87 ± 0.01	0.79 ± 0.01	-22.50 ± 0.01	11.34 ± 0.02	11.05 ± 0.15	5.08 ± 0.20	2.60 ± 1.07
59	2.17 ± 0.02	368± 9	18.22 ± 0.02	-22.10 ± 0.01	0.84 ± 0.01	-22.80 ± 0.01	11.53 ± 0.01	11.10 ± 0.15	6.43 ± 0.19	2.37 ± 0.98
13	1.57 ± 0.03	361± 12	18.30 ± 0.03	-21.33 ± 0.01	0.76 ± 0.01	-21.91 ± 0.01	11.38 ± 0.02	10.85 ± 0.15	9.11 ± 0.39	2.70 ± 1.12
46	2.01 ± 0.07	224± 12	19.33 ± 0.07	-20.85 ± 0.01	0.86 ± 0.02	-21.65 ± 0.01	11.07 ± 0.03	10.83 ± 0.15	6.97 ± 0.47	4.04 ± 1.67
31	2.21 ± 0.05	182± 8	19.00 ± 0.05	-21.39 ± 0.01	0.71 ± 0.01	-22.01 ± 0.01	10.93 ± 0.02	10.75 ± 0.15	3.10 ± 0.17	2.05 ± 0.85
5	1.28 ± 0.04	197± 12	18.26 ± 0.06	-20.95 ± 0.01	0.75 ± 0.01	-21.78 ± 0.01	10.76 ± 0.03	10.57 ± 0.15	3.13 ± 0.22	2.01 ± 0.83
2	1.63 ± 0.03	209± 7	18.54 ± 0.04	-21.16 ± 0.01	0.74 ± 0.01	-21.82 ± 0.01	10.92 ± 0.02	10.72 ± 0.15	3.72 ± 0.16	2.35 ± 0.97
23	1.71 ± 0.02	154± 6	18.04 ± 0.02	-21.77 ± 0.00	0.67 ± 0.01	-22.29 ± 0.01	10.68 ± 0.02	10.77 ± 0.15	1.21 ± 0.05	1.52 ± 0.63
7	1.32 ± 0.02	172± 8	17.84 ± 0.04	-21.44 ± 0.01	0.70 ± 0.01	-22.12 ± 0.01	10.66 ± 0.02	10.78 ± 0.15	1.58 ± 0.08	2.09 ± 0.86
60	2.13 ± 0.02	290± 6	17.73 ± 0.02	-22.55 ± 0.00	0.74 ± 0.01	-23.23 ± 0.01	11.32 ± 0.01	11.02 ± 0.15	2.59 ± 0.07	1.29 ± 0.53
6	1.33 ± 0.04	174± 7	17.48 ± 0.05	-21.83 ± 0.01	0.69 ± 0.01	-22.38 ± 0.01	10.67 ± 0.02	10.84 ± 0.15	1.13 ± 0.05	1.66 ± 0.68
25	1.66 ± 0.03	235± 10	18.29 ± 0.04	-21.47 ± 0.01	0.78 ± 0.01	-22.07 ± 0.01	11.03 ± 0.02	10.81 ± 0.15	3.58 ± 0.17	2.17 ± 0.90
4	1.50 ± 0.04	220± 9	18.44 ± 0.05	-21.09 ± 0.01	0.77 ± 0.01	-21.74 ± 0.01	10.93 ± 0.02	10.69 ± 0.15	4.02 ± 0.20	2.34 ± 0.97
28	1.20 ± 0.02	206± 6	17.08 ± 0.03	-21.99 ± 0.01	0.67 ± 0.01	-22.54 ± 0.01	10.77 ± 0.01	10.84 ± 0.15	1.24 ± 0.04	1.46 ± 0.60
29	1.10 ± 0.03	297± 16	17.54 ± 0.06	-21.37 ± 0.01	0.83 ± 0.02	-22.06 ± 0.02	11.05 ± 0.02	10.88 ± 0.15	4.20 ± 0.26	2.83 ± 1.17
51	2.62 ± 0.06	227± 12	19.08 ± 0.05	-21.70 ± 0.01	0.82 ± 0.01	-22.26 ± 0.01	11.19 ± 0.02	10.93 ± 0.15	4.29 ± 0.26	2.31 ± 0.95
58	2.52 ± 0.03	253± 5	18.02 ± 0.03	-22.64 ± 0.00	0.70 ± 0.01	-23.22 ± 0.01	11.27 ± 0.01	11.18 ± 0.15	2.15 ± 0.06	1.74 ± 0.72
40	1.49 ± 0.02	229± 6	17.58 ± 0.03	-21.95 ± 0.00	0.72 ± 0.01	-22.54 ± 0.01	10.96 ± 0.01	10.88 ± 0.15	1.97 ± 0.06	1.65 ± 0.68

Table C.3. List of the derived parameters of all galaxies in our basic sample that are also parts of the galaxies provided in Taylor et al. (2010). First column: IDs used in the table in their paper. Second column: scale radius R_r of the galaxies measured in the SDSS r band (in kpc). Third column: corrected central velocity dispersion σ_0 (in km/s). Fourth column: surface brightness μ_r measured in the SDSS r band (in mag/arcsec^2). Fifth column: absolute magnitude in r band M_r. Sixth column: g-r colour $(M_g - M_r)$ (in mag). Seventh column: logarithm of the dynamical mass M_{dyn} (in solar masses). Eighth column: logarithm of the stellar mass M_* (in solar masses). Ninth column: dynamical mass-to-light ratio Υ_{dyn} (in solar units $M_\odot/L_{\odot,r}$). Tenth column: stellar mass-to-light ratio Υ_* (in solar units $M_\odot/L_{\odot,r}$).

Trujillo IDNY	SDSS DR10 ID	ra [°]	dec [°]	z	$m_{sdss,r}$ [mag]	a_{sdss} [arcsec]	σ_{sdss} [km/s]	$q_{b/a}$	$\mathcal{L}_{ETG}$
155310	1237650760782905596	186.7713	-3.2216	0.1665	17.42 ± 0.01	0.59 ± 0.01	202± 8	0.44	0.78
225402	1237651538710167661	172.5828	66.8247	0.1441	17.09 ± 0.00	0.76 ± 0.01	188± 5	0.22	0.55
460843	1237654880201932994	219.0524	4.0700	0.1534	17.50 ± 0.01	0.49 ± 0.01	204± 9	0.56	0.53
685469	1237654967138920271237654967138892027	335.4180	13.9873	0.1486	17.33 ± 0.01	0.90 ± 0.01	174± 9	0.45	0.69
321479	1237652943695184336	320.2198	11.1203	0.1274	16.64 ± 0.00	0.76 ± 0.01	216± 8	0.48	0.82
796740	1237658204522807485	221.9016	43.4960	0.1828	17.59 ± 0.01	0.70 ± 0.01	178± 9	0.34	0.69
929051	1237660412113912034	139.8602	6.8893	0.1856	17.50 ± 0.01	0.48 ± 0.01	168± 12	0.78	0.56
415405	1237654400224592070	157.7106	62.9833	0.1675	17.65 ± 0.01	0.71 ± 0.01	189± 10	0.29	0.53
411130	1237654391106896136	127.3659	46.2254	0.1683	17.66 ± 0.01	0.80 ± 0.01	199± 9	0.26	0.59
815852	1237658300604809510	151.6223	7.2351	0.1222	16.64 ± 0.00	0.83 ± 0.01	181± 7	0.62	0.62
417973	1237653665789575334	135.8508	2.4459	0.1890	17.38 ± 0.01	0.82 ± 0.01	221± 10	0.25	0.55
721837	1237657590319022174	167.9007	53.6700	0.1427	16.80 ± 0.00	0.51 ± 0.01	186± 5	0.74	0.78
824795	1237658423018389671	163.3506	6.4059	0.1873	17.65 ± 0.01	0.58 ± 0.01	189± 10	0.63	0.74
896687	1237659324945072200	218.9466	54.5913	0.1305	16.59 ± 0.00	0.66 ± 0.01	187± 6	0.96	0.80
986020	1237660962936062177	129.8227	30.6294	0.1798	17.76 ± 0.01	0.58 ± 0.01	233± 11	0.43	0.81
890167	1237659161735397586	234.8920	44.2979	0.1436	17.36 ± 0.01	0.53 ± 0.01	155± 9	0.49	0.54
1780650	1237664339328172101	180.7131	38.2790	0.1579	17.36 ± 0.01	0.67 ± 0.01	211± 10	0.57	0.60
2258945	1237667252924842120	141.8472	21.9347	0.1686	17.22 ± 0.01	0.87 ± 0.01	231± 9	0.29	0.54
2402259	1237668495245705310	177.6347	17.0510	0.1566	17.07 ± 0.00	0.56 ± 0.02	213± 10	1.00	0.76
54829	1237648720716890184	232.5811	-0.4885	0.0861	16.09 ± 0.00	0.78 ± 0.01	130± 4	0.92	0.75
1044397	1237661139034046601	154.1551	39.0343	0.1965	17.77 ± 0.01	0.62 ± 0.02	196± 10	0.68	0.80
2434587	1237668585969877156	169.2473	17.1548	0.1739	17.67 ± 0.01	0.61 ± 0.01	199± 10	0.48	0.76
1173134	1237662195064438832	188.1617	42.8557	0.1668	17.76 ± 0.01	0.84 ± 0.02	202± 12	0.30	0.79

Table C.4. List of the basic parameters of all galaxies in our basic sample that are also parts of the galaxies provided in Trujillo et al. (2009). First column: IDNYs used in the table in their paper. Second column: object ID used by SDSS DR10. Third and fourth column: equatorial coordinates of the galaxies. Fifth column: redshift z, already corrected for our motion relative to the CMB. Sixth, seventh, and eighth columns: observed uncorrected refitted SDSS parameters in the following order: observed apparent magnitude m_{sdss}, angular semi-major axis a_{sdss}, central velocity dispersion σ_{sdss}. Ninth column: axis ratio $q_{b/a}$. Tenth column: GalaxyZoo probability $\mathcal{L}_{ETG}$ of the galaxy being classified as an early-type.

Trujillo IDNY	R_r [kpc]	σ_0 [km s^{-1}]	μ_r [$\frac{mag}{arcsec^2}$]	M_r [mag]	$(M_g - M_r)$ [mag]	M_z [mag]	$\log_{10}(M_{dyn})$ [$\log_{10}(M_\odot)$]	$\log_{10}(M_*)$ [$\log_{10}(M_\odot)$]	Υ_{dyn} [$M_\odot/L_{\odot,r}$]	Υ_* [$M_\odot/L_{\odot,r}$]
155310	1.14 ± 0.02	232± 9	16.67 ± 0.05	-22.35 ± 0.01	0.69 ± 0.01	-22.91 ± 0.01	10.85 ± 0.02	11.02 ± 0.15	1.06 ± 0.05	1.57 ± 0.65
225402	0.92 ± 0.02	217± 5	16.31 ± 0.04	-22.23 ± 0.01	0.71 ± 0.01	-22.81 ± 0.01	10.70 ± 0.01	11.02 ± 0.15	0.84 ± 0.03	1.74 ± 0.72
460843	1.00 ± 0.02	234± 10	16.66 ± 0.05	-22.07 ± 0.01	0.72 ± 0.01	-22.59 ± 0.01	10.80 ± 0.02	10.94 ± 0.15	1.23 ± 0.06	1.67 ± 0.69
685469	1.58 ± 0.03	196± 10	17.49 ± 0.04	-22.23 ± 0.01	0.72 ± 0.01	-22.76 ± 0.01	10.85 ± 0.02	11.02 ± 0.15	1.18 ± 0.07	1.74 ± 0.72
321479	1.21 ± 0.02	245± 9	16.60 ± 0.03	-22.52 ± 0.01	0.63 ± 0.01	-23.01 ± 0.01	10.93 ± 0.02	10.91 ± 0.15	1.08 ± 0.05	1.04 ± 0.43
796740	1.28 ± 0.04	204± 10	16.93 ± 0.07	-22.36 ± 0.01	0.71 ± 0.01	-22.85 ± 0.02	10.79 ± 0.03	11.01 ± 0.15	0.92 ± 0.06	1.50 ± 0.62
929051	1.35 ± 0.04	192± 14	16.90 ± 0.06	-22.51 ± 0.01	0.66 ± 0.01	-22.98 ± 0.02	10.76 ± 0.03	10.98 ± 0.15	0.75 ± 0.06	1.24 ± 0.51
415405	1.12 ± 0.02	217± 12	16.91 ± 0.04	-22.08 ± 0.01	0.75 ± 0.01	-22.65 ± 0.01	10.79 ± 0.02	11.00 ± 0.15	1.18 ± 0.07	1.92 ± 0.79
411130	1.20 ± 0.03	228± 10	17.02 ± 0.06	-22.13 ± 0.01	0.73 ± 0.01	-22.66 ± 0.01	10.86 ± 0.02	10.99 ± 0.15	1.34 ± 0.07	1.82 ± 0.75
815852	1.45 ± 0.03	204± 8	17.21 ± 0.04	-22.30 ± 0.01	0.67 ± 0.01	-22.90 ± 0.01	10.85 ± 0.02	10.95 ± 0.15	1.10 ± 0.05	1.40 ± 0.58
417973	1.33 ± 0.04	252± 12	16.68 ± 0.06	-22.71 ± 0.01	0.67 ± 0.01	-23.23 ± 0.01	10.99 ± 0.02	11.14 ± 0.15	1.06 ± 0.06	1.51 ± 0.62
721837	1.11 ± 0.02	212± 6	16.48 ± 0.04	-22.46 ± 0.00	0.64 ± 0.01	-22.94 ± 0.01	10.76 ± 0.01	11.01 ± 0.15	0.78 ± 0.03	1.38 ± 0.57
824795	1.47 ± 0.04	215± 12	17.20 ± 0.06	-22.41 ± 0.01	0.70 ± 0.01	-23.02 ± 0.01	10.90 ± 0.03	11.05 ± 0.15	1.13 ± 0.07	1.59 ± 0.66

Trujillo IDNY	R_r [kpc]	σ_0 [km s^{-1}]	μ_r [$\frac{mag}{arcsec^2}$]	M_r [mag]	$(M_g - M_r)$ [mag]	M_z [mag]	$\log_{10}(M_{dyn})$ [$\log_{10}(M_\odot)$]	$\log_{10}(M_*)$ [$\log_{10}(M_\odot)$]	Υ_{dyn} [$M_\odot/L_{\odot,r}$]	Υ_* [$M_\odot/L_{\odot,r}$]
896687	1.51 ± 0.03	211± 7	17.15 ± 0.04	-22.46 ± 0.00	0.64 ± 0.01	-22.87 ± 0.01	10.89 ± 0.02	10.98 ± 0.15	1.06 ± 0.04	1.31 ± 0.54
986020	1.17 ± 0.03	268± 12	16.89 ± 0.06	-22.22 ± 0.01	0.73 ± 0.01	-22.79 ± 0.01	10.99 ± 0.02	11.01 ± 0.15	1.65 ± 0.09	1.72 ± 0.71
890167	0.95 ± 0.02	178± 10	16.66 ± 0.05	-21.96 ± 0.01	0.68 ± 0.01	-22.61 ± 0.01	10.54 ± 0.03	10.91 ± 0.15	0.76 ± 0.05	1.75 ± 0.72
1780650	1.41 ± 0.04	239± 11	17.29 ± 0.06	-22.19 ± 0.01	0.69 ± 0.01	-22.72 ± 0.01	10.97 ± 0.02	10.91 ± 0.15	1.63 ± 0.09	1.42 ± 0.59
2258945	1.38 ± 0.04	262± 10	16.88 ± 0.06	-22.56 ± 0.01	0.74 ± 0.01	-23.12 ± 0.01	11.04 ± 0.02	11.18 ± 0.15	1.36 ± 0.07	1.85 ± 0.76
2402259	1.55 ± 0.05	241± 11	17.19 ± 0.06	-22.49 ± 0.01	0.61 ± 0.01	-22.97 ± 0.01	11.02 ± 0.02	11.03 ± 0.15	1.37 ± 0.08	1.42 ± 0.59
54829	1.22 ± 0.01	146± 5	16.86 ± 0.03	-22.23 ± 0.00	0.63 ± 0.01	-22.75 ± 0.01	10.48 ± 0.01	10.95 ± 0.15	0.50 ± 0.02	1.47 ± 0.61
1044397	1.72 ± 0.06	223± 12	17.56 ± 0.08	-22.39 ± 0.01	0.73 ± 0.01	-22.95 ± 0.01	10.99 ± 0.03	11.11 ± 0.15	1.43 ± 0.09	1.84 ± 0.76
2434587	1.28 ± 0.04	228± 12	17.14 ± 0.06	-22.14 ± 0.01	0.71 ± 0.01	-22.70 ± 0.01	10.89 ± 0.02	10.97 ± 0.15	1.40 ± 0.09	1.70 ± 0.70
1173134	1.34 ± 0.05	230± 13	17.40 ± 0.08	-21.99 ± 0.01	0.73 ± 0.01	-22.62 ± 0.02	10.92 ± 0.03	11.00 ± 0.15	1.73 ± 0.12	2.09 ± 0.86

Table C.5. List of the derived parameters of all galaxies in our basic sample that are also parts of the galaxies provided in Trujillo et al. (2009). First column: IDNYs used in the table in their paper. Second column: scale radius R_r of the galaxies measured in the SDSS r band (in kpc). Third column: corrected central velocity dispersion σ_0 (in km/s). Fourth column: surface brightness μ_r measured in the SDSS r band (in mag/arcsec^2). Fifth column: absolute magnitude in r band M_r. Sixth column: g-r colour $(M_g - M_r)$ (in mag). Seventh column: logarithm of the dynamical mass M_{dyn} (in solar masses). Eighth column: logarithm of the stellar mass M_* (in solar masses). Ninth column: dynamical mass-to-light ratio Υ_{dyn} (in solar units $M_\odot/L_{\odot,r}$). Tenth column: stellar mass-to-light ratio Υ_* (in solar units $M_\odot/L_{\odot,r}$).

References

Abazajian, K., Adelman-McCarthy, J. K., Agüeros, M. A., et al. 2003, *AJ*, 126, 2081

Abazajian, K. N., Adelman-McCarthy, J. K., Agüeros, M. A., et al. 2009, *ApJS*, 182, 543

Ahn, C. P., Alexandroff, R., Allende Prieto, C., et al. 2014, *ApJS*, 211, 17

Aihara, H., Allende Prieto, C., An, D., et al. 2011, *ApJS*, 193, 29

Belli, S., Newman, A. B., & Ellis, R. S. 2014, *ApJ*, 783, 117

Bernardi, M., Hyde, J. B., Fritz, A., et al. 2008, *MNRAS*, 391, 1191

Bernardi, M., Sheth, R. K., Annis, J., et al. 2003, *AJ*, 125, 1866

Bertin, G., Ciotti, L., & Del Principe, M. 2002, *A&A*, 386, 149

Bezanson, R., van Dokkum, P., van de Sande, J., Franx, M., & Kriek, M. 2013, *ApJ*, 764, L8

Blakeslee, J. P., Holden, B. P., Franx, M., et al. 2006, *ApJ*, 644, 30

Blanton, M. R. & Roweis, S. 2007, *AJ*, 133, 734

Blanton, M. R., Schlegel, D. J., Strauss, M. A., et al. 2005, *AJ*, 129, 2562

Burstein, D., Bender, R., Faber, S., & Nolthenius, R. 1997, *AJ*, 114, 1365

Cappellari, M., Bacon, R., Bureau, M., et al. 2006, *MNRAS*, 366, 1126

Cappellari, M., di Serego Alighieri, S., Cimatti, A., et al. 2009, *ApJ*, 704, L34

Cappellari, M., Emsellem, E., Bacon, R., et al. 2007, *MNRAS*, 379, 418

Chevance, M., Weijmans, A.-M., Damjanov, I., et al. 2012, *ApJ*, 754, L24

Chilingarian, I. V., Melchior, A., & Zolotukhin, I. Y. 2010, *MNRAS*, 405, 1409

Chilingarian, I. V. & Zolotukhin, I. Y. 2012, *MNRAS*, 419, 1727

Conroy, C., Dutton, A. A., Graves, G. J., Mendel, J. T., & van Dokkum, P. G. 2013, *ApJ*, 776, L26

Conroy, C., Gunn, J. E., & White, M. 2009, *ApJ*, 699, 486

Damjanov, I., Geller, M. J., Zahid, H. J., & Hwang, H. S. 2015, ArXiv e-prints

Damjanov, I., Hwang, H. S., Geller, M. J., & Chilingarian, I. 2014, *ApJ*, 793, 39

Damjanov, I., McCarthy, P. J., Abraham, R. G., et al. 2009, *ApJ*, 695, 101

Djorgovski, S. & Davis, M. 1987, *ApJ*, 313, 59

Dressler, A., Lynden-Bell, D., Burstein, D., et al. 1987, *ApJ*, 313, 42

Emsellem, E. 2013, *MNRAS*, 433, 1862

Emsellem, E., Cappellari, M., Krajnović, D., et al. 2007, *MNRAS*, 379, 401

Hyde, J. B. & Bernardi, M. 2009, *MNRAS*, 396, 1171

Jorgensen, I., Franx, M., & Kjaergaard, P. 1995, *MNRAS*, 276, 1341

Kauffmann, G., Heckman, T. M., White, S. D. M., et al. 2003, *MNRAS*, 341, 33

Krajnović, D., Bacon, R., Cappellari, M., et al. 2008, *MNRAS*, 390, 93

Kriek, M., van Dokkum, P. G., Franx, M., et al. 2008, *ApJ*, 677, 219

Kriek, M., van Dokkum, P. G., Franx, M., et al. 2006, *ApJ*, 649, L71

La Barbera, F., de Carvalho, R. R., de La Rosa, I. G., & Lopes, P. A. A. 2010, *MNRAS*, 408, 1335

Läsker, R., van den Bosch, R. C. E., van de Ven, G., et al. 2013, *MNRAS*, 434, L31

Lintott, C., Schawinski, K., Bamford, S., et al. 2011, *MNRAS*, 410, 166

Lintott, C. J., Schawinski, K., Slosar, A., et al. 2008, *MNRAS*, 389, 1179

Mendel, J. T., Simard, L., Palmer, M., Ellison, S. L., & Patton, D. R. 2014, *ApJS*, 210, 3

Mieske, S., Frank, M. J., Baumgardt, H., et al. 2013, *A&A*, 558, A14

Misgeld, I. & Hilker, M. 2011, *MNRAS*, 414, 3699

Newman, A. B., Ellis, R. S., Treu, T., & Bundy, K. 2010, *ApJ*, 717, L103

Norris, M. A., Kannappan, S. J., Forbes, D. A., et al. 2014, ArXiv e-prints

Onodera, M., Renzini, A., Carollo, M., et al. 2012, *ApJ*, 755, 26

Poggianti, B. M., Moretti, A., Calvi, R., et al. 2013, *ApJ*, 777, 125

Quilis, V. & Trujillo, I. 2013, *ApJ*, 773, L8

Salim, S., Rich, R. M., Charlot, S., et al. 2007, *ApJS*, 173, 267

Saulder, C., Mieske, S., Zeilinger, W. W., & Chilingarian, I. 2013, *A&A*, 557, A21

Schlegel, D. J., Finkbeiner, D. P., & Davis, M. 1998, *ApJ*, 500, 525

Seth, A. C., van den Bosch, R., Mieske, S., et al. 2014, *Nature*, 513, 398

Simard, L., Mendel, J. T., Patton, D. R., Ellison, S. L., & McConnachie, A. W. 2011, *ApJS*, 196, 11

Strauss, M. A., Weinberg, D. H., Lupton, R. H., et al. 2002, *AJ*, 124, 1810

Taylor, E. N., Franx, M., Glazebrook, K., et al. 2010, *ApJ*, 720, 723

Terlevich, R., Davies, R. L., Faber, S. M., & Burstein, D. 1981, *MNRAS*, 196, 381

Toft, S., Gallazzi, A., Zirm, A., et al. 2012, *ApJ*, 754, 3

Trujillo, I., Cenarro, A. J., de Lorenzo-Cáceres, A., et al. 2009, *ApJ*, 692, L118

Trujillo, I., Ferré-Mateu, A., Balcells, M., Vazdekis, A., & Sánchez-Blázquez, P. 2014, *ApJ*, 780, L20

Trujillo, I., Feulner, G., Goranova, Y., et al. 2006, *MNRAS*, 373, L36

Valentinuzzi, T., Fritz, J., Poggianti, B. M., et al. 2010, *ApJ*, 712, 226

van de Sande, J., Kriek, M., Franx, M., Bezanson, R., & van Dokkum, P. G. 2015, *ApJ*, 799, 125

van de Sande, J., Kriek, M., Franx, M., et al. 2013, *ApJ*, 771, 85

van den Bosch, R., Gebhardt, K., Gültekin, K., Yıldırım, A., & Walsh, J. 2015, ArXiv e-prints

van den Bosch, R. C. E., Gebhardt, K., Gültekin, K., et al. 2012, *Nature*, 491,

729

van der Wel, A., Chang, Y.-Y., Bell, E. F., et al. 2014a, *ApJ*, 792, L6

van der Wel, A., Franx, M., van Dokkum, P. G., et al. 2014b, *ApJ*, 788, 28

van der Wel, A., Holden, B. P., Zirm, A. W., et al. 2008, *ApJ*, 688, 48

van der Wel, A., Rix, H.-W., Wuyts, S., et al. 2011, *ApJ*, 730, 38

van Dokkum, P. G., Franx, M., Kriek, M., et al. 2008, *ApJ*, 677, L5

van Dokkum, P. G., Kriek, M., & Franx, M. 2009, *Nature*, 460, 717

Wegner, G., Colless, M., Saglia, R. P., et al. 1999, *MNRAS*, 305, 259

Yıldırım, A., van den Bosch, R. C. E., Gebhardt, K., et al. submitted, MNRAS

Zahid, H. J., Damjanov, I., Geller, M., & Chilingarian, I. 2015, ArXiv e-prints

37

100

Chapter 6

The matter distribution in the local universe as derived from galaxy groups in SDSS DR10 and 2MRS

This paper provides the last pillar for my cosmological test. In this paper, we derive an accurate model of the mass distribution in the local universe, which is used to derive the finite infinity regions (see Chapter 2.2 and especially Figure 2.3). Hence, it is an essential part of my thesis and ongoing research. Aside from the finite infinity regions, this paper provides two galaxy group catalogues (one using SDSS data and the other one using 2MRS data) of the local universe ranging from the richest clusters to isolated galaxies. Furthermore, it contains accurate mass calibrations of those groups, which help to better constrain the finite infinity regions. I also cross-matched the fundamental plane data of my previous paper with the SDSS groups presented in this paper. Thereby, I obtained more precise redshift independent distances for groups hosting more than one early-type galaxy. This catalogue will form the list of objects for which I calculate the line of sight structure in the final execution of the cosmological test in Chapter 7.

My paper "The matter distribution in the local universe as derived from galaxy groups in SDSS DR10 and 2MRS" was submitted to Astronomy & Astrophysics on June 10th 2015. We are currently working through the referee's suggestions. Being the first author of this paper, I wrote the majority of the text. Eelco van Kampen helped me design and calibrate the group finder algorithm. Steffen Mieske's input was of great help in improving the mass calibrations and the quality of the paper. Furthermore, I acknowledge the contribution of all my collaborators in proof-reading the paper.

The matter distribution in the local universe as derived from galaxy groups in SDSS DR10 and 2MRS

Christoph Saulder[1,2], Eelco van Kampen[2], Steffen Mieske[3], and Werner W. Zeilinger[1]

[1] Department of Astrophysics, University of Vienna, Türkenschanzstraße 17, 1180 Vienna, Austria
 e-mail: `christoph.saulder@equinoxomega.net`

[2] European Southern Observatory, Karl-Schwarzschild-Straße 2, 85748 Garching bei München, Germany

[3] European Southern Observatory, Alonso de Córdova 3107, Vitacura, Casilla 19001, Santiago, Chile

Abstract

Context. Friends-of-friends algorithms are a common tool to detect galaxy groups and clusters in large survey data. For them to be as precise as possible, they have to be carefully calibrated using mock-catalogues.
Aims. To create an accurate and robust description of the matter distribution in the local universe using the most up-to-date available data. This will provide input for a specific cosmological test planned as follow-up to this work, and will be useful for general extragalactic and cosmological research.
Methods. We create a set of galaxy group catalogues based on the 2MRS and SDSS DR10 catalogues using a friends-of-friends based group finder algorithm. The algorithm is carefully calibrated and optimised on a new set of wide-angle mock catalogues from the Millennium simulation, such as to provide accurate total mass estimates of the galaxy groups taking into account the relevant observational biases in 2MRS and SDSS.
Results. We provide four different catalogues: 1) a 2MRS based group catalogue; 2) a SDSS DR10 based group catalogue reaching out to a redshift of 0.11; 3) a catalogue providing additional fundamental plane distances for all groups of the SDSS catalogue that host elliptical galaxies; 4) a catalogue of the mass distribution in the local universe based on a combination of our 2MRS and SDSS catalogues. The latter catalogue is especially designed for a specific cosmological test planned as follow-up to this work.
Conclusions. While motivated by a specific cosmological test, three of the four catalogues that we produced are well suited to act as reference databases for a variety of extragalactic and cosmological science cases. Our catalogue of fundamental plane distances for SDSS groups provides further added value to this paper.

Key words. galaxies: clusters: general – galaxies: distances and redshifts – cosmology: large-scale structure of Universe – galaxies: statistics –

1. Introduction

Galaxy clusters and groups have been an important tool in extragalactic astronomy since the discovery of their nature. Zwicky (1933) used the internal dynamics of nearby clusters to postulate dark matter for the first time. Messier was the first to notice an overdensity of nebulae in the Virgo constellation (Biviano 2000) and thereby discovered the first galaxy cluster without being aware of its nature or the nature of the nebulae (galaxies). The investigation of galaxy clusters started shortly after the Great Debate, when it became established knowledge that the universe contains other galaxies than our own. The first milestone was the already mentioned discovery of dark matter in galaxy clusters (Zwicky 1933). The first significant cluster catalogues were produced by Abell (1958) and Zwicky et al. (1961). Starting with the pioneering work of Turner & Gott (1976) and heavily applied in Huchra & Geller (1982), Zeldovich et al. (1982) and Press & Davis (1982), the methods of finding clusters became more sophisticated and reproducible. The most common algorithm even up to the present day is the friend-of-friends algorithm (Press & Davis 1982), although there are other techniques (Yang et al. 2005; Gal 2006; Koester et al. 2007; Hao et al. 2010; Makarov & Karachentsev 2011; Muñoz-Cuartas &

Müller 2012) existing and being used. A comprehensive comparison between halo finder algorithms for simulated data can be found in Knebe et al. (2011). A detailed study on the optimization of cluster and group finders with a focus on friend-of-friends (FoF) algorithms was performed by Eke et al. (2004a). Efficient and reliable algorithms become more and more important, especially during the last decade and in the time of big data and surveys, such as 2MASS (Skrutskie et al. 2006), SDSS (Ahn et al. 2014), 2dFGRS (Colless et al. 2001), 6dF Galaxy Survey (Jones et al. 2004, 2009), and GAMA (Driver et al. 2011). Information on galaxy grouping and clustering is important because it provides a laboratory to study the dependence of galaxy morphology on the environment (Einasto et al. 1974; Oemler 1974; Davis & Geller 1976; Dressler 1980; Postman & Geller 1984; Dressler et al. 1997; Goto et al. 2003; van der Wel et al. 2010; Wilman et al. 2011; Cappellari et al. 2011) or environmental influence on different properties of galaxies and groups (Huertas-Company et al. 2011; Luparello et al. 2013; Hearin et al. 2013; Hou et al. 2013; Yang et al. 2013; Wetzel et al. 2013; Budzynski et al. 2014; Einasto et al. 2014). It also provides a way to study the halo mass-luminosity relationship (Yang et al. 2009; Wake et al.

1

2011) and thereby helps us understand the dark matter distribution in the universe.

Notable group and cluster catalogues besides those already mentioned are Turner & Gott (1976), Moore et al. (1993), Eke et al. (2004b), Gerke et al. (2005), Yang et al. (2007), Berlind et al. (2006), Brough et al. (2006), Crook et al. (2007), Knobel et al. (2009) and Tempel et al. (2012). In this paper, we will from here on refer to all groups and clusters independent of their sizes as groups. This also includes individual galaxies to which we refer to as a group with just one member.

In this paper, we use observational data from the 10th data release of the Sloan Digital Sky Survey (Ahn et al. 2014)) and the 2MASS Redshift Survey (Huchra et al. 2012b) to map the matter distribution in the local universe. The main intention and use of our group catalogue is to serve as a foreground model for a cosmological test of "timescape cosmology" (Wiltshire 2007), that is outlined in Saulder et al. (2012), for which we need to properly model all potential biases introduced by the measurement of the matter distribution in the local universe. For the group catalogues we present in this paper, the main focus is on an accurate and complete estimate of the masses of these agglomerations. The use of the 2MRS data is motivated by the fact that SDSS does not contain spectroscopic data (redshifts) of bright galaxies in the local universe due to its saturation limit on spectroscopy. 2MRS does not suffer from this problem and thereby it is a good tool to complement the SDSS data. In the end, we require a merged catalogue of 2MRS and SDSS data with solid mass estimates for all groups in them. We use this description of the matter distribution to calculate the so-called "finite infinity regions", which are required for our cosmological test. Since our cosmological test does not only require a detailed description of the matter distribution in the local universe, but also reliable redshift independent distances for a large number of objects, we cross-match our SDSS group catalogue with a large sample of elliptical galaxies from our recently accepted paper (Saulder et al. 2015), which is based on our earlier calibrations of the fundamental plane (Saulder et al. 2013). We provide an additional catalogue with the fundamental plane distances of a large number of groups based on SDSS data. While one main motivation for this paper is a specific cosmological test for an alternative theory that will use the catalogues, the results are kept relatively general, allowing for applications of our data outside its original purpose.

It is important to make a suitable choice for the linking length, which is the distance that defines which object is still a "friend" of others. Most FoF algorithms differ in the choice of scaling the linking length (Huchra & Geller 1982; Ramella et al. 1989; Nolthenius & White 1987; Moore et al. 1993; Robotham et al. 2011; Tempel et al. 2012), which is an important modification of all non-volume limited samples. In the way we implement the FoF algorithm of the group finder, we mainly follow Robotham et al. (2011) and use the corrected luminosity function of our sample for scaling.

Finally, it is crucial to calibrate the group finder on a set of mock catalogues to test its reliability. To this end, we create suitable mock catalogues using the Millennium Simulation (Springel et al. 2005). When calculating the group catalogue, we pay specific attention that the mass in the considered volume matches the mass predicted by the used cosmology. The group catalogues which we obtain will provide valuable insights into the matter distribution of the local universe.

This paper is structured as follows: In Section 2, we describe the samples and data sets, which we use for the group finder and its calibration. These calibrations are explained in detail in

Section 3. The results of the group finder are provided in Section 4 and they are discussed in Section 5. In Section 6, we give a conclusion and summary. The appendices provide information on additional calibrations used in the paper.

2. Samples

In this paper, we use a variety of different data sources: the 10th data release of the Sloan Digital Sky Survey (SDSS DR10 (Ahn et al. 2014)) and the 2MASS Redshift Survey (2MRS (Huchra et al. 2012b)) form the observational data, whereas several data sets based on the Millennium simulation (Springel et al. 2005) are used to create the mock catalogues.

The data sets from SDSS and 2MRS are used to create a detailed description of the matter distribution in the local universe. The 2MRS data is used to compensate for some incompleteness in the SDSS data with respect to the brighter objects in the very nearby universe. Furthermore, 2MRS provides almost full sky coverage up to its depth, while the spectroscopic coverage of SDSS is limited to about a quarter of the sky. On the other hand, SDSS provides a much deeper sample and enables us to trace the matter distribution up to higher redshifts than 2MRS. A group finder based on a modified friends-of-friends algorithm is applied to the observational data in order to locate clusters and groups of galaxies as well as individual field galaxies. We focus on an accurate and complete estimate of the masses of these agglomerations. The group finder is calibrated using a set of 16 mock catalogues (8 for SDSS and 8 for 2MRS), which are based on the dark matter halo distribution of the Millennium simulation and the semi-analytical galaxies models placed within them.

2.1. SDSS

From the SDSS database we retrieved data for 422475 galaxies, which form our basic SDSS sample, using the following criteria. Firstly, there has to be a photometric and spectroscopic identification and a classification of the detected object as a galaxy, which means that *PhotoObj.type* has to be set to 3 and the *SpecObj.class* is required to be 'GALAXY'. Furthermore, a galaxy qualifies for our basic SDSS sample, if it is located in a redshift range between 0 and 0.112[1] and the flag *SpecObj.zWarning* is set to zero. We obtained the photometric object ID, the equatorial coordinates, the galactic coordinates, the spectroscopic redshift, the composite magnitudes in the g, r, and i band, their measurement errors, and the extinction values based on Schlegel et al. (1998).

We use this data to derive the redshift z_{cor} corrected for the reference frame of the cosmic microwave background (CMB) from the observed redshift z. To this end, we take the measurements from Hinshaw et al. (2009), which indicate that the solar system moves into the direction of $l_{cmb} = 263.99° \pm 0.14°$ $b_{cmb} = 48.26° \pm 0.03°$ (galactic coordinates) with a velocity of $v_{cmb} = (369.0 \pm 0.9)\,km\,s^{-1}$ relative to the CMB and correct the redshift following the method explained in Saulder et al. (2013), Appendix A.

We calculate the extinction and K-corrected apparent magnitudes m_{app} for g and r band the following way:

$$m_{cor} = m_{sdss} - A_{Schlegel} \tag{1}$$

---

[1] The upper value of 0.112 is necessary, to avoid an asymmetric cut off due to the corrections for our motion relative to the CMB. It will be reduced to 0.11 later.

2

$$K(z, m_{\mathrm{cor},f_1} - m_{\mathrm{cor},f_2}) = \sum_{i,j} B_{ij} z^i (m_{\mathrm{cor},f_1} - m_{\mathrm{cor},f_2})^j \qquad (2)$$

$$m_{\mathrm{app}} = m_{\mathrm{cor}} - K(z, m_{\mathrm{cor},f_1} - m_{\mathrm{cor},f_2}). \qquad (3)$$

The uncorrected SDSS magnitude is denoted by m_{sdss} and the galactic extinction according to Schlegel et al. (1998) by A_{Schlegel}. We use the K-correction $K(z, m_{\mathrm{cor},f_1} - m_{\mathrm{cor},f_2})$ from Chilingarian et al. (2010) with updated coefficients B_{ij} that can be found in Saulder et al. (2013). To this end, we need the (extinction-corrected) colour $m_{\mathrm{cor},f_1} - m_{\mathrm{cor},f_2}$ and the (not CMB-corrected) redshift z_{cor} of the galaxy. f_1 and f_2 stand for the names of two different bands. We also calculate the luminosity distance $D_L(z_{\mathrm{cor}})$ using the following equation:

$$D_L(z_{\mathrm{cor}}) = \frac{c \cdot z_{\mathrm{cor}}}{H_0} \left(1 + \left(\frac{z_{\mathrm{cor}} \cdot (1 - q_0)}{\sqrt{1 + 2q_0 \cdot z_{\mathrm{cor}}} + 1 + q_0 \cdot z_{\mathrm{cor}}}\right)\right) \qquad (4)$$

$$q_0 = \frac{\Omega_M}{2} - \Omega_\Lambda. \qquad (5)$$

To be consistent with the mock catalogues, which are based on a rerun of the Millennium Simulation using WMAP7 cosmology (Guo et al. 2013), we use the same cosmology here. Hence we assume a Hubble parameter H_0 of 70.4 km/s/Mpc, a matter density Ω_M of 0.272, and a dark energy density Ω_Λ of 0.728 (Komatsu et al. 2011). The deceleration parameter q_0 is defined by Equation 5. With the help of the distance modulus:

$$m_{\mathrm{app}} - M_{\mathrm{abs}} = 5 \cdot \log_{10}(D_L/\mathrm{pc}) - 5 \qquad (6)$$

one is able to obtain the absolute magnitude M_{abs} using the luminosity distance D_L and the apparent magnitude m_{app}.

After having derived all these additional parameters from the observational data, we apply finer cuts on the sample to render it more easily comparable to the mock catalogues. We demand the r band absolute magnitude M_{abs} to be brighter than -15 mag because this is the limit applied on the data selection for the mock catalogues from the Millennium simulation (see subsection 2.3). We remove all galaxies with a corrected redshift z_{cor} higher than 0.11 from the sample as well as galaxies with negative corrected redshifts. Furthermore, we introduce a cut that is half a magnitude fainter than the official limiting magnitude in the r band (17.77 mag (Strauss et al. 2002)) to clean the sample of poorly identified or misclassified objects. We also remove all galaxies whose measured magnitude error is greater than 1 mag in the r or g band. All these additional constraints reduce the final SDSS sample to 397612 galaxies, which are about 94% of the downloaded data set. For the group finder, we use equatorial coordinates, the corrected redshifts, and absolute magnitudes (in the g and r band). The i band data is only used for the SDSS-2MASS transformation, as described in detail in Appendix A.

2.2. 2MRS

We retrieved data for 44599 galaxies (*table3.dat* from Huchra et al. (2012a)) from the 2MRS (Huchra et al. 2012b), which is a spectroscopic follow-up survey of the Two Micron All Sky Survey (2MASS (Skrutskie et al. 2006)). We obtain the 2MASS-ID, the equatorial coordinates, the galactic coordinates, the extinction-corrected total extrapolated magnitudes in all three 2MASS bands (K_s, H, and J), the corresponding errors, the foreground galactic extinction, the redshift (in km/s), and its error.

We remove from the sample those objects that do not have any redshift information and end up with 43534 galaxies. Since the magnitudes provided are already extinction corrected, we

only need to apply a K-correction (using Equations 2 and 3) to obtain the corrected apparent magnitudes. We follow the same procedure as for the SDSS data. We correct the redshift for the motion relative to the CMB and derive the luminosity distance (Equation 4) and the absolute magnitude (Equation 6). We remove from the sample all galaxies whose apparent magnitude is more than half a magnitude fainter than the official limiting magnitude in the K_s band (11.75 mag (Huchra et al. 2012b)). Our final 2MRS sample consists of 43508 galaxies (more than 97.5% of the downloaded data set). We use equatorial coordinates, the corrected redshifts and the absolute magnitudes (in the J and K_s band) for the group finder. The H band data is only used for the SDSS-2MASS transformation (see Appendix A for details).

2.3. Millennium-Simulation data

The Millennium Simulation (Springel et al. 2005) forms the basis for our mock catalogues. Ideally one would use the most recent rerun (Guo et al. 2013) based on WMAP7 cosmology. However, this re-run lacks the friends-of-friends group dataset, which is essential for calibrating the group finder. Therefore, we use the original Millennium run (Springel et al. 2005) with its cosmological parameters listed in Table 1 in combination with the semi-analytic galaxy models from Guo et al. (2011) based on it.

We retrieved several data sets from the Virgo-Millennium Database [2]. First of all, since our main objective is to provide a robust description of the matter distribution in the local universe, which will be used for a cosmological test which is roughly outlined in Saulder et al. (2012), we limit the volume according to our needs. We restricted the depth of our SDSS data set to a redshift of 0.11, which corresponds to a comoving distance of about 322.7 Mpc/h_{100}. To reduce the overlap between the mock catalogues (see Section 3.1), we use a cube of 400 Mpc/h_{100} side length. We would have preferred the whole 500 Mpc/h_{100} cube, but we had to restrict ourselves to 400 Mpc/h_{100} due to limits in our computational facilities. To avoid any problem of missing information along the edges, we shift the origin 10 Mpc/h_{100} inwards in all directions later on.

We did not only retrieve the present day snapshots, but also all snapshots up to a redshift that is slightly higher than our redshift limit of 0.11. The snapshots used and their corresponding redshifts are listed in Table 2. When combing them, we follow Kitzbichler & White (2007) and do not interpolate, because the evolution between these snapshots at late times is sufficiently slow (for more details see section 3.1).

We obtain all friends-of-friends (FOF) groups from the Millenium simulation within the 400 Mpc/h_{100} side length cube for all snapshots listed in Table 2. We use the raw FOF data *MField..FOF*, which contains all FOF groups with at least 20 particles. For this dataset, we obtained the ID number, the comoving coordinates and the number of particles in the FOF group. In total, we find about 48 million FOF groups fulfilling these conditions.

The number of FOF groups with 20 particles or more (see Table 2) decreases slightly with the snapshot number, while the percentage of the number of particles which are bound in those groups increases. Overall, only about 50% of all particles in the volume of our selected cube are bound in the detected halos.

Since a main motivation for this work is to create an as complete as possible model of the matter distribution in the local universe, it is important to correctly account for those missing

---

[2] `http://gavo.mpa-garching.mpg.de/MyMillennium/`

3

	Ω_M	Ω_b	Ω_Λ	h_{100}	n_s	σ_8	N_p	m_p [M$_\odot/h_{100}$]	L [Mpc/h_{100}]	ϵ [kpc/h_{100}]
Millennium	0.25	0.045	0.75	0.73	1	0.9	2160^3	$8.61 \cdot 10^8$	500	5
MM	0.25	0.045	0.75	0.73	1	0.9	270^3	$8.61 \cdot 10^8$	62.5	5

Table 1. The first Millennium Simulation (Springel et al. 2005) and the *millimil* run (MM) use the same set (aside from the smaller volume of MM and fewer particles) of cosmological parameters. The total matter density is represented by Ω_M, the baryonic matter density by Ω_b and the dark energy density by Ω_Λ. h_{100} stands for the Hubble parameter H_0 divided per 100 km/s/Mpc. n_s is the spectral index of density perturbations and σ_8 is the size of linear density fluctuation at 8 Mpc/h_{100}. N_p denotes the number of particles used in the simulation and m_p their individual masses. The simulation ran in a cubic box with a side length L and with a force softening parameter ϵ.

snapnum	redshift	number of FOF groups	number of galaxies	percentage of particles in groups
63	0.000	7913369	6981224	46.8
62	0.020	7933951	7032122	46.5
61	0.041	7955548	7124656	46.2
60	0.064	7979530	7226286	45.8
59	0.089	8003794	7337200	45.4
58	0.116	8033674	7455464	45.0

Table 2. List of number of galaxies, number of FOF groups and the percentage of all particles in these groups (with at least 20 particles) by used snapshot and corresponding redshifts.

particles and to see if they are contained in smaller groups, in the further outskirts of the considered groups, or in the actual 'field' population.

2.3.1. Millimil simulation data

Unfortunately, information on individual particles is not available for the main Millennium run or any other big Millennium run and the analysis of this amount of data would exceed our available computational resources anyway. However, the small *millimil* run (MM) contains not only the merger tree, but also full information on each particle. Aside from a smaller volume, its cosmological parameters are the same as the ones of the main run listed in Table 1. Consequently, MM is well suited to explore the issue of the missing particles in a smaller yet comparable volume.

We obtained the FOF group ID, the Cartesian coordinates, the number of particles in the FOF group, and the radius $R_{200,\mathrm{NFW}}$, within which the FOF group has an overdensity 200 times the critical density of the simulation when fitted by a NFW-profile, for all FOF groups of the last snapshot (*millimil..FOF.snapnum*=63) of the *millimil* run. In addition to this dataset, we also obtain full particle information (the Cartesian coordinates of each particle) for the last snapshot of MM. There are 31428 FOF groups (with at least 20 particles) in MM and we find 19683298 particles [3] in MM.

In order to analyse the particle distribution in relation to the detected halos, we count the number of particles located within certain distances from the halos' cores. The results are listed in Table 3. For the overall sample, we find that 48.5% of all particles in MM are members of FOF groups with at least 20 particles. The value is comparable to what we found for the last snapshot of the main Millennium run (see Table 2). Within the $R_{200,\mathrm{NFW}}$ radius obtained from the simulation, there are about one third of all particles. Within ten times this radius, a region comprising slightly less than one quarter of the full simulation volume, one can already find more than 80% of all particles.

In general terms, one can derive a radius R_m for every halo with mass M_{halo} in which the average density is equal to the critical density times any multiple m:

$$R_m = \left(\frac{3M_{\mathrm{halo}}}{4\pi\rho_{\mathrm{crit}}m} \right)^{1/3} \qquad (7)$$

ρ_{crit} denotes the critical density for the cosmology assumed for the model. Since we particularly aim to map overdense structures in the universe, the percentage of particles within regions (spheres in this approximation) of an average density equal to the critical density are especially interesting. We find that 74.2% of all particles are located within these regions, which cover about 9% of the volume. By iteratively considering the total mass of all particles within those regions and expanding them accordingly, we find that 80.0% of all particles are distributed in these regions around clusters and galaxies. However, the volume in which these particles can be found increases disproportionally to about 15% of the MM volume. In homogeneous spheres corresponding to 200 and 100 times the critical density, there are 36.9% respectively 42.6% of all particles within far less than one percent of the simulation's volume. It is interesting to see that the percentage within R_{200} matches the percentage within $R_{200,\mathrm{NFW}}$ relatively closely.

As mentioned before, this work will form the basis of a cosmological test, which was outlined in Saulder et al. (2012). Here we do not go into more detail on the test or the tested theory than absolutely necessary. We derive the percentage of all particles located within so-called "finite infinity" regions. The term was coined by Ellis (1984) and describes a matter horizon (Ellis & Stoeger 1987) of the particles that will eventually be bound. These regions are used in "timescape cosmology" (Wiltshire 2007), a cosmological theory explaining the accelerated expansion of the universe by backreactions due to General Relativity and the observed inhomogeneities in the universe instead of introducing dark energy. In our approach, we approximate the finite infinity regions with spheres of a mean density equal to the renormalized critical density ("true critical density" in Wiltshire (2007)), which is slightly lower than the critical density in the Λ-CDM model. The radius associated with these regions is denoted by R_{fi}. We find that 77.4% of all particles are within the finite in-

---

[3] Somehow two particles went missing (comparing to Table 1), but given the total number, this will not make any difference for our purposes.

condition	percentage for FOF groups	percentage for galaxies	percentage of volume in groups
particles in FOF groups	48.5	-	-
particles within $R_{200,\text{NFW}}$	33.9	-	0.04
particles within $10\,R_{200,\text{NFW}}$	82.3	-	24.20
particles within R_1	74.2	70.8	9.29
particles within R_{100}	42.6	43.0	0.13
particles within R_{200}	36.9	37.9	0.06
particles within R_{fi}	77.4	74.0	13.82
particles within $R_{1,\text{iter}}$	80.0	74.9	15.25
particles within $R_{\text{fi,iter}}$	81.8	79.2	23.26

Table 3. List of the percentage of particles located within certain distances from the FOF groups' cores and within a certain distance from the galaxies in MM. Furthermore, this table provides the percentage of the volume of the MM cube covered by the groups within their given radii.

finity regions covering almost 14% of the simulation's volume and after doing the same iterations as for the critical density regions, we get 81.8%. The volume of the simulation occupied by these finite infinity regions is 23.26%, which is similar to the expected present day value using the first estimate from Wiltshire (2007), which is about 25%. We used periodic boundary conditions, because the spherical regions around our galaxies extend beyond the simulation cube's volume. This means, we compensate for this loss of volume by letting reach this region into the cube again on the opposite side (i.e. a periodic simulation volume).

When investigating the population of FOF groups, we find that about half (16015 of 31428) of them are dark, which means that they contain no galaxies with an absolute magnitude brighter than -15 mag. However, these dark FOF groups only contain 2.6% of the total mass (compared to 48.5 % in all FOF groups). We retrieved all galaxies brighter than -15 mag in the SDSS r band from the MM database to test how well the luminous matter traces the mass distribution in the simulation. We use the masses associated with the 27086 galaxies, which we found that way, to count the number of particles located within certain radii (see Equation 7) around these galaxies. We found fractions only marginally lower than for the dark matter groups (see Table 3).

With our small analysis using *millimil* data, we thus demonstrate that about three quarter of all particles are located around the detected FOF groups. The rest of the particles can be assumed to be either uniformly distributed all across the voids or arranged in tendrils (fine filaments in voids using the terminology of Alpaslan et al. (2014)) of small halos (less than 20 particles) outside the main clusters and groups.

Aside from information on the dark matter distribution, we also require data on the luminous part of the universe. To this end, we obtained all semi-analytic galaxies brighter than -15 mag in the SDSS r band within the 400 Mpc/h_{100} side length cube for all snapshots listed in Table 2. We obtained the galaxy ID, the ID of the FOF group to which the galaxy belongs, the comoving Cartesian coordinates, the peculiar velocities, the number of particles in the galaxy's halo, the dusty absolute SDSS magnitudes in the g, r, and i band for the more than 43 million galaxies (see Table 2) fulfilling the selection criteria. The semi-analytic models we used are from Guo et al. (2011). These were created using the L-galaxies galaxy formation algorithm (Croton et al. 2006; De Lucia et al. 2006). Due to merging and evolutionary effects the number of galaxies per snapshot that fulfil our criteria decreases at lower redshifts.

3. Method

3.1. Mock catalogues

Here we describe how we construct mock galaxy catalogues from cosmological simulations tailored to reproduce the observational limits of SDSS and 2MRS. This will in the following subsections allow us to assign total masses (=luminous+dark) to the galaxy groups detected within the actual SDSS and 2MRS by our group finder algorithm.

3.1.1. Converting cosmological simulations to observables

With a complete set of simulated galaxies from the Millennium simulation in hand, we obtain our mock catalogues by reverting the procedure done in subsection 2.1 and considering a few other selection effects. The data from Guo et al. (2011) do not contain any 2MASS magnitudes, therefore we had to derive them from the SDSS magnitudes using a colour transformation inspired by Bilir et al. (2008), which is given in Appendix A.2. To get more than a single mock catalogue from our data cube, we put the origin into each of its 8 corners[4] and thereby obtain 8 different viewpoints, which will be largely independent from each other once we include the Malmquist-bias into our calculations. The 8 mock catalogues are not completely independent, because the brightest galaxies can be seen across the entire cube (within the selected redshift limit of 0.11) and thereby some of them will be part of every mock catalogue (yet at different distances/redshifts and consequently different evolutionary states). In the central region of our cube, there will be a substantial overlap, because a larger number of (even medium-bright) galaxies can be detected from every corner and they are at about the same distance/redshift from every corner and thereby in the same evolutionary phase. Nevertheless, there is still a large number of unique galaxies (especially at their specific evolutionary state) in every mock catalogues. The overlaps of the different mock catalogues are illustrated in Figures 1 and 2 for different geometrical arrangements between a set of two mock catalogues. In the case of origins in neighbouring corners of the cube, the overlap is about 8-9%; for corners which are on the same plane the overlap is about 3.5-4% of the galaxies in the mock catalogue for SDSS; finally, in the case of the totally opposite corner it is about 0.1%. The overlap for the shallower 2MRS consists only of a handful of galaxies and is always well below 1%. The overlaps of our mock catalogues could have been even less, if we used the full 500 Mpc/h_{100} side length cube of the Millennium simulations,

---

[4] The origin shift is in fact handled by rotations in a way that all galaxies and halos are located in the first octant as seen from the origin.
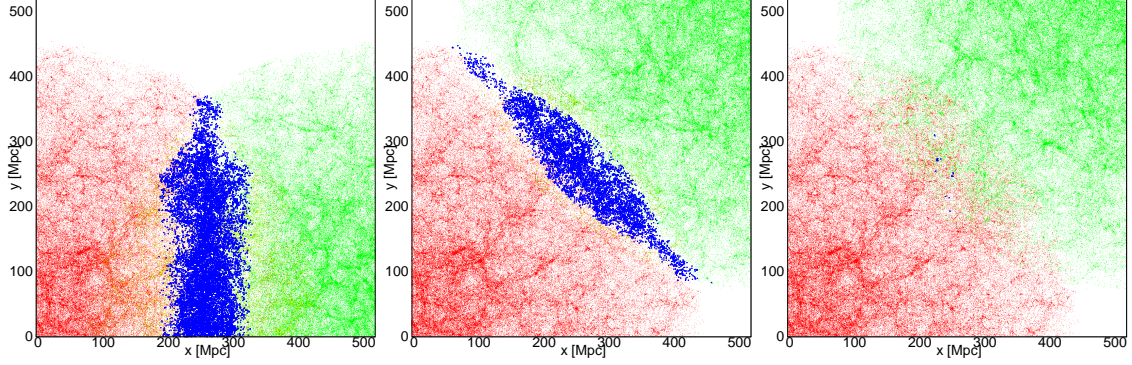
5

Figure 1. Projections of the distribution of the galaxies in the SDSS mock catalogues and their overlaps. The fine green and red pixel in every plot show the projected (on the xy-plane) areas, where galaxies from two mock catalogues can be found belonging to only one of the two catalogues. The blue pixels indicate galaxies that can be found in both catalogues in the same evolutionary stage (from the same redshift snapshot). The left panel shows the overlap of two mock catalogues whose (coordinate) origins are located in neighbouring corners. The central panel shows the overlap of two mock catalogues whose origins are located in opposite corners, yet in the same plane (side of the cube). The right panel shows overlap of two mock catalogues whose origins are located diagonally opposite across the entire cube.
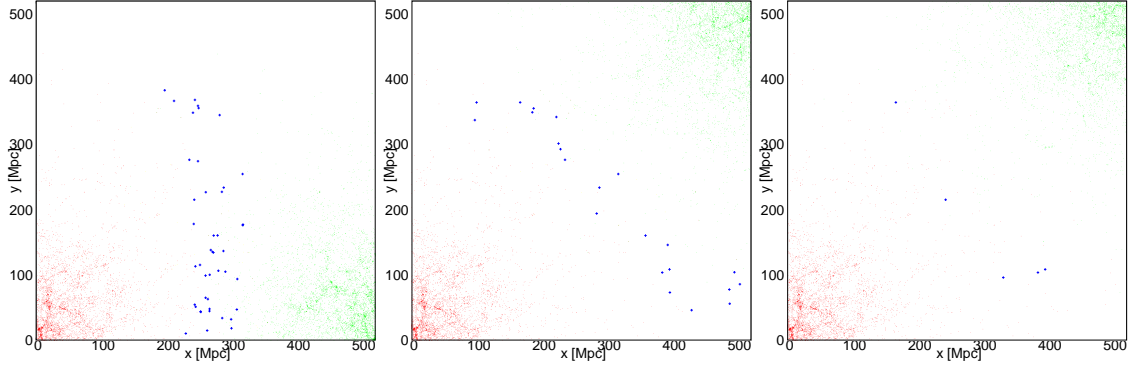
Figure 2. Projections of the distribution of the galaxies in the 2MRS mock catalogues and their overlaps. Symbols as in Fig. 1.

but due to the limits of our computational facilities, we had to restrict ourselves to a 400 Mpc/h_{100} side length cube. In the next step, we move the origin 10 Mpc/h_{100} inwards in all directions to avoid loosing dark matter information on cut-off groups in our sample, when we restrict "our view" to the first octant.

We start off by calculating the mean galactic extinction $\bar{A}_{\mathrm{Schlegel}}$ and its standard deviation $\sigma_{A_{\mathrm{Schlegel}}}$ in the g and r band using the values based on Schlegel et al. (1998), which we retrieved for our sample's galaxies from the SDSS DR10 database.

We found $\bar{A}_{\mathrm{Schlegel}}$=0.126 mag for the g band and $\bar{A}_{\mathrm{Schlegel}}$=0.091 mag for the r band, with $\sigma_{A_{\mathrm{Schlegel}}}$=0.096 mag for the g band and 0.070 mag for the r band. The mean photometric error of the model magnitudes $\bar{m}_{\mathrm{err}}$ for r and g band is calculated using errorbars of the final SDSS sample. We get a $\bar{m}_{\mathrm{err}}$ of 0.007 mag for the g band and 0.006 mag for the r band. Furthermore, we assume a astrometric precision σ_a of 0.1 arcseconds [5] and a red-

---

[5] http://www.sdss3.org/dr10/scope.php#opticalstats

6

shift accuracy σ_z of 30 km/s. We use the symbol $\mathfrak{G}$ to indicate a random Gaussian noise with a standard deviation σ of 1, which was implemented in our code using the function *gasdev* (Normal (Gaussian) Deviates) from (Press et al. 1992). The symbol $\mathfrak{R}$ indicates a homogeneously distributed random variable between 0 and 1.

The cosmological redshift z_{cosmo} is calculated using the following equation:

$$z_{cosmo} = \frac{\sqrt{\left(c^4 + p_1^2(1 - 2q_0)\right)(q_0 - 1)^2} + p_1 + c^2(q_0 - 1) - p_2^2}{(c - p_2)^2}$$

(8)

To this end, we use the same values for H_0 and q_0 (see Equation 5) as used in the Millennium simulation (see Table 1 for the actual values). We make use of the auxiliary variables $p_1 = cD_C H_0$ and $p_2 = q_0 D_C H_0$ in this calculation, with D_C being the comoving distance.

The luminosity distance D_L relates to the comoving distance as

$$D_L = D_C(1 + z_{cosmo}).$$

(9)

It is required to derive the apparent magnitude m_{app} from the absolute magnitude M_{abs} (see Equation 6), which is obtained directly from the semi-analytical galaxy models in the Millennium simulation.

The apparent redshift z_{app}:

$$z_{app} = z_{cosmo} + \frac{p_x v_x + p_y v_y + p_z v_z}{c \cdot D_C}$$

(10)

is the sum of the cosmological redshift and the redshift produced by the projection of the peculiar motion v_x, v_y, and v_z on the line of sight.

To qualitatively mimic the extinction map used in SDSS, we create random extinction values A_{model} in the following way:

$$A_{model} = \bar{A}_{Schlegel} + \sigma_{A_{Schlegel}} \cdot \mathfrak{G}.$$

(11)

Here the parameter $\bar{A}_{Schlegel}$ stands for the mean galactic extinction and $\sigma_{A_{Schlegel}}$ for its standard deviation.

The observed magnitude m_{obs} is calculated using

$$m_{obs} = m_{app} + \bar{K}(z_{app}, (m_{1,app} - m_{2,app})) + A_{model} + \bar{m}_{err} \cdot \mathfrak{G}. \quad (12)$$

This is derived by adding an mock K-correction $\bar{K}(z_{app}, (m_{1,app} - m_{2,app}))$, extinction and photometric uncertainty to the apparent magnitude m_{app}. The mock K-correction is explained in detail in Appendix B.

The "observed" redshift z_{obs} is given by

$$z_{obs} = z_{app} + \frac{\sigma_z}{c} \cdot \mathfrak{G}$$

(13)

This also considers measurement error, besides from the cosmological redshift and the redshift due to peculiar motions, which are already taken into account in the apparent redshift z_{app}.

Observations do not directly yield 3D positions as we have in the simulated data, but a 2D projection on the sky plus a redshift. The equatorial coordinates α' and δ' are obtained by simple geometry:

$$\alpha' = \arctan\left(\frac{p_y}{p_x}\right)$$

(14)

$$\delta' = \arcsin\left(\frac{p_x}{D_C}\right).$$

The observed equatorial coordinates α and δ:

$$\alpha = \alpha' + \mathfrak{G} \cdot \sigma_a \sin(2\pi \cdot \mathfrak{R}) \cos(\delta)$$

(15)

$$\delta = \delta' + \mathfrak{G} \cdot \sigma_a \cos(2\pi \cdot \mathfrak{R})$$

are affected by the finite astrometric precision σ_a.

The evolutionary effects on the galaxies and their distribution are taken into account by only using the galaxies from the snapshot (see Table 2 for the redshifts of the snapshots) closest to their cosmological redshift z_{cosmo}. This simplification is justified because passive evolution is sufficiently slow for nearby ($z_{cosmo} <\sim 0.1$) galaxies (Kitzbichler & White 2007).

3.1.2. Including observational limits into the mock catalogues

A very important step in the creation of our mock catalogue are the cuts introduced into them, which represent the observational limits. The most important one is the Malmquist bias, introduced by removing all galaxies with an "observed" (apparent) magnitude m_{obs} fainter than the limiting magnitude of the survey.

SDSS: In the case of SDSS, it is r=17.77 mag (Strauss et al. 2002). A redshift cut excludes all galaxies with observed redshifts z_{obs} higher than 0.11. We also restrict our view to the first octant of the coordinate system, which is necessary, because we shifted the origin by 10 Mpc/h_{100} inwards earlier to avoid potential problems with the groups of the mock catalogue contributing to the visible distribution being partially cut. This restriction of our view ensures that we have the same depth in all directions considered and simplifies the calculation of the mock catalogue's volume.

One also has to consider the overall spectroscopic completeness of the survey. The SDSS sample, before considering additional cuts due to fibre collision, is more than 99% complete (Blanton et al. 2003). To mimick this, we randomly remove 1% of all galaxies that are still in the sample after the cuts.

Taking the fibre collision into account correctly is very important, since this is more likely to happen in clusters or close groups of galaxies, which are objects that are essential for our group finder. The size of the fibre plugs of SDSS does not allow two spectra to be taken closer than 55 arcseconds of one another (Blanton et al. 2003). Consequently if we find any galaxy in our mock catalogue that is closer than this minimal separation to another galaxy we remove one of the two galaxies at random. Due to the SDSS tiling algorithm (Blanton et al. 2003), some areas are covered more than once, which allows spectra to be taken from galaxies that were blocked due to fibre collision the first time around. An overall sampling rate of more than 92% is reached. We take this into account by randomly re-including galaxies, which were previously removed due to fibre collision until an overall sampling rate of 92% is reached. Since we have selected *SpecObj.class* to be 'GALAXY' for our SDSS sample, we have to remove a number of galaxies from the mock catalogue, which would correspond to QSO in SDSS sample, because they have a different *SpecObj.class*. There are 1889 objects classified as QSO within the redshift range of our SDSS sample. Given the spectroscopic sky coverage of SDSS DR10, which is 9274 square degree(Aihara et al. 2011) and the fact that the mock catalogue covers one octant of the sky (hence ~5157 square degree), we remove 1050 galaxies from the mock catalogue to take the QSO fraction into account.

At this point, the preliminary versions of the mock catalogue contains the equatorial coordinates α and δ, the "observed"[6] redshift z_{obs}, the "observed" magnitudes m_{obs} in two different filters (g and r band), and the corresponding model extinction values A_{model}. This set of mock data is comparable to our set of real observational data obtained by SDSS.

We applied the same calibration and cuts to the preliminary mock catalogue as to the real data (see Section 2.1). After correcting the 'observed' magnitudes for (model) extinction and applying the K-correction, we use these plus the observed redshift to derive the "observed" absolute magnitudes M_{obs}. We also remove all bright galaxies which are above the saturation limit of SDSS in this step. The final set of our eight SDSS mock catalogues only contain the coordinates α and δ, the observed redshift z_{obs} and the observed absolute magnitudes M_{obs} in the g and r band and represent the same set of data as the one created from the real SDSS sample.

2MRS: For our set of mock catalogues for 2MRS, we proceed in a similar way as for the SDSS mock catalogues. However, there are a couple of important differences to be pointed out. There are different values for the mean photometric error of the apparent magnitudes $\bar{m}_{err}$ for the K_s and J band, which are derived from the measured values e_Ktmag and e_Jtmag of the 2MRS catalogue. We find a $\bar{m}_{err}$ of 0.037 mag for the J band and 0.056 mag for the K_s band. The redshift accuracy σ_z is obtained from averaging the e_cz parameter of the 2MRS and we find a value of about 32 km/s. No correction for extinction is applied to the 2MRS magnitudes, because the magnitudes obtained from the catalogue are already corrected for extinction. K-correction, peculiar motions, photometric and spectroscopic errors and evolutionary effects are considered in the same way as for the SDSS mock catalogues. The completeness of 2MRS of 97.6% (Huchra et al. 2012b) is taken into account by randomly removing 2.4% of the galaxies from the mock catalogue. Given the way the 2MRS was performed, there is no need for fibre collision corrections or similar corrections beyond the completeness consideration. The preliminary mock catalogues are put through the observational pipeline used in Section 2.2. The eight 2MRS final mock catalogues are composed of the coordinates α and δ, the observed redshift z_{obs} and the observed absolute magnitudes M_{obs} in the J and K_s band.

When measuring the completeness (the ratio of number of the galaxies in the mock catalogue compared to the number of galaxies in the survey normalised to the same volume), one finds an overall good agreement. The completeness of the SDSS mock catalogues (see Table 4) is about five to ten percent below 100%, while the completeness of the 2MRS mock catalogues varies around 100% with a larger scatter, because it is, due to its shallower depths, more affected by local variations in the matter distribution. We attribute the systematically lower completeness of the SDSS mock catalogue to small differences between the cosmological parameters used in the simulation and the measured cosmological parameter of our Universe.

3.1.3. Dark matter catalogues

We also created a set of mock catalogues containing the full dark matter information, which will be essential for the mass calibration later on. The same shifts and rotations as for the galaxy catalogues are performed for the cube of dark matter FOF groups

mock catalogue	number of galaxies	completeness
preliminary SDSS 1	197436	89%
preliminary SDSS 2	221117	100%
preliminary SDSS 3	198301	90%
preliminary SDSS 4	214345	96%
preliminary SDSS 5	210393	95%
preliminary SDSS 6	206105	93%
preliminary SDSS 7	200092	90%
preliminary SDSS 8	204055	92%
final SDSS 1	194563	88%
final SDSS 2	218606	99%
final SDSS 3	196306	89%
final SDSS 4	209800	95%
final SDSS 5	208276	94%
final SDSS 6	203793	92%
final SDSS 7	197860	90%
final SDSS 8	202203	91%
preliminary 2MRS 1	5747	96%
preliminary 2MRS 2	6469	108%
preliminary 2MRS 3	5286	88%
preliminary 2MRS 4	8138	136%
preliminary 2MRS 5	5452	91%
preliminary 2MRS 6	5525	92%
preliminary 2MRS 7	5521	92%
preliminary 2MRS 8	5127	86%
final 2MRS 1	5746	96%
final 2MRS 2	6459	108%
final 2MRS 3	5286	88%
final 2MRS 4	8101	136%
final 2MRS 5	5452	91%
final 2MRS 6	5525	92%
final 2MRS 7	5521	92%
final 2MRS 8	5127	86%
FOF groups 1	8022033	-
FOF groups 2	8021983	-
FOF groups 3	8022371	-
FOF groups 4	8021796	-
FOF groups 5	8021151	-
FOF groups 6	8021263	-
FOF groups 7	8021219	-
FOF groups 8	8021352	-
all galaxies 1	7405697	-
all galaxies 2	7403914	-
all galaxies 3	7406327	-
all galaxies 4	7405116	-
all galaxies 5	7404890	-
all galaxies 6	7406332	-
all galaxies 7	7407193	-
all galaxies 8	7406941	-

Table 4. List of all mock catalogues created as part of this paper.

obtained from the Millennium simulations. We calculate the cosmological redshift z_{cosmo} (see Equation 8) for every halo. The masses of the FOF groups are obtained by multiplying the number of particles in them *MField..FOF.np* and the mass per particle (see Table 1). The redshift evolution is considered in the same way as for the previous mock catalogues described in this paper. There are no cuts or selections introduced into this sample, since we want to take advantage of having the full information on the dark matter distribution. Two different outputs are created for each of the eight FOF group mock catalogues: one containing the FOF ID, the Cartesian 3D coordinates from the simulation and the masses of the FOF groups and another one containing the FOF ID, the equatorial coordinates (obtained using Equation 15), the cosmological redshift and the masses of the FOF groups.

---

[6] These "observed" quantities are not actually observed, because they are mock data. However, they would be the quantities that would be observed, if it was real data, hence the name.

A set of unbiased mock catalogues containing the full data of all available simulated galaxies is created to better quantify estimates and extrapolations from the mock catalogues, which consider observational limitations. To this end, we take all galaxy data before applying any biases and just apply the evolution correction (by using different snapshot at different cosmological redshifts). Then we create two different outputs similar to the halo mock catalogues: one with the Cartesian coordinates and the other with the equatorial coordinates and the redshift for all galaxies. The output contains the original absolute magnitudes from the simulation (not the virtually re-observed ones) of the SDSS g and r band and also the absolute 2MASS magnitudes of the J and K_s band, which are derived using the colour transformation from Appendix A.

3.2. Basic Parameters of the Group Finder

A friends-of-friends (FOF) group finder uses a simple idea to find galaxies which are grouped together. It recursively finds all galaxies which are separated by less than the so-called linking length b_{link} from any other member of the group. If one has a complete sample with full information on the 3D positions of all galaxies in it, it is a straight forward procedure. However, in reality one has to account for Malmquist bias, projection effects, and other biases. We roughly follow Robotham et al. (2011) in defining the linking length and its dependences on observational effects.

We define a basic value for the linking length called $b_{link,0}$, which is the average distance from one galaxy to the nearest galaxy in the sample. We calculate the distances between all galaxies in the MM and take for every galaxy the distance to its nearest visible neighbour. We use a minimum absolute magnitude for the galaxies to qualify for their inclusion in this calculation to avoid dwarf galaxies. Galaxies have to be brighter than -15 mag in the SDSS r band and -18 mag in 2MASS K_s band. For the average of the nearest neighbour distances in our sample, we get $b_{link,0} \sim 0.64$ Mpc for 2MRS and $b_{link,0} \sim 0.67$ Mpc for SDSS (interestingly very similar to the distance between the Milky Way and M31). This parameter will be fine-tuned using the mock observations later in Section 3.3. The effective linking length b_{link} is not a constant equal to its basic value $b_{link,0}$, but has several dependences, which will be discussed below.

The dominant of these biases is the Malmquist bias, which drastically removes the fainter end of the galaxy luminosity function from our sample at larger distances. Since we know the limiting magnitude of our data and the mock catalogues very well, it is straightforward to derive a correction for the Malmquist bias using volume weights. The limiting luminosity distance $D_{L,limit}$ until a galaxy with an absolute magnitude M_{abs} is still included in a survey with a limiting magnitude m_{limit} can be derived using the distance modulus (see Equation 6) and yields Equation 16.

$$\log_{10}\left(D_{L,limit}\right) = \frac{-M_{abs} + m_{limit} + 5}{5} \tag{16}$$

By inverting Equation 4, it is possible to obtain the following equation:

$$z = \frac{1}{c^2}\Bigg(c^2 q_0 - c^2 + c\,D_L H_0 q_0 +$$

$$\sqrt{c^2 q_0^2 - 2c^4 q_0 + c^4 + 2c^3 D_L H_0 q_0^2 - 4c^3 D_L H_0 q_0 + 2c^3 D_L H_0}\Bigg). \tag{17}$$
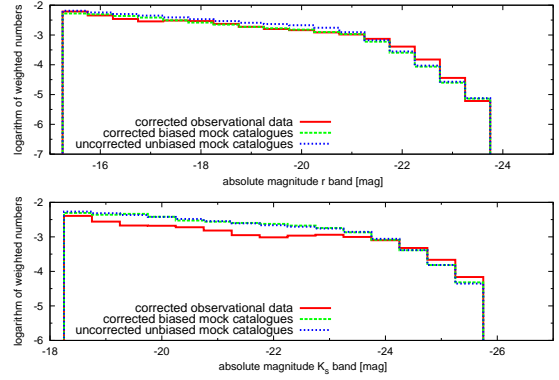

Figure 3. The luminosity function for SDSS data in top panel and for 2MRS data in lower panel. The green dashed line indicates the "true" luminosity function derived using all galaxies from the unbiased mock catalogues, while the blue dashed line indicated the corrected (reconstructed) luminosity function from the Malmquist biased mock catalogues. The corrected observational data is indicated by the red solid line.

$$V_C(z_1, z_2) = \frac{4\pi}{3}\frac{A_{survey}}{A_{sky}}\left(D_C^3(z_2) - D_C^3(z_1)\right) \tag{18}$$

By inserting the results of a combination of Equations 9 and 17 into Equation 18, one is able to get the comoving volume V_C between the two cosmological redshifts z_1 and z_2 for a survey covering A_{survey} of the total sky area A_{sky}.

With z_2 being the higher of the redshift corresponding to the limiting luminosity distance $D_{L,limit}$ or the limiting redshift of the survey and with z_1 being either zero or the redshift corresponding to the saturation limit (defined in the same way as the Malmquist bias), one obtains the comoving volumes $V_{C,i}$, which are used for the definition of the volume weights in the following equation:

$$w_{vol,i} = \frac{(V_{C,i})^{-1}}{\sum_j (V_{C,j})^{-1}}. \tag{19}$$

With the help of the volume weights $w_{vol,i}$, we correct the observed luminosity function (either from observational data or from our mock catalogues) as it is illustrated in Figure 3. In the SDSS data the corrected luminosity function from the mock catalogues follows closely the observed luminosity function as well as the "true" luminosity function from the unbiased mock catalogues with minor deviations only. For the 2MRS data both, the corrected luminosity function from the mock catalogues and the "true" luminosity function agree very well with each other, whereas the observed luminosity function shows an excess of very bright galaxies and a shortage of medium bright galaxies compared to the mock catalogue based data. We attribute the poorer fit of the mock 2MRS data to the observations to the additional uncertainty introduced into the mock data by using the SDSS-2MRS colour transformation (see Appendix A). Overall, we find good agreement.

We have shown that we can retrieve the "true" luminosity function fairly easily and with sufficient quality using volume weights. Due to the Malmquist bias, the fainter members of a group will not be visible any more at higher redshifts. To avoid letting two sufficiently bright galaxies, which are members of the same group, appear separated due to the unseen members in

9

between, one has to adjust the linking length accordingly for our FOF group finder. Since the Malmquist bias reduces the number of galaxies visible per volume by introducing a redshift-dependent cut in the luminosity function $\Phi(m)$, it stands to reason to use the luminosity function to correct for it.

$$b_{\text{cor},\Phi}(z) = \left(\frac{\int_{-\infty}^{-5\log_{10}(D_L(z))+m_{\text{limit}}+5} \Phi(m)\, dm}{\int_{-\infty}^{M_{\text{abs,min}}} \Phi(m)\, dm} \right)^{-1/3} \quad (20)$$

The modification factor $b_{\text{cor},\Phi}(z)$ will be used to rescale the basic linking length $b_{\text{link},0}$ as a function of redshift z. The number density of galaxies decreases towards higher luminosity distances D_L by removing the fainter galaxies from the luminosity function due to the limiting magnitude m_{limit} of the survey (see Equation 16). The parameter $M_{\text{abs,min}}$ denotes the minimal absolute magnitude to which the luminosity function is still considered in our sample. For SDSS, it is -15 mag in the r band and for 2MRS, it is -18 mag in the K_s band.
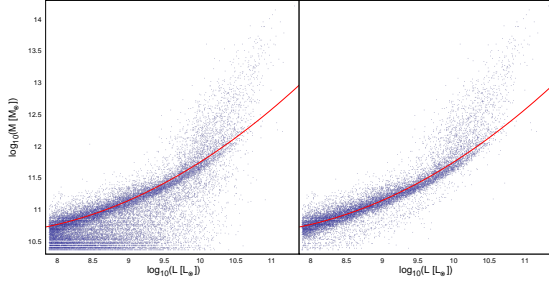
Figure 4. The left panel shows the distribution of all galaxies of the MM in the luminosity-mass plane using the r band luminosities of SDSS, while the right panel only displays the galaxies that are also in the centre of a halo. The solid red line indicates our fit to the most prominent correlation in these plots.
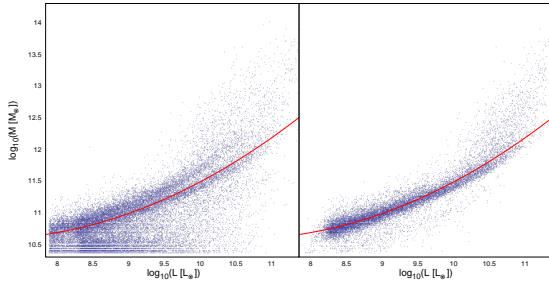
Figure 5. The left panel shows the distribution of all galaxies of the MM in the luminosity-mass plane using the K_s band luminosities of 2MASS, while the right panel only displays the galaxies that are also in the centre of a halo. The solid red line indicates our fit to the most prominent correlation in these plots.

Another common modification to the FOF-algorithm is to vary the linking length with luminosity. Given that luminosity is a proxy for the total mass of a galaxy's halo, it stands to reason that brighter galaxies have a stronger gravitational influence than fainter ones and therefore one should adapt the linking length

accordingly. We use the galaxies from MM to calibrate this relation. In the right panels of Figures 4 and 5, a relatively tight relation between the masses of central galaxies in halos and their luminosity becomes evident. For the most massive groups, the central galaxies deviate from this tight relation towards larger dynamical masses at a given luminosity. We do not expect any significant impact on the algorithm due to this deviation, because of the high galaxy density in these massive groups. We performed a least-square fit with recursive 3-σ clipping using a second order polynomial to describe these relations:

$$\log_{10}\left(\frac{M_{\text{halo}}}{M_\odot}\right) = a_{ml}\left(\log_{10}\left(\frac{L_{\text{gal}}}{L_\odot}\right)\right)^2 + b_{ml}\log_{10}\left(\frac{L_{\text{gal}}}{L_\odot}\right) + c_{ml}. \quad (21)$$

The variable M_{halo} denotes the mass of the galaxy's halo and L_{gal} is the r band luminosity of that galaxy. a_{ml}, b_{ml}, and c_{ml} are the fit coefficients. The results of the fits for the SDSS r band and the 2MASS K_s are provided in Table 5. We obtain a rescale factor:

$$b_{\text{cor},M}(L_{\text{gal}}) = \frac{M_{\text{halo}}(L_{\text{gal}})}{\overline{M_{\text{halo}}}} \quad (22)$$

by dividing the halo mass $M_{\text{halo}}(L_{\text{gal}})$ obtained from the fit by the average halo mass $\overline{M_{\text{halo}}}$.

In physical space the linking length is an isotropic quantity, it does not depend on the direction. However, when observing galaxies projected on the sky one only obtains two coordinates directly, while the third dimension is derived from the redshift. This observed redshift cannot be exclusively attributed to the metric expansion of space-time, but also to the peculiar radial velocity of the galaxy. The imprint on the observed redshift from these peculiar motions cannot be distinguished a priori from the cosmological redshift. Hence, using a redshift-distance relation to convert redshifts in distances the thereby estimated positions will be smeared out in the radial direction with respect to the true positions. In the case of galaxy groups, this effect is known as the "Fingers of God" effect (Jackson 1972; Arp 1994; Cabré & Gaztañaga 2009). A similar effect but in opposite direction is the Kaiser effect (Kaiser 1987). Assuming a coherent infall of galaxies into a group or cluster, one gets positive peculiar velocities for galaxies in front of a group and negative ones for those behind a group. This causes a flattening of groups in the line of sight in redshift-space. However, the Kaiser effect is significantly smaller than the Finger of God effect.

Although deforming the sphere with the linking length as radius to an ellipsoid seems the natural way to incorporate these effects into FOF-group finder algorithms, Eke et al. (2004a) found that cylinders along the line of sight are more efficient. Therefore, instead of one linking length we use two separate linking lengths: an angular linking length α_{link} and a radial linking length R_{link}. The angular linking length is unaffected by the redshift-space distortion and directly relates to the linking length in real space b_{link} by simple trigonometry:

$$\alpha_{\text{link}} = \tan\left(\frac{b_{\text{link}}}{D_A}\right) \quad (23)$$

The angular diameter distance D_A is defined as

$$D_A = D_C (1 + z_{\text{cosmo}})^{-1}. \quad (24)$$

The radial linking length is larger than the linking length in real space because of the scatter in redshift space due to the peculiar motions. We transform the b_{link} distance into a corresponding redshift difference:

$$R_{\text{link}} = b_{\text{link}} + 2\sigma_{\text{rad}} \quad (25)$$

band	a_{ml}	b_{ml}	c_{ml}	s_{rms}	N_{gal}
SDSS r	0.113 ± 0.018	-1.55 ± 0.33	15.9 ± 1.5	0.091	13787
2MASS K_s	0.099 ± 0.016	-1.38 ± 0.30	15.4 ± 1.4	0.093	13931

Table 5. The coefficients and other parameters of the fit on the luminosity-mass relation are listed in this table for the SDSS r band and the 2MASS K_s band. a_{ml}, b_{ml}, and c_{ml} are the fit coefficients according to Equation 21. The root mean square s_{rms} and the number of galaxies N_{gal} used for the fit are also provided.
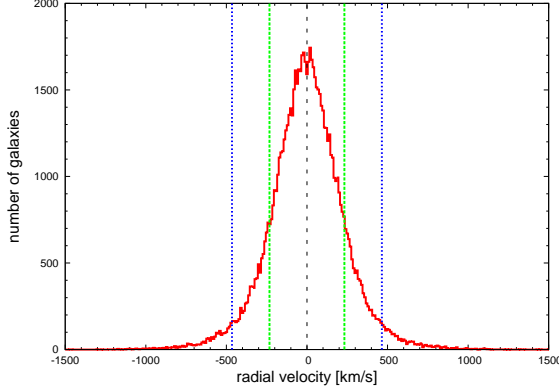
Figure 6. The red solid line shows the distribution of radial proper motions in MM, which has a roughly Gaussian shape. The black dashed line highlights the zero radial velocity bin. The green dashed lines indicate the dispersion of the radial peculiar velocities σ_{rad}, which corresponds to the standard deviation of the plotted distribution. The blue dashed lines show the two σ-interval, which is used to stretch the radial linking length.

By adding the dispersion of radial peculiar velocities σ_{rad} to the linking length in real space, one gets a first estimate of the radial linking length R_{link}. In MM, we find a σ_{rad} of ~ 232.5 km/s, hence about 95% of all possible radial velocity differences are included in an envelope of ± 465 km/s, as illustrated in Figure 6.

We combine all these corrections and modifications to the linking length and obtain one set of equations:

$$\alpha_{eff} = \alpha_{opt} \cdot \alpha_{link} \cdot \left(b_{cor,M}(L_{gal})\right)^{\gamma_{opt}} \cdot \left(b_{cor,\Phi}(z)\right)^{\lambda_{gal}} \quad (26)$$

$$R_{eff} = R_{opt} \cdot R_{link} \cdot \left(b_{cor,M}(L_{gal})\right)^{\gamma_{opt}} \cdot \left(b_{cor,\Phi}(z)\right)^{\lambda_{opt}}. \quad (27)$$

The effective angular linking length α_{eff} and the effective radial linking length R_{eff} define the linking conditions of our group finder. The exponents γ_{opt} and λ_{opt} allow for variations of the luminosity-mass relation (see Equation 22) and the completeness correction (see Equation 20) respectively. The coefficients α_{opt}, R_{opt}, γ_{opt}, and λ_{opt}, which allow us to fine-tune our group finder, will be optimized with the help of our mock catalogues in the next step.

3.3. Group Finder fine tuning

The first step in optimizing the group finder is to define a function that provides a solid measurement of the quality of the group finder's results. We follow Robotham et al. (2011) and define a group cost function by the following set of equations:

$$E_{fof} = \frac{N_{bij}(n_{limit})}{N_{fof}(n_{limit})} \quad (28)$$

$$E_{mock} = \frac{N_{bij}(n_{limit})}{N_{mock}(n_{limit})} \quad (29)$$

$$E_{tot} = E_{mock} \cdot E_{fof} \quad (30)$$

The global halo finding efficiency measurement E_{tot} is defined using the halo finding efficiencies of the mock catalogue E_{mock} and the FOF catalogue E_{fof}. The parameters $N_{mock}(n_{limit})$ and $N_{fof}(n_{limit})$ are the number of groups with at least n_{limit} members in the mock catalogue and in the results of our FOF-based group finder. $N_{bij}(n_{limit})$ is the number of groups that are found bijectively in both samples (the mock catalogue, which consists of the "true" group information based purely on the simulation, and the FOF catalogue, which consists of the grouping found after applying the group finder on the mock catalogue). This means that at least 50% of the members found in a group in one sample must make up at least 50% of a corresponding group in the other sample as well.

$$Q_{fof} = \frac{\sum_{i=1}^{N_{fof}} P_{fof}(i) \cdot N_{members,fof}(i)}{\sum_{i=1}^{N_{fof}} N_{members,fof}(i)} \quad (31)$$

$$Q_{mock} = \frac{\sum_{i=1}^{N_{mock}} P_{mock}(i) \cdot N_{members,mock}(i)}{\sum_{i=1}^{N_{fof}} N_{members,mock}(i)} \quad (32)$$

$$Q_{tot} = Q_{mock} \cdot Q_{fof} \quad (33)$$

The global grouping purity Q_{tot} is defined using the grouping purity of the mock catalogue Q_{mock} and the FOF catalogue Q_{fof}. The variables $N_{members,mock}(i)$ and $N_{members,fof}(i)$ are the numbers of galaxies in individual groups i of the mock catalogue and the FOF catalogue respectively. The purity products $P_{mock}(i)$ and $P_{fof}(i)$ are defined as the maximal product of the ratio of shared galaxies to all galaxies within a group of one catalogue and the ratio of the same shared galaxies within the other catalogue. An illustrative example is provided in Robotham et al. (2011).

$$S_{tot} = E_{tot} \cdot Q_{tot} \quad (34)$$

The group cost function S_{tot} is defined as the product of the global halo finding efficiency measurement E_{tot} and the global grouping purity Q_{tot}. Following the definitions, S_{tot} will assume values between 0 (total mismatch) and 1 (perfect match).

We start our optimization by performing a coarse parameter scan for the four coefficients α_{opt}, R_{opt}, γ_{opt}, and λ_{opt} in one of our mock catalogues to get an initial guess for the order of magnitude of optimal coefficients. We then use a Simplex algorithm (Nelder & Mead 1965) to maximise the median group cost function S_{tot} of all of our 8 mock catalogues. The optimal coefficients for both samples, SDSS and 2MRS, are listed in Table 6. For the calculation of S_{tot} and the optimisation we use $n_{limit} = 2$. We also repeated it with different values for n_{limit} and found very similar optimal coefficients (a few percent difference).

The coefficients α_{opt} and R_{opt} are well within an order of magnitude of unity, indicating that our initial definitions of the effective linking lengths are reasonable. The fact that the coefficient γ_{opt} is close to zero reduces the correction of the linking

11

sample	α_{opt}	R_{opt}	γ_{opt}	λ_{opt}	S_{tot}
2MRS	0.467 ± 0.010	0.533 ± 0.010	0.023 ± 0.010	0.922 ± 0.010	0.342
SDSS	0.394 ± 0.010	0.520 ± 0.010	0.053 ± 0.010	1.084 ± 0.010	0.229

Table 6. Optimal coefficients for the group finder for 2MRS and SDSS. The coefficient α_{opt} allows for proper scaling of the angular linking length, which the coefficient R_{opt} does the same for the radial linking length (in redshift space). The coefficients γ_{opt} and λ_{opt} provide the best dependence on the scaling of the linking length on the mass of the galaxies and on the scaling of the Malmquist bias correction respectively. S_{tot} is the median value of the group cost function calculated using all mock catalogues and the optimal coefficients.
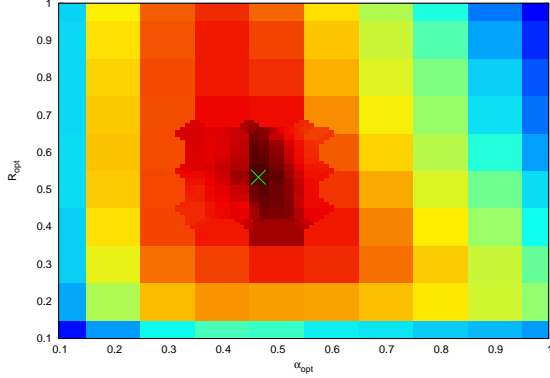
Figure 7. Distribution of the values of the median group cost function S_{tot} using the 2MRS mock catalogues for different values of α_{opt} and R_{opt}. High values of S_{tot} are indicated by dark red, while low values are indicated by dark blue. γ_{opt} and λ_{opt} are fixed to their optimal values, which are listed in Table 6. The green X denotes result of the optimal values of α_{opt} and R_{opt} according to our simplex fit.
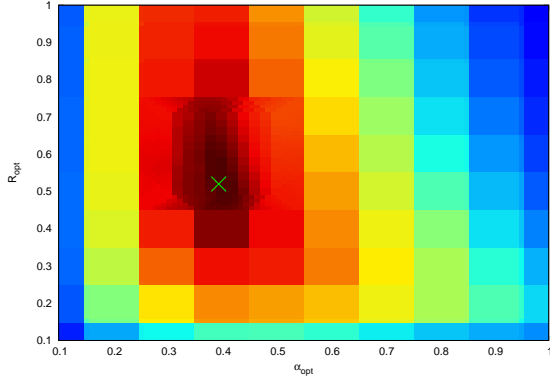
Figure 8. Distribution of the values of the median group cost function S_{tot} using the SDSS mock catalogues for different values of α_{opt} and R_{opt}. High values of S_{tot} are indicated by dark red, while low values are indicated by dark blue. γ_{opt} and λ_{opt} are fixed to their optimal values, which are listed in Table 6. The green X denotes result of the optimal values of α_{opt} and R_{opt} according to our simplex fit.

length depending on the galaxy's absolute luminosity to a minor effect. However, the coefficient λ_{opt} is close to unity, which means that the Malmquest-bias correction of the linking length based on the luminosity function is an important contribution to the efficiency of our group finder. The distribution of the median group cost function depending on the coefficient α_{opt} and R_{opt} is illustrated in Figures 7 and 8.

3.4. Group parameters

The last step is the calculation of various parameters for our groups, such as the position of their centre, their size, mass, and luminosity. To this end, we use the methods that Robotham et al. (2011) found to be the most efficient and robust.

3.4.1. Group velocity dispersion

For groups with a multiplicity of two or more, we calculate the group velocity dispersions. For this purpose we use the "gapper" estimator of Beers et al. (1990) including the modification of Eke et al. (2004a).

$$\sigma_{\text{gap}} = \frac{\pi}{N_{\text{fof}}(N_{\text{fof}} - 1)} \sum_{i=1}^{N_{\text{fof}}-1} w_i g_i \qquad (35)$$

$$w_i = i \cdot (N_{\text{fof}} - i) \qquad (36)$$

$$g_i = v_{i+1} - v_i \qquad (37)$$

$$\frac{v_i}{c} = \frac{1 + z_{\text{obs},i}^2 - 1}{1 + z_{\text{obs},i}^2 + 1} \qquad (38)$$

$$\sigma_{\text{group}} = \sqrt{\frac{N_{\text{fof}}}{N_{\text{fof}} - 1} \sigma_{\text{gap}}^2 - \sigma_{\text{err}}^2} \qquad (39)$$

The gapper velocity dispersion σ_{gap} of a group with N_{fof} member is calculated by summing up the product of the weights w_i and the radial velocity gaps g_i for all all its members. It is essential that the radial velocities v_i are ordered for this approach, which we assure by a simple sorting algorithm applied for each group. The radial velocities v_i are calculated using the observed redshifts $z_{\text{obs},i}$. The group velocity dispersion σ_{group} also takes into account the measurement errors of the redshift determination σ_{err}, which are 30 km/s for SDSS and $\sim$ 32 km/s for 2MRS. In the case that the obtained group velocity dispersion is lower than the measurement errors of the redshift determination, we set them to σ_{err}.

3.4.2. Total group luminosity

The observed group luminosity L_{obs} is calculated by adding up the emitted light, in the SDSS r band or the 2MASS K_s band respectively, of the group members.

$$L_{\text{obs}} = \sum_{i=1}^{N_{\text{fof}}} L_i \qquad (40)$$

$$L_i = 10^{-0.4 \cdot (M_{\text{abs},i} - M_{\text{abs},\odot})} \qquad (41)$$

The calculation of the luminosity of individual galaxy L_i requires the absolute r band magnitudes $M_{\text{abs},i}$ and the solar absolute magnitude $M_{\text{abs},\odot}$ in the r band of 4.76 mag or in the K_s of 3.28 mag respectively.

12

$$L_{tot} = L_{obs} \frac{\int_{-\infty}^{M_{abs,min}} \Phi(m) \, dm}{\int_{-\infty}^{-5\log_{10}(D_L(z))+m_{limit}+5} \Phi(m) \, dm} \qquad (42)$$

The total group luminosity L_{tot} has to be obtained by rescaling the observed group luminosity D_L with the fraction of the luminosity function $\Phi(m)$ visible at the group's luminosity distance. m_{limit} is the limiting magnitude of the survey and the parameter $M_{abs,min}$ denotes the minimal absolute magnitude to which the luminosity function is still considered in our sample.

3.4.3. Group centre

In the next step, we locate the group centre. We treat the radial group centre, which is calculated only using the measured redshifts of the group's members, differently from the projected group centre, which is calculated using the observed coordinates of the group members. In Robotham et al. (2011), different approaches on how to best find the group centre are discussed and compared. We employ the method which they found to be the most efficient and reliable. In the case of the radial group center, this constitutes simply taking the median of the redshifts of all group members. Finding the projected group centre is more complicated and the most efficient method is an iterative approach using the centre of light of the group members as explained in Robotham et al. (2011). At first the coordinates of the centre of light, which is the luminosity-weighted (using L_i as weights), are calculated using all group members. Then the group member which is the furthest away from is rejected and the new centre of light is calculated with the remaining members. This process is repeated iteratively until only one galaxy remains and its coordinates are used as the coordinates of the projected group center.

3.4.4. Group radius

For groups with two or more members, we calculate a projected characteristic radius of the group. Following Robotham et al. (2011) again, we define our group radius R_{group} as the radius around the projected group center in which 50% of the group members are located. This means that for a group with five members, the radius corresponds to the distance of the third most distant member from the group centre. In the case of a group with four members, the radius is the mean between the distance from the group center of the second and third most distant members.

3.4.5. Dynamical mass

Using the previously defined group radii and group velocity dispersions, one can calculate approximate dynamical masses M_{dyn} for our groups using the following equation (Robotham et al. 2011; Chilingarian & Mamon 2008):

$$M_{dyn} \sim \frac{10}{G} \cdot \sigma_{group}^2 \cdot R_{group}. \qquad (43)$$

They serve as a first approximation of the group masses, which are obtained in the next section.

3.4.6. Group mass

To get robust mass estimates for the detected groups, we calibrate mass functions depending on several parameters to our mock catalogues. We split the sample into three sub-samples: isolated galaxies (groups with one visible member only) and all

coefficients	2MRS	SDSS
a_1	-14.4 ± 0.3	-5.3 ± 0.3
a_2	1.23 ± 0.03	0.40 ± 0.03
a_3	-0.0322 ± 0.0008	-0.006 ± 0.001
a_4	-2.4 ± 0.3	-2.1 ± 0.1
a_5	2.5 ± 0.2	1.16 ± 0.06
a_6	-0.72 ± 0.04	-0.22 ± 0.01
a_7	65.0 ± 1.3	32.1 ± 1.0
s_{rms}	0.3293	0.2642

Table 7. Coefficients of the mass dependence on observed parameters of isolated galaxies. They were obtained by a least-square fit on mock catalogue data using Equation 44.
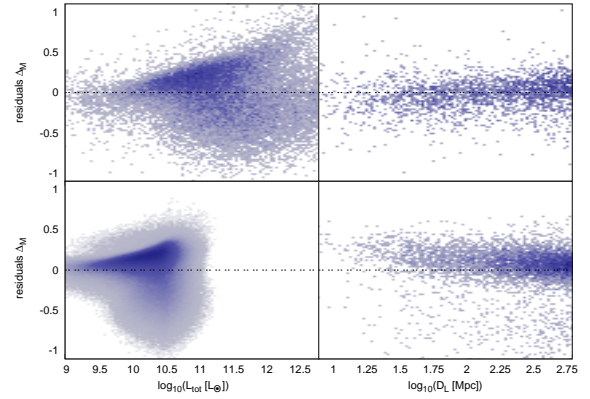

Figure 10. Residuals of the fit for the mass determination of groups with only one visible member depending on the fitting parameter. Top-left panel: residuals depending on the total K_s band group luminosity for the 2MRS data. The top-right panel: residuals depending on the luminosity distance for the 2MRS data. Bottom-left panel: residuals depending on the total r band group luminosity for the SDSS data. The Bottom-right panel: residuals depending on the luminosity distance for the SDSS data.

other groups with two to four members, and groups with more than four members. In the case of the isolated galaxies, we have just two quantities at our disposal to derive their masses: luminosity and distance. We fit the following function to these parameters:

$$\log_{10}(M_{group}) = \sum_{i=1}^{3} \left(a_i \left(\log_{10}(L_{tot}) \right)^i \right) + \sum_{i=1}^{3} \left(a_{i+3} \left(\log_{10}(D_L) \right)^i \right) + a_7 \qquad (44)$$

The group mass M_{group} depends on the group luminosity L_{tot} and the luminosity distance D_L. The coefficients a_1, a_2, a_3, a_4, a_5, a_6, and a_7 are estimated using a least-square fit to our mock catalogues. The results are listed in Table 7 and the residuals $\Delta_M = \log_{10}(M_{fit}) - \log_{10}(M_{group})$ depending on the group mass of these fits are illustrated in Figure 9. Apparently, there is a tendency of our fit to underestimate the true masses of groups with just one visible member in the case of high mass groups, which is most prominent in the tail of the distribution for the SDSS galaxies (see Figure 9). However, the dependence of the residuals on the fitted parameters (see Figure 10) do not show any clear trends, which indicates that considering higher order terms in the fit would not improve our mass function.
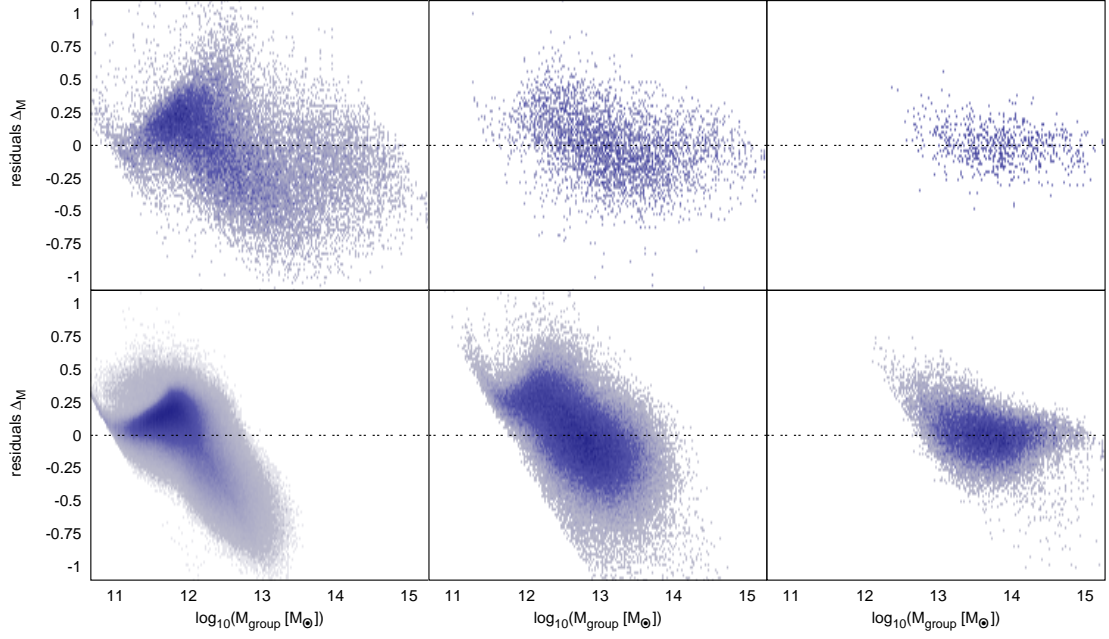
13

Figure 9. Residuals of the fit for the mass determination of groups using 2MRS and SDSS mock data. Top-left panel: residuals of our fit using isolated galaxies (groups with one visible member only) for the 2MRS data. Top-central panel: residuals of groups with two to four members using 2MRS data. Top-right panel: residuals of groups with five or more members using 2MRS data. Bottom-left panel: residuals of our fit using isolated galaxies (groups with one visible member only) for the SDSS data. Bottom-central panel: residuals of groups with two to four members using SDSS data. Bottom-right panel: residuals of groups with five or more members using SDSS data.

coefficients	2MRS	SDSS
a_1	-51.4 ± 10.4	200.6 ± 17.5
a_2	5.6 ± 1.3	-30.6 ± 2.6
a_3	-0.26 ± 0.07	2.1 ± 0.2
a_4	0.004 ± 0.002	-0.051 ± 0.004
a_5	-2.3 ± 0.5	-3.2 ± 0.6
a_6	2.4 ± 0.3	1.3 ± 0.3
a_7	-0.66 ± 0.07	-0.20 ± 0.04
a_8	0.01 ± 0.21	1.2 ± 0.2
a_9	-0.004 ± 0.022	-0.15 ± 0.02
a_{10}	0.0004 ± 0.0008	0.0064 ± 0.0007
a_{11}	182.5 ± 30.4	-476.4 ± 44.6
s_{rms}	0.2459	0.2799

Table 8. Coefficients of the mass dependence on observed parameters of groups with two to four members. They were obtained by a least-square fit on mock catalogue data using Equation 45.

In the case of groups with more than one detected member, we have additional parameters at our disposal. For the groups with two to four members, we include a dependence on the dynamical mass into the fitting function, which is defined as follows:

$$\log_{10}(M_{\mathrm{group}}) = \qquad (45)$$
$$\sum_{i=1}^{4} \left(a_i \left(\log_{10}(L_{\mathrm{tot}}) \right)^i \right) +$$
$$\sum_{i=1}^{3} \left(a_{i+4} \left(\log_{10}(D_L) \right)^i \right) +$$
$$\sum_{i=1}^{3} \left(a_{i+7} \left(\log_{10}(M_{\mathrm{dyn}}) \right)^i \right) + a_{11}.$$

The dynamical group mass σ_{group} is used in addition to parameters of the previous fit to obtain the coefficients a_1 to a_{11}. The results of the fit are listed in Table 8, whereas the residuals of these fits depending on the group mass are shown in Figure 9. The residuals of the fits depending on the fit parameters, which are shown in Figure 11, do not indicate any strong trends.

14
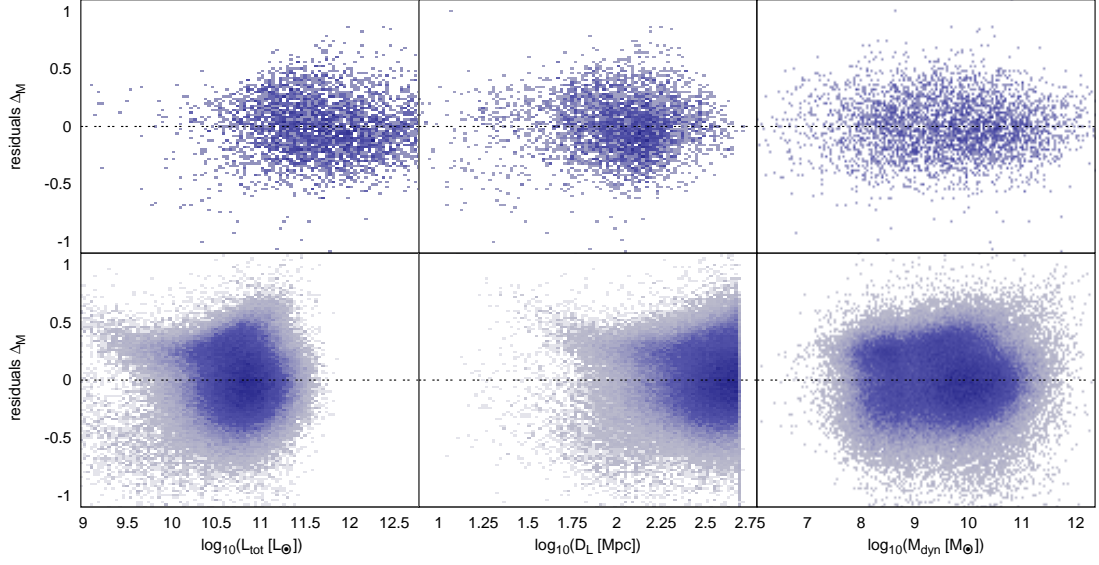
Figure 11. Residuals of the fit for the mass determination of groups with two to four members depending on the fitting parameter. Top-left panel: residuals depending on the K_s band luminosity for the 2MRS data. Top-central panel: residuals depending on the luminosity distance for the 2MRS data. Top-right panel: residuals depending on the dynamical mass for the 2MRS data. Bottom-left panel: residuals depending on the r band luminosity for the SDSS data. Bottom-central panel: residuals depending on the luminosity distance for the SDSS data. Bottom-right panel: residuals depending on the dynamical mass for the SDSS data.
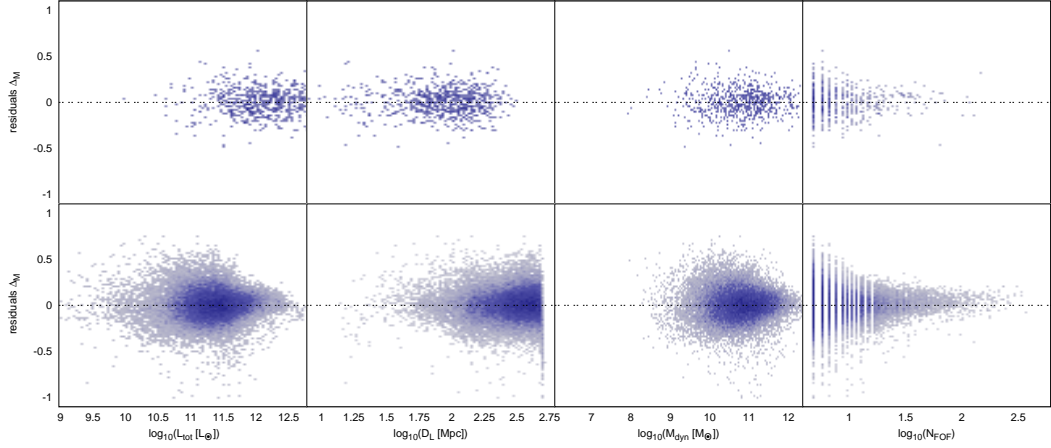
Figure 12. Residuals of the fit for the mass determination of groups with five or more members depending on the fitting parameter. First panel on the top row: residuals depending on the K_s band luminosity for the 2MRS data. Second panel on the top row: residuals depending on the luminosity distance for the 2MRS data. Third panel on the top row: residuals depending on the dynamical mass for the 2MRS data. Fourth panel on the top row: residuals depending on the number of galaxies detected inside a group for the 2MRS data. First panel on the bottom row: residuals depending on the r band luminosity for the SDSS data. Second panel on the bottom row: residuals depending on the luminosity distance for the SDSS data. Third panel on the bottom row: residuals depending on the dynamical mass for the SDSS data. Fourth panel on the bottom row: residuals depending on the number of galaxies detected inside a group for the SDSS data.

For the richest groups in our catalogue (with five or more members), we can define the following fitting function:

$$\log_{10}(M_{\text{group}}) = \tag{46}$$

$$\sum_{i=1}^{5} \left(a_i \left(\log_{10}(L_{\text{tot}}) \right)^i \right) +$$

$$\sum_{i=1}^{3} \left(a_{i+5} \left(\log_{10}(D_L) \right)^i \right) +$$

$$\sum_{i=1}^{3} \left(a_{i+8} \left(\log_{10}(M_{\text{dyn}}) \right)^i \right) +$$

$$a_{12}\log_{10}(N_{\text{fof}}) + a_{13}.$$

The number of detected galaxies within a group N_{fof} is used in addition to the parameters of the previous fit to obtain the coefficients a_1 to a_{13}. The results of the fit are listed in Table 9, whereas the residuals of these fits depending on the group mass are shown in Figure 9. The residuals of the fits depending on the fit parameters, which are shown in Figure 12, do not indicate any strong trends.

15

coefficients	2MRS	SDSS
a_1	327.4 ± 689.6	271.9 ± 197.6
a_2	-58.0 ± 114.4	-45.0117 ± 36.5
a_3	5.0 ± 9.5	3.6 ± 3.4
a_4	-0.2 ± 0.4	-0.1 ± 0.2
a_5	0.004 ± 0.006	0.002 ± 0.003
a_6	2.5 ± 0.7	4.0 ± 0.6
a_7	-1.5 ± 0.5	-2.4 ± 0.3
a_8	0.3 ± 0.1	0.48 ± 0.04
a_9	-1.9 ± 1.6	-5.2 ± 0.7
a_{10}	0.2 ± 0.2	0.51 ± 0.07
a_{11}	-0.007 ± 0.005	-0.016 ± 0.002
a_{12}	0.50 ± 0.05	0.607 ± 0.009
a_{13}	-708 ± 1658	-615.5 ± 427.4
s_{rms}	0.1410	0.1588

Table 9. Coefficients of the mass dependence on observed parameters of groups with more than four members. They were obtained by a least-square fit on mock catalogue data using Equation 46.

3.5. Finite infinity regions scaling

Since the main motivation for this paper is to provide useful datasets for a cosmological test (Saulder et al. 2015b in preparation), we have to develop scaling relations between the halo masses and the masses inside finite infinity regions. We know from Table 2 that slightly less than half of the particles of the simulation are assigned to the FoF groups. Therefore, when summing up the masses for our detected groups as derived in Section 3.4.6, we will find only half the mass expected for a universe with a matter density of $\Omega_m = 0.25$. However, we also know from Table 3 that about three quarters of all simulation particles are within spherical regions around these FoF groups which have on average the renormalized critical density of timescape cosmology using the FoF masses and Equation 7. By considering these new masses and iteratively expanding the regions accordingly, we finally find that about 80% of all particles are within the finite infinity regions.

Taking advantage of this knowledge, we define a procedure that allows us to enhance the masses of our groups to create the best possible set of finite infinity regions. We possess the full particle information of the *millimil* run, which we use to calibrate our method. We take the last six snapshots of the *millimil* run, which is sufficient to cover the same redshift depth as our catalogue. We consider the selection effect due to Malmquist bias of SDSS only, because we will use a combined catalogue of SDSS and 2MRS to obtain the distribution of groups and mass, which is used in Section 4.4 and compensates for the selection effect due to the SDSS saturation limit. As illustrated in Table 10, naturally the number of groups still hosting detectable members decreases at higher redshifts. Although an effect on the total mass within the finite infinity regions is there (a decrease from $\sim$ 80% to $\sim$ 65%), it is not as striking and significant as the impact on the number of detected groups. This means, that although we will miss some of the smaller structures, the biggest contributors to the mass are still detected at higher redshifts. Furthermore, many of the smaller masses are close to the bigger ones, so we still obtain a good representation of the finite infinity regions. In fact, of the 31 428 FOF-groups detected in the last snapshot of the *millimil* run, which have assigned 48.5% of the simulation's particles/mass, 15 413 are visible in the latest snapshot and only 1002 in the earliest snapshot used, but still holding 43.4% and 36.4% of the mass, respectively.

We use this knowledge and the results of Section 2.3.1, the first step is to assign radii according to Equation 7 (with $m = 0.61$ for timescape cosmology) to the FoF groups using their masses. We remove all groups that are fully within the radii of other groups and add their masses to their "host" groups and shift their centre of mass accordingly. Afterwards we count the particles inside these radii. Particles that are located within more than one group are assigned weights corresponding to the reciprocal values of the number of groups they are shared with. At this point we adjust the masses of our groups by using the masses of the particles within the provided radii.

We use this first rescaling to calibrate the following relation:

$$\log_{10}(M_{\mathrm{fi}}) = f_0 \left(\log_{10} \left(\sum_{i=1}^{n} M_{\mathrm{group},i} \right) \right)^2 + f_1 \log_{10} \left(\sum_{i=1}^{n} M_{\mathrm{group},i} \right) + f_2 \tag{47}$$

between the mass of the "finite infinity" region M_{fi} and the sum of group masses it is composed of M_{group}. The coefficients f_0, f_1, and f_2 are obtained by a least-square fit and their values are listed in Table 10. We apply this fit to each snapshot. The distribution of the parameters and our fit on them is illustrated in Figure 13.

We continue to expand the radii of the finite infinity regions based on the number of particles (using the same weighting procedure as before) within the new radii. We also keep on removing groups that are fully within finite infinity regions of other groups and add their masses to their hosts and shift the centres of mass accordingly. We repeat this procedure iteratively until the change of total mass within all finite infinity regions is less than 0.1% from one step to the next.

We derive another rescaling relation, which connects the final masses of the groups to the sum of the initial masses of FoF groups. For this final rescaling, we also use Equation 47 and fit it to the data to obtain the coefficients, which are listed in Table 10. The distribution of the parameters and our fit on them is illustrated in Figure 14.

With all calibrations done, we now summarise how we apply our rescaling method on real data:

For a group catalogue with masses obtained using the calibrations of Section 3.4.6, we calculate the radii of our finite infinity regions using Equation 7 with the coefficients corresponding to the snapshot closest in redshift to every group. In the next step, we remove all groups that are fully within the first estimate of the finite infinity regions by merging them with their host in the same fashion as before. Afterwards, we apply the first rescaling of the masses and consequently the radii of the finite infinity regions. Then we iteratively merge all groups fully within the finite infinity regions of other groups and adjust their hosts' masses and radii accordingly. Once this is completed, we apply the final mass rescaling using the sum of the initial masses of the groups that merged as a basis. We use the initial masses for the final rescaling instead of the masses obtained after the first rescaling, because the overall uncertainty is slightly lower this way. The reason to do the first rescaling at all, and not to proceed directly to the final rescaling without it, is that the merging process, which is done after it, slightly shifts the distribution of the mass function and we would introduce an unnecessary source of error by skipping it.

After all the rescaling and calibrations, there is still more than 20% of the mass of the simulation that is not in any finite infinity regions. Given that the model described in Wiltshire (2007) is only a two-phase model with completely empty voids and walls (the space inside finite infinity regions) with their renormalized critical density, we have two options on how to

rescaling	redshift	f_0	f_1	f_2	s_{rms}	mass within fi-regions	volume within fi-regions	groups detected/used
first	0	0.008 ± 0.002	0.77 ± 0.06	1.7 ± 0.3	0.1247	74.68%	13.27%	15413
final	0	0.028 ± 0.004	0.26 ± 0.11	5.1 ± 0.6	0.2187	80.28%	22.76%	9187
first	0.020	0.005 ± 0.003	0.85 ± 0.08	1.3 ± 0.5	0.1230	72.16%	12.80%	8952
final	0.020	0.031 ± 0.006	0.17 ± 0.15	5.7 ± 0.9	0.2188	78.24%	22.27%	5676
first	0.041	0.007 ± 0.005	0.80 ± 0.12	1.7 ± 0.7	0.1198	69.15%	12.10%	4993
final	0.041	0.030 ± 0.009	0.16 ± 0.22	5.9 ± 1.3	0.2197	75.61%	21.35%	3415
first	0.064	0.001 ± 0.006	0.95 ± 0.15	0.8 ± 0.9	0.1158	66.35%	11.59%	3165
final	0.064	0.026 ± 0.012	0.24 ± 0.30	5.6 ± 1.8	0.2210	73.20%	20.63%	2336
first	0.089	0.003 ± 0.008	0.89 ± 0.21	1.2 ± 1.3	0.1165	62.45%	10.82%	1941
final	0.089	0.031 ± 0.016	0.10 ± 0.41	6.7 ± 2.6	0.2237	69.93%	19.85%	1530
first	0.116	0.001 ± 0.012	0.93 ± 0.31	1.0 ± 1.9	0.1184	55.60%	9.44%	1002
final	0.116	0.043 ± 0.024	-0.24 ± 0.61	9.1 ± 3.9	0.2313	64.75%	18.75%	826

Table 10. Coefficients of the mass rescaling for the finite infinity regions and the mass as well as the volume covered by them. Column one: indicator if first of final rescaling of finite infinity regions, column two: cosmological redshift of that snapshot, column three to five: coefficients of the fit (see Equation 47), column six: root mean square of that fit, column seven: percentage of mass within fi-regions compared to the total mass in the simulation, column eight: percentage of volume within fi-regions compared to the total volume in the simulation, column nine: number finite infinity regions/groups used for the fit and remaining after iteration.
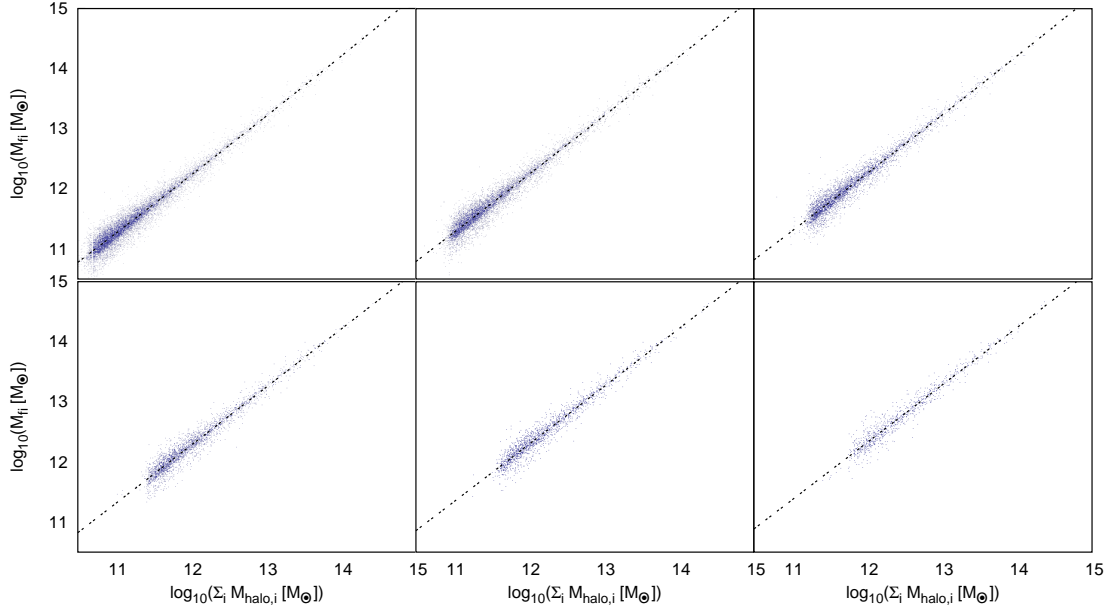
Figure 13. Distribution of the masses within the finite infinity regions before expanding them iteratively depending on the sum of the masses of the groups they are composed of. The dotted black line indicates our fit on this relation. The panels show the 6 snapshots used from the last one (number 63) in the top left panel to the earliest one (number 58) in the bottom right panel.

proceed: 1) we can either add the $20 - 30\%$ missing mass to the detected finite infinity regions and adjust their sizes accordingly, or we can 2) assume that the $20 - 30\%$ missing mass is distributed homogeneously throughout the rest of the simulations volume (the voids) and define them as not completely empty. Since we are still working on which way is the best-suited one, we keep both options open for a more considerate deliberation of their possible implications on the theory in our follow-up paper (Saulder et al. 2015c in preparation), where we will perform the cosmological test to which we are building up here. Therefore, we will provide the data for both options.

4. Results

We provide four group catalogues, which are made available on VizieR: (link follows as soon as the paper is accepted).

17
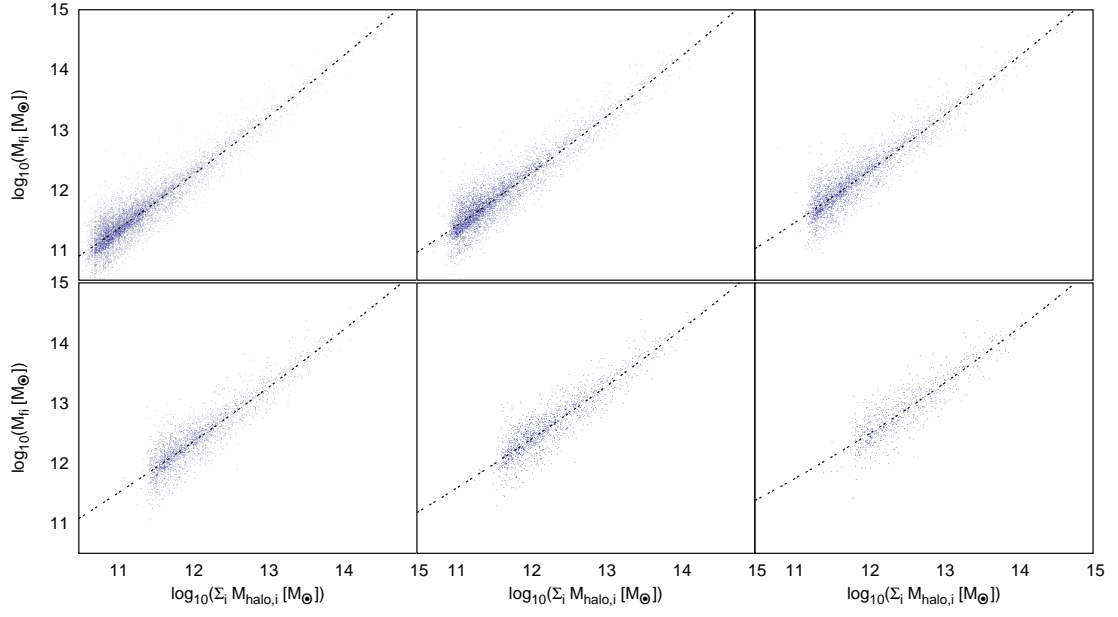
Figure 14. Distribution of the final masses of the finite infinity regions depending on the sum of the masses of the groups they are composed of. The dotted black line indicates our fit on this relation. The panels show the 6 snapshots used from the last one (number 63) in the top left panel to the earliest one (number 58) in the bottom right panel.

18

ID	α_{group} [°]	δ_{group} [°]	z_{group}	$\log_{10}\left(L_{\text{tot,K}_s}\right)$ [$\log_{10}\left(L_\odot\right)$]	$\log_{10}\left(L_{\text{obs,K}_s}\right)$ [$\log_{10}\left(L_\odot\right)$]	$\log_{10}\left(M_{\text{group}}\right)$ [$\log_{10}\left(M_\odot\right)$]	$\log_{10}\left(M_{\text{dyn}}\right)$ [$\log_{10}\left(M_\odot\right)$]	σ_{group} [km/s]	R_{group} [kpc]	a_{group} [°]	D_L [Mpc]	N_{group}
8	187.9967	14.4204	0.0044	12.77	12.76	14.63	11.90	557.4	1110	3.4932	18.3	131
11	54.7163	-35.5944	0.0047	12.33	12.32	13.96	10.74	230.5	447	1.3365	19.3	33
100	192.5164	-41.3820	0.0121	12.77	12.72	14.62	11.88	851.7	455	0.5311	50.2	66
303	157.6104	-35.3595	0.0101	12.35	12.32	14.17	11.30	515.5	323	0.4503	42.0	37
324	243.7661	-60.9072	0.0167	13.04	12.97	14.92	11.96	745.5	704	0.5978	69.8	101
371	49.9510	41.5117	0.0173	12.96	12.89	14.87	12.04	1038.6	440	0.3627	72.0	94
381	159.1784	-27.5283	0.0131	12.68	12.63	14.61	11.77	635.1	628	0.6778	54.5	76
478	195.0338	27.9770	0.0241	13.18	13.02	15.04	12.15	921.4	713	0.4240	101.1	87
581	28.1936	36.1518	0.0155	12.62	12.55	14.48	11.51	453.4	677	0.6203	64.4	50
1064	176.0090	19.9499	0.0223	12.89	12.76	14.75	11.80	676.2	595	0.3813	93.5	53
3939	241.11047	17.7420	0.0359	13.21	12.82	14.97	12.23	795.1	1159	0.4692	151.8	33

Table 11. Parameters of a selected sample of groups as they appear in our 2MRS group catalogue. Column 1: ID, column 2 and 3: equatorial coordinates of the group centre, column 4: redshift of the group centre, column 5: total group luminosity in the K_s band, column 6: observed group luminosity in the K_s band, column 7: group mass, column 8: dynamical mass of the group, column 9: group velocity dispersion, column 10: physical group radius, column 11: angular group radius, column 12: luminosity distance to the group centre, and column 13: detected group members.

ID	α_{group} [°]	δ_{group} [°]	z_{group}	$\log_{10}\left(L_{\text{tot,r}}\right)$ [$\log_{10}\left(L_\odot\right)$]	$\log_{10}\left(L_{\text{obs,r}}\right)$ [$\log_{10}\left(L_\odot\right)$]	$\log_{10}\left(M_{\text{group}}\right)$ [$\log_{10}\left(M_\odot\right)$]	$\log_{10}\left(M_{\text{dyn}}\right)$ [$\log_{10}\left(M_\odot\right)$]	σ_{group} [km/s]	R_{group} [kpc]	a_{group} [°]	D_L [Mpc]	N_{group}
38870	247.4372	40.8116	0.0301	12.72	12.69	15.25	12.27	614.9	2139	1.0250	126.9	502
44039	227.7808	5.3173	0.0793	12.99	12.86	15.30	12.67	852.0	2799	0.5368	348.0	297
83856	50.0647	41.3986	0.0162	12.02	12.02	14.71	12.03	933.6	526	0.4617	67.4	128
102802	167.9317	40.8208	0.0765	12.81	12.69	15.23	12.36	644.1	2366	0.4691	334.9	220
111101	239.5833	27.2334	0.0897	13.16	13.00	15.35	12.48	770.3	2207	0.3780	397.3	365
132281	14.0672	-1.2554	0.0431	12.55	12.51	15.05	12.19	627.2	1691	0.5742	183.6	217
153024	241.1491	17.7216	0.0368	12.58	12.55	15.10	12.11	666.7	1242	0.4909	155.9	293
155904	195.0339	27.9769	0.0242	12.75	12.74	15.32	12.27	845.8	1107	0.6549	101.6	690
157845	240.5828	16.3460	0.0363	12.62	12.58	15.17	12.16	718.0	1204	0.4819	153.8	367
167635	167.6785	28.6931	0.0341	12.38	12.35	14.95	11.93	611.8	987	0.4201	144.0	207
185409	176.0090	19.9498	0.0224	12.30	12.29	14.92	11.91	704.9	701.0	0.4478	93.7	218

Table 12. Parameters of a selected sample of groups as they appear in our SDSS group catalogue. Column 1: ID, column 2 and 3: equatorial coordinates of the group centre, column 4: redshift of the group centre, column 5: total group luminosity in the r band, column 6: observed group luminosity in the r band column 7: group mass, column 8: dynamical mass of the group, column 9: group velocity dispersion, column 10: physical group radius, column 11: angular group radius, column 12: luminosity distance to the group centre, and column 13: detected group members.

4.1. The 2MRS group catalogue
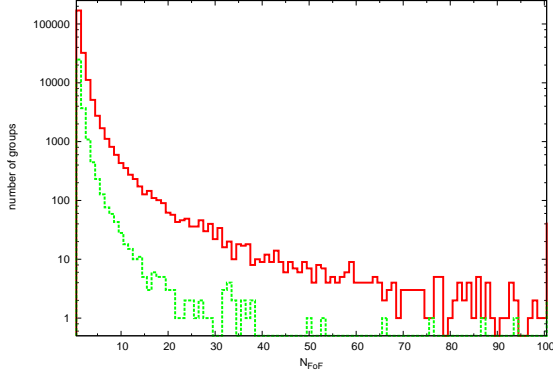
Figure 15. Distribution of the multiplicity N_{FoF} of the groups detected in 2MRS (green dotted line) and in SDSS (red solid line).

Our 2MRS based group catalogue is composed of 43425 galaxies from Huchra et al. (2012b) covering 91% of the sky. Using our group finder with the optimal coefficients from Table 6, we detect 30695 groups in the 2MRS data. As illustrated in Figure 15, the majority (24782 to be precise) of the galaxies can be found in groups with only one visible member. This does not necessarily mean that all of them are isolated objects, but that there is only one galaxy sufficiently bright to be detected by 2MRS. We identify 5796 groups within the multiplicity range from two to ten and only 117 with higher multiplicities (two of them with more than 100 members each). Figure 15 clearly shows that the number of groups rapidly decreases with increasing number of multiplicity.

We identified some of the richest clusters [7]. The cluster with the most detected members and the 2MRS group ID 8 in our catalogue is the well-known Virgo cluster. Furthermore, we identified the following clusters with their parameters listed in Table 11: the Fornax Cluster with the ID 11,the Centaurus Cluster with the ID 100, the Antlia Cluster with the ID 303, the Norma cluster with the ID 324, the Perseus Cluster with the ID 371, the Hydra Cluster with the ID 381, the Coma Cluster with the ID 478, Abell 262 with the ID 581, the Leo Cluster with the ID 1064, and the Hercules Cluster with the ID 3939. It is very encouraging to see that we were able to locate many well-known cluster in our catalogue.

We provide a list of all detected groups containing their 2MRS group ID, the coordinates of the group centre (right ascension and declination are both given in degrees), the median redshifts, the total group luminosity in the K_s band, the observed group luminosity in the K_s band, the calculated group mass (using the method explained in Section 3.4.6), the dynamical mass of the group, the group velocity dispersion, the physical group (given in kpc), the angular group radius (given in degree), the luminosity distance to the group centre (given in Mpc), and the number of detected group members. An excerpt of this list is provided in Table 11. In addition to that list, a list of all the galaxies used is provided, containing the our internal galaxy IDs, the

---

[7] We use the NASA/IPAC Extragalactic Database (`http://ned.ipac.caltech.edu/`) for a manual search by coordinates to identify this and all other other groups in this section.

2MRS group IDs of the group the galaxy belongs to, and the 2MASS IDs of the galaxies.

4.2. The SDSS DR10 group catalogue

Our SDSS based group catalogue is composed of 397263 galaxies from Ahn et al. (2014) covering 9274 square degree. Using our group finder with the optimal coefficients from Table 6, we detect 228123 groups in the SDSS DR10 data up to a redshift of 0.11. As illustrated in Figure 15, a large fraction (169623 to be precise) of the galaxies can be found in groups with only one visible member. Similar to the results of the 2MRS catalogue, the number of groups rapidly decreases with increasing number of multiplicity, but since the SDSS sample is much deeper, there are more groups with higher multiplicity than for the 2MRS sample. We identify 42 group with more than 100 visible members each.

We identified some of the richest clusters in our catalogue: the Coma Cluster with the ID 155904, the Perseus Cluster with the ID 83856, the Leo Cluster with the ID 185409, Abell 2142 with the ID 111101 and the Hercules Cluster with the ID 153024. A list of these clusters and others with more than two hundred detected members is provided in Table 12. Due to the saturation limits of SDSS spectroscopy, there is a dearth of galaxies in the SDSS survey at very low redshifts. Hence, we do not detect as many rich nearby groups as in the 2MRS survey, even when taking the smaller sky coverage into account. However it is encouraging to see that we are able to identify some of the same groups and clusters in both survey data.

We provide a list of all detected groups containing their SDSS group ID, the coordinates of the group centre (right ascension and declination are both given in degrees), the median redshifts, the total group luminosity in the r band, the observed group luminosity in the r band, the calculated group mass (using the method explained in Section 3.4.6), the dynamical mass of the group, the group velocity dispersion, the physical group (given in kpc), the angular group radius (given in degree), the luminosity distance to the group centre (given in Mpc), and the number of detected group members. An excerpt of this list is provided in Table 12. In addition to that list, a list of all the galaxies used is provided, containing the our internal galaxy IDs, the SDSS group IDs of the group the galaxy belongs to, and the SDSS object IDs of the galaxies.

4.3. The fundamental plane distance group catalogue

We take advantage of our previous work (Saulder et al. 2013) on the fundamental plane of elliptical galaxies to provide additional information for a subset of groups of our SDSS catalogue. We provide redshift independent fundamental plane distances for all groups that contain at least one early-type galaxy based on our extended and up-dated fundamental plane calibrations in the Appendix of our recent paper (Saulder et al. 2015). We find 49504 early-type galaxies distributed over 35786 groups of our SDSS group catalogue. As illustrated in Figure 16, the majority (29871 to be exact) of the early-type galaxies are the only detected early-type galaxy in their group. We also find 5915 groups hosting two or more early-type galaxies and 808 of these groups even contain five or more early-type galaxies.

We provide three lists (one of them is shown in Table 13 as an example) of all our SDSS groups hosting elliptical galaxies for three slightly different sets of cosmological parameters. Naturally, since this paper uses the cosmology of the Millennium simulation (see Table 1 for the parameters), one of our lists is

20

ID	α_{group} [°]	δ_{group} [°]	z_{group}	$D_{A,FP}$ [Mpc]	$D_{C,FP}$ [Mpc]	$D_{L,FP}$ [Mpc]	$D_{A,z}$ [Mpc]	$D_{C,z}$ [Mpc]	$D_{L,z}$ [Mpc]	N_{ETG}	N_{group}
2	154.7184	-0.9826	0.0959	339.7	370.8	404.6	355.4	389.5	426.8	2	7
6	150.9243	-0.5669	0.0965	315.3	341.8	370.6	356.9	391.3	429.0	1	4
9	159.3740	-0.6780	0.0968	381.4	421.0	464.6	358.3	393.0	431.0	1	13
10	160.9982	-0.5883	0.0617	195.7	205.6	216.0	236.7	251.3	266.8	1	8
12	162.9378	-0.4380	0.0739	271.9	291.4	312.3	279.8	300.5	322.7	1	1
17	152.1050	0.1759	0.0968	345.5	378.4	414.4	358.4	393.1	431.2	8	26
19	157.7624	-0.0892	0.0952	331.3	360.8	392.8	352.9	386.5	423.2	2	4
21	159.7015	-0.1747	0.0962	288.0	310.0	333.7	356.2	390.5	428.0	1	1
22	159.9015	-0.1472	0.0960	373.8	411.8	453.6	355.7	389.9	427.3	1	1
23	161.7152	-0.1086	0.0412	284.0	305.3	328.3	161.6	168.3	175.2	1	3

Table 13. Parameters of a selected sample of groups as they appear in our fundamental plane distance catalogue. Column 1: SDSS cluster ID, column 2 and 3: equatorial coordinates of the group centre, column 4: redshift of the group centre, columns 5 to 7: the angular diameter distance, the co-moving distance, and the luminosity distance all calculated using the fundamental plane, columns 8 to 10: the angular diameter distance, the co-moving distance, and the luminosity distance all calculated using the redshift, column 11: number of detected early-type galaxies, and column 12: all detected group members.
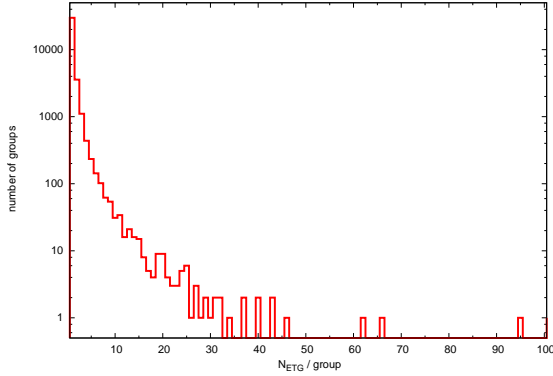
Figure 16. Distribution of the number of early-type galaxies found in our SDSS groups.

Figure 17. The difference in the distance measurements for our clusters by comparing the fundamental plane distances with the redshift distances depending on the number of early-type galaxies N_{ETG} per group. The black dashed line indicates the average ratio per early-type galaxies multiplicity bin. The red solid line marks the corresponding 1-σ intervals. The green dashed line indicates the expected progression of the 1-σ intervals around one based on the root mean square of our fundamental plane distance error of 0.0920.

based on it. Another list is based on the cosmological parameters of our previous papers (Saulder et al. 2013), which are $H_0 = 70$ km/s/Mpc, $\Omega_M = 0.3$, and $\Omega_\Lambda = 0.7$, while the last list uses the cosmological parameters of the Planck mission (Planck Collaboration et al. 2014a), which are $H_0 = 67.3$ km/s/Mpc, $\Omega_M = 0.315$, and $\Omega_\Lambda = 0.685$ (Planck Collaboration et al. 2014b). The lists contain their SDSS group ID, the co-ordinates of the group centre (right ascension and declination are both given in degrees), the median redshifts, the angular, co-moving, and luminosity fundamental plane distances, the angular, co-moving, and luminosity redshift distances, the number of elliptical galaxies hosted in that group and the total number of detected group members. As an example of our catalogue, the top ten lines of our Millennium simulation cosmology catalogue is provided in Table 13.

In Figure 17, we show that the difference between the co-moving fundamental plane distance and the co-moving redshift distance decreases with the increasing number of elliptical galaxies per group. For higher multiplicities the the statistics are affected by the small number of groups hosting so many detected elliptical galaxies. We compare this to the expected decrease based on the root mean square (of 0.0920 in the z-band) of our fundamental plane calibration in our recent paper (Saulder et al. 2015) and find that the measured decrease is comparable to

the expected one, although there is a trend for the mean value to rise with higher early-type multiplicity per cluster.

4.4. The finite infinity regions catalogues - merging 2MRS and SDSS

While the three previous catalogues are kept relatively general allowing for a wide range of applications, the catalogue of finite infinity regions is exclusively made as a preparatory work for our next paper Saulder et al. (2015c in preparation). It contains the already mentioned finite infinity regions, which are required for a cosmological test that we plan on executing in our future work.

The reason for using the 2MRS catalogue in addition the the SDSS catalogue is the fact that the SDSS suffers from additional incompleteness at very low redshifts due to the saturation of their spectroscopic data. The 2MRS catalogue has no saturation limit and allows us to fill in gaps. The merging of the two catalogues is a delicate procedure, which requires some deliberations be-

21
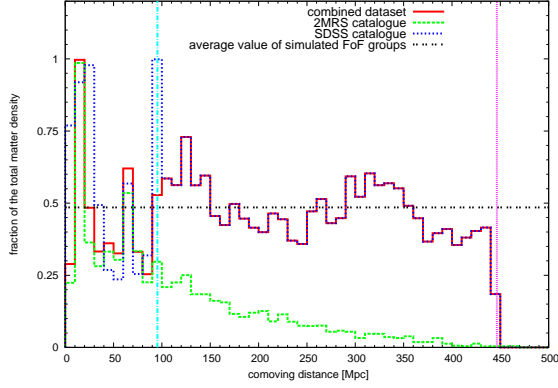
Figure 18. Distribution of the matter density in dependence of the distance for our catalogues. The dotted black line indicates the expected average value based on the mock catalogue used to calibrate the groups' masses. The dotted blue line marks the density distribution of our SDSS catalogue and the dashed green line marks the density distribution of our 2MRS catalogue. The solid red line indicates the density distribution of our combined dataset, which is a mixture of the SDSS and 2MRS catalogues below the distance at which the SDSS saturation limit becomes negligible (indicated by dashed-dotted cyan line) and only the SDSS catalogue above this distance. The maximum depth of catalogue, which is cut of at a redshift of 0.11 is indicated by the dotted magenta line.
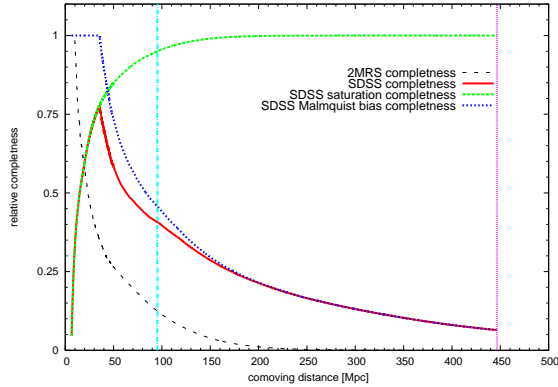
Figure 19. Completeness of our catalogues based on the luminosity function of their galaxies depending on the co-moving distance. The dashed black line indicates the completeness function of the 2MRS catalogue, which is only affected by the Malmquist-bias. The solid red line marks the completeness function of SDSS, which is affected by the Malmquist-bias (indicated by the dotted blue line) and a saturation limit (indicated by the dashed green line). The dashed-dotted cyan line denotes the point, when the impact of saturation limit on the completeness function of SDSS becomes negligible (the saturation limit completeness rises about 95%). The maximum depth of catalogue, which is cut of at a redshift of 0.11 is indicated by the dotted magenta line.

forehand. When plotting the matter density as function of distance (see Figure 18), the density of the 2MRS catalogue fluctuates (due to large local structures) around the average value expected from the mock catalogues in the inner mass shells, but then drops drastically in the outer shells. The density of SDSS catalogue tends to be lower than the density of the 2MRS catalogue in the innermost shells, but then rises and stays with rea-

sonable range around the expected value from the mock catalogue in most shells.

To get the best of both worlds, we use a combination of the 2MRS and SDSS catalogue up to a certain distance and beyond that the SDSS catalogue only. We define this limit as the distance at which the effect of saturation limit on SDSS starts becoming negligible, because the main reason for including the 2MRS catalogue in the first place was to compensate for this effect. The specific choice of this limit is to some extent arbitrary. We decide to place it at a co-moving distance of 95.4 Mpc, which corresponds to where 95% of the luminosity function (down to an absolute magnitude of -15 mag in the r band, which was our limit on SDSS data) is unaffected by the saturation limit as illustrated in Figure 19. This is also where the mass density of 2MRS starts dropping significantly below the expected value (see Figure 18). The 2MRS catalogue is already strongly effected by the Malmquist bias at this distance. As illustrated in Figure 19 only the brightest 5% of the luminosity function (down to an absolute magnitude of -18 mag in the K_s band, which was our limit on 2MRS data) are still visible.

The first step in merging the 2MRS and SDSS catalogue is to remove all 20502 2MRS groups beyond a co-moving distance of 95.4 Mpc. From this distance outward, only SDSS data is used. In the overlapping area we can encounter three cases, for which the third case requires careful assessment: 1) A group is detected only in SDSS, because its galaxies are too faint for 2MRS. 2) The group is only detected in 2MRS because they are too near and too bright for SDSS or simply because they are outside the area covered by SDSS. In both cases the groups will be fully included in the new merged catalogue. 3) The same group (or parts of them) is detected in both catalogues. In this case, both detections need to be merged in a meaningful manner.

For this group merging, we take our truncated 2MRS catalogue and see how many SDSS groups are within one linking length of our 2MRS groups. We use the definition of the linking length of Equations 26 and 27 with the optimised parameters for 2MRS from Table 6 but with λ_{opt} set to zero, because the corresponding term was calibrated using the galaxy luminosities and not the group luminosities and it was a minor correction anyway. If one of the linking lengths α_{eff} or R_{eff} is smaller than the group angular radius or the group velocity dispersion respectively, it is scaled up accordingly. We find that 2460 of the 12598 SDSS groups in the overlapping volume need to be merged with 1903 2MRS groups. There are obviously several cases in which we find more than one SDSS group within a 2MRS group. The parameters of the newly merged groups are the weighted averages of the parameters of their predecessors. One part of the weights is the completeness function:

$$f_c(z) = \frac{\int_{-5\log_{10}(D_L(z))+m_{sat}+5}^{-5\log_{10}(D_L(z))+m_{limit}+5} \Phi(m)\,dm}{\int_{-\infty}^{M_{abs,min}} \Phi(m)\,dm}. \tag{48}$$

It depends on the luminosity distance D_L derived from the redshift z, the saturation limit m_{sat}, which is 14 mag in the SDSS r band and none existent for 2MRS, the limiting magnitude m_{limit} of the survey, which is 17.77 mag in the r band for SDSS and 11.75 mag in the K_s band for 2MRS. We use the corrected observed luminosity function $\Phi(m)$ as illustrated in Figure 3. The 2MRS and SDSS completeness functions are plotted in Figure 19. The other part of the weights $w_{merge} = f_c \cdot N_{FoF}$ used for merging the groups is the number of members per group N_{FoF}. This will ensure that the masses of galaxy clusters are not biased by a single galaxy from the other survey. In the merging process

the centre of mass of the new groups will be adjusted according to the weights as well. Our combined catalogue consists of 235856 groups. They contain in total 44.6% of mass expected for the volume using the Millennium simulation cosmology, comparable with the 43.4% of matter in visible groups in the latest snapshot of the *millimil* simulation.

We apply the method explained in Section 3.5 on our combined catalogue to obtain the finite infinity regions. We assign radii for the first estimate of the finite infinity regions based on the masses in the combined catalogue and merge all groups that are fully within theses regions of other groups into their hosts. We end up with 186245 groups after performing this procedure. The masses of theses groups are rescaled using Equation 47 with the coefficients for the first rescaling from Table 10 of the snapshot nearest in redshift to our groups. We calculate the new finite infinity radii and repeat the merging procedures to find 183863 groups containing 74.8% of the mass expected for the volume and the cosmology used. The masses of the 183863 groups are rescaled again using the sum of the original masses of "member groups" as a basis and the coefficients for the final rescaling from Table 10 of the snapshot nearest in redshift to our groups. The total mass of the groups adds up to 77.7% and the finite infinity regions occupy 21.5% of the volume covered by our combined catalogue. These values are within the expected range (see Table 10) for a combined dataset of all snapshots. We note that based on the theory of the two-phase model of Wiltshire (2007), we expect ~ 25% of the volume to be inside finite infinity regions.

c_x [Mpc]	c_y [Mpc]	c_z [Mpc]	$\log_{10}(M_{fi})$ [$\log_{10}(M_\odot)$]	R_{fi} [Mpc]
-0.750	0.451	2.365	12.31	1.752
-7.424	-2.913	-7.405	13.28	3.680
-6.883	-2.021	-8.389	13.00	2.975
-8.143	-3.669	-5.129	13.01	3.005
-17.946	-1.329	4.686	15.31	17.565
8.906	12.502	-10.477	14.33	8.245
9.505	8.167	-0.003	12.73	2.427
4.607	5.361	-6.168	12.28	1.714
3.170	2.640	3.373	12.76	2.478
2.240	4.199	13.022	13.07	3.141

Table 14. Parameters of a selected sample of groups as they appear in our finite infinite regions catalogue. Column 1 to 3: the Cartesian co-moving coordinates of the centre of the finite infinity region, column 4: the mass within the finite infinity region, and column 5: the radius of the finite infinity region.

We provide a list of all 164509 remaining groups containing their Cartesian co-moving coordinates c_x, c_y, and c_z, their final masses, and their radii for the finite infinity regions. A sample of the first ten lines of our catalogue is given in Table 14.

Additionally, we provide another list in the same format, in which the masses of the groups have been rescaled so that their sum covers the full mass expected for the catalogue's volume and the Millennium simulation cosmology. We also applied the merging procedure on the rescaled groups, which leaves us with 152442 groups whose finite infinity regions cover 28.3% of the catalogue's volume.

5. Discussion

To provide a robust model of the matter distribution in the local universe, we used data from the SDSS DR10 (Ahn et al. 2014)

and the 2MRS (Huchra et al. 2012b). After we preform some filtering and calibrate the data, we end up using 43425 of 43534 galaxies from the entire 2MRS catalogue and 397263 of 422475 galaxies from the SDSS below a redshift of 0.112[8]. To best exploit our given data, we created several mock catalogues from the Millennium simulation to carefully calibrate our tools.

For the SDSS sample and the 2MRS sample, we provide eight independent mock catalogues each. Every one of them covers one eighth of the sky and the distribution of the luminous matter in them is based on semi-analytic galaxy models from (Guo et al. 2011). The 2MRS mock catalogues consider the Malmquist bias, peculiar motions and all possible measurement uncertainties. The SDSS mock catalogues takes the same effects into account as for the 2MRS mock catalogues, but also includes the saturation limits and fibre collisions bias of SDSS. We also provide a corresponding set of dark catalogues, which were used to optimise the group finder and calibrate the masses derived from the groups. Although our mock catalogues were primarily designed as a calibration tool for our group finder algorithm presented in this paper, they are kept sufficiently general to be used in future work as well.

The core piece of this paper is the group finder which we developed. It is strongly inspired by the one presented in (Robotham et al. 2011). We consider several effects for our group finder algorithm, which we have to calibrate independently for the 2MRS and the SDSS sample. First, we calculated the basic linking length $b_{link,0}$, which we define as the average co-moving distances between the two nearest sufficiently luminous (this requirement excludes (most) dwarf galaxies) neighbour galaxies in our unbiased mock catalogue. The thereby obtained parameters provides a first basic estimate of order of magnitude our adaptive linking length used in our algorithm. The linking length is split into a radial and angular (transversal) component and the later is modified to account for stretching effect in redshift space due to peculiar motions inside of groups (illustrated in Figure 6). We also consider that the differently luminous galaxies have different masses (see Figures 5 and 4) and thereby a large sphere of gravitational influence. However, when optimizing the free parameters of our group finder algorithm in the next, it turns out that this correction is of minor significance. Another correction rescales the linking length depending on the fraction of the galaxy luminosity function (see Figure 3) that is visible at a certain distance. This rescaling effectively corrects for the incompleteness of our data due to the Malmquist bias. The final linking length, which is defined in Equations 26 and 27, depends on four free coefficients, that are α_{opt}, R_{opt}, γ_{opt}, and λ_{opt}. Following Robotham et al. (2011), they are optimized by maximizing the group coast function (see Equations 28 to 34) using a Simplex algorithm (Nelder & Mead 1965). The results of the optimization can be found in Table 6. As already mentioned before, the coefficient γ_{opt} is close to 0, thereby clearly reducing the significance of the mass dependency of the linking length. λ_{opt} is around one, while α_{opt} and R_{opt} are located between 0.4 and 0.6. The optimized group finder was applied on our data sets in the next step.

The 2MRS group catalogue is composed of 30695 groups, which host a total of 43425 galaxies. We identify many well-known structures of the local universe in this catalogue. Aside from basic parameters such as coordinates and redshifts, the most important quantity for our groups are their masses. Therefore, we use our mock catalogues to carefully calibrate the

---

[8] This value was reduced during the filtering after applying a correction for our motion relative to the CMB to 0.11.

mass function (see Equations 44, 45, and 46) depending on several other parameters of the groups. The results of our fits on the mass functions can be found in Tables 7, 8, and 9. The advantages of the 2MRS catalogue are its wide sky coverage and its high completeness at very low redshifts.

The SDSS group catalogue is composed of 228123 groups, which host a total of 397263 galaxies. It is restricted to a smaller area of the sky than the 2MRS group catalogue, but it is also deeper providing a clearly more complete sample at higher (up to our limiting redshift of 0.11) redshifts. At very low redshifts the SDSS group catalogue suffers from some additional incompleteness due to the saturation limits of SDSS spectroscopy. This is the main reason why we also provide the 2MRS catalogue to complement the SDSS catalogue a very low redshifts. The two catalogues are not completely disjunct, there is some overlap between them and we are able to identify a few prominent galaxy clusters in both catalogues.
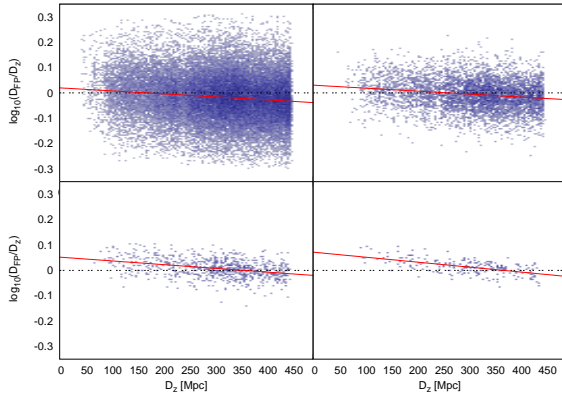
Figure 20. Dependencies of the difference in the distance measurements for our clusters by comparing the co-moving fundamental plane distances with the co-moving redshift distances on the co-moving redshift distance itself and the number of elliptical galaxies per group. Top-left panel: all groups that contain at least one elliptical galaxy. Top-right panel: all groups containing at least two elliptical galaxies. Bottom-left panel: all groups that host five or more elliptical galaxies. Bottom-right panel: all groups hosting at least 10 elliptical galaxies. The solid red lines indicate the fits on the displayed data, which show an increasing dependence of the ratio between the fundamental plane distance and the redshift distance on the redshift distance with an increasing number of elliptical galaxies per group. The dashed black line only provides a reference, if this trend was not detected.

The fundamental plane distance catalogue is obtained by combining the SDSS group catalogue with some of our previous work. We provided very detailed calibration of the fundamental plane in Saulder et al. (2013) and listed updated coefficients based on an extended sample in our recently submitted paper (Saulder et al., 2015). The aim of the fundamental plane distance catalogue is to provide redshift independent distance measurements for groups hosting elliptical galaxies. As illustrated in Figure 17, the accuracy of our alternative (to redshift) distance measurements improves for groups with higher elliptical galaxy multiplicities, but there are some residual trends visible. The fundamental plane distances tend to be on average larger than the redshift distances for groups with a higher number of early-type galaxies detected in them.

When we examine our sample closer, we discover a trend in the ratio between the fundamental plane distance and the redshift distance. As illustrated in Figure 20, there is a trend that the ratio between the co-moving fundamental plane distance and the co-moving redshift distance slightly decreases with a growing co-moving redshift distance. The astonishing fact is that this trend becomes steeper for groups hosting more and more elliptical galaxies, as already hinted at in Figure 17. We considered a selection effect on the elliptical galaxies in the nearer groups, a general dependence of elliptical galaxies on their environment, or some selection effect on measurement of the median redshift of the groups. Understanding this systematic trend will be especially relevant for of our planned cosmological test (Saulder et al. 2015b in preparation). We notice a dearth of early-type galaxies, and consequently groups hosting them, at low distances, which we attribute to the saturation limit of SDSS of 14 mag in the r band. The average absolute r and magnitude of an elliptical galaxy (not counting dwarf galaxies) of roughly -21 mag (Saulder et al. 2013), which means that a significant part of the elliptical galaxies at a luminosity distance of about 100 Mpc is still not included in the sample. A comparison with our mock catalogues allows us to rule out that this selection effect is a major contributor to the observed trend, hence we conclude that it is primarily due to effects of the environment on early type galaxies.

We provide catalogues of fundamental plane distances for all cluster hosting early-type galaxies for three different cosmological: the Millennium simulation cosmology, the cosmology used in Saulder et al. (2013) and the recent Planck cosmology (Planck Collaboration et al. 2014b).

The final catalogue of this paper contains the finite infinity regions, which are a necessary part of the foreground model for our planned cosmological test. We found for the mock catalogues and the Millimil simulation that slightly less than half of the simulation's particles are actually bound to the FoF groups. However, when calculating the finite infinity regions around the groups we see that up to 80% of the particles of the simulations are within them. We use this to develop and calibrate a rescaling method, which allows us to calculate the finite infinity regions from the groups' masses as explained in Section 3.5. We apply this method on a combined dataset of the 2MRS and SDSS catalogue. The two catalogues were merged using weights based on their completeness function (see Figure 19) and multiplicities of the groups for the groups, which are in both catalogues. Furthermore, we do not use any 2MRS data beyond 95.4 Mpc. In the end, we provide a catalogue of 164509 groups and the sizes of the finite infinity regions surrounding them. They contain 77.7% of the total mass expected for the catalogues volume and occupy 21.5% of it. Since the distribution of remaining mass will influence the cosmological test, we prepare data for two different scenarios. In one, we assume that the rest is distributed sufficiently homogeneous in the voids between the finite infinity regions. In the other one, we add the missing mass to detected groups and rescale their masses in a way that their sum will account for all of the expected mass in the catalogue's volume. In our next paper, we study in detail which one is a better description of the real data.

6. Summary and Conclusions

We created a set of group catalogues with the intention to use them for a cosmological test in our next paper. In the process, we devised a set of wide-angle mock catalogues for 2MRS and SDSS, which consider all possible biases and uncertainties. We

use them to calibrate and optimize our FoF-based group finder algorithm and a mass function. After applying the group finder on 2MRS and SDSS data, we obtain a set of group catalogues, which can be used for various future investigation, even beyond the initial motivation of this paper. As matter of fact, three of the four catalogues, which we create in the process of this paper, are fully independent of the intended cosmological test and could also be motivated by their general usefulness. The 2MRS and the SDSS group catalogue complement the existing group catalogues based on these surveys, such as Crook et al. (2007), Yang et al. (2007), Tempel et al. (2012) and others. The advantages of our catalogues are that they consider all groups of all sizes ranging from individual galaxy to massive clusters and that they have provide well-calibrated masses. The fundamental plane distance catalogue adds an extremely useful and unique dataset to results of this paper. The final catalogue was obtained by merging or 2MRS and SDSS group catalogue and calculating of the finite infinity regions around the groups. In our upcoming paper Saulder et al. (2015c in preparation), we will perform our test of timescape cosmology by using the fundamental distance catalogue and the finite infinity region catalogue.

Acknowledgments

Appendix A: SDSS-2MASS transformation

The results of the rerun of the Millennium simulation using a WMAP7 cosmology (Guo et al. 2013) do not contain any 2MASS magnitudes for the semi-analytic galaxy models in contrast to models in previous runs (De Lucia et al. 2006). Since we want to use the WMAP7 cosmology and the corresponding data from the Millennium simulation for our mock catalogues, we require a way to extrapolate from the SDSS magnitudes, which

coefficients	J	H	K_s
d	1.43 ± 0.02	1.45 ± 0.02	1.37 ± 0.02
e	1.32 ± 0.03	1.53 ± 0.03	1.75 ± 0.03
f	1.027 ± 0.01	1.62 ± 0.01	1.83 ± 0.01
rms	0.143	0.150	0.169

Table A.1. Linear correlation coefficients of the fundamental-plane residuals for all possible combinations of the five SDSS filters.

are given in the data (Guo et al. 2013) to 2MASS magnitudes. In addition to the data from the Millennium simulation's first run (Springel et al. 2005) with its semi-analytic galaxy models (De Lucia et al. 2006), we have the full data from the 2MASS Redshift Survey (Huchra et al. 2012b) and all the galaxies from the 10th data release of SDSS (Ahn et al. 2014) at hand. We find 698 galaxies which are in both data sets (2MRS and SDSS) [9] and we therefore have 2MASS and SDSS magnitudes for them. We adopt the functional form of the SDSS-2MASS colour transformation proposed by Bilir et al. (2008):

$$(m_g - m_X) = d_X(m_g - m_r) + e_X(m_r - m_i) + f_X. \qquad (A.1)$$

The wild card X stands for any of the 3 2MASS bands (J, H, and K_s). The relation connects the 3 SDSS magnitudes m_g, m_r, and m_i with one 2MASS magnitude m_X. We find that the values given for the coefficients d_X, e_X, and f_X in Bilir et al. (2008) are of no good use for galaxies. The coefficients of that paper were derived for a general populations of stars and by applying them on galaxies one gets a clear offset and tilt with respect to the values from observations (see Figure A.1 top-right panel) as well as to the values from the simulations (see Figure A.1 bottom-right panel). In a first attempt we tried to obtain the coefficients of the colour transformation by fitting it to the SDSS and 2MASS magnitudes of the semi-analytic galaxy models (De Lucia et al. 2006) from the Millennium-Simulation. However, we found that the fit derived from the simulated galaxies is not in agreement with the data from the observed galaxies (see Figure A.1 bottom-left panel). Hence we finally derived the coefficients of the colour transformation by directly fitting it to the observational data of 698 galaxies for which we have SDSS and 2MASS magnitudes both. After a 3-σ clipping to remove some clear outliers, 686 galaxies remain and we obtain the coefficients listed in Table A.1.

The root mean square (rms) increases with longer wavelength which is not surprising, because we performed an extrapolation from the SDSS wavelength range deeper into the infrared and the closer the central wavelength of a filter is located to the SDSS filters, the better is the fit. In Figure A.2, we show edge-on projections on the fitting plane for all three 2MASS bands and also the residuals, which are displayed for the 2MASS filters themselves and not the colours.

Appendix B: mock K-correction

When creating a mock catalogue, one cannot simply change the sign of same K-corrections used to corrected the observed data, because the colours before applying the K-correction are, albeit similar, not the same as the colours after applying the K-correction. Although, it is not a huge difference (see Figure B.1), it is one that can be taken into account with relatively small effort. To this end, we use the K-corrections from Chilingarian

---

[9] tolerance of angular separation: 5 arcseconds, tolerance for separation in redshift space: 300 km/s
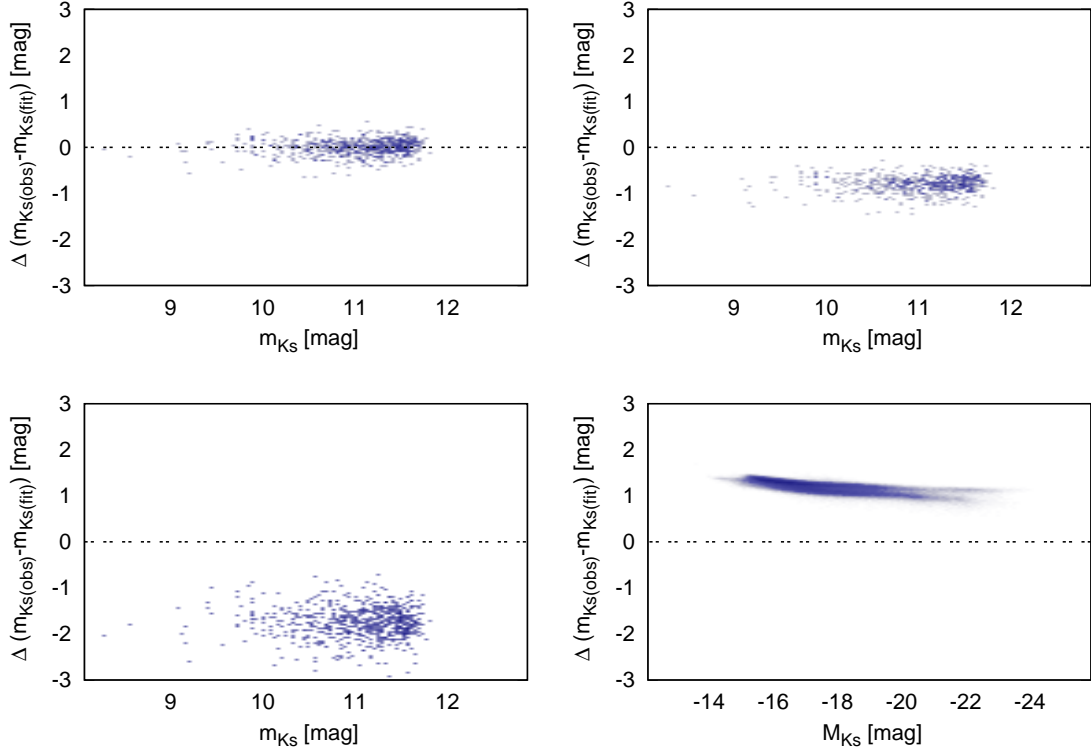
Figure A.1. Comparison of the correlations between SDSS and 2MASS magnitudes. The top-left panel shows our fit on observational data. The top-right panel shows the correlation from Bilir et al. (2008) as the straight dashed line, which has a clear off-set from our observational data. The bottom-left panel shows the performance of the relation derived from the one used in the Millennium-Simulation, which also deviates clearly from our observational data. The bottom-right panel shows the correlation from Bilir et al. (2008) applied on the Millennium-Simulation data, which does not fit either.

et al. (2010) with the updated coefficients for SDSS from Saulder et al. (2013) and the new coefficients for the 2MASS filters taken directly from `http://kcor.sai.msu.ru/`. To derive the new mock K-correction coefficients $\bar{B}_{ij}$, we fit a two-dimensional polynomial function:

$$K(z, m_{\mathrm{uncor},f_1} - m_{\mathrm{uncor},f_2}) =$$
$$\bar{K}(z, m_{\mathrm{Kcor},f_1} - m_{\mathrm{Kcor},f_2}) = \qquad (B.1)$$
$$\sum_{i,j} \bar{B}_{ij} z^i (m_{\mathrm{Kcor},f_1} - m_{\mathrm{Kcor},f_2})^j$$

which is similar to Equation 2 to the obtained K-corrections $K(z, m_{\mathrm{uncor},f_1} - m_{\mathrm{uncor},f_2})$, K-corrected colours $(m_{\mathrm{Kcor},f_1} - m_{\mathrm{Kcor},f_2})$ and redshifts z of the galaxies from the SDSS and 2MASS galaxies and a grid of artificial values following the K-correction equation. The wild cards f_1 and f_2 stand for two different filters. By definition, the real K-corrections K for the uncorrected colours $(m_{\mathrm{uncor},f_1} - m_{\mathrm{uncor},f_2})$ are the same as the mock K-corrections $\bar{K}$ for the K-corrected colours $(m_{\mathrm{Kcor},f_1} - m_{\mathrm{Kcor},f_2})$. The coefficients $\bar{B}_{ij}$ of the mock K-correction are listed in Tables B.1 to B.4 for all colours and filters used in this paper.

	$(g-r)^0$	$(g-r)^1$	$(g-r)^2$	$(g-r)^3$
z^0	0	0	0	0
z^1	-0.230125	1.76255	6.30428	-10.4609
z^2	-41.3522	15.2747	139.091	23.9396
z^3	726.982	-1337.47	-443.452	0
z^4	-1827.06	5009.87	0	0
z^5	-5260.39	0	0	0

Table B.1. Coefficients for the inverse K-correction in the g band using g-r colours.

	$(g-r)^0$	$(g-r)^1$	$(g-r)^2$	$(g-r)^3$
z^0	0	0	0	0
z^1	2.64192	-3.63656	3.87578	-2.8507
z^2	-51.1976	58.4272	15.9944	-0.19916
z^3	356.875	-537.807	31.3718	0
z^4	-554.669	1091.06	0	0
z^5	-2439.93	0	0	0

Table B.2. Coefficients for the inverse K-correction in the r band using g-r colours.

26
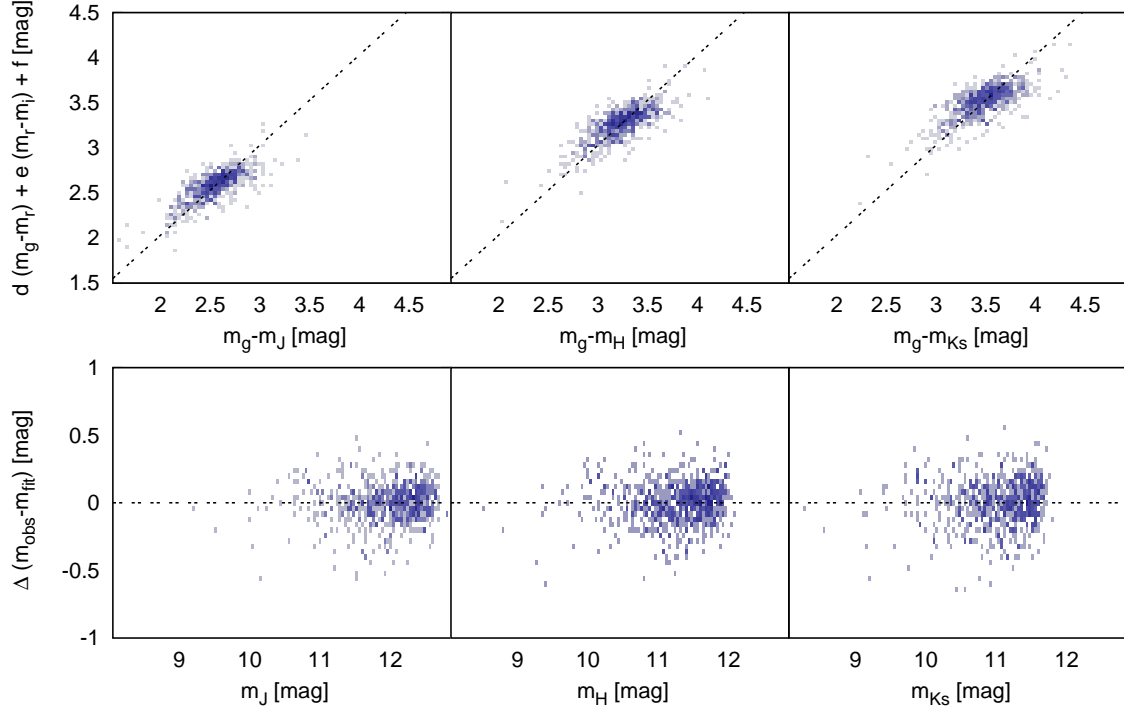
Figure A.2. Performance of our fit for the SDSS-2MASS transformation. The top panels show an edge-on view on the colour-colour-colour plane for all 2MASS bands (J in the top-left panel, H in the top-middle panel, and K_s in the top-right panel). Our fits are always indicated by the dashed black lines. The bottom panels show the residuals of the fit shown as the difference between the observed magnitude and the magnitude derived from the fit depending on the apparent magnitude in the 3 2MASS bands (J in the bottom-left panel, H in the bottom-middle panel, and K_s in the bottom-right panel).

	$(J-K_s)^0$	$(J-K_s)^1$	$(J-K_s)^2$	$(J-K_s)^3$
z^0	0	0	0	0
z^1	-2.90632	1.84899	0.687978	-0.435851
z^2	28.7738	-35.0671	12.645	0.814889
z^3	-124.868	44.1619	-33.6223	0
z^4	671.941	123.024	0	0
z^5	-1864.17	0	0	0

Table B.3. Coefficients for the inverse K-correction in the J band using J-K_s colours.

	$(J-K_s)^0$	$(J-K_s)^1$	$(J-K_s)^2$	$(J-K_s)^3$
z^0	0	0	0	0
z^1	-5.23228	0.0686118	4.15743	-0.901711
z^2	73.2808	-63.8764	-0.528324	2.40482
z^3	-398.914	197.991	-27.4839	0
z^4	1726.93	-30.6288	0	0
z^5	-4240.1	0	0	0

Table B.4. Coefficients for the inverse K-correction in the K_s band using J-K_s colours.

27
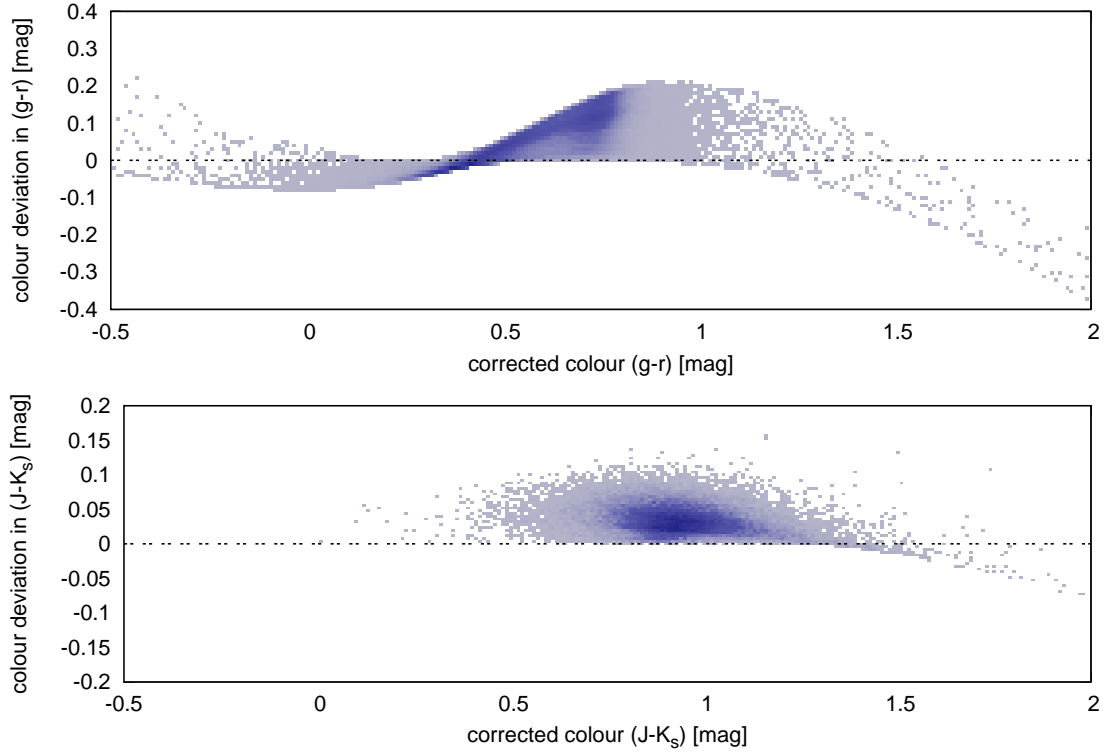
Figure B.1. Deviation of the uncorrected colour from the K-corrected colour using the real values for each survey. Top panel: SDSS colours. Bottom panel: 2MASS colours.

References

Abell, G. O. 1958, *ApJS*, 3, 211
Ahn, C. P., Alexandroff, R., Allende Prieto, C., et al. 2014, *ApJS*, 211, 17
Aihara, H., Allende Prieto, C., An, D., et al. 2011, *ApJS*, 193, 29
Alpaslan, M., Robotham, A. S. G., Obreschkow, D., et al. 2014, *MNRAS*
Arp, H. 1994, *ApJ*, 430, 74
Beers, T. C., Flynn, K., & Gebhardt, K. 1990, *AJ*, 100, 32
Berlind, A. A., Frieman, J., Weinberg, D. H., et al. 2006, *ApJS*, 167, 1
Bilir, S., Ak, S., Karaali, S., et al. 2008, *MNRAS*, 384, 1178
Biviano, A. 2000, in Constructing the Universe with Clusters of Galaxies
Blanton, M. R., Lin, H., Lupton, R. H., et al. 2003, *AJ*, 125, 2276
Brough, S., Forbes, D. A., Kilborn, V. A., & Couch, W. 2006, *MNRAS*, 370, 1223
Budzynski, J. M., Koposov, S. E., McCarthy, I. G., & Belokurov, V. 2014, *MNRAS*, 437, 1362
Cabré, A. & Gaztañaga, E. 2009, *MNRAS*, 396, 1119
Cappellari, M., Emsellem, E., Krajnović, D., et al. 2011, *MNRAS*, 416, 1680
Chilingarian, I. V. & Mamon, G. A. 2008, *MNRAS*, 385, L83
Chilingarian, I. V., Melchior, A., & Zolotukhin, I. Y. 2010, *MNRAS*, 405, 1409
Colless, M., Dalton, G., Maddox, S., et al. 2001, *MNRAS*, 328, 1039
Crook, A. C., Huchra, J. P., Martimbeau, N., et al. 2007, *ApJ*, 655, 790
Croton, D. J., Springel, V., White, S. D. M., et al. 2006, *MNRAS*, 365, 11
Davis, M. & Geller, M. J. 1976, *ApJ*, 208, 13
De Lucia, G., Springel, V., White, S. D. M., Croton, D., & Kauffmann, G. 2006, *MNRAS*, 366, 499
Dressler, A. 1980, *ApJ*, 236, 351
Dressler, A., Oemler, Jr., A., Couch, W. J., et al. 1997, *ApJ*, 490, 577
Driver, S. P., Hill, D. T., Kelvin, L. S., et al. 2011, *MNRAS*, 413, 971
Einasto, J., Saar, E., Kaasik, A., & Chernin, A. D. 1974, *Nature*, 252, 111
Einasto, M., Lietzen, H., Tempel, E., et al. 2014, *A&A*, 562, A87
Eke, V. R., Baugh, C. M., Cole, S., et al. 2004a, *MNRAS*, 348, 866
Eke, V. R., Frenk, C. S., Baugh, C. M., et al. 2004b, *MNRAS*, 355, 769
Ellis, G. F. R. 1984, in General Relativity and Gravitation Conference, ed. B. Bertotti, F. de Felice, & A. Pascolini, 215–288
Ellis, G. F. R. & Stoeger, W. 1987, Classical and Quantum Gravity, 4, 1697

Gal, R. R. 2006, ArXiv Astrophysics e-prints
Gerke, B. F., Newman, J. A., Davis, M., et al. 2005, *ApJ*, 625, 6
Goto, T., Yamauchi, C., Fujita, Y., et al. 2003, *MNRAS*, 346, 601
Guo, Q., White, S., Angulo, R. E., et al. 2013, *MNRAS*, 428, 1351
Guo, Q., White, S., Boylan-Kolchin, M., et al. 2011, *MNRAS*, 413, 101
Hao, J., McKay, T. A., Koester, B. P., et al. 2010, *ApJS*, 191, 254
Hearin, A. P., Zentner, A. R., Newman, J. A., & Berlind, A. A. 2013, *MNRAS*, 430, 1238
Hinshaw, G., Weiland, J. L., Hill, R. S., et al. 2009, *ApJS*, 180, 225
Hou, A., Parker, L. C., Balogh, M. L., et al. 2013, *MNRAS*, 435, 1715
Huchra, J. P. & Geller, M. J. 1982, *ApJ*, 257, 423
Huchra, J. P., Macri, L. M., Masters, K. L., et al. 2012a, VizieR Online Data Catalog, 219, 90026
Huchra, J. P., Macri, L. M., Masters, K. L., et al. 2012b, *ApJS*, 199, 26
Huertas-Company, M., Aguerri, J. A. L., Bernardi, M., Mei, S., & Sánchez Almeida, J. 2011, *A&A*, 525, A157
Jackson, J. C. 1972, *MNRAS*, 156, 1P
Jones, D. H., Read, M. A., Saunders, W., et al. 2009, *MNRAS*, 399, 683
Jones, D. H., Saunders, W., Colless, M., et al. 2004, *MNRAS*, 355, 747
Kaiser, N. 1987, *MNRAS*, 227, 1
Kitzbichler, M. G. & White, S. D. M. 2007, *MNRAS*, 376, 2
Knebe, A., Knollmann, S. R., Muldrew, S. I., et al. 2011, *MNRAS*, 415, 2293
Knobel, C., Lilly, S. J., Iovino, A., et al. 2009, *ApJ*, 697, 1842
Koester, B. P., McKay, T. A., Annis, J., et al. 2007, *ApJ*, 660, 239
Komatsu, E., Smith, K. M., Dunkley, J., et al. 2011, *ApJS*, 192, 18
Luparello, H. E., Lares, M., Yaryura, C. Y., et al. 2013, *MNRAS*, 432, 1367
Makarov, D. & Karachentsev, I. 2011, *MNRAS*, 412, 2498
Moore, B., Frenk, C. S., & White, S. D. M. 1993, *MNRAS*, 261, 827
Muñoz-Cuartas, J. C. & Müller, V. 2012, *MNRAS*, 423, 1583
Nelder, J. A. & Mead, R. 1965, Computer Journal, 7, 308
Nolthenius, R. & White, S. 1987, in IAU Symposium, Vol. 117, Dark matter in the universe, ed. J. Kormendy & G. R. Knapp, 284
Oemler, Jr., A. 1974, *ApJ*, 194, 1
Planck Collaboration, Ade, P. A. R., Aghanim, N., et al. 2014a, *A&A*, 571, A1
Planck Collaboration, Ade, P. A. R., Aghanim, N., et al. 2014b, *A&A*, 571, A16

Postman, M. & Geller, M. J. 1984, *ApJ*, 281, 95

Press, W. H. & Davis, M. 1982, *ApJ*, 259, 449

Press, W. H., Teukolsky, S. A., Vetterling, W. T., & Flannery, B. P. 1992, Numerical recipes in FORTRAN. The art of scientific computing

Ramella, M., Geller, M. J., & Huchra, J. P. 1989, *ApJ*, 344, 57

Robotham, A. S. G., Norberg, P., Driver, S. P., et al. 2011, *MNRAS*, 416, 2640

Saulder, C., Mieske, S., & Zeilinger, W. W. 2012, in Dark Side of the Universe (DSU 2012)

Saulder, C., Mieske, S., Zeilinger, W. W., & Chilingarian, I. 2013, *A&A*, 557, A21

Saulder, C., van den Bosch, R. C. E., & Mieske, S. 2015, ArXiv e-prints

Schlegel, D. J., Finkbeiner, D. P., & Davis, M. 1998, *ApJ*, 500, 525

Skrutskie, M. F., Cutri, R. M., Stiening, R., et al. 2006, *AJ*, 131, 1163

Springel, V., White, S. D. M., Jenkins, A., et al. 2005, *Nature*, 435, 629

Strauss, M. A., Weinberg, D. H., Lupton, R. H., et al. 2002, *AJ*, 124, 1810

Tempel, E., Tago, E., & Liivamägi, L. J. 2012, *A&A*, 540, A106

Turner, E. L. & Gott, III, J. R. 1976, *ApJS*, 32, 409

van der Wel, A., Bell, E. F., Holden, B. P., Skibba, R. A., & Rix, H.-W. 2010, *ApJ*, 714, 1779

Wake, D. A., Whitaker, K. E., Labbé, I., et al. 2011, *ApJ*, 728, 46

Wetzel, A. R., Tinker, J. L., Conroy, C., & van den Bosch, F. C. 2013, *MNRAS*, 432, 336

Wilman, D. J., Erwin, P., De Lucia, G., Fontanot, F., & Monaco, P. 2011, The Origin of the Morphology-Density Relation, ed. I. Ferreras & A. Pasquali, 215

Wiltshire, D. L. 2007, New Journal of Physics, 9, 377

Yang, X., Mo, H. J., & van den Bosch, F. C. 2009, *ApJ*, 695, 900

Yang, X., Mo, H. J., van den Bosch, F. C., et al. 2013, *ApJ*, 770, 115

Yang, X., Mo, H. J., van den Bosch, F. C., & Jing, Y. P. 2005, *MNRAS*, 356, 1293

Yang, X., Mo, H. J., van den Bosch, F. C., et al. 2007, *ApJ*, 671, 153

Zeldovich, I. B., Einasto, J., & Shandarin, S. F. 1982, *Nature*, 300, 407

Zwicky, F. 1933, Helvetica Physica Acta, 6, 110

Zwicky, F., Herzog, E., Wild, P., Karpowicz, M., & Kowal, C. T. 1961, Catalogue of galaxies and of clusters of galaxies, Vol. I

Chapter 7

Testing timescape cosmology

7.1 Basic concept

The main aim of this thesis is to test timescape cosmology against the standard model of cosmology, the Λ-CDM model. One has to analyse observational data to quantify the systematic variance of the Hubble parameter as a function of the matter distribution in the line of sight. The main data sets for this thesis are the Sloan Digital Sky Survey (Aihara et al., 2011) and the 2MASS redshift survey (Huchra et al., 2012b), which both have already been used and prepared in the papers presented in the previous chapters.
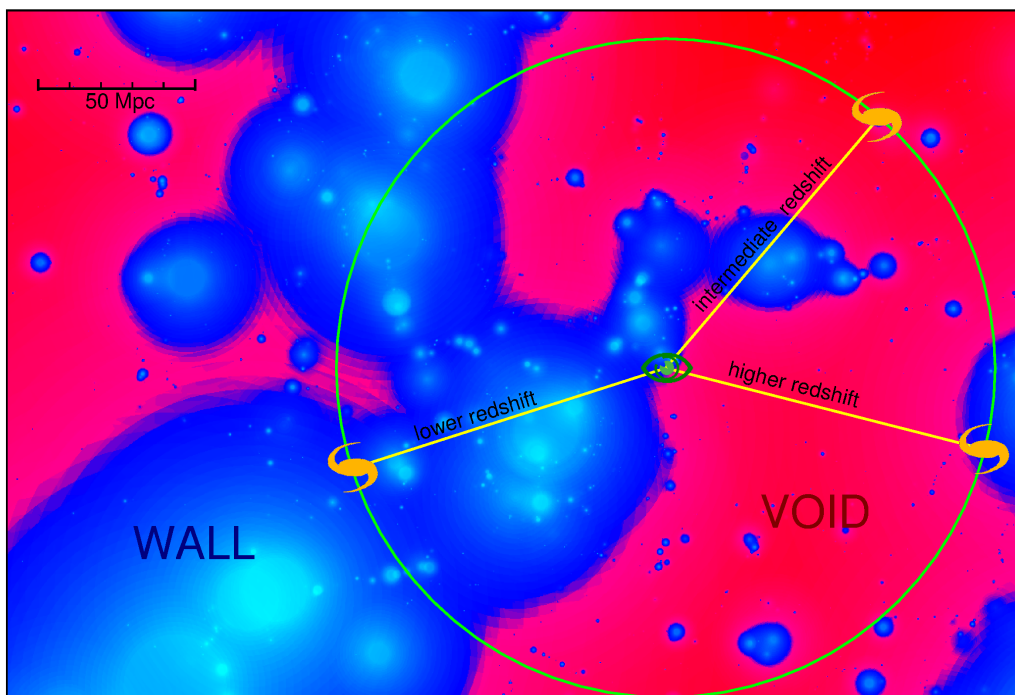
Figure 7.1: This sketch illustrates the line of sight dependence of the individual Hubble parameter. One of the expectations of timescape cosmology is that galaxies at the same distance from a observer may have different redshifts, depending on the environment in the line of sight.

As noted earlier (see Section 2.2), timescape cosmology explains the accelerated expansion of the universe without introducing new physics like dark energy. Instead, it takes one step back and tries to treat cosmology using general relativity only. This aspect makes the theory a conceptually interesting solution to the dark energy problem, but like all other theories, it has to be tested. It is required to better fit the observations than the currently adopted standard cosmological theory to survive. Therefore, the predictions of timescape cosmology that are different from our current standard model (the Λ-CDM model), must be both measurable and measured, for this theory to be accepted as a proper description of the universe. Timescape cosmology tries to explain the accelerated expansion of the universe with backreactions from inhomogeneities due to general relativity, instead of introducing dark energy. There are several predictions of timescape cosmology (Wiltshire, 2009), which make it possible to distinguish between this theory and the standard model. However, most of them are either not accessible with today's technology or extremely complicated to measure. Nevertheless, there is one feature, which can be observed relatively easily, if timescape cosmology is a proper description of the universe. One of the very basic concepts in timescape cosmology is that voids expand faster than walls and these different expansion rates (Hubble parameters) can be measured. One expects a 17 to 22% variance (Wiltshire, 2011) in the Hubble flow below the scale of the statistical homogeneity of the universe (about few 100 Mpc). To measure this variance, one needs to know the redshift and the distance to a sample of galaxies or clusters. The distance has to be measured independently of the redshift. Therefore, one has to use distance indicators like the Cepheids, surface brightness fluctuations, the Tully-Fisher relation or the fundamental plane of elliptical galaxies. I picked the last because it can be applied to sufficiently large cosmological distances and be best realised with automatic pipelines and large datasets. If timescape cosmology is a valid description of the universe, the "individual Hubble parameter" (the Hubble parameter measured for a single galaxy or cluster) of an object is larger, if the line of sight to an object is void (low density) dominated, rather than wall dominated. This is illustrated in Figure 7.1. This effect can only be measured below the scale of homogeneity, which is of the order of a few 100 Mpc, because beyond that distance, the ratio of the void and wall environment in the line of sight will approach a constant value. Though the basic idea of this test is simple, the test needs to be executed with great care to correctly take into account any relevant systematic effects and biases. This includes effects, which are expected in any cosmology, such as the coherent infall of galaxies into clusters that will be discussed in the next section.

7.2 Preparing the Λ-CDM mock catalogues
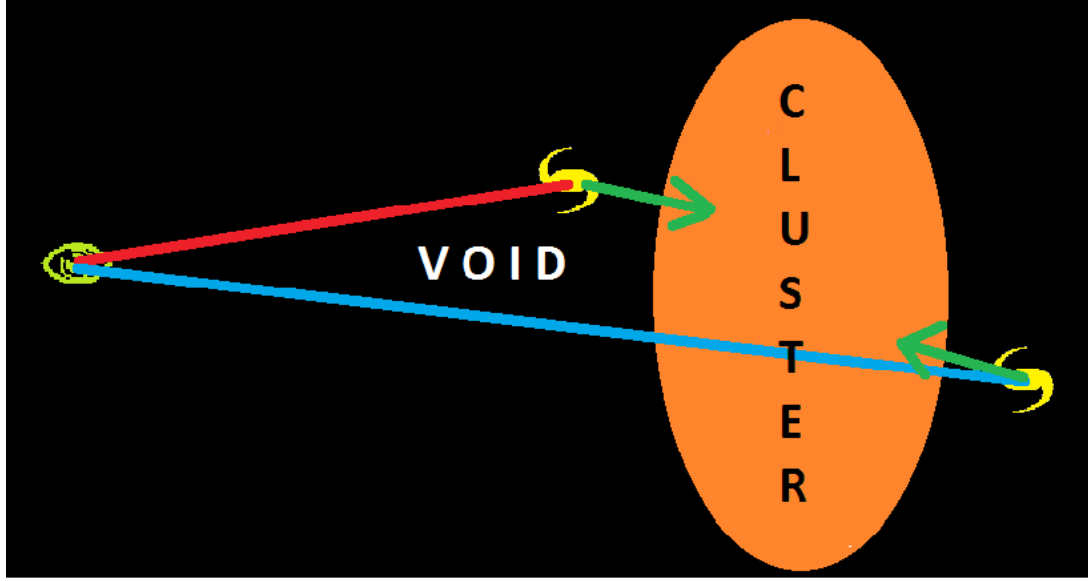
Figure 7.2: Coherent infall into clusters can mimic the expected timescape effect. Galaxies in front of a cluster have fewer overdense regions in the line of sight than galaxies behind a cluster, simply because then the cluster (which is overdense) is part of their line of sight. Due to coherent infall, the most likely direction of movement of all of these galaxies is towards the cluster, hence yielding larger redshifts (with respect to their distances) for the galaxies in front of the cluster than for those behind it. Consequently, one already gets a relation between the fraction of overdense regions in the line of sight and the individual Hubble parameter within the standard model.

First of all, one has to consider, which potential effects within Λ-CDM cosmology may generate a similar effect as the one expected from timescape cosmology. We find that coherent infall (Kaiser, 1987; Hatton & Cole, 1998; Coil et al., 2001; Outram et al., 2001) of galaxies into a cluster (see Figure 7.2) will naturally create a signal in redshift space that is qualitatively similar to the (additional) effect predicted by timescape cosmology. Thus, one has to estimate the magnitude of this effect very carefully to disentangle it from the signal of timescape cosmology. To this end, I took the mock catalogues, which were used to calibrate the group finder in Chapter 6 and applied the cosmological test on that artificial data. It is also important to pay attention to the galaxy classification, because the infall effect also depends on it(Coil et al., 2008; Loh et al., 2010) as a consequence of the density-morphology relation (Dressler, 1980; Postman & Geller, 1984; Dressler et al., 1997; Holden et al., 2007; van der Wel et al., 2010). This requires some additional considerations beyond the mock catalogues from Paper IV, which are be addressed in the next but one paragraph.

As already mentioned in Chapter 3, the basic concept of the test is relatively simple: one measures the redshift of a galaxy group and independently of it, its distance using the fundamental plane of elliptical galaxies. Taking these two quantities, one is able to calculate the "individual Hubble parameters", which are the Hubble parameters calculated for individual objects, which are the galaxy groups in our sample. One also has to calculate the fraction of the line of sight from the observer to these clusters that lies within the finite

infinity regions. The finite infinity regions are approximated by spheres within which the average density corresponds to the renormalized critical density of timescape cosmology. The line of sight towards the cluster with a given fundamental plane distance is then intersected with these spherical regions and one has to use an interval nesting algorithm to obtain the correct fraction of the line-of-sight within these regions, because the spherical regions may partially overlap. The corresponding catalogue from Chapter 6 is used for the observed distribution and sizes of the finite infinite regions. For the Λ-CDM mock catalogues, we apply our group finder algorithm from Paper IV on the mock catalogues of that paper and proceed in the same way as described there to get the finite infinite regions. The mock catalogues and real data extend to a redshift of 0.11, which is more than sufficient for the intended cosmological test. One also needs data on distances and redshifts of the groups. To this end, I use the catalogue on fundamental plane distance of groups from Paper IV, which utilizes the fundamental plane calibrations of Paper II and III for the real data.
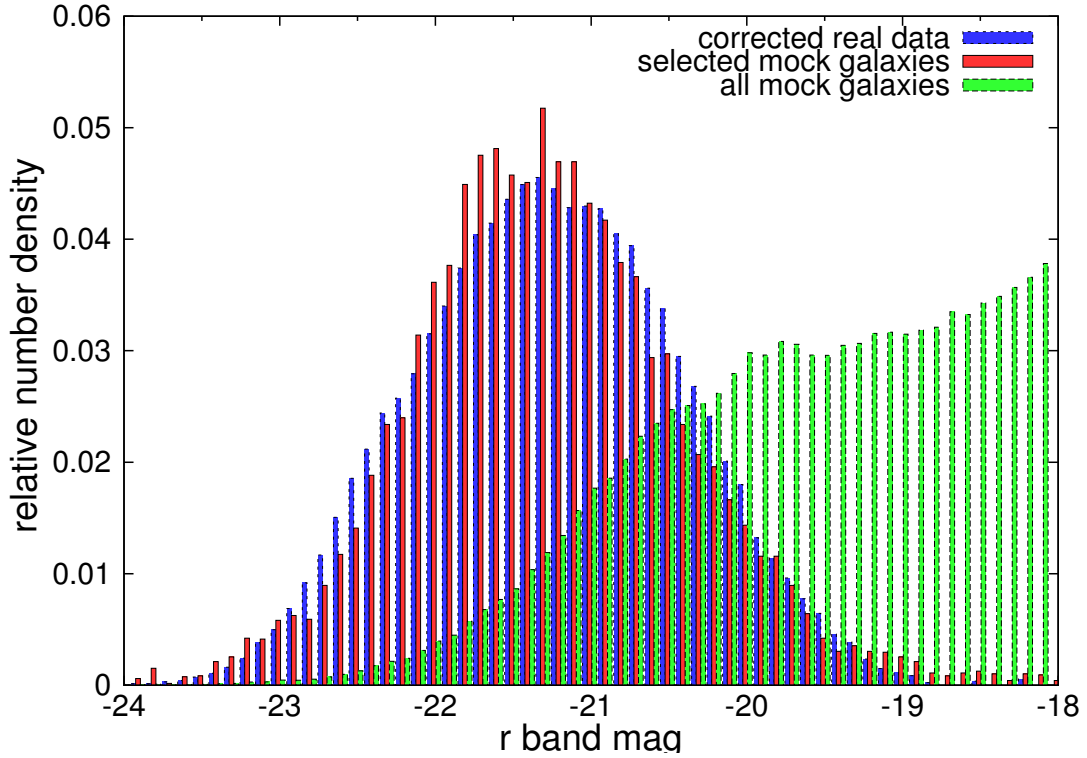
Figure 7.3: Comparison of the luminosity functions of the real data and our mock catalogue. The blue histogram represents the Malmquist-bias corrected luminosity function of the early-type galaxies used to calibrate the fundamental plane. The red histogram shows the selected early-type galaxies from the Millennium simulation with the criteria mentioned in this chapter. The green histogram represents all galaxies from the Millennium simulation for comparison.

To obtain a suitable mock catalogue for the fundamental plane distances, one has to identify early-type galaxies in the data of the Millennium simulation (Springel et al., 2005; Lemson & Virgo Consortium, 2006). I thus define a set of criteria, which yield a number density of early-type galaxies similar to our observations, but without being able to do any visual identification on the simulated data. This is an issue because we used

primarily GalaxyZoo (Lintott et al., 2008, 2011) to classify our galaxies in the real data as explained in Paper III. In the Millennium simulation, dark matter halos are populated by semi-analytical galaxies models (Guo et al., 2010). These models provide several parameters, which can be used for classifications. After testing a few approaches for the selection criteria, the following conditions yield a sample of simulated galaxies, which has a sufficiently similar luminosity function and number density as the observed GalaxyZoo-selected sample of early-type galaxies used in this thesis. The following conditions have to be fulfilled: A galaxy has to be

- bright (SDSS r band magnitude brighter than -18),

- not a satellite galaxy,

- red[1] (g-r colour greater than 0.65 mag),

- poor in cold gas (cold gas to total mass ratio less than 0.0008),

- quiescent (star formation rate by total mass less than 0.01 per 10^{10} years).

These values were chosen by an empirical analysis of the data. A comparison of the luminosity functions of the sample of simulated galaxies obtained and the sample of real galaxies used to calibrate the fundamental plane illustrates that this set of criteria yields the desired galaxy sample (see Figure 7.3). Furthermore, the colour-magnitude diagram of the hereby selected sample of simulated galaxies proves that red-sequence galaxies are indeed selected and that the distribution of the simulated galaxies is comparable to the distribution of the observed galaxies (see Figure 7.4). The galaxy density of the simulated galaxy sample is $7.4 \cdot 10^{-4}$ galaxies per Mpc^3, which is close to value measured for the SDSS sample of $7.9 \cdot 10^{-4}$ galaxies per Mpc^3. In the end, 733790 early-type galaxies from the last six snapshots (the same used in Paper IV) are identified in the Millennium simulation. Of these early-type galaxies only the ones which can also be found in the corresponding mock catalogue were used (reducing the numbers significantly). Thanks to this cross-match with the mock-catalogues, it is assured that the relevant biases are considered for them.
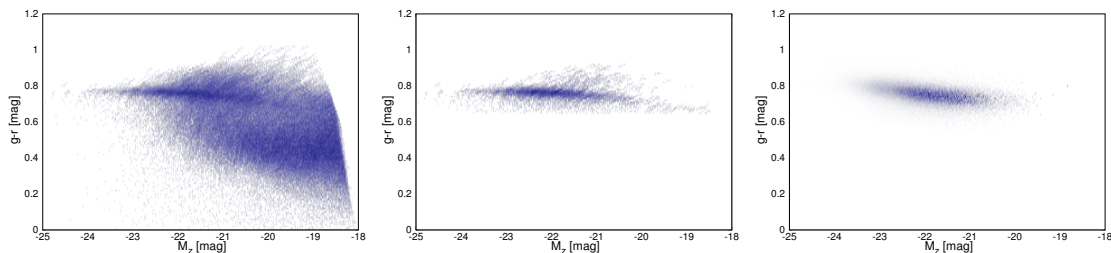
Figure 7.4: Comparison of the colour-magnitude diagrams. First panel: all galaxies with $M_{r,SDSS} < -18$ from the Millennium simulation. Second panel: early-type galaxies selected according to the listed criteria from the Millennium simulation. Third panel: the early-type galaxies from SDSS used to calibrate the fundamental plane.

The fundamental plane distance for the early-type galaxies are obtained by using the true distance (the co-moving distance directly from the simulation) and creating a

---

[1]be part of the red sequence in the colour magnitude diagram

Gaussian scatter around the logaritmized distance values with a width corresponding to the root mean square of the fundamental plane calibration[2]. The residual redshift dependence of the fundamental plane calibrations is considered too (see Paper II). The hereby obtained set of early-type galaxies with their fundamental plane distances is then cross-matched with the group catalogues based on the mock catalogues of Paper IV. This yields a mock fundamental plane distance group catalogue. In addition to that, the algorithm to obtain finite infinity regions of Paper IV is applied on the mock catalogues and yields a finite infinity regions catalogue. With all these catalogues together, I obtain a dataset, which can serve as a baseline for the comparison of the real data to the prediction of Λ-CDM cosmology.

---

[2]It is actually not the root mean square listed in Paper III, but a slightly lower value because of the consideration of the residual redshift dependence.

7.3 Preparing the timescape mock catalogues

The mock observations for timescape cosmology require additional considerations. Due to the complexity of the theory, there are no numerical simulations of comparable scale and detail as the Millennium simulations for timescape cosmology. Therefore, the assumption is used that the matter distribution in the last snapshots of the Millennium simulation is a reasonably good representation of the large scale matter distribution in the local universe (variations on small scales do not matter, because of the sizes of the finite infinity regions). The different expansion rates of voids and walls, which is the effect of timescape cosmology that is investigated here, is artificially introduced in the data by systematically adapting the redshifts in the mock catalogues. To correctly consider all the biases, two sets of finite infinity regions are created: one from the mock catalogues as before (actually the same set as used for the Λ-CDM mock catalogues) and one from the full FoF group catalogue (dark matter halos) directly from the millennium simulation. For the latter the missing particles[3] are considered in the same way as done in Paper IV. The finite infinity region catalogue based on the FoF groups is used to get the true fraction of the line of sight within the finite infinity regions, while the other provides the same parameter, but for the mock observations. This way, the bias due to the modelling of the finite infinity regions is considered. Based on the results with the true finite infinity regions the individual Hubble parameters of the mock catalogue results are modified. Depending on the exact fraction of the line of sight within finite infinity regions the individual Hubble parameters are decreased by up to 21.88% (in the case of full wall line-of-sight, in the case of full void line-of-sight, they remain unchanged). The value is derived from the ratio of the different Hubble parameters for walls and voids, which are 48.2 km s^{-1} Mpc^{-1} and 61.7 km s^{-1} Mpc^{-1}, respectively. These values are necessary to reproduce the accelerated expansion in the framework of timescape cosmology (Wiltshire, 2007; Leith et al., 2008; Wiltshire, 2011), as explained in greater detail in Section 2.2. To remain compatible with the calibrations of the distance indicator the individual Hubble parameters are renormalized afterwards to have the same mean value as for the Λ-CDM mock catalogues.

With the three different data sets (the real data, the Λ-CDM mock data, and the timescape mock data) at hand, the test can be concluded by a comparison of the results.

---

[3]The FoF groups only host about half the mass/particles, which are in the simulation (see Paper IV).

Chapter 8

Results

8.1 Λ-CDM mock catalogues
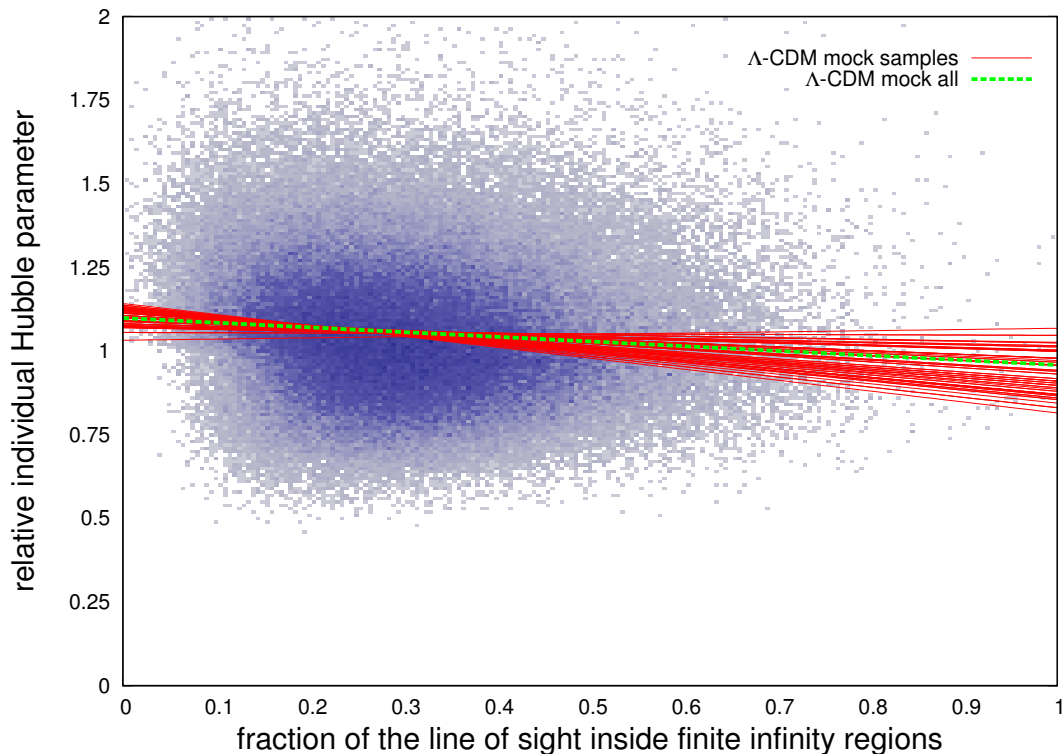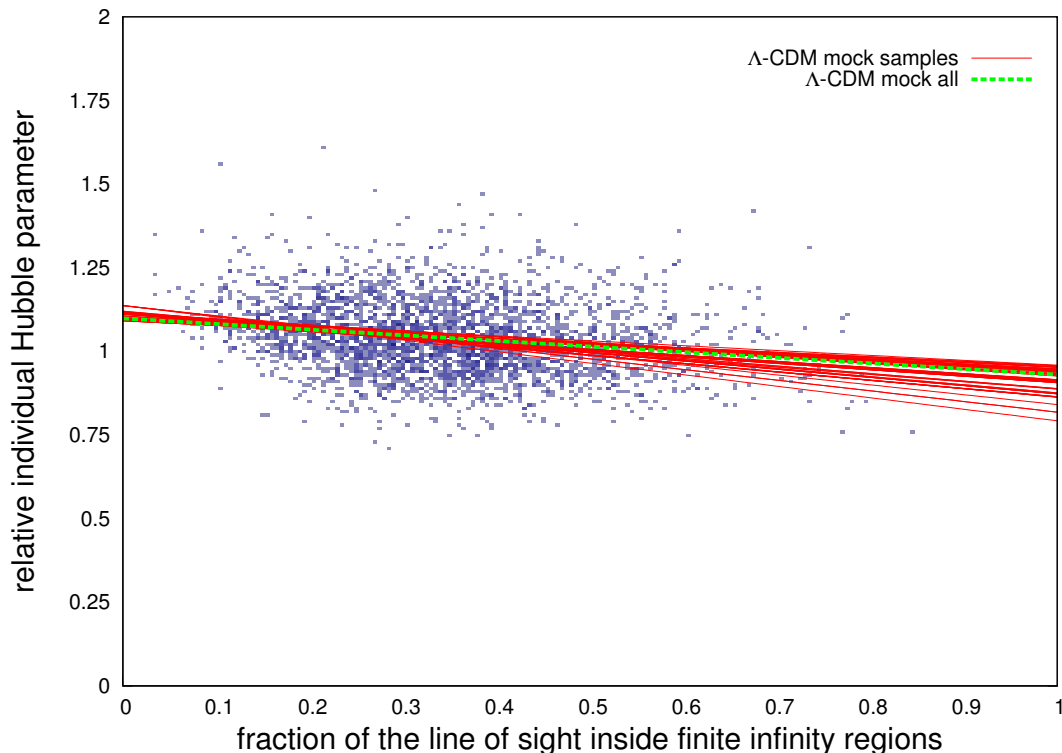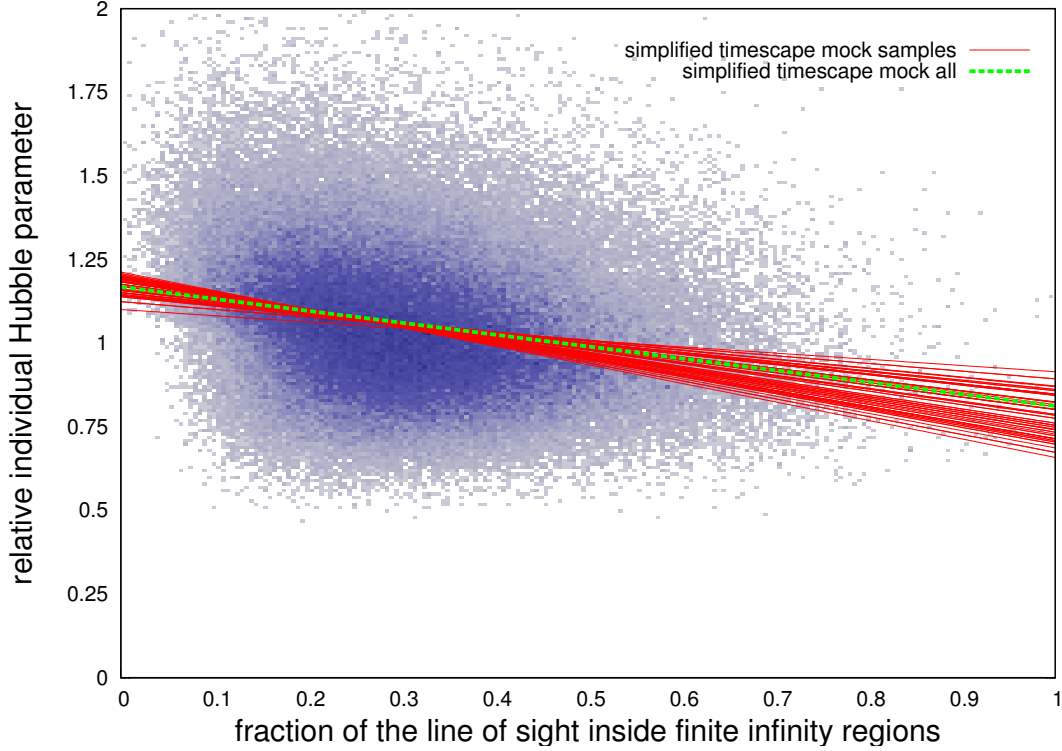

Figure 8.1: Diversity of the combined Λ-CDM mock catalogues. Red solid lines: weighted fits on combined mock catalogues; green dashed line: weighted fit on the combined data of all mock catalogues; bluish point cloud: distribution of all groups in all mock catalogues.

The results of the mock catalogues using Λ-CDM cosmology form the baseline for the cosmological test presented in this thesis. Any significant deviations from these results would challenge our current understanding of the universe. The eight mock catalogues from Paper IV with the extensions of Chapter 7 are used to calculate the expectations of Λ-CDM cosmology. Taking into account, that the area covered by one mock catalogue is only one eighth of the entire sky, while the real observations cover almost one quarter of the sky (to be precise $\sim 22.5\%$ (Ahn et al., 2014)). To make the mock catalogues and the

observations better comparable, two mock catalogues are always combined in the following analysis. The combined mock catalogues cover 25% of the sky, which is reasonable close to the SDSS spectroscopic sky coverage and allows for a direct comparison between the combined mock catalogues and the real observations. Hence, a sample of 64^1 combined mock catalogues is created of which 36 are unique (28 are combinations of two different mock catalogues, of which each appears twice in the sample, while the eight combinations of the same mock catalogues with itself only appear once, thereby providing the correct statistical weights for the likelihood of the combinations). Thanks to the fact that each combined mock catalogue covers an area of the sky comparable to the real observations, one is able to derive probabilities and statistics for the real observations. In Figure 8.1, the weighted (by the number of group members) fits on all the different mock combined catalogues are displayed.
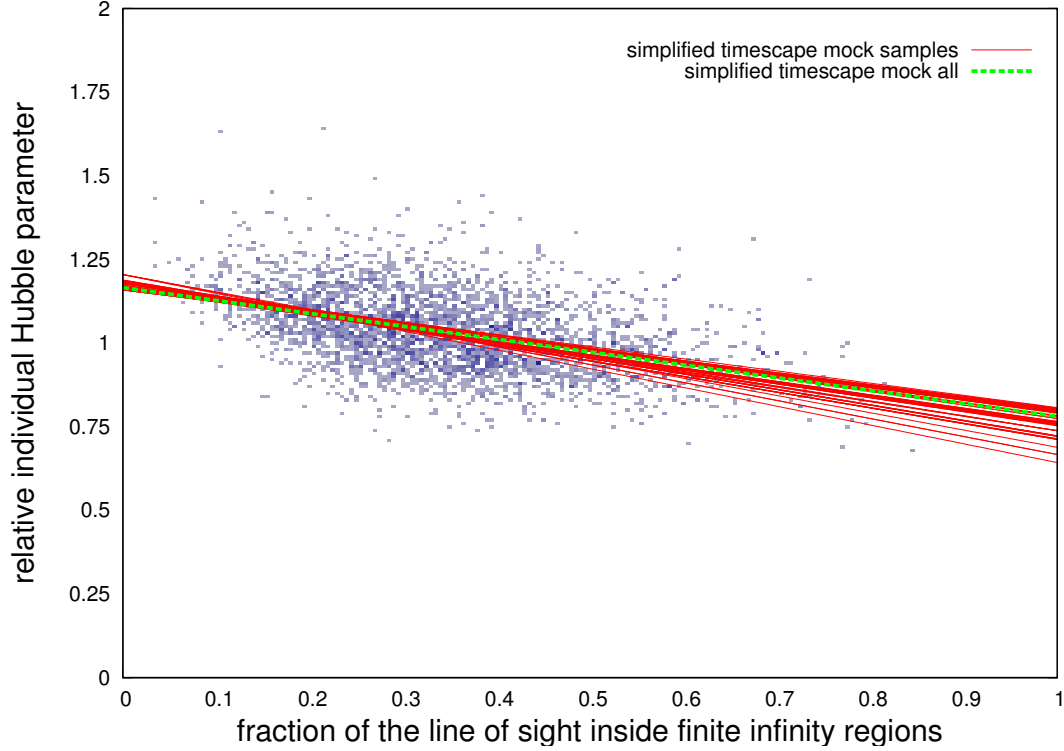

Figure 8.2: Diversity of the combined Λ-CDM mock catalogues. Red solid lines: weighted fits on combined mock catalogues only containing a selected sub-sample of groups; green dashed line: weighted fit on the combined data of a selected sub-sample of all mock catalogues; bluish point cloud: distribution of a selected sub-sample of groups in all mock catalogues.

To reduce the scatter, which is primarily caused by the intrinsic scatter in the fundamental plane distance measurements to individual galaxies, a sub-sample is selected using the follow criteria: at least three early-type galaxies in the group[2], and a co-moving fundamental plane distance of less than 402.8 Mpc (which corresponds to the redshift limit of the foreground model for the cosmology of the Millennium simulation). As illustrated in Figure 8.2, these criteria visibly reduce the scatter of the weighted least-square

---

[1]Considering all possible 2-combinations of the 8 mock catalogues.
[2]The mean parameters (redshift, fundamental plane distance, ...) of the group are used.

fits. The disadvantage of this procedure is that it reduces the size of sample. This is not unproblematic, because there is a dearth of rich groups in all simulated mock catalogues compared to observed data. There is an apparent shortage of galaxy groups with many detectable members in the mock catalogues, when compared to the statistics for the observed data from SDSS. Hence, any criterion selecting groups based on their richness reduces the sample size disproportionally. This issue with the mock catalogues is inherent in the Millennium simulation and grows worse when looking for groups hosting early-type galaxies. Hence, there is little that can be done to avoid it and it has to be considered as a systematic bias.

8.2 Timescape mock catalogues

Figure 8.3: Diversity of the combined timescape mock catalogues. Red solid lines: weighted fits on combined mock catalogues; green dashed line: weighted fit on the combined data of all mock catalogues; bluish point cloud: distribution of all groups in all mock catalogues.

Due to unexpected limitations on the computational facilities available to me at the moment, I had to do a simpler approach for the simulated timescape cosmology data as initially planned. I could not perform the sophisticated estimate on the influence of the uncertainties in modelling the finite infinity on the data (see Section 7.3). Thus, the second best possible approach was adopted and only modified the Λ-CDM mock catalogues to provide an approximate representation of the timescape mock catalogues. The individual Hubble parameters of the Λ-CDM data were modified according to the following set of equations:

$$H'_{ts} = H_{\Lambda-CDM} \cdot (1 + ((1-b)\frac{48.2 - 61.7}{61.7}) \cdot f_{fi})$$ (8.1)

$$H_{ts} = H'_{ts} \cdot \frac{\sum_{i=1}^{n} H_{\Lambda-CDM,i}}{\sum_{i=1}^{n} H'_{ts,i}}$$ (8.2)

$H_{\Lambda-CDM}$ is the individual Hubble parameter from the results of the Λ-CDM mock catalogues and f_{fi} is the fraction of the line of sight within finite infinity regions according to those results. The variable b stands for the bias parameter, which is 0 if the foreground model perfectly resembles the finite infinity regions and 1 if the uncertainties in the foreground model render the predictions of timescape cosmology totally indistinguishable from Λ-CDM cosmology. n is the number of galaxies in the mock catalogue. The approximated individual Hubble parameters for the timescape mock catalogues H_{ts} are renormalized, so

Figure 8.4: Diversity of the combined timescape mock catalogues. Red solid lines: weighted fits on combined mock catalogues only containing a selected sub-sample of groups; green dashed line: weighted fit on the combined data of a selected sub-sample of all mock catalogues; bluish point cloud: distribution of a selected sub-sample of groups in all mock catalogues.

that that is has on average the same value as the ones from the Λ-CDM mock catalogues. The values 48.2 and 61.7 in Equation 8.1 are the different Hubble parameters for walls and voids, respectively, given in (km/s)/Mpc according to the best fit on supernovae type Ia, CMB, and BAO data for timescape cosmology by Leith et al. (2008). These values are extremely low (even lower than the Planck value of (67.80 ± 0.77) (km/s)/Mpc (Planck Collaboration et al., 2013)), however they are fine within the framework of timescape cosmology (Wiltshire, 2010). All distances in this thesis are measured relative to each other by assuming a specific value for the Hubble parameter based on the cosmology used in the calibrations. Therefore, the absolute values can be rescaled easily. Furthermore in the final analysis, absolute values for the individual Hubble parameter are intentionally avoided to better show that the results are independent of absolute scales. To take into account the uncertainties in the foreground model, a moderate bias parameter b of 0.1 is adopted for the rest of this analysis.

The same analysis as before with Λ-CDM mock catalogues is performed with the approximate timescape mock catalogues. Due to the way the timescape catalogues were obtained, the distributions (see Figures 8.3 and 8.4) are similar to the Λ-CDM mock catalogues with a comparable scatter, however with a clearly steeper trend for the individual Hubble parameters depending on the fraction of the line of sight within finite infinity regions (wall environment).
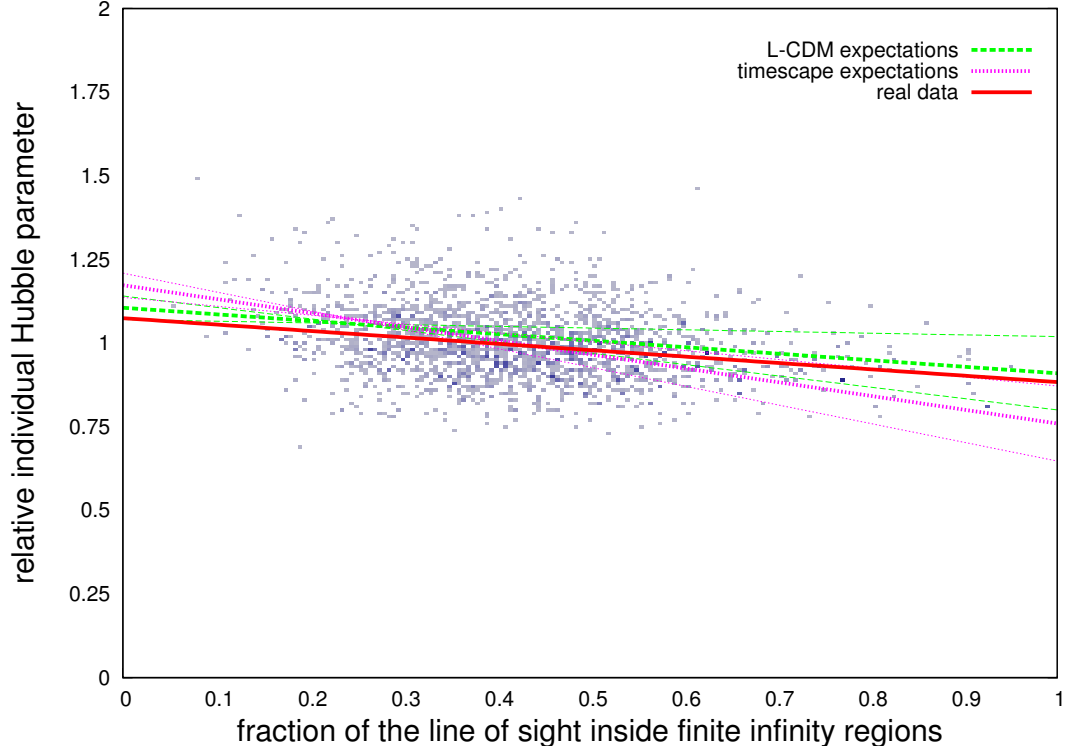
8.3 Observed data

8.3.1 Linear regression
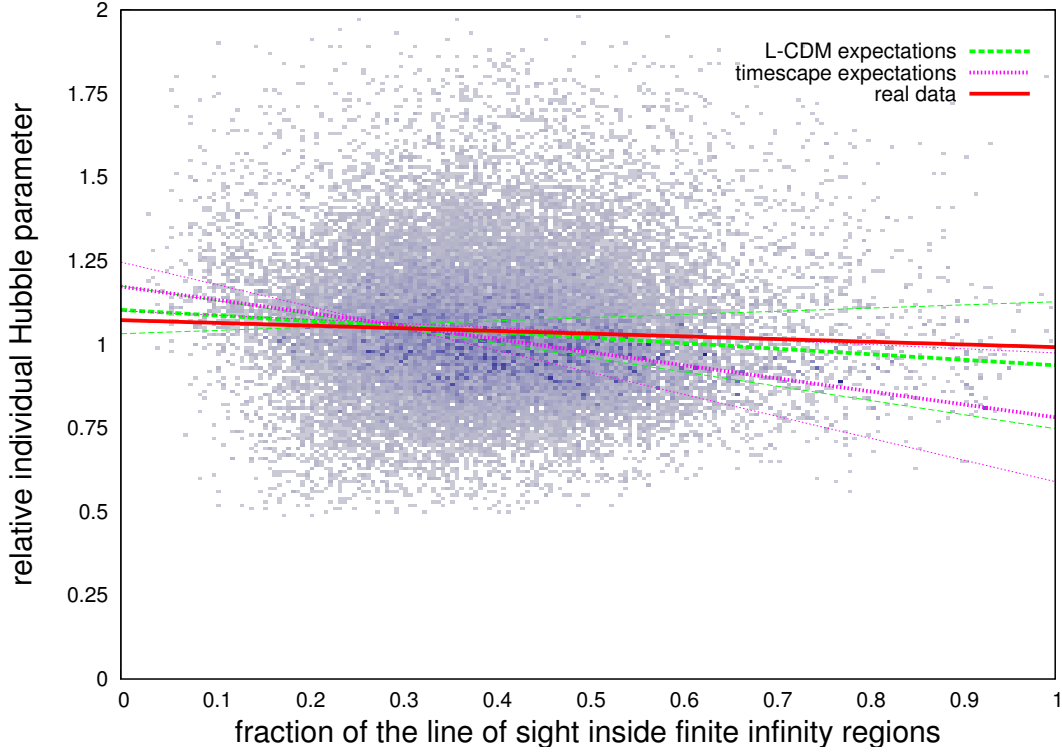
Figure 8.5: Full observational data compared to the model predictions. Red solid line: weighted least-square fit on the observed data; green dashed lines: expectations and 3-σ limits of the Λ-CDM model; magenta dotted lines: expectations and 3-σ limits of the timescape model.

In the next step, the observations are compared to the mock data. In SDSS, 29565 groups containing at least one early-type galaxies were identified within a redshift range of 0 and 0.11 distributed over 9274 square degree (Ahn et al., 2014) and 152442 finite infinity regions in the same area (see Paper IV). Each of the combined mock catalogues contains between 34894 and 40870 groups hosting early-type galaxies and between 175320 and 202498 finite infinity regions distributed over about 10313 square degree[3] and up to a redshift of 0.11. The groups hosting early-type galaxies, with their individual Hubble parameters (derived from the group's average redshift and fundamental plane distance) and ratios of the finite infinity regions in the line of sight, form the data points in the subsequent analysis. As illustrated in Figure 8.5 and shown in Table 8.1, the gradient of the weighted least square fitted linear regression on the observational data is extremely close to expectations of Λ-CDM cosmology, while timescape cosmology is off by more than 3-σ. The absolute zero point of the linear regression is not essential for the analysis, because it is extremely sensitive to the normalization of the data and does not allow for a proper distinction between the two cosmological theories.

---

[3]One quarter of the entire sky.

Figure 8.6: Selected observational data compared to the model predictions. Red solid line: weighted least-square fit on the observed data; green dashed lines: expectations and 3-σ limits of the Λ-CDM model; magenta dotted lines: expectations and 3-σ limits of the timescape model.

When using a selected sample, according to the conditions mentioned in Section 8.1, the size of the observational data is reduced to 1974 galaxy groups (the number of finite infinity regions in the foreground model remains unchanged). Each of the combined mock catalogues will only contain between 540 and 1228 galaxy group, which are clearly lower values than one would expect based on numbers from the observational data. This is due to the already mentioned dearth of rich clusters in the Millennium simulation. Despite disproportionally reducing the sample size, the differences in the expected gradient between the various combined mock catalogues of each theory is significantly reduced. This allows one to continue the analysis. It is illustrated in Figure 8.6 that the fit on the observed data is nearly parallel to the average expectations of Λ-CDM cosmology. As shown in Table 8.1, the preference for Λ-CDM cosmology is even stronger when using the selected sample.

model	k_{obs}	$\overline{k_{\mathrm{mock}}}$	$\sigma_{k,\mathrm{mock}}$	$\Delta k[\sigma]$	P	$\mathcal{L}$
Λ-CDM (full)	-0.08	-0.17	0.09	0.98	0.33	0.9986
Λ-CDM (selected)	-0.19	-0.20	0.05	0.10	0.92	0.999993
timescape (full)	-0.08	-0.39	0.09	3.51	0.0004	0.0014
timescape (selected)	-0.19	-0.41	0.05	4.49	0.000007	0.000007

Table 8.1: Coefficients, probabilities and likelihoods of the observations fitting the different models. k_{obs}: gradient of the weight least square fitted linear regression on the observational data; $\overline{k_{\mathrm{mock}}}$: mean expected gradient for a specific model; $\sigma_{k,\mathrm{mock}}$: standard deviation of the gradient for a specific model (derived using the different combined mock catalogues); Δk: deviation of the observations from the mean value of the model, given in standard deviations; P: probability for the observations to be represented by the model; $\mathcal{L}$: likelihood for the model (only assuming Λ-CDM and timescape cosmology as possible options).

8.3.2 Analysis of individual bins

Aside from a least square fitted linear regression, one can perform a binned analysis on the data. To this end, the data in the final plots is split into ten bins corresponding to different ranges in the fraction of the line of sight within finite infinity regions. Within these bins the weighted averages of the relative individual Hubble parameters are calculated. As illustrated in Figure 8.7, this is done for all the previously described combined mock catalogues for the Λ-CDM model. In the case of the selected sample, the outermost bins are sometimes empty due to dearth of rich groups. This is a serious issue. The bins with very low and very high fractions of the line of sight within finite infinity regions are the most important ones, because the expected difference between the Λ-CDM model and the timescape model will be the largest there. As illustrated in Figure 8.8, the scatter between the different combined mock catalogues increases at both extremes. One has to keep these issues in mind, when proceeding to the final analysis.

For the timescape models, the same analysis is performed. Because in this approach, the timescape model is just a modified version of the Λ-CDM model, the same issues are encountered. While the full sample contains sufficient galaxies groups in every bin but the highest one, although fewer in the lower and higher bins (see Figure 8.9), the selected sample has issues in several bins to get sufficient data for proper statistics (see Figure 8.10).

In the final step, the data of the two models is compared with the observations. In the case of the full dataset, the observations lie close to expectation of the Λ-CDM model (see Figure 8.11). A statistical analysis shows that the Λ-CDM model is preferred in almost every bin (see Table 8.2). The only exception is the bin between 0 and 0.1, where both models have approximately the same likelihood.

As illustrated in Figure 8.12, the results for the selected (using the same set of criteria as before) sample are by far less clear. First of all, not only the 0.9-1 bin does not have sufficient data for proper statistic, but also the 0.8-0.9. Furthermore, all bins expect the central ones, which are the ones with the least difference between the two models is expected, have a higher scatter due to the smaller number of galaxy groups in the mock catalogues used for the calibration. When calculating the likelihoods for individual bins (see Table 8.3), there are some in which the timescape model has a significantly higher one, while in other the Λ-CDM model takes clear preference. Moreover, there are few bins
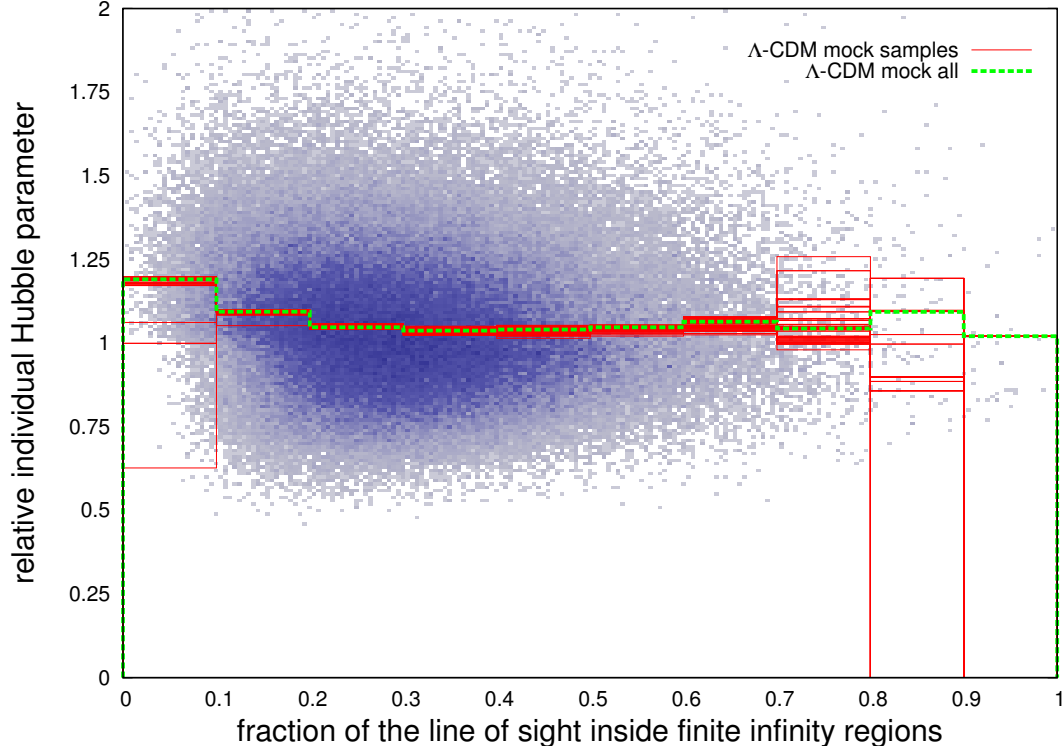
Figure 8.7: Diversity of the combined Λ-CDM mock catalogues. Red solid lines: weighted average in the bins of combined mock catalogues; green dashed line: weighted average in the bins of the combined data of all mock catalogues; bluish point cloud: distribution of all groups in all mock catalogues.

with high probabilities for either model.

By combining the results of the individual bins, one is able to obtain a more solid statistical analysis. In a first approach, a weighted mean of the deviations of the observation from the model is used. The assigned weights correspond to the number of observed galaxies (not number of galaxy groups) in the bins. The probability and likelihood of the models is calculated using these mean deviations. Only the bins, which contain sufficient data are used, which means that the highest bin for the full dataset and the two highest bins for the selected dataset are excluded. The results are listed in Table 8.4. When using the full data, the Λ-CDM model is strongly preferred. However, the tables turn with the selected sample and the timescape model is preferred. This is an obvious contradiction to the results of the previous analysis using the gradient of the linear regression.

In a slightly different approach, the weighted mean of the probabilities is calculated for both theories. The results are listed in Table 8.5. They show the same behaviour as the previous results: for the full dataset the Λ-CDM model is more likely to be represented by the observational data, while with the selected dataset the timescape model is preferred. The only notable difference between the results of the two approaches is that in the latter one, the preferences for a certain model are slightly weaker.

model	bin range	$\overline{H_{\mathrm{obs}}}$	$\overline{H_{\mathrm{mock}}}$	$\sigma_{H,\mathrm{mock}}$	$\Delta H[\sigma]$	P	$\mathcal{L}$
Λ-CDM	0-0.1	1.201	1.173	0.079	0.357	0.72	0.497
timescape	0-0.1	1.201	1.229	0.083	0.345	0.73	0.503
Λ-CDM	0.1-0.2	1.082	1.093	0.006	1.692	0.09	1.000
timescape	0.1-0.2	1.082	1.126	0.007	6.258	0.00	0.000
Λ-CDM	0.2-0.3	1.044	1.047	0.005	0.676	0.4965	0.9991
timescape	0.2-0.3	1.044	1.060	0.004	3.513	0.0004	0.0009
Λ-CDM	0.3-0.4	1.040	1.037	0.006	0.501	0.62	0.911
timescape	0.3-0.4	1.040	1.028	0.006	1.885	0.06	0.089
Λ-CDM	0.4-0.5	1.036	1.038	0.009	0.301	0.764	0.998
timescape	0.4-0.5	1.036	1.009	0.008	3.227	0.001	0.002
Λ-CDM	0.5-0.6	1.033	1.045	0.007	1.547	0.12	1.000
timescape	0.5-0.6	1.033	0.993	0.007	5.875	0.00	0.000
Λ-CDM	0.6-0.7	1.032	1.058	0.013	1.928	0.05359	0.9991
timescape	0.6-0.7	1.032	0.985	0.012	4.079	0.00005	0.0008
Λ-CDM	0.7-0.8	1.026	1.051	0.055	0.466	0.64	0.783
timescape	0.7-0.8	1.026	0.958	0.050	1.349	0.18	0.217
Λ-CDM	0.8-0.9	1.018	1.017	0.128	0.011	0.99	0.755
timescape	0.8-0.9	1.018	0.908	0.112	0.987	0.32	0.245
Λ-CDM	0.9-1	0.936	1.021	-	-	-	-
timescape	0.9-1	0.936	0.885	-	-	-	-

Table 8.2: Coefficients, probabilities and likelihoods of the observations using the full dataset calculated for individual bins. First column: specific model; second column: bin range for the fraction of the line of sight within finite infinity regions; third column: average observed relative individual Hubble parameter $\overline{H_{\mathrm{obs}}}$ within the bin; fourth column: mean relative individual Hubble parameter $\overline{H_{\mathrm{mock}}}$ based on the mock catalogues within the bin; fifth column: standard deviation of the relative individual Hubble parameter $\sigma_{H,\mathrm{mock}}$ within the bin; sixth column: deviation of the observations from the mean value of the model within the bin (given in standard deviation); seventh column: probability P for the observations to be represented by the model within the bin; eighth column: likelihood $\mathcal{L}$ for the model within the bin (only assuming Λ-CDM and timescape cosmology as possible options).

model	bin range	$\overline{H_{\mathrm{obs}}}$	$\overline{H_{\mathrm{mock}}}$	$\sigma_{H,\mathrm{mock}}$	$\Delta H[\sigma]$	P	$\mathcal{L}$
Λ-CDM	0-0.1	1.204	1.139	0.026	2.509	0.012	0.016
timescape	0-0.1	1.204	1.195	0.028	0.331	0.741	0.984
Λ-CDM	0.1-0.2	1.060	1.090	0.010	3.023	0.003	1.000
timescape	0.1-0.2	1.060	1.124	0.096	6.671	0.000	0.000
Λ-CDM	0.2-0.3	1.023	1.051	0.009	3.257	0.001113	0.996
timescape	0.2-0.3	1.023	1.063	0.009	4.609	0.000004	0.004
Λ-CDM	0.3-0.4	1.002	1.030	0.010	2.937	0.003	0.084
timescape	0.3-0.4	1.002	1.021	0.009	2.096	0.036	0.916
Λ-CDM	0.4-0.5	0.986	1.022	0.012	3.096	0.002	0.004
timescape	0.4-0.5	0.986	0.993	0.011	0.700	0.484	0.996
Λ-CDM	0.5-0.6	0.978	1.015	0.018	2.101	0.036	0.071
timescape	0.5-0.6	0.978	0.929	0.017	0.732	0.465	0.929
Λ-CDM	0.6-0.7	0.963	1.001	0.043	0.879	0.379	0.496
timescape	0.6-0.7	0.963	0.930	0.038	0.867	0.384	0.504
Λ-CDM	0.7-0.8	0.931	0.969	0.043	0.884	0.38	0.642
timescape	0.7-0.8	0.931	0.882	0.039	1.254	0.21	0.358
Λ-CDM	0.8-0.9	0.926	0.898	-	-	-	-
timescape	0.8-0.9	0.926	0.799	-	-	-	-
Λ-CDM	0.9-1	0.871	-	-	-	-	-
timescape	0.9-1	0.871	-	-	-	-	-

Table 8.3: Coefficients, probabilities and likelihoods of the observations using the selected dataset calculated for individual bins. First column: specific model; second column: bin range for the fraction of the line of sight within finite infinity regions; third column: average observed relative individual Hubble parameter $\overline{H_{\mathrm{obs}}}$ within the bin; fourth column: mean relative individual Hubble parameter $\overline{H_{\mathrm{mock}}}$ based on the mock catalogues within the bin; fifth column: standard deviation of the relative individual Hubble parameter $\sigma_{H,\mathrm{mock}}$ within the bin; sixth column: deviation of the observations from the mean value of the model within the bin (given in standard deviation); seventh column: probability P for the observations to be represented by the model within the bin; eighth column: likelihood $\mathcal{L}$ for the model within the bin (only assuming Λ-CDM and timescape cosmology as possible options).

model	$\overline{\Delta H}[\sigma]$	P	$\mathcal{L}$
Λ-CDM (full)	0.758	0.4472	0.9986
timescape (full)	3.415	0.0006	0.0014
Λ-CDM (selected)	2.662	0.0078	0.094
timescape (selected)	1.782	0.0751	0.906

Table 8.4: Probabilities and likelihoods of the observations calculated for a weighted average of all bins using the average deviation from the model. First column: specific model; second column: mean deviation of the observations from the model (given in standard deviation); third column: probability P for the observations to be represented by the model; fourth column: likelihood $\mathcal{L}$ for the model (only assuming Λ-CDM and timescape cosmology as possible options).
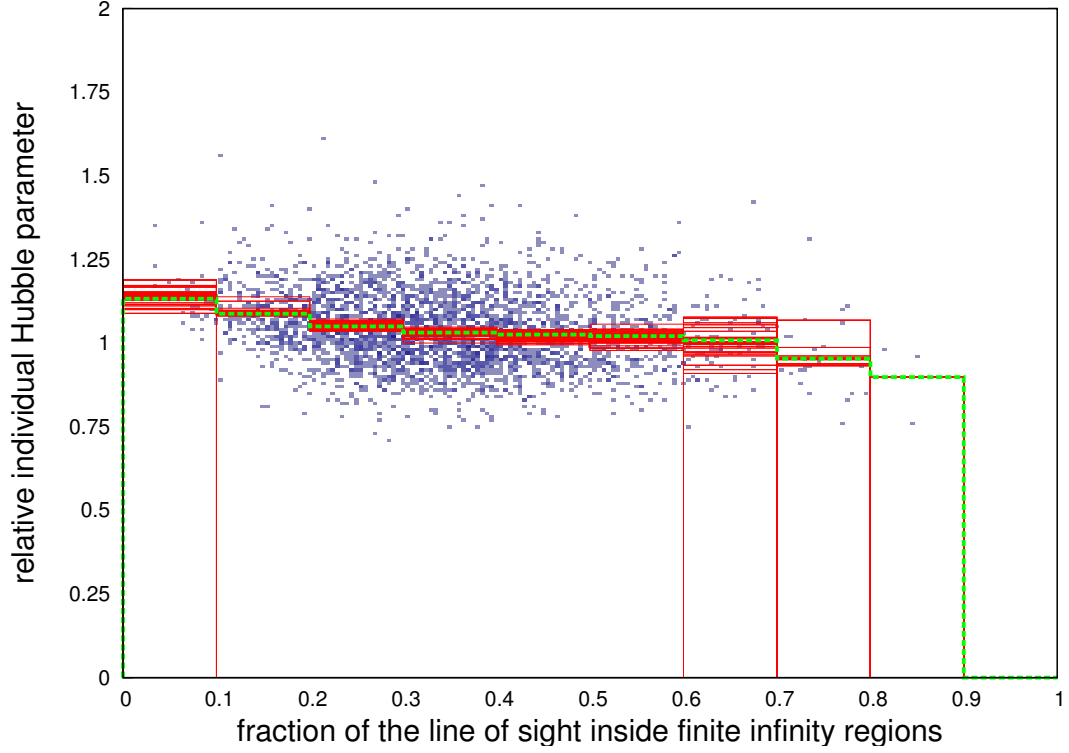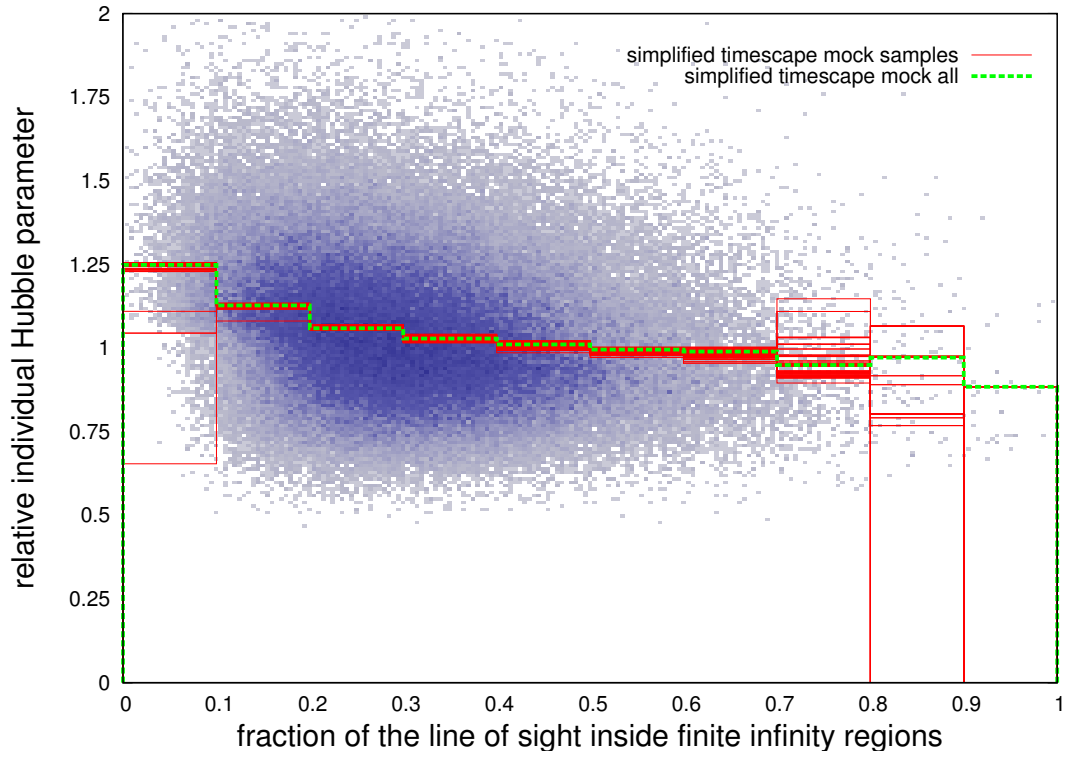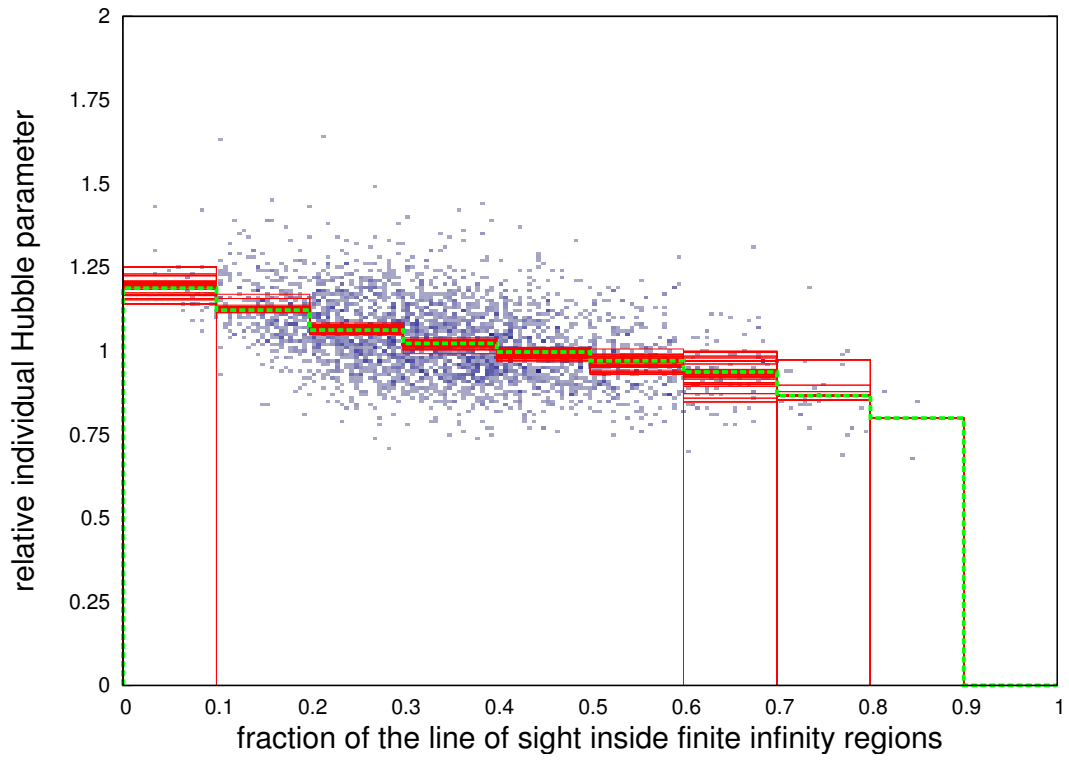
Figure 8.8: Diversity of the combined Λ-CDM mock catalogues. Red solid lines: weighted average in the bins of combined mock catalogues only containing a selected sub-sample of groups; green dashed line: weighted average in the bins of the combined data of a selected sub-sample of all mock catalogues; bluish point cloud: distribution of a selected sub-sample of groups in all mock catalogues.
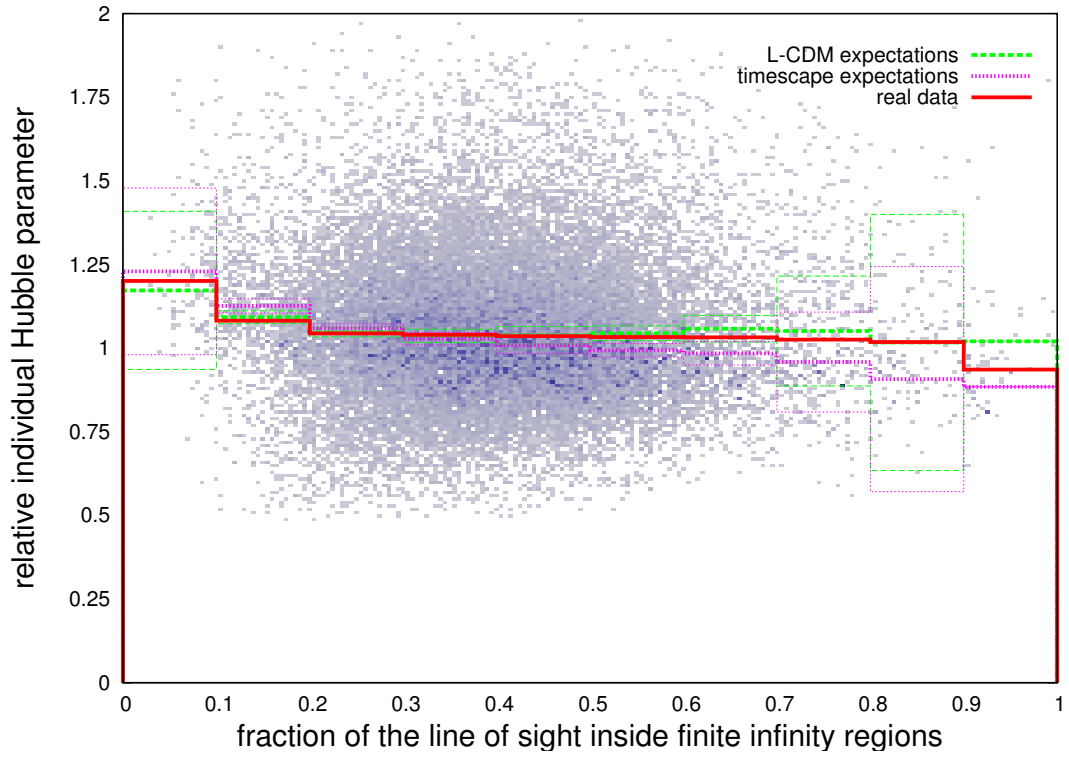
model	$\overline{P}$	$\mathcal{L}$
Λ-CDM (full)	0.512	0.952
timescape (full)	0.026	0.048
Λ-CDM (selected)	0.047	0.147
timescape (selected)	0.271	0.853

Table 8.5: Probabilities and likelihoods of the observations calculated for a weighted average of all bins using the average probability for the model. First column: specific model; second column: probability P for the observations to be represented by the model; third column: likelihood $\mathcal{L}$ for the model (only assuming Λ-CDM and timescape cosmology as possible options).

Figure 8.9: Diversity of the combined timescape mock catalogues. Red solid lines: weighted average in the bins of combined mock catalogues; green dashed line: weighted average in the bins of the combined data of all mock catalogues; bluish point cloud: distribution of all groups in all mock catalogues.

Figure 8.10: Diversity of the combined timescape mock catalogues. Red solid lines: weighted average in the bins of combined mock catalogues only containing a selected sub-sample of groups; green dashed line: weighted average in the bins of the combined data of a selected sub-sample of all mock catalogues; bluish point cloud: distribution of a selected sub-sample of groups in all mock catalogues.

Figure 8.11: Full observational data compared to the model predictions. Red solid line: weighted average in the bins of the observed data; green dashed lines: expectations and 3-σ limits of the Λ-CDM model for the bins; magenta dotted lines: expectations and 3-σ limits of the timescape model for the bins.
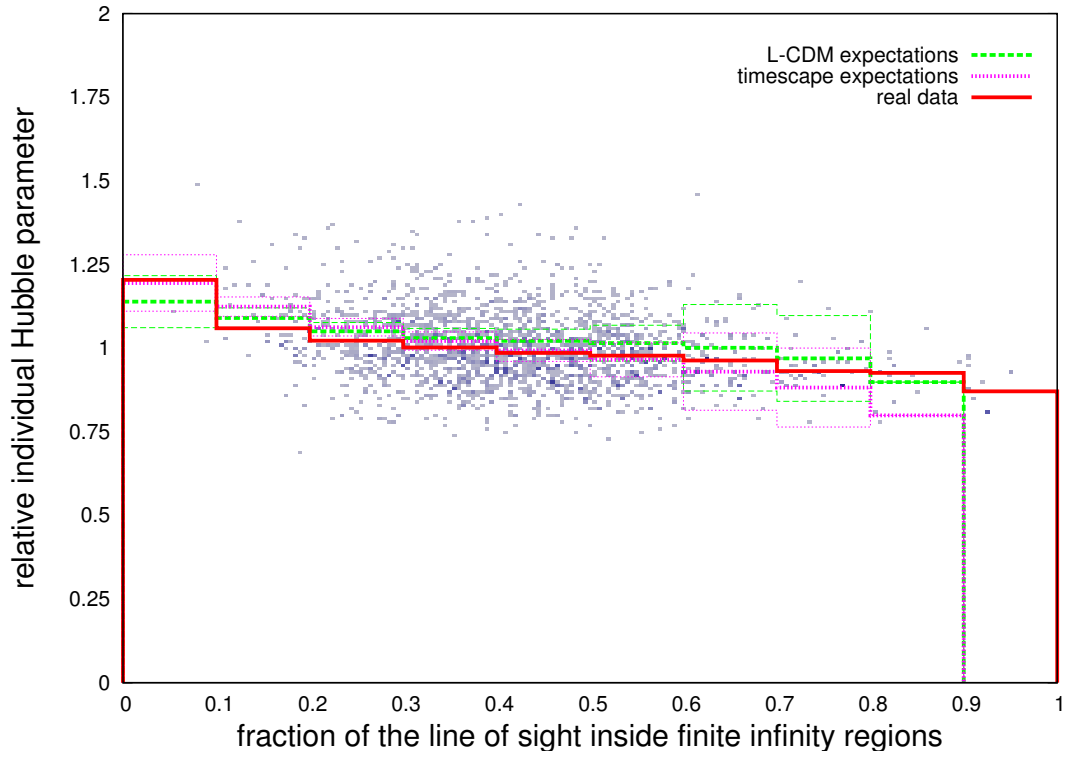
Figure 8.12: Selected observational data compared to the model predictions. Red solid line: weighted average in the bins of the observed data; green dashed lines: expectations and 3-σ limits of the Λ-CDM model for the bins; magenta dotted lines: expectations and 3-σ limits of the timescape model for the bins.

8.3.3 Linear regression on binned data
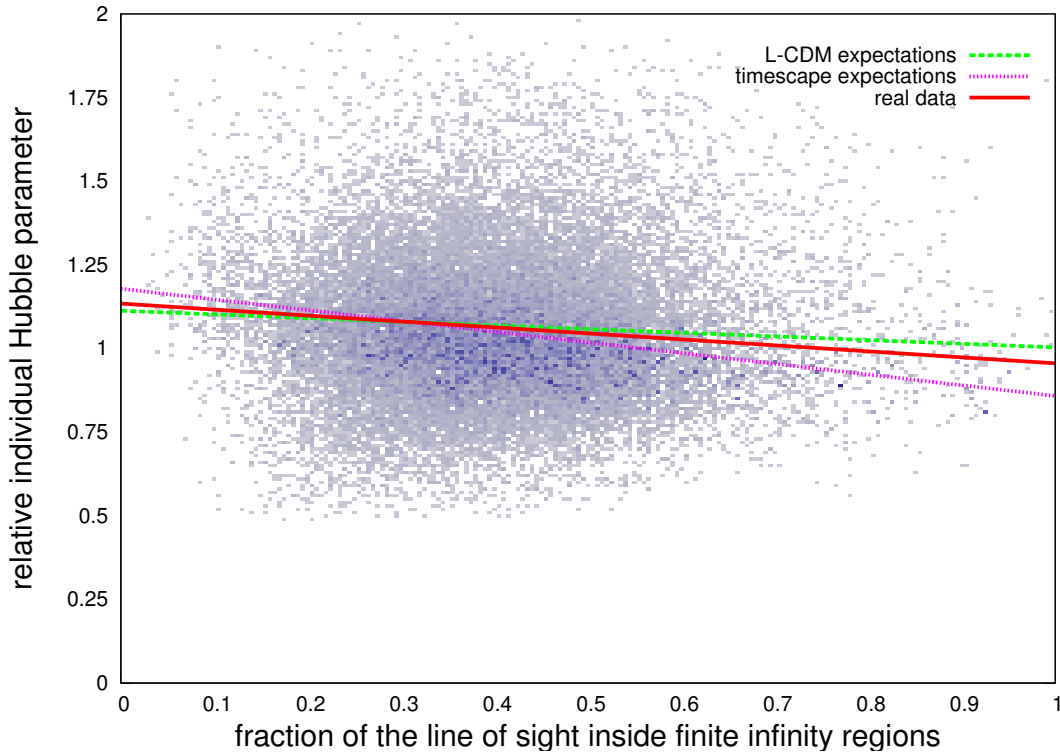
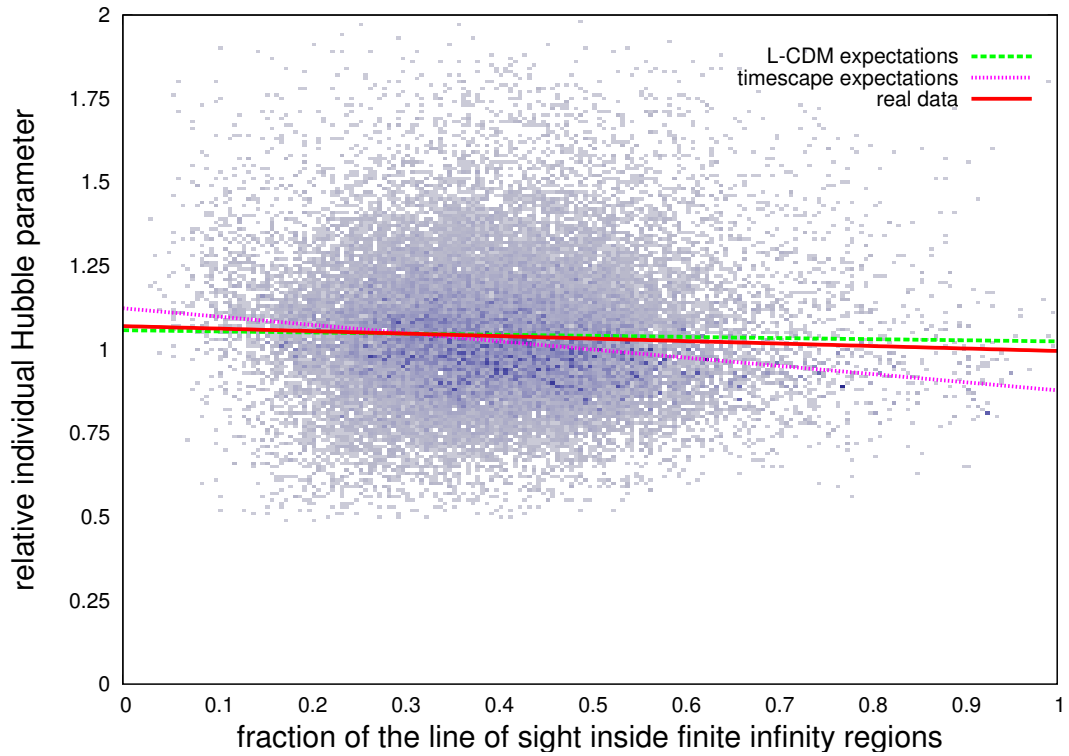Figure 8.13: Full observational data compared to the model predictions. Red solid line: linear regression fit on the equally weighted bins of the observed data; green dashed lines: linear regression fit on the equally weighted bins of the Λ-CDM mock catalogues; magenta dotted lines: linear regression fit on the equally weighted bins of the timescape mock catalogues. The bins are the same as in Figure 8.11, but are not explicitly shown to keep the plot clean.

Because the analysis of the likelihoods of the individual bins yielded some ambiguous results, a different approach is used to clarify the results. The average values of the individual Hubble parameters in each bin are used (at least for the bins where they were available, which excludes the highest bin of the selected data) together with the central value for the ratio of the finite infinity regions in the line of sight of each bin to create a set of data points. The values for the bins are taken from the previous section, specifically from Tables 8.2 and 8.3. All the bins are equally weighted in the first approach and linear regression is fitted using least squares. The results for this fit using the full dataset is shown in Figure 8.13 and using the selected dataset is shown in Figure 8.14. In both cases, the gradient of the observed data is clearly closer to the gradient derived from the Λ-CDM mock catalogues than to the one derived from the timescape mock catalogues. This is quantified in Table 8.6, which shows a strong preference for Λ-CDM cosmology. Interestingly, this is not only the case for the full data, but also for the selected data, which yielded opposite results in the analysis of probabilities of the individual bins.

As an alternative to the equally weighted bins, weights based on the number of galaxies in each bin are used for the fit. As illustrated in Figures 8.15 and 8.16, the gradient of the observed data is close to the gradient expected for Λ-CDM cosmology for both, the full and the selected, data. The numerical results are listed in Table 8.6 and clearly favour
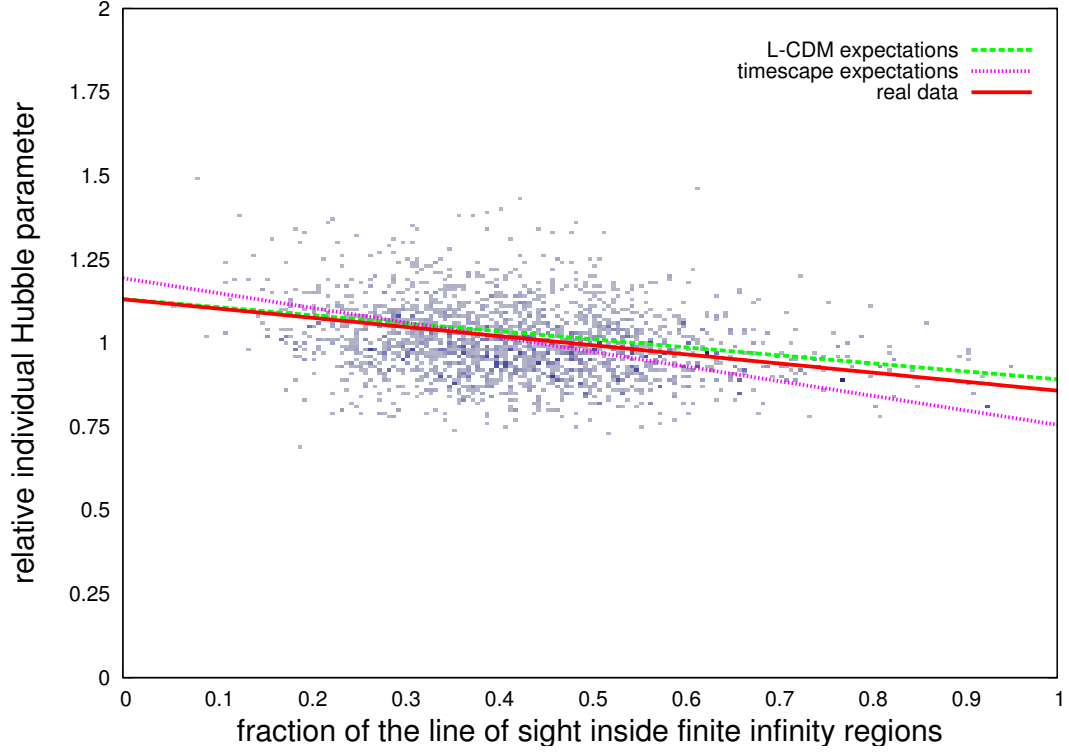
Figure 8.14: Selected observational data compared to the model predictions. Red solid line: linear regression fit on the equally weighted bins of the observed data; green dashed lines: linear regression fit on the equally weighted bins of the Λ-CDM mock catalogues; magenta dotted lines: linear regression fit on the equally weighted bins of the timescape mock catalogues. The bins are the same as in Figure 8.12, but are not explicitly shown to keep the plot clean.

the Λ-CDM model. For mathematical reasons, the values are similar to the results for the linear regression fitted on the "unbinned" data presented in Table 8.1.

Figure 8.15: Full observational data compared to the model predictions. Red solid line: linear regression fit on the galaxy count weighted bins of the observed data; green dashed lines: linear regression fit on the galaxy count weighted bins of the Λ-CDM mock catalogues; magenta dotted lines: linear regression fit on the galaxy count weighted bins of the timescape mock catalogues. The bins are the same as in Figure 8.11, but are not explicitly shown to keep the plot clean.
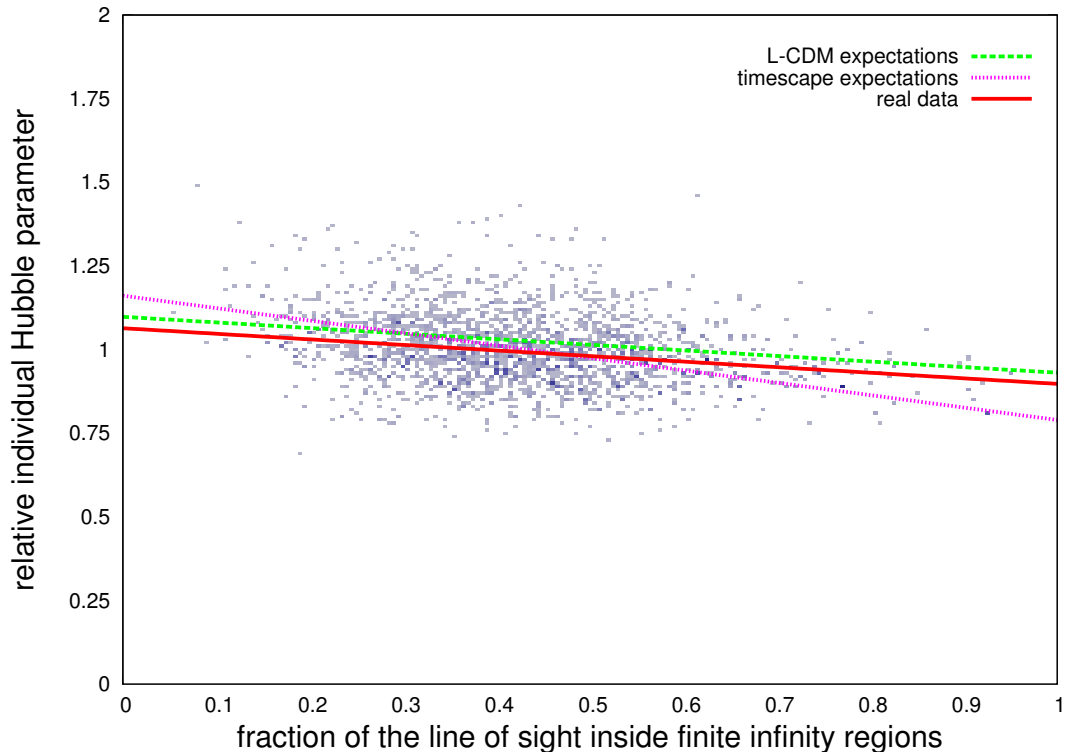
Figure 8.16: Selected observational data compared to the model predictions. Red solid line: linear regression fit on the galaxy count weighted bins of the observed data; green dashed lines: linear regression fit on the galaxy count weighted bins of the Λ-CDM mock catalogues; magenta dotted lines: linear regression fit on the galaxy count weighted bins of the timescape mock catalogues. The bins are the same as in Figure 8.12, but are not explicitly shown to keep the plot clean.

model	k_{obs}	k_{mock}	$\sigma_{k,\mathrm{mock}}$	$\Delta k[\sigma]$	P	$\mathcal{L}$
Λ-CDM (full,equally)	-0.179	-0.110	0.036	1.899	0.05742	0.998
timescape (full,equally)	-0.179	-0.321	0.037	3.868	0.0001	0.002
Λ-CDM (selected,equally)	-0.273	-0.240	0.028	1.209	0.226	1.000
timescape (selected,equally)	-0.273	-0.438	0.026	6.449	0.000	0.000
Λ-CDM (full,galaxy count)	-0.074	-0.033	0.035	1.155	0.250121	0.999994
timescape (full,galaxy count)	-0.074	-0.321	0.035	4.852	0.000001	0.000006
Λ-CDM (selected,galaxy count)	-0.166	-0.167	0.030	0.020	0.984	1.000
timescape (selected,galaxy count)	-0.166	-0.372	0.029	7.044	0.000	0.000

Table 8.6: Linear regression to the bins. Coefficients, probabilities and likelihoods of the observations using both, the full and the selected, datasets calculated for the linear regression fitted to the averages in the bins (equally weighted and weighted by galaxy count). First column: specific model; second column: gradient k_{obs} using the observations; third column: gradient H_{mock} fitted on the mock catalogue data; fourth column: standard deviation $\sigma_{k,\mathrm{mock}}$ of the gradient fitted to the mock catalogue ; fifth column: deviation of the observed gradient from the gradient in the mock catalogue (given in standard deviation); sixth column: probability P for the observations to be represented by the model; seventh column: likelihood $\mathcal{L}$ for the model (only assuming Λ-CDM and timescape cosmology as possible options).

Chapter 9

Discussion

In general, the results of the cosmological test performed in Chapter 8 show a preference for Λ-CDM cosmology over timescape cosmology. However, there are several issues which have to be considered.

9.1 Differences between the preliminary and the final results

First of all, the final results of this cosmological test are a clear contradiction to the preliminary results presented in Paper I. It is important to have a closer look on the changes made between the initial design of the test (Paper I) and the final execution and results to better understand the difference.

The model of the matter distribution of the local universe in Paper I was still very basic: a fixed mass-to-light ratio was assumed for every SDSS galaxy instead of a proper mass estimate covering the entire range from individual galaxies to galaxy clusters as done in Paper IV. However in unpublished intermediate results (see Appendix A), an already improved model of the matter distribution (Yang et al., 2007, 2009) in the local universe was used and a gradient was found which was largely in agreement with the timescape. The major disadvantage of that data was that it did not contain any galaxies below a redshift of 0.01 and the nearby regions are important for a solid test of timescape cosmology versus the Λ-CDM model. This was the main reason for me to start working on the data leading up to Paper IV, in which the 2MRS data was used to complete[1] an SDSS based model of the local universe. Furthermore, the total amount of matter in the Yang et al. (2009) catalogue was only a fraction of which would be expected for that volume based on cosmological observations, even at the lower redshifts. Rescaling the masses of that catalogue to the expected value did not take into account the distribution of the matter correctly. In addition to that, the same issues were present with the mock catalogues based on the Millennium simulation for the intermediate data. As of Paper IV, all those issues have been fixed and lead to a significantly better model of the matter distribution in the local universe in both, the observed data and the mock catalogues.

In Paper I, the assumption was that there is no gradient in the data for Λ-CDM cosmology, which was not taking into account coherent infall and other biases from the peculiar motions. Nevertheless, the observed data showed a much steeper gradient of the linear regression fitted to the data than even the expectation of timescape cosmology

---

[1]The SDSS spectroscopic sample suffers from a saturation bias, which excludes bright nearby galaxies.

(which was not taking into account that bias neither). In the intermediate data (see Appendix A), these biases have already been considered and resulted in a fit on the observational data, which was steeper than the prediction of timescape cosmology (but all biases not yet considered had a lowering effect on it). In the final data presented here, all tools and catalogues used in test are calibrated consistently. The steepness of the gradient of the individual Hubble parameters depending on the fraction of the line of sight within finite infinity regions is sensitive to normalization and the total amount of matter in the calibrations, because it affects the sizes of the finite infinity regions and consequently the total volume covered by them. The self-consistency of the calibration is definitely the most important improvement from the first results in Paper I to the final results here. The fundamental plane calibrations are another improvement since Paper I. The fundamental plane calibrations used in Paper I did not consider the Malmquist-bias and other effects. This was fixed in Paper II, in which the fundamental plane is properly calibrated using a huge SDSS sample. The calibrations of Paper II were already used for the intermediate data (see Appendix A), which did not affect the overall outcome that much. Further improvement on the fundamental plane was made in Paper III. These calibrations have be used for the final results. Considering all the changes and improvement, the differences between the first results (Paper I), the intermediate results (Appendix A), and the final results presented in Chapter 8 appear well understandable.

9.2 Simplifications in the timescape mock catalogues

A possible issue with the final results are the simplifications in timescape mock catalogues, especially those necessary for reasons of limited computational time. First of all, no simulation using timescape cosmology has been performed on any scales remotely comparable to the Millennium simulation so far. Therefore, it is necessary to extrapolate from other simulations. To gain the best compatibility with Λ-CDM models, which were used for comparison, the Millennium simulation is used as a foundation for the extrapolated timescape cosmology model. By doing so, it is assumed that the later snapshots of the Millennium simulation are a reasonably good representation of the matter distribution in the late universe. There are issues with the simulation, such as the missing satellite problem (Mateo, 1998; Klypin et al., 1999; Bullock, 2010; Wang et al., 2012). However, these are all on much smaller scales than the sizes of the finite infinity regions and therefore do not have any notable impact on the cosmology test. A significant issue with the data from the Millennium simulation is the dearth of rich clusters in the results of the simulation compared to the observational data (see Chapter 7). It has to be considered as a systematic bias affecting both (Λ-CDM and timescape) sets of mock catalogues in the same way. Aside from using other numerical simulations, which is not feasible due to large volume required to construct the mock catalogues for this test, there is no way to properly correct for this bias. Another issue is the fact that all the FoF-groups detected in the Millennium simulation together contain less than half the mass/particles used in the simulation. Using the full particle information from the millimil run, $\sim 80\%$ of the particles were found to be within the finite infinity regions around the FoF groups, if their masses/sizes are rescaled accordingly (see Paper IV). This knowledge was used to extrapolate the mass of the groups and cluster. The remaining $\sim 20\%$ of the missing mass was included by simply rescaling the finite infinity regions accordingly. Due to the relatively large scatter between the different mock catalogues of the same cosmology (see Chapter 8), this way was preferred to the alternative (weakening the gradient of the effect of timescape cosmology accordingly, as discussed in Paper IV). Thereby, the mock catalogues became better comparable. Another issue, which requires consideration when using the Millennium simulation is the no longer up-to-date cosmology used for it. There is already a significant difference between the cosmological parameters of the simulation and the cosmological parameters obtained by the latest CMB observations (Planck Collaboration et al., 2013). There are reruns (Guo et al., 2013) using a more present-day set of cosmological parameters (from WMAP7 (Komatsu et al., 2011)) and also rescales versions of the original run (Guo et al., 2013). However, the public database of the reruns does not contain the FoF-group catalogue, which are essential for the calibration of the group finder (Paper IV) and the finite infinity regions derived from its results. Furthermore, the rescaled versions yield incorrect (incompatible with the observations) number densities for the galaxies, which were inserted into the dark matter halos using semi-analytical models (De Lucia et al., 2006). For these reasons, the original Millennium run was used for this thesis. The cosmological parameters of the Millennium simulation were used consistently in the final results and every calibration leading up to them. Despite all these issues, the Millennium simulation is the best available model, which has a sufficiently large volume and all the additional data that is need for the cosmological test performed in this thesis. The next question, which has to be addressed, is if artificially introducing the different expansion rates of voids and walls for the timescape model, which were obtained by fitting the timescape model (Wiltshire, 2007; Leith et al., 2008) to observed data of

supernovae Typ Ia (Riess et al., 2007), CMB (Bennett et al., 2003; Spergel et al., 2007) and Baryonic acoustic oscillations (Cole et al., 2005; Eisenstein et al., 2005), into the data of the Millennium simulation is justified. To this end, it is important to remember how the Hubble expansion in general is considered in n-body simulations. The metric expansion of space is a general relativistic effect, which has to be incorporated in an elsewise fully Newtonian simulation. The expansion of the universe is handled by using co-moving coordinates, which require to add an additional term (similar to a drag force) to the Newtonian gravity. Consequently, the Hubble expansion in the Λ-CDM simulation was already introduced as an artificial feature rather than an intrinsic property. Because the present day matter distribution is the only feature drawn from the simulation, calculating slightly different redshift values from this data in the last snapshots, where structure formation is slow, is therefore a justified approximation. Naturally, a full cosmological simulation using timescape cosmology would be preferable and more self-consistent, but such a thing does not exist. Using the Millennium simulation instead is the best practicable option.

A more important issue than all of the before mentioned approximations is the fact that a simpler model for the timescape cosmology mock catalogues had to be used than initially planned. The masses of the groups in the mock catalogues , which were derived using the group finder, are not 100% accurate and neither are the positions of the groups. The uncertainties in the model of the matter distribution in the local universe affect the measured values of the fraction of the line of sight within finite infinity regions. As explained in Chapter 7, this requires the full (unbiased) FoF group data from the Millennium simulation for each of the eight mock catalogues. They contain more than 8 000 000 FoF groups each, which have to be merged and rescaled in the same fashion as done in Paper IV. The large number of groups, which have to be merged by an recursive algorithm, requires a considerable amount of computational time and resources, which are currently very limited to me. Therefore, the results of the best possible timescape mock catalogues are deferred to future work beyond this thesis. As a consequence, the second best possible implementation of the timescape mock catalogues is presented in the results (see Section 8.2). The timescape mock catalogues do not include a sophisticated model of the bias introduced by the uncertainties of modelling the matter distribution in the local universe. It only adjusts the gradient of the Λ-CDM model and takes the before-mentioned bias only in form of a bias factor into account. The bias effect will not be zero but on the other hand it is not expected to be huge because the sizes of the finite infinity region are not very sensitive to small uncertainties in their masses. Their radii only scale with the cube root of their masses according to Equation 7 in Paper IV. As an educated guess, this factor is chosen to be 0.1. If the bias factor were significantly higher, it would become difficult to distinguish Λ-CDM and timescape cosmology with the provided test data. While having to settle with the second best possible mock catalogues for timescape cosmology for the thesis, I hope to have the best possible model ready for the follow-up paper.

9.3 Fundamental plane residuals

The fundamental plane of elliptical galaxies was used as a distance indicator in this thesis. It was calibrated and discussed in great detail in Paper II. Further improvements were made in Paper III. In Paper IV, a systematic variation of the residual distance dependence of the ratio between the fundamental plane distance and redshift distance depending on the multiplicity of the groups was detected. The fundamental plane distances, using the calibrations of Paper III, have a small residual distance/redshift dependence. However, it seems to strongly increase with the richness of the groups. This effect was not detected in the mock catalogues, where the fundamental plane distances were not derived from the galaxies' parameters, but just from their co-moving distances and a statistical scatter (also considering the residual redshift dependence of the fit of Paper III). Hence, it is fair to assume that this is an environmental effect on the fundamental plane parameters. This would be in agreement with the findings of Joachimi et al. (2015). To test how the residual redshift dependence influences the results of the cosmological test, a set of mock catalogues was created, which does not include the residual redshift dependence in the mock fundamental plane distance. The cosmological test was performed using this alternative set of mock catalogues instead of the previously used ones. A comparison showed that no significant difference could be found between the alternative results and the results presented in Chapter 8. I conclude that the variations in the fundamental plane residuals do not have any significant impact on the outcome of the cosmological test presented in this thesis.

9.4 Future improvements on Paper IV

Paper IV is currently undergoing the referee process and several small improvements will be made before acceptance. For example the extinction corrects, the uncertainties in the mock-observed magnitudes and the transformation from SDSS to 2MASS magnitudes will be improved. Also the optimal parameters of the FoF group finder algorithm and the mass estimates will be reworked aside with a few other minor changes. Due to the before mentioned shortage in computational resources, all those improvements, which require a full rerun of all programmes and calibrations perform for Paper IV, are already partially completed. However, to keep the work in this thesis self-consistent, the new results are not used or presented here. The cosmological test, which would also have to be re-computed (and will be for the follow-up paper), still uses the data of Paper IV as presented in the version included in this thesis. From the status of the improved results of Paper IV so far, no significant changes in the results of the cosmological test are expected.

9.5 Statistical analysis

The results of the statistical tests performed in Chapter 8 tend to favour Λ-CDM cosmology over timescape cosmology. The least square fits show that the observed gradient in Figures 8.5 and 8.6 is compatible with the Λ-CDM model, while the measured value would be a more than $3 - \sigma$ outlier for timescape cosmology (see Table 8.1). Selecting only the galaxy groups with the most solid data yields an even stronger favour for Λ-CDM cosmology. However, fitting a linear regression using least squares is not the most sophisticated statistical analysis, which one can perform on a such a data set. Binning the data was the subsequent step. The mean values of the relative individual Hubble parameters are calculated in ten bins each 0.1 wide in the fraction of finite infinity regions within the line of sight. With the full data (see Figure 8.11), the Λ-CDM cosmology is preferred in every bin except the lowest one (where the likelihood is about the same as for timescape cosmology, see Table 8.2). Also the combined analysis of all bins together shows a clear preference for Λ-CDM cosmology. However, with the selected sample (see Figure 8.12), many bins (see Table 8.3) as well as the combined analysis (see Tables 8.4 and 8.5) show a moderate preference for timescape cosmology. The support for timescape cosmology in the selected data using a binned analysis is not nearly as strong as the likelihoods from all other analysis, but it is an odd fact that requires careful consideration. There are a couple of issues with the selected data, which can explain the apparent contradictory results: the dearth of rich cluster in mock catalogues and the thereby even more impoverished statistics due to the lower numbers in the sample and the bins, but also the sensitivity of the binning method to the normalisation of the data. Although the full sample of the observed data and the mock catalogues use the same normalisation, there might be a systematic shift in the selected sample as a consequence of the selection criteria and dearth of rich clusters in the mock catalogues. It would explain that the measured values for the probabilities in the bins are neither really good matches for Λ-CDM cosmology nor timescape cosmology, but slightly better for the latter. Removing the weights based on the number of galaxies in each bin and considering each bin with the same impact, the likelihood for timescape cosmology is reduced further, but still remains higher than the likelihood for Λ-CDM cosmology. Giving the issues with the individual bins, a linear regression is fitted to the mean values in the bins. In two different approaches all bins are either weighted equally or weighted by the number of galaxies in the bins. The gradients (illustrated in Figures 8.13 to 8.16) show a clear preference for the Λ-CDM model in all cases (see Table 8.6), even with the selected data. Figure 8.16 shows a strong indication that the issues with binned analysis in the case the selected sample is due to a normalization issue. The fits of the observed data and the Λ-CDM cosmology are parallel, but slightly shifted. Given the overwhelming results in favour of Λ-CDM cosmology from the other statistical analyses, results for the selected sample and the binning analysis are attributed to the normalization issue in combination with the poorer statistics and data loss when binning. In addition to the already mentioned test, a Kolmogorov-Smirnov test (KS test) was also performed using the implementation from the Numerical Recipes (Press et al., 1992) for the two-sample case of the two-dimensional KS test. The results were inconclusive, because the algorithm yielded probability values for either set of mock catalogues resembling the observed distribution of the order of 1^{-40}, which is a suspiciously tiny value. The results strongly favour Λ-CDM cosmology over timescape cosmology after this basic analysis. More sophisticated techniques and improvements in the model may further enhance the significance, but are highly unlikely to provide any

support for timescape cosmology.

Chapter 10

Summary and Conclusions

A meaningful test, which compares observational indications of Λ-CDM cosmology and timescape cosmology is presented in this thesis. Timescape cosmology is an alternative theory that aims to explain the observed accelerated expansion of the universe by back-reactions from inhomogeneities due to effects from General Relativity instead of introducing dark energy. The most tangible prediction of this conceptionally interesting theory, different expansion rates in voids and walls, has remained untested so far. A test was designed and outlined in Paper I. It required a redshift-independent distance indicator, for which the fundamental plane of elliptical galaxies was chosen and carefully calibrated in Paper II and even further improved in Paper III. Another essential requirement for the proposed test was a solid model of the matter distribution in the local universe, which was provided in Paper IV. The final version of the cosmological test, which distinguishes timescape cosmology and Λ-CDM cosmology based on observational data, is presented in Chapter 7 alongside all necessary calibrations and mock catalogues. Several improvements were made for the final test compared to its initial design and first results in Paper I and intermediate results shown in Appendix A. The results of the cosmological test are presented in Chapter 8. A comparison with the mock catalogues shows that the gradient of the linear regression fitted on the observed data clearly supports the Λ-CDM model for both the full and the selected sample. Using the full sample, the analysis of the individual bins also favours Λ-CDM cosmology. However, the binning analysis using the selected sample moderately favours timescape cosmology. This may be caused by systematic effects, which strongly manifest themselves in the selected sample and the binning is especially sensitive to them. Fitting a linear regression to the binned data, which can be either equally weighted or weighted by galaxy count, yields gradients, which clearly favour the Λ-CDM model over timescape cosmology. There are still several minor issues with the data, which are all discussed in detail in Chapter 9.

Due to the before-mentioned issues with the analysis of the individual bins, the significance of the final results are not as high as may have been naively expected from the outset of the test. The scatter between the different combined mock catalogues (see Chapter 8) is higher than expected. A couple of simplification were necessary to make the test feasible. Furthermore, a few additional approximations had to be made due to a shortage on computation time and facilities, something which will be solved in the follow-up paper. With these caveats in mind, the results of the cosmological test performed in this thesis favour the Λ-CDM model over time-scape cosmology. The impact of inhomogeneities on the cosmological parameters is apparently not strong enough to explain the accelerated expansion of the universe without dark energy. The strength of the back-reaction effect

as predicted by Wiltshire (2007) thus appears over-estimated. Assuming the observational signatures of models with dark energy and back-reactions(Clarkson et al., 2012; Umeh et al., 2014a,b; Clarkson et al., 2014) are weaker albeit similar to the signatures of timescape cosmology, those models cannot explicitly be excluded by the data presented here, because they would be hidden in the scatter. My results (except for the problematic results of the binned analysis of the selected sample) agree well with recent calculations (Kaiser & Peacock, 2015; Lavinto & Rasanen, 2015) that the impact of back-reaction effects from General Relativity due the inhomogeneous distribution of matter in the universe are indeed tiny and that the assumption of an on average homogeneous space-time, which results in Λ-CDM cosmology, is justified.

For this thesis, only publicly available data was used and no additional observations beyond the public surveys were necessary. SDSS (Stoughton et al., 2002; Aihara et al., 2011; Ahn et al., 2014) and SDSS-based material such as the classifications from Galaxy-Zoo (Lintott et al., 2008, 2011) or the refitted galaxy catalogues (Simard et al., 2011; Mendel et al., 2014) containing additional measurements formed the foundation of the observational data. It was supplemented by the 2MASS-based (Skrutskie et al., 2006) 2MRS catalogue (Huchra et al., 2012b,a). The data from the Millennium simulation (Springel et al., 2005; Lemson & Virgo Consortium, 2006) provided a basis for the mock catalogues, which were necessary to properly quantify the theoretical predictions. This thesis is an excellent example what can be achieved in the new and growing field of data astronomy.

The remaining issues (see Chapter 9) that can be solved will be addressed in the follow-up paper. With the basics already at hand, I plan to repeat the test with an extended sample (including GAMA (Liske et al., 2015) and 6dFGS (Jones et al., 2004, 2009)) and a different distance indicator such as the Tully-Fisher relation (Tully & Fisher, 1977) to further reduce any potential systematics. Since the cosmological test required redshift data and another independent distance indicator, implicitly lots of peculiar motion data was obtained, which opens the opportunity for many follow-up investigations on peculiar motions and bulk flows (similar to Tully et al. (2013)), especially in combination with the model of the matter distribution in the local universe (Paper IV). Paper III has already illustrated that the data calibrated and analysed as part of this thesis has the potential for interesting projects beyond the cosmological test it was intended for.

Acknowledgments

Utah, Vanderbilt University, University of Virginia, University of Washington, and Yale University.

Bibliography

Ahn, C. P. et al. 2014, *ApJS*, 211, 17, 1307.7735

Aihara, H., Allende Prieto, C., & et al. 2011, *ApJS*, 193, 29, 1101.1559

Alexander, S., Biswas, T., Notari, A., & Vaid, D. 2009, jcap, 9, 25, 0712.0370

Armendariz-Picon, C., Mukhanov, V., & Steinhardt, P. J. 2000, Physical Review Letters, 85, 4438, arXiv:astro-ph/0004134

Bass, S. D. 2011, Journal of Physics G Nuclear Physics, 38, 043201

Basu, A., Wadadekar, Y., Beelen, A., Singh, V., Archana, K. N., Sirothia, S., & Ishwara-Chandra, C. H. 2015, *ApJ*, 803, 51, 1502.00330

Bell, E. F. et al. 2004, *ApJ*, 608, 752, astro-ph/0303394

Bennett, C. L. et al. 2003, *ApJS*, 148, 1, astro-ph/0302207

Buchert, T. 2000a, Journal of Geophysical Research (Biogeosciences), 306, arXiv:gr-qc/0001056

Buchert, T. 2000b, General Relativity and Gravitation, 32, 105, arXiv:gr-qc/9906015

Buchert, T. 2001, General Relativity and Gravitation, 33, 1381, arXiv:gr-qc/0102049

Buchert, T., & Carfora, M. 2003, Physical Review Letters, 90, 031101, arXiv:gr-qc/0210045

Buchert, T., Kerscher, M., & Sicka, C. 2000, *Phys. Rev. D*, 62, 043525, arXiv:astro-ph/9912347

Bullock, J. S. 2010, ArXiv e-prints, 1009.4505

Bundy, K. et al. 2010, *ApJ*, 719, 1969, 0912.1077

Cappellari, M. et al. 2007, *MNRAS*, 379, 418, astro-ph/0703533

Cappellari, M. et al. 2011, *MNRAS*, 416, 1680, 1104.3545

Chilingarian, I. V., & Zolotukhin, I. Y. 2012, *MNRAS*, 419, 1727, 1102.1159

Clarkson, C., Ananda, K., & Larena, J. 2009, *Phys. Rev. D*, 80, 083525, 0907.3377

Clarkson, C., Ellis, G. F. R., Faltenbacher, A., Maartens, R., Umeh, O., & Uzan, J.-P. 2012, *MNRAS*, 426, 1121, 1109.2484

Clarkson, C., Umeh, O., Maartens, R., & Durrer, R. 2014, JCAP, 11, 36, 1405.7860

Clowe, D., Bradač, M., Gonzalez, A. H., Markevitch, M., Randall, S. W., Jones, C., & Zaritsky, D. 2006, *ApJ*, 648, L109, arXiv:astro-ph/0608407

Coil, A. L., Davis, M., & Szapudi, I. 2001, *PASP*, 113, 1312, astro-ph/0107541

Coil, A. L. et al. 2008, *ApJ*, 672, 153, 0708.0004

Cole, S. et al. 2005, *MNRAS*, 362, 505, astro-ph/0501174

Crocker, A. F., Jeong, H., Komugi, S., Combes, F., Bureau, M., Young, L. M., & Yi, S. 2009, *MNRAS*, 393, 1255, 0812.0178

Davis, T. A. et al. 2011, *MNRAS*, 414, 968, 1102.4877

De Lucia, G., Springel, V., White, S. D. M., Croton, D., & Kauffmann, G. 2006, *MNRAS*, 366, 499, astro-ph/0509725

Djorgovski, S., & Davis, M. 1987, *ApJ*, 313, 59

Dressler, A. 1980, *ApJ*, 236, 351

Dressler, A., Lynden-Bell, D., Burstein, D., Davies, R. L., Faber, S. M., Terlevich, R., & Wegner, G. 1987, *ApJ*, 313, 42

Dressler, A. et al. 1997, *ApJ*, 490, 577, astro-ph/9707232

Eisenstein, D. J. et al. 2005, *ApJ*, 633, 560, astro-ph/0501171

Ellis, G. F. R. 1984, in General Relativity and Gravitation Conference, ed. B. Bertotti, F. de Felice, & A. Pascolini, 215–288

Ellis, G. F. R., & Jaklitsch, M. J. 1989, *ApJ*, 346, 601

Ellis, G. F. R., & Stoeger, W. 1987, Classical and Quantum Gravity, 4, 1697

Emsellem, E. et al. 2011, *MNRAS*, 414, 888, 1102.4444

Ferrarese, L., & Merritt, D. 2000, *ApJ*, 539, L9, astro-ph/0006053

Gebhardt, K. et al. 2000, *ApJ*, 539, L13, astro-ph/0006289

Gladders, M. D., López-Cruz, O., Yee, H. K. C., & Kodama, T. 1998, *ApJ*, 501, 571, astro-ph/9802167

Graves, G. J., & Faber, S. M. 2010, *ApJ*, 717, 803, 1005.0014

Graves, G. J., Faber, S. M., & Schiavon, R. P. 2009a, *ApJ*, 693, 486, 0810.4334

Graves, G. J., Faber, S. M., & Schiavon, R. P. 2009b, *ApJ*, 698, 1590, 0903.3603

Graves, G. J., Faber, S. M., & Schiavon, R. P. 2010, *ApJ*, 721, 278, 1007.3260

Guo, Q., White, S., Angulo, R. E., Henriques, B., Lemson, G., Boylan-Kolchin, M., Thomas, P., & Short, C. 2013, *MNRAS*, 428, 1351, 1206.0052

Guo, Q., White, S., Li, C., & Boylan-Kolchin, M. 2010, *MNRAS*, 404, 1111, 0909.4305

Harker, J. J., Schiavon, R. P., Weiner, B. J., & Faber, S. M. 2006, *ApJ*, 647, L103, astro-ph/0607400

Harwit, M. 1995, *ApJ*, 447, 482

Hatton, S., & Cole, S. 1998, *MNRAS*, 296, 10, astro-ph/9707186

Holden, B. P. et al. 2007, *ApJ*, 670, 190, 0707.2782

Huchra, J. P. et al. 2012a, VizieR Online Data Catalog, 219, 90026

Huchra, J. P. et al. 2012b, *ApJS*, 199, 26, 1108.0669

Ishibashi, A., & Wald, R. M. 2006, Classical and Quantum Gravity, 23, 235, arXiv:gr-qc/0509108

Joachimi, B., Singh, S., & Mandelbaum, R. 2015, ArXiv e-prints, 1504.02662

Jones, D. H. et al. 2009, *MNRAS*, 399, 683, 0903.5451

Jones, D. H. et al. 2004, *MNRAS*, 355, 747, astro-ph/0403501

Kai, T., Kozaki, H., Nakao, K., Nambu, Y., & Yoo, C. 2007, Progress of Theoretical Physics, 117, 229, arXiv:gr-qc/0605120

Kaiser, N. 1987, *MNRAS*, 227, 1

Kaiser, N., & Peacock, J. A. 2015, ArXiv e-prints, 1503.08506

Klypin, A., Kravtsov, A. V., Valenzuela, O., & Prada, F. 1999, *ApJ*, 522, 82, astro-ph/9901240

Kolb, E. W., Matarrese, S., & Riotto, A. 2006, New Journal of Physics, 8, 322, arXiv:astro-ph/0506534

Komatsu, E. et al. 2011, *ApJS*, 192, 18, 1001.4538

Krajnović, D. et al. 2011, *MNRAS*, 414, 2923, 1102.3801

Kwan, J., Francis, M. J., & Lewis, G. F. 2009, *MNRAS*, 399, L6, 0902.4249

Lane, R. R., Salinas, R., & Richtler, T. 2014, ArXiv e-prints, 1412.3402

Lavinto, M., & Rasanen, S. 2015, ArXiv e-prints, 1507.06590

Leith, B. M., Ng, S. C. C., & Wiltshire, D. L. 2008, *ApJ*, 672, L91, 0709.2535

Lemson, G., & Virgo Consortium, t. 2006, ArXiv Astrophysics e-prints, astro-ph/0608019

Lintott, C. et al. 2011, *MNRAS*, 410, 166, 1007.3265

Lintott, C. J. et al. 2008, *MNRAS*, 389, 1179, 0804.4483

Liske, J. et al. 2015, *MNRAS*, 452, 2087, 1506.08222

Loh, Y.-S. et al. 2010, *MNRAS*, 407, 55, 1004.3382

Marra, V., & Pääkkönen, M. 2010, jcap, 12, 21, 1009.4193

Martin, D. C. et al. 2007, *ApJS*, 173, 342, astro-ph/0703281

Mateo, M. L. 1998, *ARA&A*, 36, 435, astro-ph/9810070

Mattsson, M., & Mattsson, T. 2010, jcap, 10, 21, 1007.2939

Mavromatos, N. 2007, in Lecture Notes in Physics, Berlin Springer Verlag, Vol. 720, The Invisible Universe: Dark Matter and Dark Energy, ed. L. Papantonopoulos, 333, arXiv:hep-th/0607006

Mendel, J. T., Simard, L., Palmer, M., Ellison, S. L., & Patton, D. R. 2014, *ApJS*, 210, 3, 1310.8304

Nandra, K. et al. 2007, *ApJ*, 660, L11, astro-ph/0607270

Nigoche-Netro, A., Ruelas-Mayorga, A., Lagos, P., Ramos-Larios, G., Kehrig, C., Kemp, S. N., Montero-Dorta, A. D., & González-Cervantes, J. 2014, ArXiv e-prints, 1410.1469

Outram, P. J., Hoyle, F., & Shanks, T. 2001, *MNRAS*, 321, 497, astro-ph/0009387

Paranjape, A. 2009, ArXiv e-prints, 0906.3165

Peacock, J. A. 1999, Cosmological Physics (Cambridge University Press)

Perlmutter, S. et al. 1999, *ApJ*, 517, 565, arXiv:astro-ph/9812133

Planck Collaboration et al. 2013, ArXiv e-prints, 1303.5062

Postman, M., & Geller, M. J. 1984, *ApJ*, 281, 95

Press, W. H., Teukolsky, S. A., Vetterling, W. T., & Flannery, B. P. 1992, Numerical recipes in FORTRAN. The art of scientific computing (Cambridge University Press)

Räsänen, S. 2006, jcap, 11, 3, arXiv:astro-ph/0607626

Riess, A. G. et al. 1998, *AJ*, 116, 1009, arXiv:astro-ph/9805201

Riess, A. G. et al. 2007, *ApJ*, 659, 98, astro-ph/0611572

Robotham, A. S. G. et al. 2011, *MNRAS*, 416, 2640, 1106.1994

Saulder, C., Mieske, S., & Zeilinger, W. W. 2012, in Dark Side of the Universe (DSU 2012), 18, 1211.1926

Saulder, C., Mieske, S., Zeilinger, W. W., & Chilingarian, I. 2013, *A&A*, 557, A21, 1306.0285

Saulder, C., van den Bosch, R. C. E., & Mieske, S. 2015, *A&A*, 578, A134, 1503.05117

Schawinski, K. 2009, in American Institute of Physics Conference Series, Vol. 1201, American Institute of Physics Conference Series, ed. S. Heinz & E. Wilcots, 17–20, 0909.1106

Schmidt, B. P. et al. 1998, *ApJ*, 507, 46, astro-ph/9805200

Schwarz, D. J. 2010, ArXiv e-prints, 1003.3026

Simard, L., Mendel, J. T., Patton, D. R., Ellison, S. L., & McConnachie, A. W. 2011, *ApJS*, 196, 11, 1107.1518

Simon, P., Hetterscheidt, M., Wolf, C., Meisenheimer, K., Hildebrandt, H., Schneider, P., Schirmer, M., & Erben, T. 2009, *MNRAS*, 398, 807, 0805.3459

Skrutskie, M. F. et al. 2006, *AJ*, 131, 1163

Spergel, D. N. et al. 2007, *ApJS*, 170, 377, astro-ph/0603449

Springel, V. et al. 2005, *Nature*, 435, 629, arXiv:astro-ph/0504097

Steinhardt, P. J., Wang, L., & Zlatev, I. 1999, *Phys. Rev. D*, 59, 123504, arXiv:astro-ph/9812313

Stoughton, C. et al. 2002, *AJ*, 123, 485

Szekeres, P. 1975, Communications in Mathematical Physics, 41, 55

Tikhonov, A. V., & Karachentsev, I. D. 2006, *ApJ*, 653, 969, arXiv:astro-ph/0609109

Tolman, R. C. 1934, Proceedings of the National Academy of Science, 20, 169

Tomita, K. 2001, *MNRAS*, 326, 287, arXiv:astro-ph/0011484

Tully, R. B. et al. 2013, *AJ*, 146, 86, 1307.7213

Tully, R. B., & Fisher, J. R. 1977, *A&A*, 54, 661

Umeh, O., Clarkson, C., & Maartens, R. 2014a, Classical and Quantum Gravity, 31, 202001, 1207.2109

Umeh, O., Clarkson, C., & Maartens, R. 2014b, Classical and Quantum Gravity, 31, 205001, 1402.1933

van den Hoogen, R. J. 2010, ArXiv e-prints, 1003.4020

van der Wel, A., Bell, E. F., Holden, B. P., Skibba, R. A., & Rix, H.-W. 2010, *ApJ*, 714, 1779, 1004.0319

Wang, J., Frenk, C. S., Navarro, J. F., Gao, L., & Sawala, T. 2012, *MNRAS*, 424, 2715, 1203.4097

Wiltshire, D. L. 2007, New Journal of Physics, 9, 377, arXiv:gr-qc/0702082

Wiltshire, D. L. 2009, *Phys. Rev. D*, 80, 123512, 0909.0749

Wiltshire, D. L. 2010, in American Institute of Physics Conference Series, Vol. 1241, American Institute of Physics Conference Series, ed. J.-M. Alimi & A. Fuözfa, 1182–1191, 0912.5236

Wiltshire, D. L. 2011, ArXiv e-prints, 1102.2045

Wyder, T. K. et al. 2007, *ApJS*, 173, 293, 0706.3938

Yang, X., Mo, H. J., & van den Bosch, F. C. 2009, *ApJ*, 695, 900, 0808.0539

Yang, X., Mo, H. J., van den Bosch, F. C., Pasquali, A., Li, C., & Barden, M. 2007, *ApJ*, 671, 153, 0707.4640

Zalaletdinov, R. M. 1992, General Relativity and Gravitation, 24, 1015

Zehavi, I. et al. 2011, *ApJ*, 736, 59, 1005.2413

Zibin, J. P., Moss, A., & Scott, D. 2008, Physical Review Letters, 101, 251303, 0809.3761

Zlatev, I., Wang, L., & Steinhardt, P. J. 1999, Physical Review Letters, 82, 896, arXiv:astro-ph/9807002

Appendices

Appendix A

Poster with intermediate results

The intermediate results of my research have not been officially published, because they were still incomplete at that time. However, as a report on the state of my research, they were presented as poster at the "Ripples in the Cosmos" conference, which took place in Durham in July 2013. The poster contains a comprehensive analysis of the research to that point in time.

Observational tests of an inhomogeneous cosmology

Christoph Saulder[1,2], Steffen Mieske[1], Werner W. Zeilinger[2]

e-mail: csaulder@eso.org, smieske@eso.org, werner.zeilinger@univie.ac.at

affiliations: 1: ESO, Chile; 2: University of Vienna

institut für astrophysik
UNIVERSITÄTSSTERNWARTE WIEN

Christoph Saulder

Abstract

One of the biggest mysteries in cosmology is Dark Energy, which is required to explain the accelerated expansion of the universe within the standard model. But maybe one can explain the observations without introducing new physics, by simply taking one step back and re-examining one of the basic concepts of cosmology, homogeneity. In standard cosmology, it is assumed that the universe is homogeneous, but this is not true at small scales (a few 100 Mpc). Since general relativity, which is the basis of modern cosmology, is a non-linear theory, one can expect some backreactions in the case of an inhomogeneous matter distribution. Estimates of the magnitude of these backreactions (feedback) range from insignificant to being perfectly able to explain the accelerated expansion of the universe. In the end, the only way to be sure is to test predictions of inhomogeneous cosmological theories, such as timescape cosmology, against observational data. If these theories provide a valid description of the universe, one expects aside other effects, that there is a dependence of the Hubble parameter on the line of sight matter distribution. The redshift of a galaxy, which is located at a certain distance, is expected to be smaller if the environment in the line of sight is mainly high density (clusters), rather than mainly low density environment (voids). Here we present a test for this prediction using redshifts and fundamental plane distances of elliptical galaxies obtained from SDSS DR8 data. In order to get solid statistics, which can handle the uncertainties in the distance estimate and the natural scatter due to peculiar motions, one has to systematically study a very large number of galaxies. Therefore, the SDSS forms a perfect basis for testing timescape cosmology and similar theories. The amazing preliminary results of this cosmological test are shown here.

Preliminary results

At the moment

Using the data and models, that are currently available to us, we already managed to obtain some impressive preliminary results. At the moment we consider:

- **34000 elliptical galaxies** (within a redshift-interval of [0.01,0.1])
- distances obtained using the fundamental plane
- onlz **SDSS data** (+GalaxyZoo for classifications)
- foreground model based on an extended version of the Yang et al 2008 catalogue

The main issues with our preliminary results are:

- no foreground model below a redshift of 0.01 yet
- the simulated results to which we compare them assume perfect knowledge of the matter distribution
- the statistical analysis of the results is still very simple
- normalisation issues when comparing two different cosmologies

Our calculations are simple from a mathematical point of view (intersecting a straight line (of sight) with a bunch of spheres (the foreground model) and doing some interval nesting (the spheres might overlap) afterwards), we have to do them many (34000×155000) times. Because this is computationally very expensive, we have to use the **AstroCluster** in Vienna to perform our calculations.

In the future

We want to improve our results by:

- using distances of clusters than individual galaxies
- completing the foreground model using NED
- using better estimates of the mass distribution in the foreground
- applying more advanced statistical methods to distinguish between Λ-CDM and timescape cosmology
- considering uncertainties in the foreground model for the simulations

Our test does not require any additional observation because all the necessary data can be found in archives.
Additional scientific results:

- new calibrations of the **fundamental plane** (published)
- improved model of **mass distribution** in the local universe
- **peculiar velocities**

In the end, we hope to learn if the dark energy is really necessary to explain to accelerated expansion of the universe or if it just is "the greatest blunder" of our time. **Testing timescape cosmology** is an important step on this way.
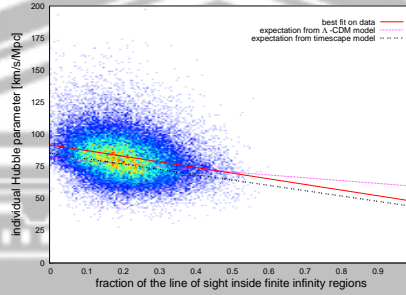

FIGURE 1: Our preliminary results based on real data. The inclination of our best fit tends to favour timescape cosmology at the moment. However, there are still several open issues with our model, which have to be addressed first before drawing any conclusions.

Theoretical motivation

Timescape cosmology

The general idea of inhomogeneous cosmology has been around for a very long time (Tolman,1934 and Bondi,1947). During the last 15 years significant advances were made on this initial very exotic field, mainly due to the work of Büchert (1997, 2000, 2002, 2003, 2011), Räsänen (2004, 2006, 2009, 2011), Wiltshire (2007, 2008, 2009, 2010, 2011, 2012) and others. The basic assumption is that since **general relativity** is a non-linear theory, **inhomogeneities** like voids and cluster can cause some **backreactions** (feedback), which may explain the observed accelerated expansion of the universe. To fully understand it a simple perturbative approach alone (Räsänen, 2006; Kolb et al., 2006; Ishibashi and Wald, 2006) is not sufficient. Therefore, Wiltshire (2007) developed a very sophisticated model of an inhomogeneous cosmology, which can mimic dark energy. It is called "timescape cosmology". He uses a simple two-phase model consisting of a **Swiss-cheese** distribution of **empty voids** and **dense walls** (clusters and filaments). Both regions are separated by the **finite infinity boundary** (see Fig.1), which encloses gravitationally bound regions and disconnects them from the freely expanding voids.
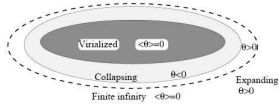

FIGURE 2: A schematic illustration of the concept of finite infinity (by David Wiltshire, 2007).

In this model, a backreaction also causes significant differences in the time flow, due to effects of quasilocal gravitational energy: the universe in the middle of a void is older than in the centre of a cluster. As a consequence of the importance of the local geometry in this model, the Hubble flow is not uniform anymore and the empty voids expand faster than the dense walls. At large scales these **different expansion rates** will lead to the signature of an **overall accelerated expansion** of the universe, because in timescape cosmology the fraction of the volume occupied by voids constantly increases with time. According to Wiltshire, the dynamics of this Swiss-cheese model can be described by following equations:

$$\left(\frac{\dot{a}}{a}\right)^2 + \frac{f_v^2}{9f_v(1-f_v)} - \frac{\alpha^2 f_v^{1/3}}{a^2} = \frac{8\pi G}{3}\bar{\rho}_0\frac{a_0^3}{a^3}$$

$$\ddot{f}_v + \frac{\dot{f}_v^2(2f_v-1)}{2f_v(1-f_v)} + 3\frac{\dot{a}}{a}\dot{f}_v - \frac{3\alpha^2 f_v^{1/3}(1-f_v)}{2a^2} = 0$$

The variable f_v denotes the volume fraction of voids in the universe, $\bar{a}$ is the scale factor and $\bar{\rho}_0$ denotes the renormalised critical density in this theory. Despite the elegance of this theory, the magnitude of these backreactions and their influence on cosmology is topic of hot discussion, with estimates on their significance from negligible to extremely important (Marra & Pääkkönen, 2010; Mattsson & Mattsson, 2010; Kwan et al., 2009; Clarkson et al., 2009; Paranjape, 2009; van den Hoogen, 2010). In the end, only a test of theory's predictions can provide an answer.

A more detail description of timescape cosmology and the test, we want to perform, can be found in our proceeding paper from last year:

http://arxiv.org/abs/1211.1926

Predictions and simulations

Testable predictions

The most accessible and most direct test of timescape cosmology is to find a **correlation** between the **individual Hubble parameter** (the Hubble parameter measured for one galaxy or cluster) and the **matter distribution** (the fraction with finite infinite regions (wall environment)) in the **line of sight** (to that galaxy or cluster).

- can only be measured in the local universe (Schwarz, 2010)
- difference of 17 to 22 % (Wiltshire, 2011) in the expansion rate between voids and walls to explain the observed accelerated expansion.
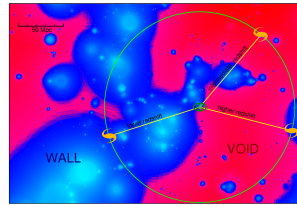

FIGURE 3: Redshift dependence on the line-of-sight matter distribution at a given distance. **Voids expand faster than walls.**

Simulations

To better qualify the expected correlation between the individual Hubble parameter and the fraction of the line sight within finite infinity regions (bound regions with an, on average, renormalised critical density), we used data from the **Millennium simulation**. One may naively assume that in the Λ-CDM model, there may be no correlation at all between the two parameters. However, one has to take account of biases due to the sample's selection and coherent infall into clusters. Assuming that the last snap-shot of the Millennium simulation provides a good representation of the present-day matter distribution in the universe, we introduce the effect of timescape cosmology artificially and compare the results for both cosmologies.

We **consider**:

- errors in the **redshift-measurement**
- **peculiar motions**
- the **Malmquist-bias**
- the selection of **elliptical galaxies only**
- uncertainties in the **distance measurement**

We do not yet consider:

- uncertainties in modelling the matter distribution from observations
- differences between extension of the finite infinite regions derived from the observed and the simulated matter distribution
- future enhancement in the distance measurement by using clusters instead of individual galaxies
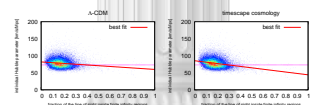- potential influence from the choice of the observer galaxy

FIGURE 4: The **expectation** for the Λ-CDM model and timescape cosmology from simulated data. With an simple fit, one is already able distinguish between the two cosmologies. More sophisticated statistical methods will provide even better criteria.

Observational data

To perform the suggested test one needs:

- **redshift** data
- an **independent distance indicator**
- a large **homogeneous sample** covering a large area of the sky
- a model of the **mass distribution** in the local universe

Therefore, we use:

- the Sloan Digital Sky Survey (SDSS)
- GalaxyZoo (for galaxy classification)
- the NASA Extragalactic Database (NED)

The fundamental plane

$$\log_{10}(R_0) = a \cdot \log_{10}(\sigma_0) + b \cdot \log_{10}(I_0) + c$$

For practical reasons, we decided to use the fundamental plane of giant elliptical galaxies as our distance indicator. It is a relation between:

- the physical radius R_0
- the central velocity dispersion σ_0
- the renormalised surface brightness $\log_{10}(I_0)$

Using the largest sample ever and the best available correction, we managed to achieve an accuracy in the **distance measurement** for individual galaxies of about **15%**.
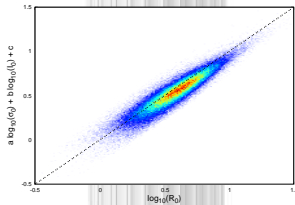
FIGURE 5: Our new calibration of the fundamental plane using about 93000 elliptical galaxies from SDSS DR8.

More details on our calibrations of the fundamental plane can be found in our recently accepted paper:

http://arxiv.org/abs/1306.0285

The foreground model

Since available SDSS-based catalogues of the mass distribution in the local universe are significantly more incomplete than claimed, we will build our own model using:

- **SDSS** DR8 redshifts
- **NED** (since SDSS is highly incomplete for redshifts lower than 0.01)
- a group finding algorithm (in development) bases on Eke et al., 2003
- **masses** derived from peculiar motions inside clusters
- masses from halo mass-luminosity relations (Yang et al., 2009)
- comparison with mock catalogues

Appendix B

Deutsche Zusammenfassung

Ein beobachtungsorientierter Test, welcher zwischen der Λ-CDM Kosmologie und einer alternativen Theorie namens Timescape Kosmologie zu unterscheiden vermag, wird in dieser Dissertation präsentiert. Letztere Theorie ist möglicherweise in der Lage die beobachtete beschleunigte Expansion des Universums im Rahmen der allgemeinen Relativitätstheorie ohne eine kosmologische Konstante zu erklären. Dazu berücksichtigt jene Theorie die beobachteten Inhomogenitäten und sagt unterschiedliche Expansionsraten für "Voids" und "Walls" (Filamente/Galaxienhaufen) voraus. Um dies zu testen wird eine Analyse von systematischen Variationen im lokalen Hubblefluss benötigt. Die Fundamentalebene der elliptischen Galaxien wird kalibriert und als Entfernungsindikator für diese Untersuchung benutzt. Weiters wird ein solides Modell der Materieverteilung im lokalen Universum aus SDSS und 2MRS Daten erstellt. "Mockkataloge" werden basierend auf der Millennium Simulation zusammengestellt um die Vorhersagen der Λ-CDM Kosmologie und der Timescape Kosmologie mit den Beobachtungen zu vergleichen. Die gesammelten Daten und die Mockkataloge werden einer detaillierten Analyse unterzogen um zu enthüllen ob dunkle Energie tatsächlich nötig ist um die beschleunigte Expansion des Universums zu erklären oder ob es sich dabei lediglich um einen Rückkopplungseffekt der allgemeinen Relativitätstheorie handeln könnte. Es wurden starke Hinweise gefunden, dass die Timescape Kosmologie nicht die beschleunigte Expansion erklären kann und dass stattdessen die Λ-CDM Kosmologie das von den Beobachtungsdaten bevorzugte Modell ist.

Appendix C

Curriculum Vitae

Personal

Name	Christoph
Surname	Saulder
Date of Birth	23$^{\text{rd}}$ October 1984
Place of Birth	Wels, Austria

Education

April 2010 - ongoing (waiting for defence)	**PhD in astronomy** University of Vienna
May 2013 - ongoing (graduation planned for autumn 2015)	**MSc in physics** University of Vienna
17$^{\text{th}}$ April 2013	BSc in physics graduated accreditation by changing from diploma programme
April 2013	**BSc in physics** University of Vienna
14$^{\text{th}}$ April 2010	MSc (Mag.rer.nat.) in astronomy graduated with distinction topic of the master thesis: **Dynamics of the Local Group in different theories of gravity**
October 2007 - April 2010	**MSc in astronomy** University of Vienna
30$^{\text{th}}$ August 2007	BSc (Bakk.rer.nat.) in astronomy graduated with distinction topic of the bachelor thesis: **Lie-Integrator**
October 2004 - August 2007	**BSc in astronomy** University of Vienna
October 2004 - April 2013 (moved to new programme)	**diploma study in physics** University of Vienna
21$^{\text{st}}$ June 2003	**Matura** ($\sim$ British A-level)
3$^{\text{rd}}$ July 2001 - 12$^{\text{th}}$ July 2001	**summer school** - course: **bionics** Sommerakademie für begabte Schülerinnen und Schüler; Bad Leonfelden, Austria
September 1995 - June 2003	**grammar school** with focus on **science** Bg. & Brg. Brucknerstraße; Wels, Austria
September 1991 - July 1995	**elementary school** Volksschule 9; Wels, Austria

Languages

German	English	Spanish	French	Russian
native	fluent	very good	good	moderate

Work experience

February 2015 - June 2015	**tutor, teaching assistant for mathematics** VHS Wien; Vienna, Austria
January 2014 - October 2014	**PhD student, researcher** European Southern Observatory; Garching bei München, Germany
November 2011 - October 2013	**PhD student, researcher** European Southern Observatory; Santiago, Chile
September 2008 - February 2009	**private tutor for mathematics** Schülerhilfe Wien; Vienna, Austria
July 2006	**janitor and gardener assistant** Berufsschule Kremsmünster; Kremsmünster, Austria
June 2006	**organisation assistant** Vienna Seminar of Nobel Laureates; Vienna, Austria
November 2005 - November 2009 about one week each year	**organisation assistant, catering assistant** Vienna Seminar on Particle Physics and Quantum field theory; Vienna, Austria
September 2005	**interviewer for a gerontological survey** department of social science, University of Vienna; Vienna, Austria
September 2004	**trade fair shop assistant** Socher; Sattledt, Austria
August 2004	**construction worker** Floortec; Pichl bei Wels, Austria
July 2004	**assembly line worker** Trodat; Wels, Austria
September 2003 - April 2004	compulsory military service: **soldier**, clerk Austrian armed forces; Kirchdorf an der Krems, Austria
July 2003 - August 2003	**promoter** Wesser; Grünstadt and Worms, Germany

Scientific publications

Hubble flow variations as a test for inhomogeneous cosmology	by **Saulder, C**; Mieske, S.; Zeilinger, W. W. & van Kampen, E. in preparation
The matter distribution in the local universe as derived from SDSS DR10 and 2MRS data	by **Saulder, C**; van Kampen, E.; Mieske, S. & Zeilinger, W. W. submitted to Astronomy & Astrophysics (June 2015)
Dozens of compact and high dispersion early-type galaxies in SDSS	by **Saulder, C**; van den Bosch, R. & Mieske, S. in Astronomy & Astrophysics, Volume 578, id.A134, 36 pp.
Calibrating the fundamental plane with SDSS DR8 data	by **Saulder, C**; Mieske, S.; Zeilinger, W. W. & Chilingarian, I. in Astronomy & Astrophysics, Volume 557, id.A21, 36 pp.
Observational aspects of an inhomogeneous cosmology	by **Saulder, C**; Mieske, S. & Zeilinger, W. W. in Proceedings of VIII International Workshop on the Dark Side of the Universe (DSU 2012)

Talks, Conferences, Workshops, and Visits

20th - 24th July 2015	**talk** at Alpine Cosmology **workshop** 2015; Silvretta mountains, Austria/Switzerland
8th - 9th July 2015	**visit** to ESO; Garching, Germany
22nd - 26th June 2015	**talk** at EWASS 2015 **conference**; Tenerife, Spain
20th - 21st October 2014	**visit** to MPIA; Heidelberg, Germany
3rd December 2013	**talk** at ESO; Santiago, Chile
18th - 22nd November 2013	**LOC member** & **poster** at Deconstructing Galaxies **conference**; Santiago, Chile
22nd - 26th July 2013	**poster** at Ripples in the Cosmos **conference**; Durham, UK
16th April 2013	**talk** at Vienna University of Technology; Vienna, Austria
2nd October 2012	**talk** at University of Valparaiso; Valparaiso, Chile
8th - 10th August 2012	**talk** & **visit** to University of Concepcion; Concepcion, Chile
27th July 2012	**talk** at Cosmology Today **workshop**; Santiago, Chile
10th - 15th June 2012	**talk** & **poster** at Dark Side of the Universe **workshop**; Buzios, Brazil
14th - 17th May 2012	**poster** at Testing General Relativity with Astrophysical Systems **conference**; Boston, USA
7th - 11th May 2012	**visit** to the Harvard-Smithsonian CfA; Boston, USA
12th October 2010	**talk** at Vienna University of Technology; Vienna, Austria

Outreach and Press

30th October 2013	**experiments for children** at the family day celebrating the 50th anniversary of ESO in Chile
10th October 2013	**educative workshop** on "planets and rockets" with experiments for children at the National Science Fair; Santiago, Chile
13th August 2013	**talk with experiments** on "The solar system and beyond" for children at Deutsche Schule St. Thomas Morus; Santiago, Chile
2nd July 2013	**talk with experiments** on "The solar system and beyond" for children at Colegio Dunastair; Santiago, Chile
16th April 2013	**interview** with me on the Austrian **radio** Ö1
12th March 2013	meeting with the **Austrian Minister of Science** at the Austrian embassy; Santiago, Chile
19th December 2012	**interview** with me in the Austrian **newspaper** Kurier
6th December 2012	meeting with the **Austrian President** at ESO; Santiago, Chile
23th November 2012	guiding a group of Austrian **journalists** through the ESO premises; Santiago, Chile
10th November 2012	**ESO outreach** at 170th anniversary of the Univerdad de Chile on Cerro Calan; Santiago, Chile
16th November 2011	meeting with a delegation of several **members of the Austrian parliament** at ESO; Santiago, Chile
15th June 2011	**public observations** of the lunar eclipse at the Institute for Astronomy of the University of Vienna; Vienna, Austria
14th May 2011	**Day of Astronomy** at the Institute for Astronomy of the University of Vienna; Vienna, Austria